WALDBUSSER, AMY L. MS. Electrocatalytic C–H/N–H Functionalization Mediated by Ferrocene Derivatives. (2021)
Directed by Dr. Shabnam Hematian. 175 pp.

The functionalization of carbon- or nitrogen-centered radical species is an important process in many chemical reactions aimed at turning simple chemical feedstocks, such as those in petroleum products, into chemicals of higher complexity and value. Although there exist a variety of methods to perform these reactions, electrochemistry stands out as a powerful approach, due to its mild, cost effective, and tunable features. Electrochemical oxidation of a substrate offers more control over the process by isolating the produced radical species, allowing further functionalization reactions to occur, and lowering the chance for unwanted side reactions. Additionally, a redox mediator can be utilized to eliminate issues that can occur with direct substrate oxidation, particularly that of primary amines, such as fouling of the electrode surface or degradation of the substrate. Ferrocene (Fc) and its analogs are ideal compounds for this role, as their well-known one-electron redox couple going between ferrocene and ferricenium (Fc^+) is very reversible. Additionally, their redox potentials are in the appropriate range for the oxidation of amines and can be easily tuned by altering the nature of the substituents on the cyclopentadienyl (Cp) rings. We begin with a thorough electrochemical study of ferrocene and nine of its derivatives with either electron-donating or electron-withdrawing substituents in three different solvents and with two different supporting electrolytes (Chapter 1). This investigation gave us a variety of possible redox mediators that we could use to perform the electrocatalytic anaerobic oxidation of benzylic amine substrates (Chapter 2).

Chapter 1 details a facile and effective strategy for the preparation of a series of ferricenium complexes bearing either electron-donating or electron-withdrawing substituents with weakly coordinating anions such as $[B(C_6F5)_4]^-$ or SbF_6^-. These systems were thoroughly investigated for their ground state electronic structures in both solution and solid states using infrared (IR) and nuclear magnetic resonance (NMR) spectroscopies as well as single crystal X-ray crystallography. We also present the redox

behavior of the corresponding ferricenium/ferrocene redox couples including potential values ($E_{1/2}$), peak-to-peak separation ($\Delta E_{1/2}$), anodic/cathodic peak current ratios (i_{pa}/i_{pc}) and diffusion coefficients (D) of the redox active species in order to provide a better understanding of our library of ferrocene redox mediators in deferent media. Our electrochemical studies involved three different solvents and two *tetra-n*-butylammonium supporting electrolytes with a more traditional anion, hexafluorophosphate (PF_6^-), as well as pentafluoro substituted *tetra*-phenylborate, $[B(C_6F_5)_4]^-$. Notably, our findings point to the significant effect of ion pairing in lowering the energy necessary for reduction of the ferricenium ion and the overall half-wave potential values in lower-polarity media.

Chapter 2 describes the anaerobic electrocatalytic oxidation of two benzylic primary amines (i.e., benzylamine and 2-picolylamine) in the presence of an electron deficient ferrocene derivative as a redox mediator. The use of the appropriate redox mediator prevented fouling of the electrode surface, which is dominant during the direct electrochemical oxidation, as well as decreased the half-wave potential at which the catalytic oxidation reaction occurred ($E_{cat/2}$). Cyclic voltammetry studies revealed an E_rC_i' catalytic process between the ferrocene derivative and both substrates. Through anaerobic controlled-potential electrolysis, we have demonstrated a method that utilized 90% of electrons removed from the system towards forming the desired coupled imine product of benzylamine oxidation while avoiding an excess of problematic hydrolysis and other side reactions. The major and minor products obtained from bulk electrolysis experiments were characterized through IR, ^{1}H- and ^{13}C-NMR spectroscopies and proposed mechanistic steps were laid out for the electrocatalytic process. Our results can guide the development of new electrocatalytic systems aimed at oxidizing and transforming simple compounds into chemicals of higher complexity and value.

ELECTROCATALYTIC C–H/N–H FUNCTIONALIZATION MEDIATED BY FERROCENE DERIVATIVES

by

Amy L. Waldbusser

A THESIS

Submitted to
the Faculty of The Graduate School at
The University of North Carolina at Greensboro
in Partial Fulfillment
of the Requirements for the Degree
Master of Science

Greensboro

2021

Approved by

Dr. Shabnam Hematian
Committee Chair

DEDICATION

I would like to dedicate this work to all of my incredible family and friends who have supported me through this process. I would also like to dedicate this to the Hematian group, who I am indebted to for their help and friendship these past two years. I am truly grateful to be surrounded by those who encourage me to challenge myself and stay positive, even when things get difficult.

APPROVAL PAGE

This thesis written by Amy L. Waldbusser has been approved by the following committee of the Faculty of The Graduate School at The University of North Carolina at Greensboro.

Committee Chair	Dr. Shabnam Hematian
Committee Members	Dr. Jerry Walsh
	Dr. Nadja Cech

4/29/2021
Date of Acceptance by Committee

4/14/2021
Date of Final Oral Examination

ACKNOWLEDGEMENTS

I would first like to acknowledge the amazing group that is the Hematian lab. Dr. Shabnam Hematian, who took the time to make sure I fully understood every concept I needed to in order to properly perform my research. Maria Carrasco, for all of the laughs, perfect music playlists, funny social media posts, and study sessions – not to mention the countless times she offered help in the lab. Dr. Firoz Khan, who took on the daunting task of training me as a new member of the lab. I will be forever grateful for his help and advice. Hadi Pourhadi, for constantly having fruit in the office and giving us all a reason to smile throughout the days. We have all worked extremely hard during these difficult times, and I am very proud of what we have achieved. I feel very fortunate to have been a part of this group and will never forget the memories of late nights in the lab, dance parties, and cheers to our accomplishments.

I would also like to acknowledge and thank the faculty and staff of the Chemistry and Biochemistry department at UNCG for constantly supporting their students and providing a safe environment for us. Dr. Nadja Cech, for meeting with me prior to my coming to UNCG and encouraging me to attend graduate school, as well as being a member of my committee and providing important feedback and advice. Dr. Jerry Walsh, for his electrochemistry expertise and fun chemistry demonstrations. Dr. Franklin Moy, for maintaining the NMR facility, as well as NMR training and helping us whenever we run into issues with running an experiment.

TABLE OF CONTENTS

LIST OF TABLES

LIST OF FIGURES

LIST OF SCHEMES

CHAPTER I: SYNTHETIC, SPECTROSCOPIC, STRUCTURAL, AND ELECTROCHEMICAL INVESTIGATIONS OF FERRICENIUM DERIVATIVES WITH WEAKLY COORDINATING ANIONS: ION PAIRING, SUBSTITUENT, AND SOLVENT EFFECTS

This work was co-authored with the following authors and has been recently accepted into Dalton Transactions:

Firoz Shah Tuglak Khan, Amy L. Waldbusser, Maria C. Carrasco, Hadi Pourhadi, and Shabnam Hematian

Dalton Trans. **2021**, *Just accepted.* DOI: https://doi.org/10.1039/D1DT01192H

Abstract: A facile and effective strategy for the preparation of a series of ferricenium complexes bearing either electron-donating or electron-withdrawing substituents with weakly coordinating anions such as $[B(C_6F_5)_4]^-$ or SbF_6^- is reported. These systems were thoroughly investigated for their ground state electronic structures in both solution and solid states using infrared (IR) and nuclear magnetic resonance (NMR) spectroscopies as well as single crystal X-ray crystallography and electrochemical measurements. The X-ray structures of the six electron-deficient ferricenium derivatives are of particular interest as only a handful (~5) of such derivatives have been structurally characterized to date. Comparison of the structural data for both neutral and oxidized derivatives reveals that the nature of the substituents on the cyclopentadienyl (Cp) ligands displays a more significant impact on the metal-ligand separations (Fe···Ct) in the oxidized species than in their neutral analogs. Our ^{1}H-NMR measurements corroborate that in the neutral ferrocene derivatives, electron-donating ring substitutions lead to a greater shielding of the ring protons while electron-withdrawing groups via induction deshield the nearby ring protons. However, the data for the paramagnetic ferricenium derivatives reveals that this substitutional behavior is more complex and fundamentally reversed, which is further supported by our structural studies. We ascribe this reversal of behavior in the ferrocenium derivatives to the δ back-donation from the iron atom into the Cp rings which can lead to the overall shielding of the ring protons. Interestingly, our NMR results for the electron-deficient ferricenium derivatives in solution also indicate a direct correlation between the solvent dielectric constant and the energy barrier for rotation around the metal-ligand bond in these systems, whereas such a correlation is absent or not significant in the case of the electron rich ferricenium species or the corresponding neutral ferrocene analogs. In this work, we also present the electrochemical behavior of the corresponding ferricenium/ferrocene redox couples including potential values ($E_{½}$), peak-to-peak separation ($\Delta E_{½}$), and diffusion coefficients (D) of the redox active species in order to provide a concise outline of these data in one place. Our electrochemical studies involved three different solvents and two supporting electrolytes. Notably, our findings point to the significant effect of ion pairing in lowering the energy necessary for reduction of the ferricenium ion and $E_{½}$ in lower-polarity media. This has significant implications in applications of the ferrocene or ferricenium derivatives as redox agents in low-polarity solvents where an accurate determination of redox potential is critical.

Introduction

Bis(η^5-cyclopentadienyl) iron(II), or more commonly known as ferrocene (**Fc**), was discovered in the mid-20th century.[1] Ever since, this fascinating sandwich complex has been widely studied in terms of its remarkable structure, chemical bonding and reactivity and it is often considered to be a showpiece of modern organometallic chemistry.[2] Ferrocene and its numerous derivatives have increasingly found use in catalysis, particularly those involving asymmetric and stereoselective transformations, as well as in the development of new functional materials such as optical and redox sensors, batteries, and bioconjugates for medicinal and biotechnological applications.[3]

Ferrocene can undergo a chemically reversible, outer-sphere one-electron oxidation to generate bis(η^5-cyclopentadienyl) iron(+1), also known as the ferricenium ion (**Fc⁺**).[4] This metal-based outer-sphere electron transfer in the ferricenium ion/ferrocene couple is commonly employed as an internal or external reference for electrochemical measurements in organic solvents.[5] It is worth noting that, recently, the first examples of the two-electron oxidized as well as the one-electron reduced form of ferrocene derivatives have also been structurally and spectroscopically characterized.[6]

Ferricenium salts are generally prepared through the electrochemical or chemical oxidation of the ferrocene precursors. The first isolated ferricenium salt was the dark blue crystalline ferricenium tetrachlorogallate (**Fc**[$GaCl_4$]) reported by Wilkinson in 1952.[7] Subsequently, a combination of theoretical and experimental efforts was focused on understanding the electronic structure and physicochemical properties of ferrocene and the ferricenium ion.[8]

Ferricenium salts are considered mild one-electron outer-sphere oxidants. The redox potential of the ferricenium salts can be tuned by altering the nature of the substituents on the cyclopentadienyl (Cp) rings. Thus, the ferricenium derivatives with defined redox potentials are especially useful in both redox catalysis and redox titrations or stoichiometric reactions where selective oxidation under mild conditions is desired.[9] Ferricenium salts are moderately stable in acidic aqueous solutions but they rapidly decompose in many organic solvents and in air.[10] The preparation of ferricenium derivatives, particularly those bearing electron-withdrawing substituents, is relatively difficult due their instability towards water, dioxygen, and nucleophilic reagents.[8b, 9, 11] The ferricenium ions can be prepared with a variety of counter anions, such as *tetra*-fluoroborate (BF_4^-), hexafluorophosphate (PF_6^-), hexafluoroantimonate (SbF_6^-), or *tetra*-phenylborate (BPh_4^-).[9] Ferricenium hexafluorophosphate (**Fc**[PF_6]) and ferricenium *tetra*fluoroborate (**Fc**[BF_4]) are the only commercially available and the two most commonly used ferricenium salts.[12] The nature of the counter anions not only alter the magnetic moment of ferricenium complexes, but also dictates their solubility in organic solvents.[3e, 8c, 13]

In more recent studies, fluoroarylborates such as *tetrakis*(pentafluorophenyl)borate ($[B(C_6F_5)_4]^-$ or $BArF_{20}$), or its aryl CF_3-substituted analog *tetrakis*[*3,5*-bis(trifluoromethyl)phenyl]borate ($BArF_{24}$), have been used as counter anions for the preparation of ferricenium salts.[14] These bulky counter anions with lower nucleophilicity exhibit remarkable chemical stability and their weaker ion-pairing interactions with the ferricenium ion result in a markedly increased solubility of the salts in lower-polarity media.[15] These systems are particularly very attractive one-electron chemical redox agents for synthesis, catalysis, and kinetic and mechanistic investigations of a variety of redox systems in lower-polarity solvents, particularly *low-temperature* studies.[9, 16]

In the present study, we report a concise and straightforward strategy for preparation of a series of ferricenium complexes with electron-donating and electron-withdrawing substituents with either $BArF_{20}$ or SbF_6^- as a counterion. Nine new ferricenium derivatives are readily isolated in high yields and all of them show exceptional solubility in lower-polarity solvents (e.g., tetrahydrofuran (THF), diethyl ether, toluene and benzene) as compared to their common PF_6^- or BF_4^- salts that are only soluble in high-polarity organic solvents such as acetonitrile, acetone, and alcohols. Scheme 1 shows the structures of ferricenium complexes described in this study.

Scheme 1. Synthetic Scheme for the Preparation of the Ferricenium Complexes Described in This Study.

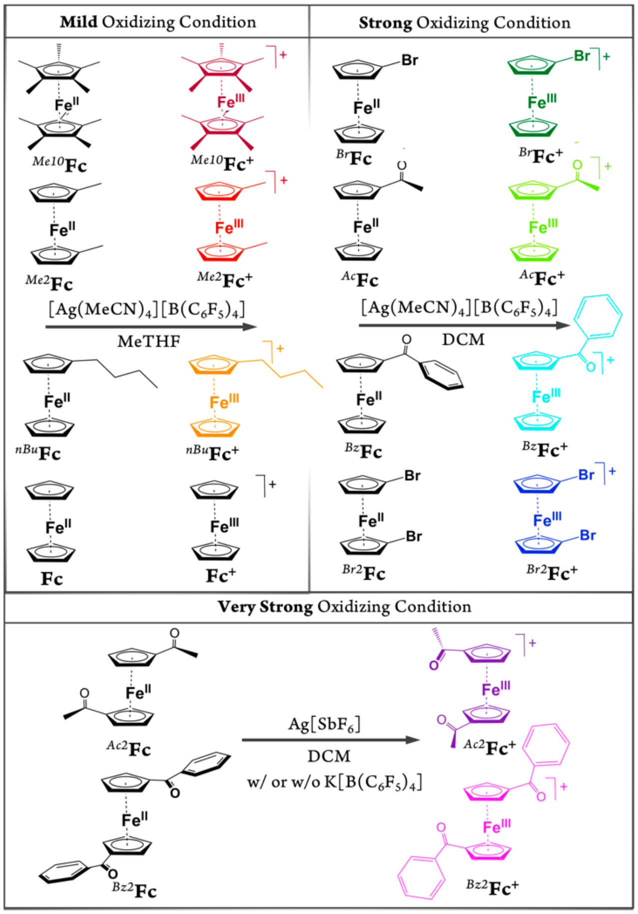

*All ferricenium complexes were prepared with BArF$_{20}$ as the counter anion, except for ^{Bz2}**Fc**[SbF$_6$]. See the Experimental Section for an alternative synthetic procedure for ^{Bz}**Fc**[B(C$_6$F$_5$)$_4$] and further details.

With the exception of the parent ferricenium BArF$_{20}$ (that has previously been structurally characterized),[17] molecular structures of all nine ferricenium derivatives used in this study were determined via single crystal X-ray crystallography. Other than the structure of *1,1'*-diacetylferricenium (^{Ac2}**Fc$^+$**) that has been previously reported as the N(SO$_2$CF$_3$)$_2^-$, NTf$_2^-$, salt,[18] the structures of five ferriceniums with electron-withdrawing substituents (i.e., ^{Br}**Fc$^+$**, ^{Ac}**Fc$^+$**, ^{Bz}**Fc$^+$**, ^{Br2}**Fc$^+$**, and ^{Bz2}**Fc$^+$**) are reported here for the first time.[19] These systems were further studied for their ground state electronic structures using infrared (IR) and nuclear magnetic resonance (NMR) spectroscopies. The latter revealed an interesting correlation between the solvent dielectric constant and the energy barrier for rotation around the Fe-Cp axis in the electron-deficient ferricenium derivatives.

Herein, we also describe the redox behavior and potential values of the corresponding ferricenium/ferrocene (**Fc**$^{+/0}$) redox couples in a number of organic media in order to provide a concise outline of these data in one place. Our electrochemical analyses involved three different solvents and two *tetra*-*n*-butylammonium supporting electrolytes with a more traditional anion, PF_6^-, as well as $[B(C_6F_5)_4]^-$. The results point to the significant effect of the ion pairing in reducing the energy necessary for reduction of the ferricenium ion and the overall $E_{½}$ potential values.

Results and Discussion

SYNTHESIS AND CHARACTERIZATION OF FERRICENIUM DERIVATIVES

We used two silver(I) salts as one-electron oxidizing agents for preparation of all of the ferricenium complexes.[20] One is the $BArF_{20}$ analog of silver(I) which is a mild to strong oxidant depending on the nature of the solvent. The synthesis of silver complex, $[Ag(MeCN)_4][B(C_6F_5)_4]$, was performed using a modified procedure of Zhang *et al*.[21] The silver(I) salt was readily prepared by metathesis of silver nitrate, $AgNO_3$, and the commercially available potassium *tetrakis*(pentafluorophenyl)borate, $K[B(C_6F_5)_4]$, in acetonitrile (MeCN). Additionally, the molecular structure of the silver complex and coordination of four acetonitrile ligands were unambiguously confirmed by ^{1}H-NMR and IR spectroscopies as well as X-ray crystallography, see Experimental Section.

The IR spectrum of $[Ag(MeCN)_4]^+$ exhibits two bands in the C≡N stretching region, at 2322 and 2295 cm^{-1}. The band at higher energy appears to arise from binary combination of the symmetric methyl deformation at 1367 cm^{-1} and symmetric C–C stretch at around 950 cm^{-1}(Figure 31). The latter is buried under the counter anion signals and upon deuteration it shifts to 840 cm^{-1}. These two vibration modes are both of A_1 symmetry, thus forming a combination mode. In the deuterated complex, $[Ag(CD_3CN)_4]^+$, the combination band is absent which further supports this supposition that only the band at 2295 cm^{-1} is due to the C≡N stretching vibration. This band appears at slightly lower frequency (2287 cm^{-1}) in the deuterated complex (Figure 32). Additionally, as a result of complexation, the C≡N stretching frequencies are shifted to higher frequencies in $[Ag(MeCN)_4]^+$ (i.e., $\Delta\upsilon_{(C\equiv N)}$: +29 cm^{-1}) as compared to free acetonitrile ($\upsilon_{free(C\equiv N)}$: 2266 cm^{-1}), which is well-known for nitrile adducts.[22]

The other oxidizing agent is the silver(I) salt with the hexafluoroantimonate counter anion, $Ag[SbF_6]$, which is commercially available and was used as a very strong oxidizing agent. A series of ferricenium $BArF_{20}$ complexes with electron-donating or electron-withdrawing groups were synthesized using three main preparative procedures with different oxidizing strengths listed here:

1. Mild oxidizing condition (< 100 mV *vs* $\mathbf{Fc^{+/0}}$): $[Ag(MeCN)_4][B(C_6F_5)_4]$ in MeTHF
2. Strong oxidizing condition (100 to 400 mV *vs* $\mathbf{Fc^{+/0}}$): $[Ag(MeCN)_4][B(C_6F_5)_4]$ in DCM
3. Very strong oxidizing condition (> 400 mV *vs* $\mathbf{Fc^{+/0}}$): $Ag[SbF_6]$ in DCM

The solvent and counter anion dependencies of the oxidation potential of silver(I) were used to provide the mild, strong, and very strong oxidizing environments in MeTHF or DCM (Scheme 1). The redox potential for the $Ag^{+/0}$ couple in nonaqueous solutions is not easily measured and generally estimated values are available in the literature. For example, the formal redox potential of the $Ag^{+/0}$ couple in THF ($E^{0\prime}$ = 410 mV *vs* $\mathbf{Fc^{+/0}}$) is reported to be about 0.24 V more negative than that in DCM ($E^{0\prime}$ = 650 mV *vs* $\mathbf{Fc^{+/0}}$).[9, 23] Our results for $[Ag(MeCN)_4][B(C_6F_5)_4]$, already bearing the four coordinated acetonitrile in MeTHF ($168 < E^{\circ\prime} < 244$ mV *vs* $\mathbf{Fc^{+/0}}$) and DCM ($357 < E^{\circ\prime} < 533$ mV *vs* $\mathbf{Fc^{+/0}}$), are in agreement with the previous reports showing that, with the increase in the coordination ability of the solvent the oxidizing strength of silver(I) salts significantly decreases.

The redox potentials of the ferrocene derivatives measured in this study (*vide infra*) were used in the Nernst equation to predict the position of the redox equilibriums in order to assign the appropriate preparation procedures. The sub-stoichiometric oxidation of all ferrocene derivatives was accomplished by limiting the amount of the appropriate silver(I) agents to assure full consumption of the oxidants. The remaining excess ferrocene complexes were simply removed by several dry hexanes rinses.

Mild oxidation of the parent ferrocene and three of its electron-rich derivatives bearing one or more electron-donating substituents, including *n*-butylferrocene (^{nBu}**Fc**), *1,1'*-dimethylferrocene (^{Me2}**Fc**), and decamethylferrocene (^{Me10}**Fc**), was achieved with the addition of a sub-stoichiometric amount of silver(I) $BArF_{20}$ salt in MeTHF solution. In turn, the sub-stoichiometric amount of silver(I) $BArF_{20}$ salt in DCM solution was employed for the oxidation of all three monosubstituted ferrocene derivatives with electron-withdrawing groups, including *1*-bromoferrocene (^{Br}**Fc**), *1*-acetylferrocene (^{Ac}**Fc**), and *1*-benzoylferrocene (^{Bz}**Fc**), as well as one *1,1'*-disubstituted derivative, *1,1'*-dibromoferrocene (^{Br2}**Fc**).

The corresponding ferricenium $BArF_{20}$ analogs were isolated in high yields (>80%). *Note:* For both ketone-substituted ferrocenes, the order of addition of reagents is reversed (i.e., the solution of substituted ferrocene is gradually added to the silver(I) solution), see Experimental Section. This is due to the ability of the acetyl or benzoyl groups on the Cp rings to coordinate to the silver(I) center which can hinder the electron transfer process from ferrocene to Ag(I). This is consistent with the considerably lower oxidizing ability of silver(I) salts in acetone ($E°' = 180$ mV *vs* $\mathbf{Fc^{+/0}}$).[9] As an alternative procedure for preparation of ^{Bz}**Fc**$[B(C_6F_5)_4]$, a 1:1 solution of the *1*-benzoylferrocene and $K[B(C_6F_5)_4]$ can be added dropwise to a solution of $Ag[SbF_6]$ in DCM.

The other two highly electron-deficient derivatives, *1,1'*-diacetylferrocene (^{Ac2}**Fc**) and *1,1'*-dibenzoylferrocene (^{Bz2}**Fc**), were oxidized using $Ag[SbF_6]$ in DCM. The stronger oxidizing strength of this silver(I) salt in DCM was confirmed through its reactivity toward the *tris*(4-bromophenyl)amine (i.e., $N(C_6H_4Br\text{-}4)_3$). While $[Ag(MeCN)_4][B(C_6F_5)_4]$ does not react with the amine in DCM, the addition of $Ag[SbF_6]$ instantly oxidizes the triarylamine forming the signature blue color of the corresponding radical cation, known as Magic Blue ($E°' = 700$ mV *vs* $\mathbf{Fc^{+/0}}$). We also independently confirmed the redox potential of *tris*(4-bromophenyl)amine in DCM, in the presence of PF_6^- (i.e., as a model for SbF_6^-) and $BArF_{20}$, to be about 705 and 675 mV *vs* $\mathbf{Fc^{+/0}}$, respectively (Figure 33).

The two oxygen atoms of the ketone moieties of both ^{Ac2}**Fc** and ^{Bz2}**Fc** can also chelate to the silver(I) center forming a red complex as observed previously for similar compounds.[24] Therefore, the order in which the reagents are added is critical to initiate the redox reaction. The isolated ^{Ac2}**Fc**[SbF$_6$] complex was then converted to the very soluble BArF$_{20}$ analog through metathesis by K[B(C$_6$F$_5$)$_4$] in *1,2*-difluorobenzene. The ^{Bz2}**Fc**[SbF$_6$] on the other hand was used as the [SbF$_6$]$^-$ salt due to its satisfactory solubility and stability.

Alternatively, the ^{Ac2}**Fc**[B(C$_6$F$_5$)$_4$] complex can be readily obtained by dropwise addition of a 1:1 mixture of ^{Ac2}**Fc** and K[B(C$_6$F$_5$)$_4$] to a solution of Ag[SbF$_6$] in DCM. Adding the first drop of the mixture leads to the development of a light pink color indicating the transient formation of the ferrocene chelated silver(I) complex. This complex is then slowly oxidized by the excess silver(I) ions present in the solution to the green ^{Ac2}**Fc$^+$** species. After this point, each additional drop of the mixture leads to fast oxidation of the ^{Ac2}**Fc** and further appearance of the green color. This suggests that the initially generated ferricenium species may act as an electron transfer mediator/relay between the ferrocene-chelated silver(I) complex and the excess silver(I) pool allowing for the faster oxidation process.

Generally, removal of silver metal as the byproduct of the oxidation of the ferrocene complexes is straightforward. However, it is important to note that due to the reversibility of the ferricenium/ferrocene couple, the presence of a slight amount of silver metal impurity can result in partial re-reduction of the ferricenium sample upon dissolution in more coordinating solvents in which the silver salt is a weaker oxidant (i.e., the product distribution is governed by the Nernst equation). Since the BArF$_{20}$ analogs of all these ferricenium derivatives are highly soluble in either MeTHF or DCM, the silver metal is a very finely divided precipitate and effective filtration can be achieved through the use of a filtration aid such as Celite.

It is also worth mentioning that all our synthetic procedures were performed under rigorous air-free conditions as many of the erratic results reported in literature for many ferricenium complexes including their relatively low extinction coefficients can be explained by the irreversible decomposition of ferricenium species in solutions exposed to air. It is confirmed that the yellow decomposition products reported in the earlier literature are not the starting ferrocene complexes.[25] Carbon and hydrogen analyses of all nine ferricenium $BArF_{20}$ complexes, as well as ^{Bz2}**Fc**[SbF_6], indicated that the compounds were ≥ 99% pure, see Experimental Section. Before we discuss further characterization of the ferricenium derivatives, it is helpful to point out the unique structural feature of the ferricenium ion. Due to a very small rotational energy barrier, **Fc**$^+$ can adopt an eclipsed (D_{5h}) or staggered (D_{5d}) conformation or with the rings slightly twisted, it can even conform to an intermediate skewed (D_5) geometry. We will expand on this point later in the discussion of the X-ray structures.

The signature blue or green color (λ_{max} ~ 621–780 nm) of the ferricenium complexes is present in all of our derivatives. This is the ligand-to-metal charge transfer (LMCT) transition which is from the e_{1u} orbitals of Cp ligands to the hole in the essentially non-bonding e_{2g} orbitals on the ferric center.[8c, 8d, 26] The lowest energy absorption maxima and extinction coefficient values for all ferricenium derivatives are provided in the Experimental Section.

Infrared Spectroscopy

The attenuated total reflection (ATR) Fourier Transform Infrared (FT-IR) spectra of the ferrocene derivatives were obtained in the solid state except for ^{nBu}**Fc** which is liquid at room temperature. The strongest fundamental vibrations for the ferrocene derivatives appear around 815, 1000, 1410 and 3100 cm^{-1} which can respectively be ascribed to C–H out-of-plane bending, C–H in-plane bending, C–C stretching and C–H stretching of the cyclopentadienyl rings.[26c, 27] One binary combination band containing the C–H out-of-plane bending and C–H stretching is also observed at around 3915 cm^{-1}. As expected, in ^{Me10}**Fc** spectrum the three signature absorptions associated with the C–H bonds of the Cp ligands, as well as the binary combination band, are absent. Tables 6, 7, and 8 in Supporting Information list the vibrational frequencies for all ferrocene and ferricenium derivatives.

Aside from the counterion peaks (i.e., $BArF_{20}$ or SbF_6^-), the infrared spectra of ferricenium derivatives noticeably have fewer strong bands than their neutral ferrocene counterparts (Figures 19-28). Due to the one-electron oxidation, the C–H stretching frequencies of the Cp rings are shifted to higher energies by about 30–40 cm^{-1} in all of the ferricenium derivatives.

The carbonyl stretching modes of the ketone-substituted ferrocene species are located in the 1620–1650 cm^{-1} region and were assigned based on previous literature reports.[24a, 28] The C=O stretching bands of all ketone-substituted ferriceniums appear at about 35–48 cm^{-1} higher frequencies when compared with the neutral counterparts, indicating a significant strengthening of the carbonyl bond in the oxidized forms, see Table 1 and Supporting Information. This is in agreement with the shorter C=O bond distances (~ 1.212 Å) obtained for the oxidized complexes from our X-ray crystallography measurements as compared to those reported for the neutral ketone-substituted ferrocenes (~ 1.224 Å), *vide infra*. The first overtone of the C=O stretching band is also observed in the 3295–3380 cm^{-1} region in both neutral and oxidized ketone-substituted species.[29]

Table 1. Comparison of C=O Stretching Frequencies and Bond Lengths in Ketone-Substituted Derivatives.

Compound	$\upsilon_{(C=O)}$ (cm^{-1})	1st Overtone $\upsilon_{(C=O)}$ (cm^{-1})	C=O (Å)	Reference for X-ray Structure
^{Ac}**Fc**	1650	3297	1.223	[30]
^{Ac}**Fc$^+$**	1698	3378	1.209	This work
^{Ac2}**Fc**	1650	3296	1.224	[31]
^{Ac2}**Fc$^+$**	1697	3376	1.209	This work
^{Bz}**Fc**	1624	3242	1.225	[32]
^{Bz}**Fc$^+$**	1659	3308	1.215	This work
^{Bz2}**Fc**	1630	3252	1.222	[33]
^{Bz2}**Fc$^+$**	1665	3315	1.215	This work

NMR Spectroscopy

All ferricenium species, like many other paramagnetic sandwich complexes, are NMR-active owing to their very short electron spin relaxation times, which is a consequence of their doubly degenerate electronic ground state (i.e., $^2E_{2g}$).[34] Therefore, the solution structures of all ten ferricenium derivatives presented in this work were conveniently confirmed by ^{1}H- and ^{19}F-NMR spectroscopies.

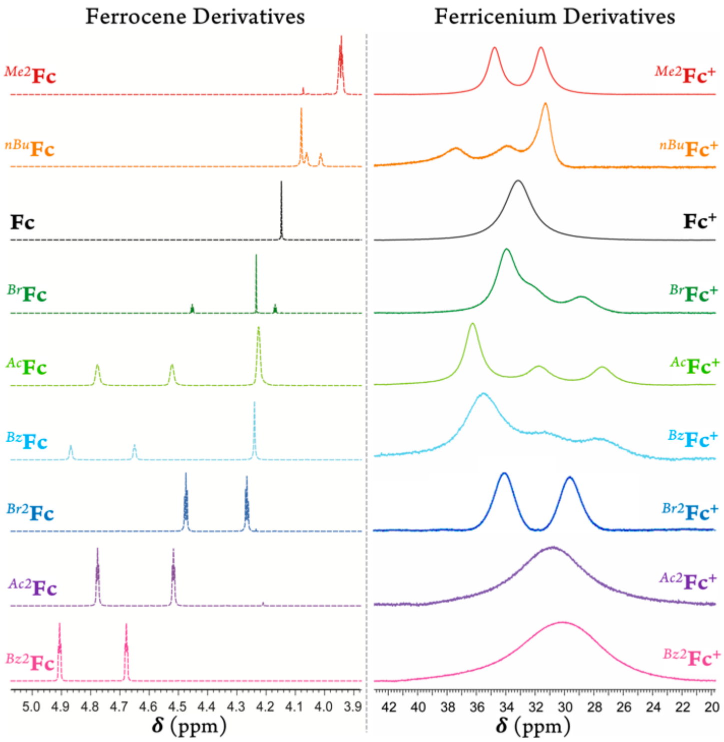

Figure 1. Part of the ^{1}H-NMR spectra of (left) the ferrocene derivatives and (right) the ferricenium analogs in acetone-d_6 at room temperature. Due to reaction with acetone, the spectra of ^{Ac2}**Fc⁺** and ^{Bz2}**Fc⁺** were recorded in CD_2Cl_2.

The ^{1}H-NMR spectrum of the parent diamagnetic **Fc** displays one sharp resonance at 4.2 ppm for the Cp rings (Figure 29). The position and multiplicity of the signal for Cp protons are sensitive to ring substitution. In the neutral ferrocene derivatives, electron-donating ring substitutions give rise to a greater shielding of the ring protons (δ = 3.9–4.1 ppm) while electron-withdrawing groups via induction deshield the nearby Cp protons (δ = 4.3–4.9 ppm). This substitutional behavior is more complex and reversed in ferricenium derivatives (Figure 1). We propose that in the oxidized complexes, the δ back-donation from the iron $d_{x2–y2}$ and d_{xy} orbitals to the Cp ring (i.e., the increase in bonding character of the e_{2g} molecular orbitals) is responsible for this reversal of behavior. In the substituted ferricenium, the ring protons of the Cp ligand with the more stabilized orbitals experience more significant shielding due to a better energy match (and overlap) with the iron and stronger δ back-donation.

The ^{1}H-NMR signal of the parent paramagnetic **Fc⁺** complex (S = ½) appears as a single broad peak at 33.2 ppm, which is shifted ~ 29 ppm downfield relative to that of **Fc** (Figure 30). Interestingly, the introduction of electron-donating group(s) in the ferricenium species have a net deshielding effect on the ring protons, whereas electron-withdrawing substituents tend to shield the substituted ring protons. The ^{1}H-NMR spectrum of the electron-rich ^{Me10}**Fc**, with no Cp ring protons, only displays a singlet at 1.66 ppm for the protons of the methyl groups. In the paramagnetic ^{Me10}**Fc⁺** counterpart, the singlet methyl proton signal shifts to a lower frequency (δ = –37.6 ppm), see Figures 31 and 32.

Mono- or *1,1'*-di-substituted ferrocenes typically exhibit NMR signals which can be readily assigned except for those from protons in the 2,5- and 3,4-positions. The assignment of these ring protons for some substituted ferrocenes have previously been achieved through specific deuteration, heteronuclear differential nuclear Overhauser effect difference (NOE) spectroscopy, or $^1J(^{13}C–^{13}C)$ coupling measurements along with selective proton decoupling.[35] By analogy, we can assign the 2,5- and 3,4-protons of all mono- and *1,1'*-di-substituted ferrocene species described in this study (Table 2). In deuterated acetone at room temperature, the resonances representing the protons in 2,5- and 3,4-positions in nearly all of our substituted ferrocenes appear as a pair of apparent triplets with the coupling constant, $^3J(^1H–^1H)$, value of about 2 Hz. Table 9 lists the coupling constants of the Cp protons for all the substituted ferrocene species. Table 2 summarizes the ^{1}H-NMR chemical shifts for the cyclopentadienyl protons of both ferrocene derivatives and their ferricenium counterparts.

Table 2. ^{1}H-NMR Chemical Shifts of Cp Protons for the Ferrocene and Ferricenium Derivatives in Acetone-d_6 or CD_2Cl_2[a].

δ (ppm)

Compound	H_{Cp}	$H_{2,5}$	$H_{3,4}$	Compound	H_{Cp}	$H_{2,5}$	$H_{3,4}$
^{Me2}**Fc**	–	3.96	3.94	^{Me2}**Fc**$^{+}$	–	34.8	31.6
^{nBu}**Fc**	4.08	4.06	4.01	^{nBu}**Fc**$^{+}$	31.3	37.4	33.9
Fc	4.20	–	–	**Fc**$^{+}$	33.2	–	–
^{Br}**Fc**	4.23	4.45	4.17	^{Br}**Fc**$^{+}$	34.0	28.8	32.0
^{Ac}**Fc**	4.23	4.78	4.52	^{Ac}**Fc**$^{+}$	36.3	27.5	31.8
^{Bz}**Fc**	4.24	4.87	4.65	^{Bz}**Fc**$^{+}$	35.4	27.6	31.3
^{Br2}**Fc**	–	4.47	4.27	^{Br2}**Fc**$^{+}$	–	29.6	34.2
^{Ac2}**Fc**	–	4.81	4.58	^{Ac2}**Fc**$^{+}$ [a]	–	30.5[b]	
^{Bz2}**Fc**	–	4.98	4.68	^{Bz2}**Fc**$^{+}$ [a]	–	30.2[b]	

Numbering scheme:

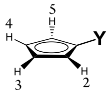

[b] Only one single broad resonance.

For ^{Me2}**Fc**, the protons of two methyl substituents resonate at 1.95 ppm and the lower symmetry of the substituted ring system predictably leads to a pair of triplets for the Cp protons (δ = 3.94 and 3.96 ppm; Figures 48 and 49). In ^{nBu}**Fc**, the 2,5-protons and, to a greater extent, the 3,4-protons experience the shielding associated with the electron-donating substituent,[34a] resulting in an upfield shift of these substituted ring protons relative to that of the unsubstituted Cp ring. The elongated *n*-butyl chain gives rise to three separate ($-CH_2-$) resonances at 2.34 (t, 2H, *a*-H), 1.48 (m, 2H, *b*-H), and 1.34 (m, 2H, *c*-H) ppm plus a triplet centered around 0.9 ppm for the three protons of the CH_3 group (Figures 35 and 36).

The presence of electron-withdrawing substituents such as bromo, acetyl, or benzoyl groups on the cyclopentadienyl rings of the neutral complexes leads to more pronounced changes in chemical shifts between the 2,5- and the 3,4-protons of the substituted Cp rings (Figures 1 and 37-44). In these electron-deficient systems, both resonances are shifted to a lower field compared to the Cp resonance of the parent ferrocene. In the case of ^{Br}**Fc**, the 2,5-proton signal appears at a lower field and the 3,4-protons resonate at a slightly higher field compared to the resonance for unsubstituted Cp ring.

For the oxidized species, in most cases, the different Cp protons can still be distinguished in spite of the broadened resonances. For example, both *1,1'*-disubstituted ^{Me2}**Fc$^+$** and ^{Br2}**Fc$^+$** complexes show two broad downfield Cp proton resonances. This is in agreement with our X-ray crystallography data that confirmed their "locked" eclipsed structures in the solid state (*vide infra)* and supporting that this conformation is retained in both solution and solid state.

In deuterated acetone, the 2,5- and 3,4-proton peaks for ^{Me2}**Fc$^+$** appear at 31.6 and 34.8 ppm and for ^{Br2}**Fc$^+$** at 29.6 and 34.2 ppm, respectively. Going from deuterated acetone to DCM, the peak separation for ^{Br2}**Fc$^+$** diminishes from 4.6 to 1.8 ppm (i.e., for ^{Br2}**Fc$^+$** δ = 32.7 and 34.5 ppm in CD_2Cl_2; ΔΔδ = –2.8 ppm) while the peak separation for ^{Me2}**Fc$^+$** remains essentially the same (i.e., for ^{Me2}**Fc$^+$** δ = 32.5 and 35.8 ppm in CD_2Cl_2; ΔΔδ = 0.1 ppm), see Figure 2 and Figures 45-48. Here, the lower dielectric constant of the media results in lowering the rotational barrier of the substituted rings in ^{Br2}**Fc$^+$** to some degree and not in ^{Me2}**Fc$^+$**. This may be due to the different nature of the bonding and overall spin density delocalization in these ferricenium complexes. The methyl protons of ^{Me2}**Fc$^+$** resonate in the upfield region as a rather sharp singlet, i.e., δ = –10.5 ppm in acetone-d_6 and δ = –9.0 ppm in CD_2Cl_2.

On the other hand, in the case of the *1,1'*-diketone-substituted ferricenium species such as ^{Ac2}**Fc$^+$** and ^{Bz2}**Fc$^+$**, only one broad Cp proton resonance is observed in CD_2Cl_2 (Figures 1, 49 and 50). Apparently, the ketone-substituted Cp rings in these complexes have lower rotational barriers and rotation rates are sufficiently high, exceeding the NMR time scale and preventing the observation of separate resonances by the 2,5- and 3,4-protons. Our X-ray crystallography data for the oxidized forms of these complexes also support a less restricted rotation around the Fe-Cp axis in these systems, *vide infra.*

In all four monosubstituted ferricenium species the 2,5- and 3,4-protons of the substituted ring along with the unsubstituted Cp protons resolve into three broad peaks. Here, the Cp ring carrying the substituent faces a larger rotational barrier in acetone-d_6 and the reduced rotation rates lie within the timescale of NMR measurements. For the electron-rich ^{nBu}**Fc$^+$**, the unsubstituted Cp ring resonance moves upfield up to 1.9 ppm from that of the parent ferrocene Cp protons. In turn, the 2,5-protons of the *n*-butyl-substituted ring and, to a lesser extent, the 3,4-protons are deshielded relative to that of the parent **Fc**$^+$ protons (Table 2, Figures 51 and 52). The protons of the *n*-butyl substituent resonate in the upfield region as four separate signals at –6.8 (2H, *a*-H), –18.3 (2H, *b*-H), 1.2 (2H, *c*-H), and –1.0 (3H, *d*-H) ppm.

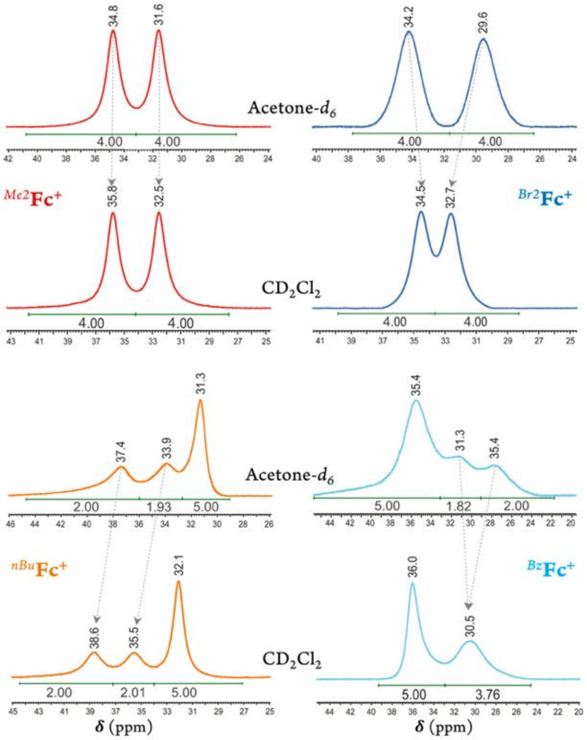

Figure 2. Part of the ^{1}H-NMR spectra of two electron rich ferricenium derivatives (left; i.e., ^{Me2}**Fc$^+$** and ^{nBu}**Fc$^+$**) and two electron-deficient analogs (right; i.e., ^{Br2}**Fc$^+$** and ^{Bz}**Fc$^+$**) recorded in deuterated acetone ($\varepsilon \approx 21$) *vs* dichloromethane ($\varepsilon \approx 9$) at room temperature. The behaviors of the 2,5- and 3,4-protons of the substituted Cp ligand are compared.

On passing from the electron-rich monosubstituted ferricenium ion to electron-deficient monosubstituted ferricenium species bearing a bromo, acetyl, or benzoyl group, the unsubstituted Cp ring signal shifts to a lower field (Δδ = 0.8–3.1 ppm) in reference to the

Cp ring signal of the parent ferricenium complex (Figures 53-58). Additionally, the protons of the 2,5-positions and to a lesser degree, the 3,4-positions of the substituted Cp ring become increasingly shielded with the increasing electronegativity of the substituent and resonate at a higher field relative to that of the parent **Fc**$^+$ protons. Here again, in CD_2Cl_2, the rotational barrier of the substituted rings decreases more significantly in the electron-deficient ferricenium species (i.e., ^{Br}**Fc**$^+$, ^{Ac}**Fc**$^+$, and ^{Bz}**Fc**$^+$) than in the electron rich system such as ^{nBu}**Fc**$^+$, and the faster ring rotation results in much more severe broadening and overlap of the 2,5- and 3,4-protons of the substituted Cp ligand, Figure 2.

It is also worth noting that the peak separations for the 2,5- and the 3,4-protons of the substituted Cp rings in both higher and lower polarity organic solvents (e.g., acetone-d_6 *vs* $CDCl_3$) stay the same across the series of neutral ferrocene derivatives discussed in this study. This points to the significant difference in bonding and electronic structures of the one electron oxidized and neutral species.

The ^{19}F-NMR spectra of the paramagnetic ferricenium salts were also recorded. The $BArF_{20}$ anion of all ferricenium species in deuterated acetone gives rise to three ^{19}F-NMR resonances at –133.0, –164.4, and –168.4 ppm for the *ortho*-, *para*-, and *meta*-fluorines in a ratio of around 8:4:8, respectively. In a lower polarity solvent such as CD_2Cl_2, these ^{19}F-NMR signals are more shielded, and the largest shift is observed for the *ortho*-fluorines by no more than –2.4 ppm, see Figures 59–73. This confirms that although the ferricenium derivatives and $BArF_{20}$ anion are unpaired in acetone, they are likely ion paired in CD_2Cl_2. As previously described, the $BArF_{20}$ anion lacks specificity in where to ion pair to the cation.[15b]

The ^{19}F-NMR spectrum of ^{Bz2}**Fc**$^+$ displays one broad resonance at 133.2 ppm for the SbF_6^- counterion with a sextet pattern ($^1J(^{19}F\text{-}^{121}Sb)$ ~ 2 kHz). Given that the two most abundant isotopes of antimony are both quadrupolar, ^{121}Sb I = 5/2 and ^{123}Sb I = 7/2, broadening of the ^{19}F-NMR signal in SbF_6^- due to the quadrupolar relaxation is expected. In the presence of Ag[SbF_6], the splitting pattern of ^{19}F resonance disappears giving a single broadened signal that is shifted to –134.7 ppm which points to a fast mode of exchange in this system (Figure 74).

X-RAY CRYSTALLOGRAPHY

A couple of decades ago, Geiger and coworkers first introduced *tetra-n*-butylammonium $BArF_{20}$, $[(nBu)_4N][B(C_6F_5)_4]$, as an ideal non-coordinating supporting electrolyte for electrochemical studies in low-polarity solvents.[36] Here, we describe an alternative procedure for preparation of this electrolyte. Diffraction quality crystals of $[(nBu)_4N][B(C_6F_5)_4]$ were obtained by slow liquid diffusion of hexanes into the DCM solution of the electrolyte and its structure was determined via single crystal X-ray crystallography at 100 K (Table 10). The electrolyte, which was previously reported by Bolte and coworkers at 173 K,[37] crystallizes in the monoclinic space group *Cc*, with one *tetra-n*-butylammonium moiety paired with one $BArF_{20}$ anion per asymmetric unit (Figure 75).

The crystals of $[Ag(MeCN)_4][B(C_6F_5)_4]$ were grown by keeping a saturated solution of the complex in acetonitrile at −35°C. Although the X-ray structure of this complex was recently reported,[38] we were able to obtain higher quality data (Table 10). The X-ray structure clearly shows the ligation of four acetonitrile molecules to the silver(I) center in a pseudo-tetrahedral fashion (i.e., ∠N–Ag–N is in the range of 91 to 136°) with one slightly bent acetonitrile ligand while $BArF_{20}$ remains in the crystal lattice as the counter anion, residing near the largest N–Ag–N angle in the silver complex (Figure 76).

Ferricenium Derivatives

Molecular structures of all the ferricenium species used in this study were determined via single crystal X-ray crystallography, except for the parent ferricenium $BArF_{20}$ that has been previously structurally characterized.[17] Suitable crystals for X-ray structure determination were grown in the glovebox, through the slow diffusion of hexanes into either MeTHF or DCM solutions of the ferricenium derivatives in 5 mm glass tubes at room temperature. Details of the data collection and refinement parameters as well as selected structural parameters are listed in Tables 11–13 and Tables 14–17, respectively.

All the complexes contain $[B(C_6F_5)_4]^-$ as the counterion, except for ^{Bz2}**Fc**$[SbF_6]$. The corresponding molecular packing patterns are presented in Figures 77–85.

As briefly discussed earlier, both ferrocene and ferricenium derivatives possess a high degree of molecular flexibility, adopting a variety of conformations. This conformation flexibility is typically in response to different electronic, steric, or crystal packing forces in different structures. In addition to their highly flexible geometries, the ferrocene or ferricenium derivatives, even symmetrically substituted ones, can become chiral to some extent or exhibit conformational chirality.[39] In the following, we analyze the overall conformational arrangements of all ferricenium derivatives reported here according to the four geometrical parameters shown in Figure 3. We also compare these values with those of the corresponding ferrocene counterparts (Tables 14 and 15).

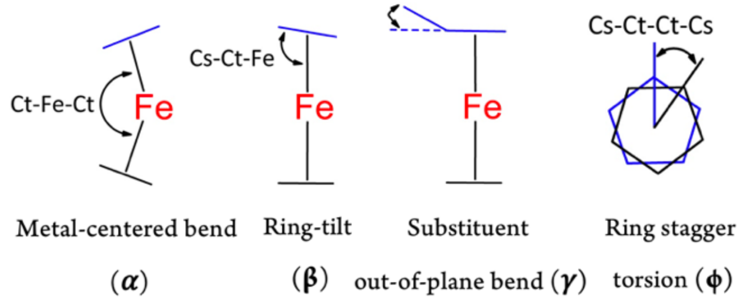

Figure 3. Schematic representation of the geometrical parameters used to describe the conformations of ferrocene and ferricenium derivatives. Ct refers to the Cp ring centroid while Cs indicates the substituted *C*-atom on the ring. In the case of monosubstituted structures, the second Cs is the closest *C*-atom on the unsubstituted ring.

Figure 4 depicts the molecular structure of the ferricenium derivatives bearing electron-donating groups in the solid state. The most electron-rich ferricenium complex described in this work, ^{Me10}**Fc**BArF$_{20}$, crystallizes as dark green single crystals in a $P2_1/c$ space group and the crystallographic asymmetric unit contains two ferricenium entities and two BArF$_{20}$ counterions. The two entities exist in slightly different relative conformations. The Cp rings in one of the ferricenium centers are almost perfectly staggered with a torsional angle of 35.9° between the two opposing methyl groups while the second ferricenium entity has the rings slightly skewed by an angle of 16.9°. Interestingly, in the case of the neutral ^{Me10}**Fc**, the Cp rings only adopt absolute staggered orientation (ϕ = 36°).[31] The

Fe–C$_{avg}$ bond distance in ^{Me10}**Fc**BArF$_{20}$ was found to be 2.101 Å which is about 0.05 Å larger than that of ^{Me10}**Fc** (Table 14). The distance between the iron center and Cp ring centroid (i.e., Fe···Ct$_{avg}$) is also about 0.06 Å longer in the ferricenium complex which highlights the small elongation of the Fe–C bonds upon oxidation. A very similar trend is observed for the neutral and oxidized states of the other ferrocene derivatives (Figure 86). This constancy of Fe–C bond length in going from the neutral ferrocene state to the ferricenium state in all derivatives has been ascribed to the very weakly bonding nature of the e$_{2g}$ orbitals.[8c, 8d, 26a] The methyl substituents in ^{Me10}**Fc**BArF$_{20}$ are slightly out of the Cp planes and away from the iron center (γ = 1.4°) which is also observed in the neutral analog, ^{Me10}**Fc**, (γ = 1.8°) pointing to the steric constraints imposed by the substitution of all Cp protons by methyl groups.

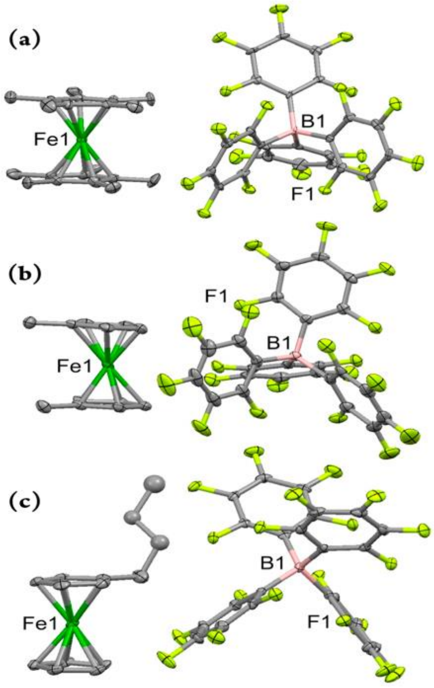

Figure 4. Perspective views of the electron-rich ferricenium derivatives at 100 K: (a) ^{Me10}**Fc**BArF$_{20}$, (b) ^{Me2}**Fc**BArF$_{20}$, and (c) ^{nBu}**Fc**BArF$_{20}$ showing 50% thermal contours for all non-hydrogen atoms. Hydrogen atoms have been omitted for clarity.

The dark blue single crystals of ^{Me2}**Fc**BArF$_{20}$ were obtained in an orthorhombic system with the *Pbcn* space group. The asymmetric unit contains three molecules and one out of the three $^{Me2}\mathbf{Fc}^{+}$ entities is disordered over two different orientations and the occupancy factor of the major component refines to 0.618(3). The methyl groups are closer to the eclipsed conformation (ϕ = 13.6°, –14.9°, or –19.2) in the oxidized complex and the torsion angle becomes even smaller on going to the neutral analog, ^{Me2}**Fc**, (ϕ = –3.6°).[31] Here, an increase of 0.06 Å in Fe–C_{avg} bond length is observed for ^{Me2}**Fc**$BArF_{20}$ relative to ^{Me2}**Fc** which is the largest elongation of the Fe–C bonds upon oxidation observed in all the derivatives discussed in this study. The separation of the Cp rings also increases by 0.17 Å, in going from ^{Me2}**Fc** to ^{Me2}**Fc**$BArF_{20}$. Unsurprisingly, in the oxidized complex, ^{Me2}**Fc**$BArF_{20}$, with the greater Cp ring separation (i.e., 3.463 Å), both methyl groups tend to come within the Cp plane with an average out-of-plane displacement of 0.01 Å as compared to 0.06 Å in ^{Me2}**Fc**.

The peacock blue ^{nBu}**Fc**$BArF_{20}$ complex crystallizes in a triclinic crystal system with *P*-1 space group. The asymmetric unit contains two molecules and the *n*-butyl moieties of both ferricenium entities are disordered over two different orientations. The occupancy factor of the major component in disorder is 0.552(9). The ^{nBu}**Fc** complex is a brownish orange liquid at room temperature and no crystal structure is available for this neutral counterpart for comparison. Instead, we used the structural data reported for the two closely related ferrocene derivatives, *n*-tetradecylferrocene (^{nC14}**Fc**) and *1,8*-bis(ferrocenyl)octane (**Fc**-$(CH_2)_8$-**Fc**).[40] In the ^{nBu}**Fc**$BArF_{20}$ complex, the substituted and unsubstituted Cp rings are nearly eclipsed (ϕ = 7.9° or –1.2°) and the iron center is about 1.702 and 1.703 Å away from the centroids of the substituted and unsubstituted Cp ligands, respectively. In the neutral analogs, the rings maintain the eclipsed structure (ϕ = –0.2° in ^{nC14}**Fc** and –7.8° in **Fc**-$(CH_2)_8$-**Fc**) and both metal-ligand separations are reduced by about 0.5 Å ($Fe\cdots Ct_{sub.}$ = 1.648 Å and $Fe\cdots Ct_{unsub.}$ = 1.650 Å). See Tables 14 and 15 for further structural details.

In moving on to the electron-deficient ferricenium derivatives, we obtained molecular structures of three monosubstituted systems bearing a bromo, acetyl, or benzoyl substituent on one of the Cp rings (Figure 5). These are the first examples of X-ray crystal structures of the ferricenium derivatives with these electron-withdrawing substituents. To date, only a very limited number of structural data for electron-deficient ferricenium species (~5) are deposited in the Cambridge Structural Database (CSD), which is most likely a reflection of challenges in their preparation due to the necessity of meticulous exclusion of potential reactive nucleophiles and reducing reagents (i.e., air, moisture, coordinating and redox-active solvents and counterions).

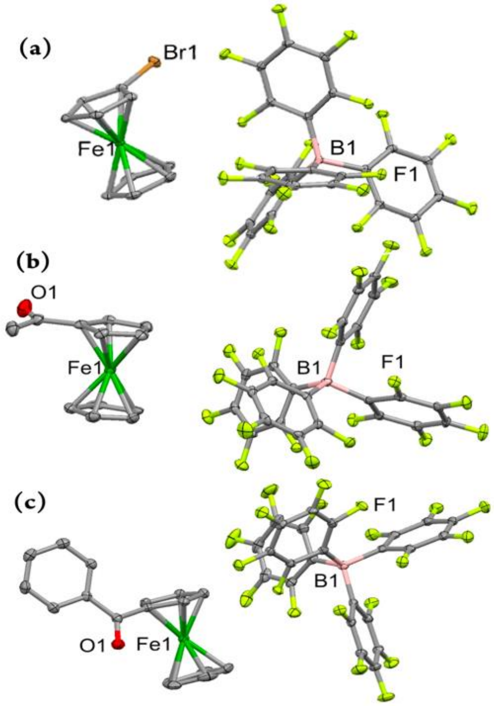

Figure 5. Perspective views of the electron-deficient monosubstituted ferricenium derivatives at 100 K: (a) ^{Br}**Fc**BArF$_{20}$, (b) ^{Ac}**Fc**BArF$_{20}$, and (c) ^{Bz}**Fc**BArF$_{20}$ showing 50% thermal contours for all non-hydrogen atoms. Hydrogen atoms have been omitted for clarity.

Our first monosubstituted ferricenium derivative of this class is ^{Br}**Fc**BArF$_{20}$ (Figure 5a) which was obtained from DCM/hexanes. This complex crystallizes in a monoclinic crystal system with $P2_1/n$ space group and the asymmetric unit contains one molecule. The Cp rings in ^{Br}**Fc$^+$** adopt an approximately eclipsed conformation with a torsion angle of 9.1° which is in the range of those found for the neutral complex, ^{Br}**Fc** (ϕ = –2.6° or 28.6°).[41] In ^{Br}**Fc$^+$**, the Fe–C$_{avg}$ and Fe⋯Ct distances are 2.089 and 1.706 Å for the bromo-substituted Cp ring while 2.082 and 1.701 Å for the unsubstituted ring, respectively. As expected, the neutral complex, ^{Br}**Fc**, possesses smaller Fe–C$_{avg}$ and Fe⋯Ct distances. Here, the oxidation results in a larger degree of elongation of the Fe⋯Ct distance for the substituted ring as compared to unsubstituted ring, while in the electron-rich ^{nBu}**Fc$^+$** complex both substituted and unsubstituted rings experienced similar degrees of displacement upon oxidation (i.e., Δ(Fe⋯Ct) ≈ 0.05 Å), *vide supra*.

Both electron-deficient mono-ketone-substituted ferricenium complexes, ^{Ac}**Fc**BArF$_{20}$ and ^{Bz}**Fc**BArF$_{20}$, crystallize in the triclinic crystal system with the *P*-1 space group. Similarly, one electron oxidation imposes larger separation (i.e., by ~ 0.1 Å) of the iron center from the substituted Cp ring as compared to the unsubstituted ligand in these complexes. The Cp rings in both ^{Ac}**Fc**$^+$ and ^{Ac}**Fc** are nearly eclipsed with the torsion angles of about –3.4° and 0.6°, respectively.[30] The acetyl group shows a rotation of 180° around the C–C bond of the Cp ring and acetyl group in going from the neutral to oxidized complex while retaining a similar degree of out-of-plane displacement in both forms.

Interestingly, the one-electron oxidation of ^{Bz}**Fc** also triggers a significant rearrangement of the benzoyl substituent. In the oxidized form, the carbonyl group of the benzoyl moiety bows toward the iron center (i.e., an out-of-plane bend of 1.8 Å) with the phenyl group having an interplanar angle of 81.8°, as compared to the significantly smaller interplanar angle of 37.7° (i.e., the benzyl moiety has an out-of-plane bend of 0.33 Å away from the iron center) in the neutral ^{Bz}**Fc** counterpart.[32] Alternatively, this substantial difference in the orientation of benzoyl groups may be due to changes in the molecular packing of the neutral and oxidized forms.

The molecular structures of the three *1,1'*-disubstituted ferricenium derivatives bearing electron-withdrawing groups are shown in Figure 6. All these complexes crystallize in centrosymmetric space groups and contain no more than one independent molecule of the compound in the asymmetric unit. The ^{Br2}**Fc**BArF$_{20}$ complex crystallizes in a monoclinic crystal system with the *P*2$_1$/*n* space group.

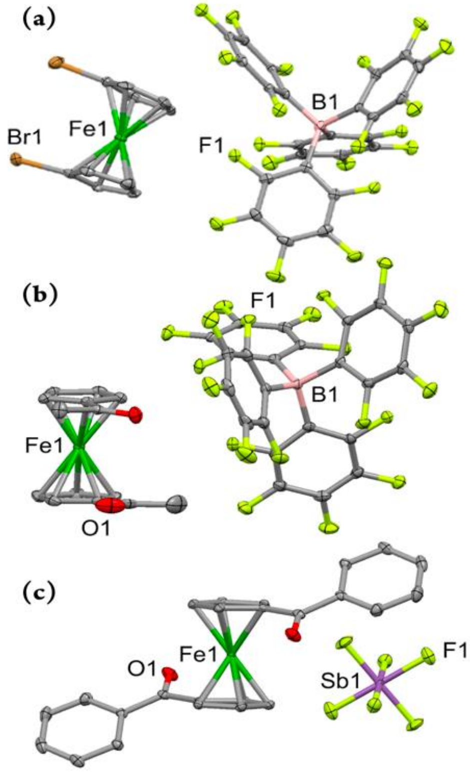

Figure 6. Perspective views of the electron-deficient ferricenium derivatives at 100 K: (a) ^{Br2}**Fc**BArF$_{20}$, (b) ^{Ac2}**Fc**BArF$_{20}$, and (c) ^{Bz2}**Fc**[SbF$_6$] showing 50% thermal contours for all non-hydrogen atoms. Hydrogen atoms have been omitted for clarity.

The Cp rings in ^{Br2}**Fc**$^+$ are approximately eclipsed with a torsion angle of about 3.5° between the two bromo substituents which is larger than that of ^{Br2}**Fc** (ϕ = 0.6°).[42] Due to the smaller torsion angle and shorter Ct⋯Ct distance (~ 3.298 Å) in the neutral analog, the two *Br*-atoms are forced out of the Cp planes with out-of-plane displacement of 0.14 Å and 0.08 Å (i.e., γ = 2.7 and 4° away from the ferrous center) and a Br⋯Br non-bonding separation of 3.617 Å. By comparison, the smaller torsion angle restraints and greater Ct⋯Ct distance (~3.405 Å) in ^{Br2}**Fc**$^+$ lead to a decrease of the out-of-plane displacement of both *Br*-atoms to less than 0.02 Å (i.e., γ = 1.1° and 1.3° toward the ferric center) and the Br⋯Br non-bonding separation is about 3.773 Å.

Among all the derivatives discussed in this study, the dibromo substituted system, in either oxidized or neutral form, exhibits the most significant metal-centered bending (α = 177.0 in ^{Br2}**Fc**$^+$ and 177.7 in ^{Br2}**Fc**$^+$). This is consistent with the overall trend observed in ferrocene derivatives highlighting that the structures with eclipsed conformations reach considerably larger bending angles.[39, 43]

The difference between structures of ^{Ac2}**Fc**BArF$_{20}$ and its neutral analog, ^{Ac2}**Fc** is even more pronounced. The ^{Ac2}**Fc^{+}** complex crystallizes in the monoclinic space group $P2_1/c$, with the Cp rings in staggered arrangements (ϕ = –26.4°) in contrast to the nearly eclipsed conformation observed for ^{Ac2}**Fc** (ϕ = 139.6°).[31] Here, upon one-electron oxidation, the two acetyl groups on the rings drastically move toward and pass each other ($\Delta\phi$ = 166°). The average out-of-plane displacement of the acetyl moieties in ^{Ac2}**Fc** is about 0.098 Å and it decreases to 0.042 Å in ^{Ac2}**Fc**BArF$_{20}$, which in turn slightly affects the relative position of the Cp rings in a way that the interplanar angle between the Cp rings changes from 1.4° in ^{Ac2}**Fc** to 2.6° in ^{Ac2}**Fc**BArF$_{20}$.

As mentioned earlier, only a handful of ferricenium derivatives with electron-withdrawing groups have been structurally characterized to date. Among the electron-deficient derivatives presented in this work, only the structure of ^{Ac2}**Fc^{+}** as the $N(SO_2CF_3)_2^-$, NTf_2^-, salt has been previously reported.[18] The Fe–C$_{avg}$ and Ct···Ct distances in this ^{Ac2}**Fc**NTf$_2$ complex are 2.093 and 3.416 Å, respectively, which are very similar to those of ^{Ac2}**Fc**BArF$_{20}$ reported here. The major structural discrepancy for these two complexes is found in the relative orientation of the acetyl substituents on the Cp rings. The torsion angle of 180.0° in ^{Ac2}**Fc**NTf$_2$ clearly indicates that acetyl groups lie in perfectly opposite positions from each other, while the acetyl groups in ^{Ac2}**Fc**BArF$_{20}$ are only 26.4° apart. Another interesting observation is the rotation of the C–C bond between one of the Cp rings and the attached acetyl group in ^{Ac2}**Fc**NTf$_2$ and both in the case of ^{Ac2}**Fc**BArF$_{20}$ as compared to the structure of neutral complex (Figure 7).

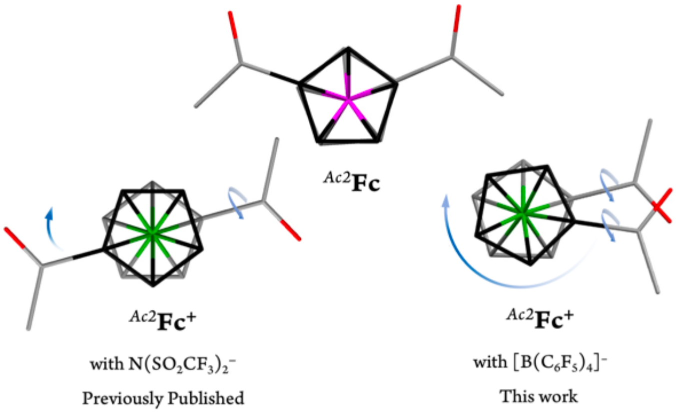

Figure 7. Top view of the capped stick representations of the molecular structures of ^{Ac2}**Fc**,[31] ^{Ac2}**Fc**NTf_2,[18] and ^{Ac2}**Fc**$BArF_{20}$. The top and bottom Cp rings are shown in black and grey, respectively. Counterions and hydrogen atoms are omitted for clarity. Arrows represent the conformational rearrangements required for the oxidized complex to adopt a similar conformation as the neutral complex.

The complex ^{Bz2}**Fc**[SbF_6] crystallizes in a triclinic crystal system with the *P*-1 space group and the asymmetric unit contains one half of the molecule where the Fe and Sb atoms are located on the crystallographic inversion center. The torsion angle between the two substituted Cp rings in ^{Bz2}**Fc**[SbF_6] is 180.0° which is significantly larger than that of the neutral counterpart, ^{Bz2}**Fc** (ϕ = 130.4°).[33] From the top view of the two complexes shown in Figure 8, it is clear that the Cp rings in ^{Bz2}**Fc**[SbF_6] are almost perfectly staggered whereas in the neutral counterpart they adopt a close to eclipsed conformation. The Fe–C_{avg} and Ct···Ct distances are about 2.042 and 3.296 Å in ^{Bz2}**Fc** while for the oxidized species, ^{Bz2}**Fc**[SbF_6], they increase to 2.089 and 3.410 Å, respectively. Since in the neutral and oxidized forms, the substituents are far apart from each other, the Cp rings are highly coplanar in both cases with interplanar angles of 0.4° and 0.0°, respectively. We will return to this point later in the electrochemistry discussion.

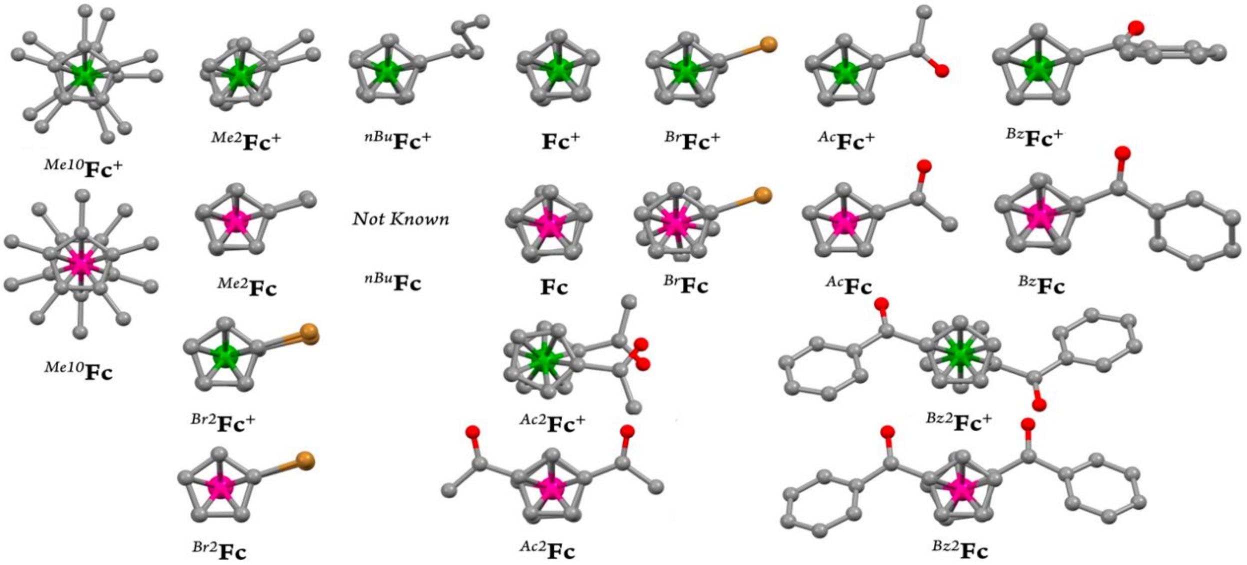

Figure 8. Ball and stick representation of the top view of the molecular structures of ferrocene and corresponding ferricenium derivatives depicting the changes in the ring stagger torsion angle that accompany the oxidation process. The ferric and ferrous centers are shown in green and pink, respectively. Hydrogen atoms are omitted for clarity.

A comparison of the iron-ring centroid distances for both ferrocene and ferricenium derivatives is shown in Figure 9. As discussed earlier, the removal of one electron from the metal e_{2g} orbitals gives rise to a larger separation between the iron and Cp ligands. This is consistent with the very weakly bonding character of the e_{2g} orbitals. Additionally, the largest Fe⋯Ct elongation (by ~ 0.085 Å) is observed for the oxidation of the dimethyl substituted system.

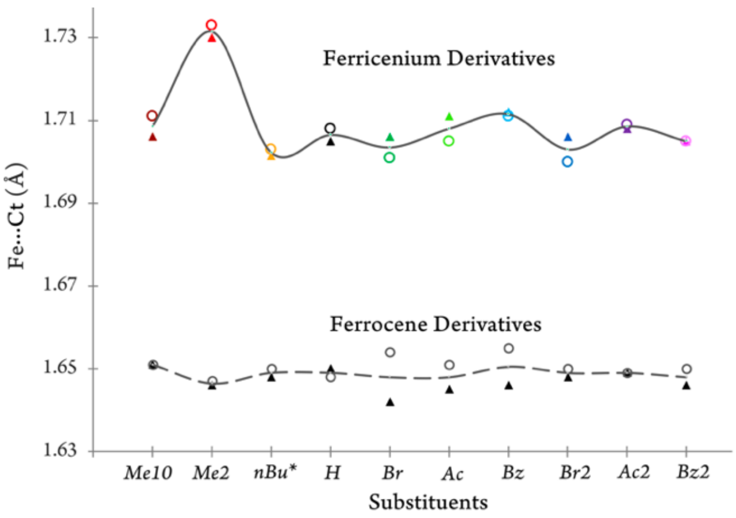

Figure 9. The separation of the iron and centroid (Fe···Ct) of the top (▲) or bottom (○) cyclopentadienyl ring is plotted for all of ferrocene and ferricenium derivatives discussed in this study. *For the neutral form average of the Fe···Ct distances for two closely related derivatives, ^{nC14}**Fc** and **Fc**-(CH_2)$_8$-**Fc**, was used.

The oxidation of ferrocene leads to more significant shortening of the C–C bond lengths in the cyclopentadienyl ligands in the parent ferricenium complex (i.e., ~ 0.033 Å) relative to those of their substituted analogs (i.e., < 0.015 Å). For example, the C–C bond length stays nearly intact throughout the oxidation of *1*-benzoylferrocene, see Table 14 for details on the average change in C–C bond length across all ferrocene and ferricenium derivatives.

A closer look at this metal-ligand separation also reveals that the nature of the substituents has a more significant effect on the Fe···Ct distances in the oxidized species (i.e., Δ(Fe···Ct) ≈ 0.03 Å) than in their neutral counterparts (i.e., Δ(Fe···Ct) ≈ 0.01 Å). Another interesting finding is that, in the monosubstituted ferrocene derivatives bearing an electron-withdrawing group (e.g., ^{Br}**Fc**, ^{Ac}**Fc**, and ^{Bz}**Fc**), the distance between the ferrous center and the unsubstituted ring is slightly larger than that of the electron-deficient substituted ring. Although smaller in magnitude, a reversal of behavior is observed in the oxidized counterparts of these electron-deficient monosubstituted systems. This reversal of behavior is in excellent agreement with our NMR results (Figure 1).

ELECTROCHEMICAL ANALYSES

In order to further understand the redox behavior of the ferrocene and ferricenium derivatives, we conducted cyclic voltammetry measurements under 5 different conditions of solvent and supporting electrolyte. All electrochemical experiments were performed in dry and oxygen-free MeCN, DCM, or MeTHF containing 0.1 M of one of two chosen supporting electrolytes, i.e., *tetra*-*n*-butylammonium *tetrakis*(pentafluorophenyl)-borate, $[(n\mathrm{Bu})_4\mathrm{N}][\mathrm{B}(\mathrm{C}_6\mathrm{F}_5)_4]$, or a more traditional electrolyte, *tetra*-*n*-butylammonium hexafluorophosphate, $[(n\mathrm{Bu})_4\mathrm{N}][\mathrm{PF}_6]$ (Figures 10 and 87-90). The latter is not soluble in MeTHF.

Prior to each cyclic voltammetry experiment, the uncompensated solution resistance (R_u) of each solvent/electrolyte combination was measured using potentiostatic electrochemical impedance spectroscopy (PEIS) at frequencies ranging from 1 MHz to 100 mHz at open circuit potential. Our results for five different media followed the trends reported in the literature,[44] see Supporting Information for further details. In DCM, using $[(n\mathrm{Bu})_4\mathrm{N}][\mathrm{B}(\mathrm{C}_6\mathrm{F}_5)_4]$ as the supporting electrolyte results in lower solution resistance compared to $[(n\mathrm{Bu})_4\mathrm{N}][\mathrm{PF}_6]$, and an opposite trend was observed in MeCN. Additionally, for a 0.1 M solution of *tetra*-*n*-butylammonium perchlorate at room temperature, the specific resistance in MeCN ($\rho = 132\ \Omega$ cm) is shown to be significantly smaller than in DCM ($\rho = 725\ \Omega$ cm).[45] Such data has not been reported for MeTHF, however, the fact that the specific resistance value obtained in THF ($\rho = 2670\ \Omega$ cm) is considerably larger than in DCM, infers that MeTHF follows a similar trend. To avoid instabilities in the potentiostat, the *iR* drop was corrected for only 85% of the uncompensated solution resistance during the cyclic voltammetry measurements through positive feedback using the Bio-Logic EC-Lab software. The half-wave potential, $E_{½}$, (V *vs* Ag/AgCl) and peak-to-peak separation, $\Delta E_{½}$, of each ferricenium/ferrocene couple in various media are listed in Table 3.

Table 3. $E_{1/2}$ and $\Delta E_{1/2}$[a] Values (*V vs* Ag/AgCl) of Various Ferrocene Derivatives in Different Media.

	MeCN				DCM				MeTHF	
	$[(n\text{Bu})_4\text{N}][\text{PF}_6]$		$[(n\text{Bu})_4\text{N}][\text{B}(\text{C}_6\text{F}_5)_4]$		$[(n\text{Bu})_4\text{N}][\text{PF}_6]$		$[(n\text{Bu})_4\text{N}][\text{B}(\text{C}_6\text{F}_5)_4]$		$[(n\text{Bu})_4\text{N}][\text{B}(\text{C}_6\text{F}_5)_4]$	
	$E_{1/2}$	$\Delta E_{1/2}$	$E_{1/2}$	$\Delta E_{1/2}$	$E_{1/2}$	$\Delta E_{1/2}$	$E_{1/2}$	$\Delta E_{1/2}$	$E_{1/2}$	$\Delta E_{1/2}$
^{Me10}**Fc**	-0.060	0.066	-0.068	0.076	0.014	0.186	0.028	0.156	0.047	0.134
^{Me2}**Fc**	0.347	0.080	0.341	0.093	0.462	0.174	0.513	0.164	0.460	0.170
^{nBu}**Fc**	0.396	0.076	0.386	0.100	0.523	0.203	0.538	0.142	0.515	0.160
Fc	0.450	0.076	0.451	0.089	0.550	0.217	0.577	0.142	0.589	0.183
^{Br}**Fc**	0.628	0.081	0.630	0.092	0.725	0.215	0.747	0.163	0.757	0.162
^{Ac}**Fc**	0.700	0.094	0.689	0.086	0.803	0.158	0.861	0.175	0.833	0.132
^{Bz}**Fc**	0.705	0.077	0.697	0.094	0.810	0.185	0.878	0.130	0.806	0.150
^{Br2}**Fc**	0.763	0.087	0.751	0.122	0.887	0.166	0.934	0.133	0.900	0.165
^{Ac2}**Fc**	0.925	0.093	0.930	0.129	1.020	0.203	1.110	0.150	1.037	0.125
^{Bz2}**Fc**	0.927	0.102	0.903	0.100	1.070	0.157	1.230	0.236	1.003	0.124

[a] The values were obtained at 100 mV·s^{-1} scan rate.

As expected, the incorporation of various electron-donating or -withdrawing substituents on the Cp rings altered the redox potential cathodically or anodically. Electron-rich systems with one or more alkyl substituent(s) such as ^{Me10}**Fc**, ^{Me2}**Fc**, and ^{nBu}**Fc** all possess redox potentials lower than that of **Fc**, while having electron-withdrawing groups on the rings creates an electron-deficient system such as ^{Br}**Fc**, ^{Ac}**Fc**, ^{Bz}**Fc**, ^{Br2}**Fc**, ^{Ac2}**Fc**, and ^{Bz2}**Fc**, hence increasing the $E°'$ values.

The cyclic voltammograms of all the derivatives in DCM with the $[(n\text{Bu})_4\text{N}][\text{PF}_6]$ supporting electrolyte are shown in Figure 10. For the cyclic voltammograms collected in the other solvent/electrolyte combinations, see section 3 of the Supporting Information. The neutral ferrocene derivatives are generally very soluble in the three solvents chosen for this study, i.e., DCM, MeTHF, and MeCN. Only ^{Me10}**Fc** has a limited (ca. 10^{-3} M) solubility in acetonitrile. For that reason, the cyclic voltammograms of all ferrocene derivatives are plotted using the molar current density (A M^{-1} cm^{-2}) rather than the current alone. This was done in order to compare the cyclic voltammetry measurements independent of the ferrocene concentration and surface area of the working electrode.

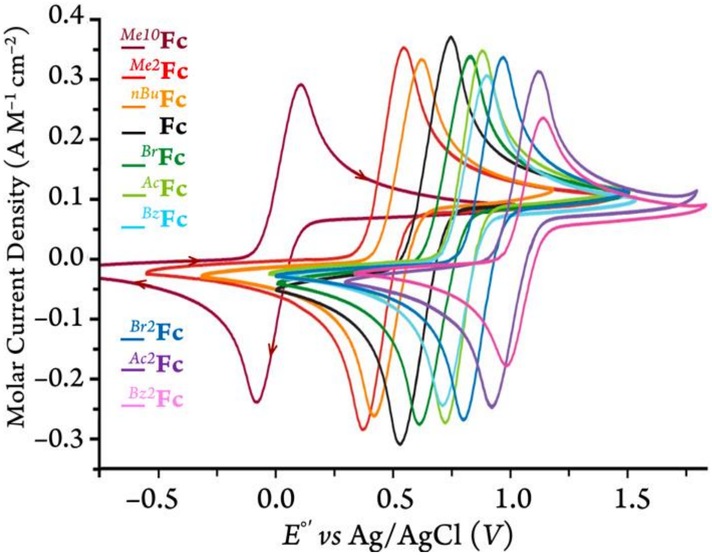

Figure 11. Normalized cyclic voltammograms of ferrocene and its derivatives in DCM with 100 mM of $[(n\text{Bu})_4\text{N}][\text{PF}_6]$ at 100 mV·s^{-1} scan rate.

The correlation between the redox potentials of the substituted ferrocenes and the sum of Hammett substituent constants in the MeTHF solution is shown in Figure 11. Typically, the $E_{½}$ data of substituted ferrocenes correlate linearly with the sum of the Hammett values, $\sum\sigma_{p,m}$, which is a combination of para- and meta-substituents (i.e., σ_p and σ_m).

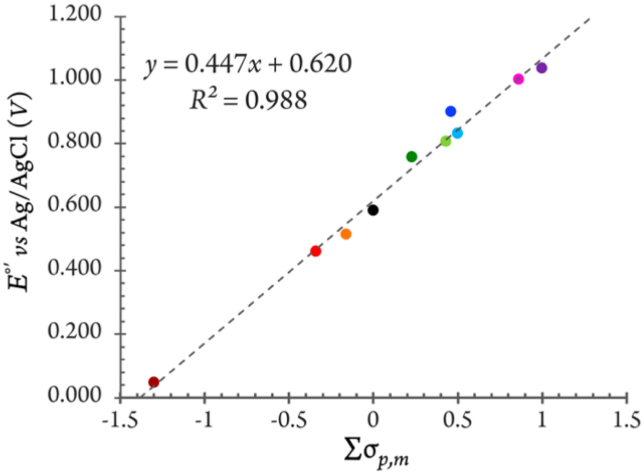

Figure 10. The half-wave potential, $E_{½}$, of all ferrocene derivatives discussed in this study in MeTHF with 100 mM of $[(n\text{Bu})_4\text{N}][\text{B}(\text{C}_6\text{F}_5)_4]$ plotted *vs* sum of the Hammett values, $\sum\sigma_{p,m}$.

For all of our mono- and *1,1'*-di-substituted ferrocenes, only σ_p was taken into account. The σ_p values for methyl, *n*-butyl, bromo, benzoyl and acetyl groups are –0.17, –0.16, +0.23, +0.43, +0.50, respectively.[46] The impact of the substitution in 3- or 4- (and 3'- or 4') positions of a Cp ring is included using σ_m.[35b, 47] For example, in ^{Me10}**Fc**, the $\sum\sigma_{p,m}$ value contains contributions of both para and meta methyl substituents (i.e., σ_m for a methyl group is –0.07 and $\sum\sigma_{p,m} = [6\times(-0.17) + 4\times(-0.07)] = -1.3$). One apparent discrepancy that merits special attention at this point is that, based on the σ_p values, the benzoyl substituted ferrocenes are expected to be less electron-deficient than the acetyl substituted analogs. This trend holds true in MeTHF but not in DCM, see Table 3.

The one-electron transfer redox processes showed quasi-reversible behavior with peak-to-peak separation values greater than 57 mV (i.e., ΔE ranging from 66 to 236 mV; see Table 3) and anodic/cathodic peak current ratios between 0.96 and 1.09 (Table 19), except for the two *1,1'*-diketone-substituted ferrocenes in MeCN (i_{pa}/i_{pc} = 1.04–1.24), *vide infra*. Our Randles-Sevcik analysis of the peak current *vs* the square root of the scan rate confirmed that in all cases the species involved in the redox reactions were freely diffusing through the electrochemical cell (Figures 12 and 91–140), rather than adsorbed on the surface of the working electrode.

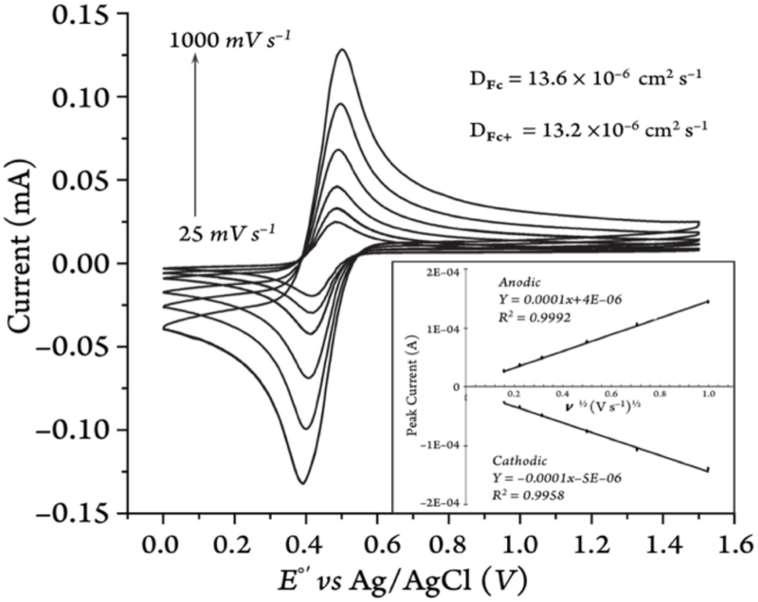

Figure 12. Representative cyclic voltammograms of the parent **Fc**$^+$/**Fc** couple (2 mM) at various scan rates in MeCN with [(nBu)$_4$N][PF$_6$] as the supporting electrolyte (100 mM). The inset shows the Randles-Sevcik plot of the CV data.

The effect of the medium on the redox potential, $\Delta E_{1/2}$, and diffusion of the redox active species is a complicated function of the interactions between solvent and solute and their overall ion-pairing.[44, 48] Some of the most important properties that govern these interactions are dielectric constant (ε), dipole moment (μ), donor number (DN), acceptor number (AN), and absolute viscosity (η). The relevant parameters for the solvents chosen for this study are listed in Table 4. Acetonitrile (MeCN), which has by far the largest dielectric constant ($\varepsilon = 36.6$), is historically favored for most electrochemical measurements in organic systems. Here, in addition to MeCN, we employed two lower polarity solvents with dielectric constants of less than 10 (i.e., DCM and MeTHF). For the latter, using [(nBu)$_4$N][B(C$_6$F$_5$)$_4$] as the supporting electrolyte, rather than the more traditional analogs such as [(nBu)$_4$N][PF$_6$], can remarkedly enhance the conductivity and decrease the overall ohmic drop.[44]

Table 4. Relevant Solvent Parameters.

	MeCN	DCM	MeTHF
Dielectric constant ε	36.6[a]	8.93[a]	6.97[b]
Dipole moment μ (D)	3.92[a]	1.60[a]	1.36[b]
Donor Number *DN*	14[a]	(0)[a]	18[b]
Acceptor number *AN*	19[a]	20[a]	3.9–8.0[c]
Absolute viscosity η (mPa·s)	0.375[d]	0.426[d]	0.492[e]

[a] From Reference[48a] [b] From Reference[49] [c] The *AN* is not reported for MeTHF, although it can be inferred to be close to values reported for tetrahydrofuran (8.0) and diethyl ether (3.9).[50] [d] From Reference[51] [e] From Reference[52]

As shown in Figure 13 and Table 3, the redox potentials of the ferrocene derivatives vary with the nature of the solvent. Considering solely the solvent polarity for a given electrolyte, the redox potentials are predicted to be the lowest in MeCN compared to those in DCM and MeTHF. All of our data follow the expected trend in acetonitrile. When comparing the two lower polarity solvents, DCM and MeTHF, the donor and acceptor numbers of the solvents are taken into consideration in predicting the redox behavior of the ferrocene derivatives in solution.

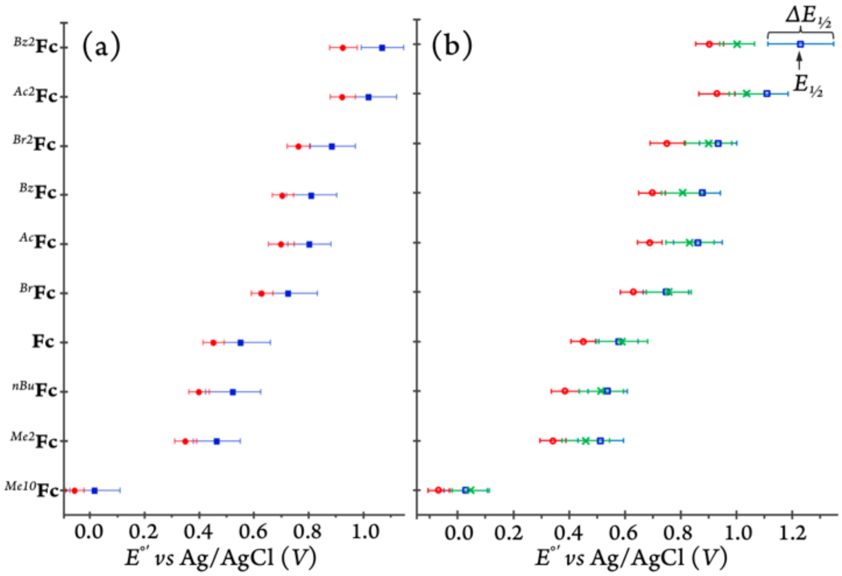

Figure 13. The half-wave potential, $E_{½}$, and peak-to-peak separation, $\Delta E_{½}$, of all ferricenium/ferrocene couples discussed in this study in different media: (a) with $[(n\mathrm{Bu})_4\mathrm{N}][\mathrm{PF}_6]$ as the supporting electrolyte in MeCN (red) and DCM (blue) and (b) with $[(n\mathrm{Bu})_4\mathrm{N}][\mathrm{B}(\mathrm{C}_6\mathrm{F}_5)_4]$ as the supporting electrolyte in MeCN (red), MeTHF (green), and DCM (blue).

The donor and acceptor numbers of DCM are reported to be around 0 and 20, respectively, while MeTHF has a donor number of 18 and an estimated acceptor number in the range of 3.9 to 8.0.[50] The differences in the donor and acceptor properties of these two solvent influence electrolyte dissociation. Additionally, higher donor number indicates that MeTHF can act more as a Lewis base stabilizing the oxidized species as well as improving the thermodynamics of the ion paring between ferricenium and the anion of the supporting electrolyte, in turn lowering the redox potential. On the other hand, the higher acceptor number of DCM suggests a higher degree of Lewis acidity, stabilizing the neutral form and in turn increasing the potential needed to oxidize the ferrocene derivatives. The pattern of higher redox potentials in DCM compared to MeTHF was observed for most ferrocene derivatives except for ^{Me10}**Fc**, **Fc**, and ^{Br}**Fc**. Lay and coworkers previously ascribed the considerably weaker solvent effects on the redox potential of ^{Me10}**Fc** to the shell of the methyl substituents that can protect the iron center against close interactions with solvents and electrolytes.[53] However, it is not clear as to why **Fc** and ^{Br}**Fc** also do not follow the pattern and further understanding of solvent and solute interactions other than electrostatic effects is necessary to explain their behavior.

The role of the two electrolyte anions, PF_6^- and $[B(C_6F_5)_4]^-$, in altering redox potentials and peak-to-peak separations in both MeCN and DCM was investigated. As described in the Introduction, the high degree of charge delocalization in a large weakly coordinating anion such as $[B(C_6F_5)_4]^-$ makes it a weak nucleophile and generally well soluble in lower-polarity solvents. This enhanced solubility can minimize adsorption problems with cationic electrode products (e.g., the ferricenium derivatives). The $[B(C_6F_5)_4]^-$ anion is also considered a weakly ion pairing anion.[48a]

In MeCN, the nature of the electrolyte anion has limited effect on the $E_{½}$ and $\Delta E_{½}$ values, as the differences observed for all the ferrocene derivatives with the two electrolyte anions, PF_6^- and $[B(C_6F_5)_4]^-$, on average are about 7 mV and 15 mV, respectively (Table 3). This is likely due to the high polarity of MeCN minimizing the ion pairing effects of the different electrolytes.[44] As for DCM, there is a more observable trend wherein ^{Me10}**Fc**, ^{nBu}**Fc**, **Fc**, and ^{Br}**Fc** experience the smallest electrolyte-induced change in $E_{½}$ (i.e., 14–27 mV) while the di-substituted ferrocenes ^{Me2}**Fc** and ^{Br2}**Fc** show differences of 47 and 51 mV, respectively.

The largest anodic shifts in $E_{½}$ (i.e., 58–160 mV) are seen for mono- and *1,1'*-di-ketone-substituted ferrocene derivatives going from $[(n\text{Bu})_4\text{N}][\text{PF}_6]$ to $[(n\text{Bu})_4\text{N}][\text{B}(\text{C}_6\text{F}_5)_4]$ in DCM. Quite curiously, the electrolyte-induced changes of $\Delta E_{½}$ follow a very different trend (Table 3). For example, the largest difference of about 77 mV in $\Delta E_{½}$ is observed for the parent **Fc** and its most electron-deficient derivative, ^{Bz2}**Fc**. However, in the presence of $[B(C_6F_5)_4]^-$ as compared to PF_6^-, the peak-to-peak separation becomes markedly smaller for the parent compound while it significantly increases for the ^{Bz2}**Fc** derivative, see Table 3.

As shown in Figure 14, the anodic peak of the parent ferrocene is barely affected (i.e., only by 8 mV) by the nature of electrolyte anion in DCM while the cathodic peak shifts by about 67 mV. This again emphasizes the fact that in low-polarity solvents the ferricenium species can be further stabilized when the electrolyte anion is changed from weakly (i.e.,

$[B(C_6F_5)_4]^-$) to relatively strongly (PF_6^-) ion pairing, highlighting the often overlooked effects of counter anions in governing the redox potentials. Also, the scan rate has the least influence on the $\Delta E_{½}$ values of different ferrocene derivatives in acetonitrile (Figures 141–150) due to negligible incomplete *iR* compensation.[54]

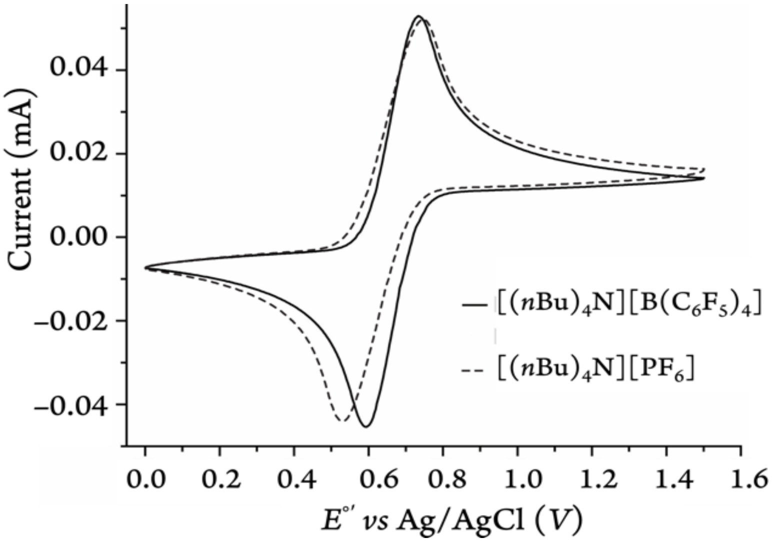

Figure 14. Representative cyclic voltammograms recorded for **Fc** (2 mM) in DCM on a glassy carbon disk electrode at 100 mV·s^{-1} in two different electrolytes.

The cyclic voltammetry measurements of ^{Bz2}**Fc** in MeCN with either electrolytes revealed a possible E_rC_i process which means that ^{Bz2}**Fc$^+$** reacts in a homogenous chemical reaction upon oxidation, thus, being chemically irreversible. While scanning at 100 mV·s^{-1}, the peak current moved closer to the baseline (Figure 15). The voltammograms become more reversible at scan rates above 100 mV·s^{-1}. It was found that 1500 mV·s^{-1} was the optimal scan rate, as that is where the cathodic/anodic peak current ratio reached the highest value at 0.81. This is a notable feature for E_rC_i reactions, at higher scan rates, the chemical reaction following the initial electron transfer step is too slow to compete, leaving more oxidized species to become subsequently reduced in the reverse scan.[55]

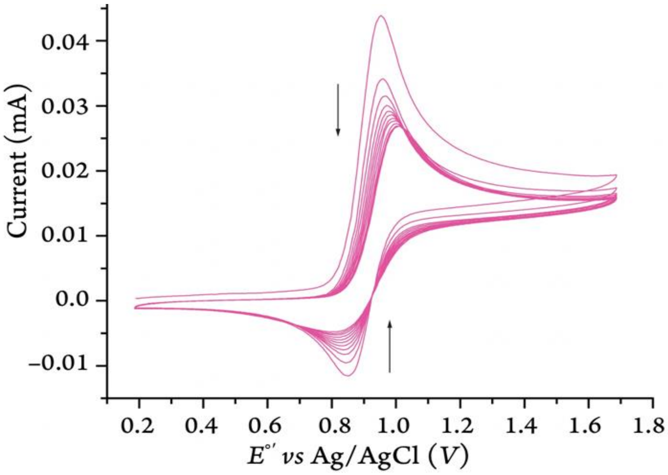

Figure 15. Cyclic voltammograms of ^{Bz2}**Fc (**2 mM) in MeCN at 100 mV·s^{-1} with 100 mM of [(nBu)$_4$N][B(C_6F_5)$_4$] as the supporting electrolyte. Arrows indicate the decay of the current towards the baseline as the scans progressed (i.e., an E_rC_i process).

As ^{Ac2}**Fc** demonstrated a similar behavior, a series of faster scan rates was also used in MeCN to outrun the chemical reaction that accompany the electron transfer process for this derivative. Therefore, for the studies of ^{Bz2}**Fc** and ^{Ac2}**Fc** in MeCN with both electrolytes, the scan rates were varied at 1500, 1250, 1000, 500, 250, and 100 mV·s^{-1} and the working electrode was cleaned between each scan rate variation. These results are consistent with our direct observation of the reactivity of the chemically synthesized ketone-substituted ferricenium derivatives toward acetonitrile. The exact mechanism of this reactivity is outside the scope of this report and will be discussed elsewhere.

As mentioned earlier, the electron transfer processes were diffusion-controlled for all the ferrocene and ferricenium derivatives used in this study in five different media. The diffusion coefficients (D) are presented in Table 5.

Table 5. Diffusion Coefficient Values of Various Ferrocene/Ferricenium Derivatives in Different Solvent/Electrolyte Solutions.

	10^6 × **D** [(cm^2·s^{-1})] in MeCN				10^6 × **D** [(cm^2·s^{-1})] in DCM				10^6 × **D** [(cm^2·s^{-1})] in MeTHF	
	[(*n*Bu)$_4$N][PF$_6$]		[(*n*Bu)$_4$N][B(C$_6$F$_5$)$_4$]		[(*n*Bu)$_4$N][PF$_6$]		[(*n*Bu)$_4$N][B(C$_6$F$_5$)$_4$]		[(*n*Bu)$_4$N][B(C$_6$F$_5$)$_4$]	
	Anodic	Cathodic	Anodic	Cathodic	Anodic	Cathodic	Anodic	Cathodic	Anodic	Cathodic
^{Me10}**Fc**	12.96 ± 0.00	13.86 ± 0.00	12.96 ± 0.00	12.66 ± 0.00	5.62 ± 0.01	6.22 ± 0.01	3.69 ± 0.01	3.36 ± 0.01	4.78 ± 0.01	3.91 ± 0.01
^{Me2}**Fc**	17.83 ± 0.00	18.79 ± 0.00	14.18 ± 0.01	15.59 ± 0.01	9.40 ± 0.04	9.05 ± 0.01	5.03 ± 0.02	2.66 ± 0.02	5.51 ± 0.01	5.92 ± 0.01
^{nBu}**Fc**	18.34 ± 0.00	18.60 ± 0.00	14.12 ± 0.01	14.84 ± 0.01	7.92 ± 0.02	7.64 ± 0.01	8.07 ± 0.01	6.93 ± 0.01	4.54 ± 0.01	4.52 ± 0.01
Fc	13.67 ± 0.00	13.28 ± 0.01	8.80 ± 0.01	13.19 ± 0.00	9.27 ± 0.02	9.37 ± 0.02	12.3 ± 0.01	12.2 ± 0.01	4.66 ± 0.01	4.59 ± 0.01
^{Br}**Fc**	13.28 ± 0.00	12.74 ± 0.00	12.31 ± 0.01	13.04 ± 0.00	7.81 ± 0.01	7.73 ± 0.01	6.70 ± 0.01	4.55 ± 0.01	5.82 ± 0.00	5.17 ± 0.01
^{Ac}**Fc**	15.30 ± 0.01	12.35 ± 0.01	13.60 ± 0.00	14.55 ± 0.01	9.81 ± 0.01	9.32 ± 0.01	5.77 ± 0.01	3.96 ± 0.01	7.20 ± 0.01	6.74 ± 0.01
^{Bz}**Fc**	13.29 ± 0.01	11.00 ± 0.01	13.38 ± 0.01	13.72 ± 0.01	6.61 ± 0.01	6.48 ± 0.01	6.11 ± 0.01	5.69 ± 0.01	5.98 ± 0.01	5.16 ± 0.01
^{Br2}**Fc**	18.08 ± 0.00	14.98 ± 0.01	11.18 ± 0.01	9.94 ± 0.01	9.15 ± 0.01	8.755 ± 0.01	10.7 ± 0.00	9.71 ± 0.01	4.60 ± 0.01	2.66 ± 0.01
^{Ac2}**Fc**	12.51 ± 0.01	10.49 ± 0.02	12.85 ± 0.00	9.78 ± 0.02	5.60 ± 0.01	5.68 ± 0.01	2.75 ± 0.00	1.30 ± 0.01	6.14 ± 0.00	3.99 ± 0.01
^{Bz2}**Fc**	9.37 ± 0.01	6.72 ± 0.01	7.30 ± 0.00	5.67 ± 0.02	2.95 ± 0.01	2.29 ± 0.02	1.33 ± 0.00	0.21 ± 0.01	4.65 ± 0.00	3.04 ± 0.01

The diffusion coefficients of the neutral ferrocene derivatives and their ferricenium counterparts are typically not very different.[56] As expected, the species moved the fastest in MeCN compared to DCM or MeTHF. This can be attributed to the high polarity of the solvent, which minimizes the analyte-electrolyte ion pairing and subsequently decreases the resistance of the solution.[48a] Another factor that can facilitate the movement of analytes in the solution is the lower absolute viscosity of acetonitrile compared to DCM and MeTHF (Table 4).[49, 51] Among the ferrocene derivatives described here, both oxidized and neutral forms of ^{Me2}**Fc**, ^{nBu}**Fc**, and ^{Br2}**Fc** diffuse faster than the parent ferrocene and ferricenium by about 35% through the acetonitrile media.

The diffusion coefficients obtained in this study for both oxidized and neutral parent ferrocene species in MeCN with $[(n\text{Bu})_4\text{N}][\text{PF}_6]$ are lower (i.e., $D_{\text{Fc}} = 1.367 \times 10^{-5}$ cm^2·s^{-1}) than most previously reported values (i.e., $D_{\text{Fc}} \approx 2 \times 10^{-5} - 2.7 \times 10^{-5}$ cm^2·s^{-1}),[55, 57] which we contribute to our rigorous efforts to minimize the amount of water present in the solutions during our electrochemical measurements,[58] see Supporting Information for more details.

Some of the complexes (i.e., ^{nBu}**Fc**, **Fc**, ^{Br}**Fc**, ^{Bz}**Fc**, and ^{Br2}**Fc)** are found to diffuse slowest in the MeTHF solution which is in line with the higher viscosity and lower dielectric constant of the solvent compared to DCM. However, the remaining derivatives such as ^{Me10}**Fc**, ^{Me2}**Fc**, ^{Ac}**Fc**, ^{Ac2}**Fc**, and ^{Bz2}**Fc** follow a reverse trend and have larger diffusion constants in MeTHF than DCM. Perhaps this stems from the fact that the substituents in these derivatives may disrupt the "normal" charge density distribution throughout the complex, interfering with ion-pairing interaction in MeTHF, therefore, disrupting the expected trend of the solvent/analyte interactions prevalent in solvents of low-polarity.[53]

Furthermore, the diffusion coefficient of a given solute is inversely proportional to the size (i.e., hydrodynamic radius) of the solute and, hence, to its molecular weight assuming all species are hard spheres and have the same density.[59] Gonzalez and coworkers described a linear correlation between the diffusion coefficient and molecular weight.[57a] As the molecular weight increases, the diffusion coefficient decreases. This was generally observed in our experiments, although not perfectly, with the highest correlation obtained in the DCM solution with $[(n\text{Bu})_4\text{N}][\text{PF}_6]$ as the supporting electrolyte. Slight outliers are labeled in Figure 151.

As mentioned earlier, all the ferrocene derivatives described here show a quasi-reversibility of the redox behavior which is in agreement with our crystallographic data confirming that the difference in Fe–C bond length between their oxidized and neutral form is not larger than 0.05 Å, except for ^{Me2}**Fc** which experiences about 0.06 Å Fe–C bond elongation upon oxidation (Table 14). Additionally, the relatively lower current density observed for ^{Bz2}**Fc** and to a lesser extent for ^{Ac2}**Fc**, particularly in DCM with $[B(C_6F_5)_4]^-$ as the counter anion (Figure 87), can be the consequence of the much slower diffusion (Table 5) and significant rearrangements of the substituents that accompany the electron transfer process. This is in agreement with our crystallographic data and the one broad Cp proton resonance observed for their oxidized forms, ^{Ac2}**Fc**$^+$ and ^{Bz2}**Fc**$^+$, in our ^{1}H-NMR studies.

Conclusion

Despite the enormous number of publications in the field of ferrocenes and their redox counterparts, ferriceniums, information on the synthesis and characterization of these complexes is relatively sparse and in most cases the reports lack the relevant experimental details. Moreover, most efforts have been focused on the electron-rich ferricenium species and very limited data are available on the electron-deficient systems. This represents a surprising knowledge gap in the literature. Herein, we attempted to address some of that gap through a systematic and thorough evaluation of a library of highly organic soluble ferricenium derivatives.

Our ^{1}H-NMR measurements revealed that the substitutional behavior in the paramagnetic ferricenium derivatives is more complex and fundamentally reversed as compared to the neutral ferrocene counterparts. We proposed that the δ back-donation from the iron atom into the substituted Cp rings leads to the overall shielding of the ring protons in the ferrocenium derivatives. This shielding through δ back-donation is more pronounced in the electron-deficient rings with lower energy molecular orbitals. Our data for the electron-deficient ferricenium derivatives in solution also drew a direct correlation between the solvent dielectric constant and the rotation of the cyclopentadienyl ligands around the Fe–Cp bond in these systems.

Here, nine new X-ray structures are also added to the library of ferricenium derivatives, five of which presented the first examples of molecular structures of such derivatives. Structural comparison of the neutral ferrocene derivatives and their oxidized counterparts revealed that the oxidation of ferrocene results in more substantial shortening of the C–C bond lengths in the Cp rings of the parent ferricenium complex relative to those of their substituted counterparts. Interestingly, our results also show that the nature of the substituents has a more significant effect on the metal-ligand separations in the oxidized species than in their neutral analogs. For the ketone-substituted ferricenium derivatives, the increase in the oxidation state was reflected in a significant strengthening of the carbonyl bond(s) by about 35–48 cm^{-1} when compared with the neutral ferrocene counterparts.

Additionally, the redox behavior of the corresponding ferricenium/ferrocene (**$Fc^{+/0}$**) redox couples such as potential values ($E_{½}$), peak-to-peak separation ($\Delta E_{½}$), and diffusion coefficients (D) of the redox active species in three different solvents and two supporting electrolytes are reported in this work. The results point to the significant effect of the ion pairing in lowering the energy necessary for reduction of the ferricenium species and the overall half-wave potential.

In order to explain some of the observed spectroscopic and structural features of the ferricenium systems, particularly those bearing electron withdrawing substituents, further investigations are required; as is often the case in bonding and electronic structures, “the devil is in the details”. Additional experimental and computational efforts are currently underway in our laboratory.

Experimental Section

GENERAL METHODS

All chemicals and solvents were of commercially available grade, unless otherwise noted. Acetonitrile (MeCN), 2-methyltetrahydrofuran (MeTHF) (inhibitor free, 673277), dichloromethane (DCM) and hexanes were purchased from Sigma-Aldrich. *1,2*-Difluorobenzene was purchased from Alfa Aesar. All solvents were further purified by passing through a 60 or 18 cm-long column of activated alumina under argon using an

Innovative Technologies or Inert PureSolv Micro solvent purification system. The solvents were further deoxygenated by either repeated freeze/pump/thaw cycles or bubbling with argon for 45–60 min followed by storage over 3 or 5 Å molecular sieves for at least 72 hours prior to use. Air- and moisture-sensitive compounds were synthesized and handled under a dry oxygen-free argon atmosphere using standard Schlenk techniques or in a Vacuum Atmospheres OMNI-Lab inert atmosphere (< 0.5 ppm of O_2 and H_2O) glovebox filled with nitrogen.

Bench-top UV-vis spectra were recorded with a Cary-60 spectrophotometer using a 2 or 10 mm modified Schlenk cuvette. Infrared (IR) spectra were obtained using a Thermo Scientific Nicolet iS5 Fourier Transform IR (FT-IR) spectrometer equipped with an iD7 attenuated total reflection (ATR) accessory. ^{1}H-NMR spectra were recorded on a JEOL 400 or 500 MHz instrument. The chemical shifts were referenced against tetramethylsilane (TMS, $\delta = 0.00$ ppm). The NMR solvent residual peaks were used as a secondary reference. Elemental analysis was accomplished at Midwest Microlab (Indianapolis, IN). Electrochemical data was collected using a Bio-Logic SP-200 potentiostat. Single-crystal X-ray data were collected using a Gemini R (Agilent Technologies) diffractometer at the X-ray diffraction facility of the Joint School of Nanoscience and Nanoengineering (JSNN). The temperature of the data collection was controlled using the system Cryojet (manufactured by Oxford Instruments).

The compounds, *1*-acetylferrocene (97%), and decamethylferrocene (99%) were purchased from Alfa Aesar; *1*-benzoylferrocene (>98%), *1,1'*-dibromoferrocene (>98%), and *1,1'*-dibenzoylferrocene (98%) from Tokyo Chemical Industry (TCI); ferrocene (98%), *1*-bromoferrocene (98.8%), *1,1'*-diacetylferrocene (97%), and ferrocenecarboxylic acid (99%) from Sigma-Aldrich; *1,1'*-dimethylferrocene (98%), and *n*-butylferrocene (99%) from Stream Chemicals. Potassium *tetrakis*(pentafluorophenyl)borate, $K[B(C_6F_5)_4]$, (99.9%) was purchased from Boulder Scientific Company; $AgNO_3$ (99.99%) from Alfa Aesar; $Ag[SbF_6]$ (98%) and *tris*(4-bromophenyl)amine from Sigma-Aldrich; *tetra-n*-butylammonium hexafluorophosphate (98%) from Oakwood Chemicals. *Tetra-n*-

butylammonium chloride hydrate (99.84%) and potassium chloride (99%) were purchased from Alfa Aesar.

Deuterated solvents including acetone-d_6 (D, 99.9%) and methylene chloride-d_2 (D, 99.8%) were purchased from Cambridge Isotope Laboratories. Distilled water was further purified by a PURELAB flex 1 Analytical Ultrapure Water System (ELGA) to obtain the specific resistance of 18.2 MΩ•cm at 25°C.

SYNTHESIS AND CHARACTERIZATION

Tetrakis(acetonitrile)silver(I) BArF20 ([Ag(MeCN)4][B(C6F5)4]): The current synthetic procedure is a slightly modified version of the method reported earlier for the synthesis of $[Ag(MeCN)_4][B(C_6F_5)_4]$.[21] In the glove box, a solution of $K[B(C_6F_5)_4]$ (863.0 mg, 1.202 mmol) in MeCN (15 mL) was added to a solution of $AgNO_3$ (204.1 mg, 1.202 mmol) in MeCN (9 mL) and the reaction mixture was stirred for 1 h under reduced light at RT. The reaction mixture was then filtered to remove the precipitate, KNO_3. The solvent was removed under vacuum. The solid semi-crystalline product was re-dissolved in a minimum amount of MeCN and was kept in the freezer at –35°C overnight to obtain white needle shaped crystals suitable for X-ray structural determination (Figure 76). After drying under vacuum, the crystals of $[Ag(MeCN)_4][B(C_6F_5)_4]$ weighed 983.2 mg (86.14% yield). Anal. calcd for $C_{32}H_{12}AgBF_{20}N_4$: C, 40.41; H, 1.27; N, 5.89. Found: C, 40.25; H, 1.28; N, 5.65. FT-IR (solid; cm^{-1}): $v_{(C\equiv N)}$ = 2295 (Figure 16). The deuterated complex, $[Ag(CD_3CN)_4][B(C_6F_5)_4]$, was prepared by the same procedure described above using deuterated acetonitrile, CD_3CN. FT-IR (solid; cm^{-1}): $v_{(C\equiv N)}$ = 2287 (Figure 17). ^{1}H-NMR (acetone-d_6, 500 MHz; δ, ppm): 2.04 (s, 12H) (Figure 152). ^{19}F-NMR (acetone-d_6, 470 MHz; δ, ppm): –133.0, –164.3, –168.2 (Figure 153).

The $BArF_{20}$ salts of the parent ferricenium complex and a series of ferricenium derivatives bearing electron-donating substituents were prepared following the general procedure described here. The complexes include ^{Me10}**Fc**$BArF_{20}$, ^{Me2}**Fc**$BArF_{20}$, ^{nBu}**Fc**$BArF_{20}$, and **Fc**$BArF_{20}$. Details are given for decamethylferricenium $BArF_{20}$, as a representative case.

Decamethylferricenium BArF$_{20}$ (^{Me10}**Fc**BArF$_{20}$): In the glove box, to a solution of decamethylferrocene (249.8 mg, 0.758 mmol) in MeTHF (5 mL) was added the solution of $[Ag(MeCN)_4][B(C_6F_5)_4]$ (648.7 mg, 0.682 mmol) in MeTHF (10 mL). The reaction mixture was allowed to stir for 1 h under reduced light at RT. The solution was then filtered through Celite to remove the silver metal. The filtrate was evaporated and washed with hexanes to remove the remaining, unreacted decamethylferrocene. The compound obtained was then dried and crystallized from MeTHF/hexanes. The crystals were further washed with hexanes and were again recrystallized from MeTHF/hexanes. Dark green crystals were obtained which were suitable for X-ray structure determination (Figure 77). After vacuum drying, the yield of ^{Me10}**Fc**BArF$_{20}$ was 88.12% (604.3 mg). Anal. calcd for $C_{44}H_{30}BF_{20}Fe$: C, 52.57; H, 3.01; N, 0.00. Found: C, 52.31; H, 2.99; N, 0.00. UV-vis [λ_{max}, nm (ε_{max}, $M^{-1}cm^{-1}$)]: 652 (215), 719 (320), 780 (580) in MeTHF and 652 (222), 715 (320), 778 (581) in MeCN. FT-IR (solid; cm^{-1}): $\nu_{(C-H):Me}$ = 2987, 2978, 2925 (Figure 19). ^{1}H-NMR (acetone-d_6, 500 MHz; δ, ppm): –37.6 (s, br, 30H) (Figure 32). ^{19}F-NMR (acetone-d_6, 470 MHz; δ, ppm): –133.0, –164.3, –168.3 (Figure 59).

1,1'-dimethylferricenium BArF$_{20}$ *(^{Me2}**Fc**BArF$_{20}$):* Prussian blue crystals were collected (Figure 78), 155.4 mg (89.67% yield). Anal. calcd for $C_{36}H_{14}BF_{20}Fe$: C, 48.41; H, 1.58; N, 0.00. Found: C, 48.34; H, 1.59; N, 0.00. UV-vis [λ_{max}, nm (ε_{max}, $M^{-1}cm^{-1}$)]: 472 (175), 572 (227), 654 (358) in MeTHF and 473 (148), 569 (203), 654 (325) in MeCN. FT-IR (solid; cm^{-1}): $\nu_{(Cp-H)}$ = 3115; $\nu_{(C-H):Me}$= 2934, 2919, 2895, 2877 (Figure 20). ^{1}H-NMR (acetone-d_6, 500 MHz; δ, ppm): 34.8 (vbr, 4H), 31.6 (vbr, 4H), –10.5 (br, 6H) (Figure 55). ^{19}F-NMR (acetone-d_6, 470 MHz; δ, ppm): –133.1, –164.4, –168.5 (Figure 60). ^{1}H-NMR (CD_2Cl_2, 500 MHz; δ, ppm): 35.8 (vbr, 4H), 32.5 (vbr, 4H), –9.0 (br, 6H) (Figure 56). ^{19}F-NMR (CD_2Cl_2, 470 MHz; δ, ppm): –134.9, –164.3, –168.9 (Figure 61).

n-Butylferricenium BArF$_{20}$ (^{nBu}**Fc**BArF$_{20}$): Peacock blue crystals were collected (Figure 79), 122.5 mg (80.59% yield). Anal. calcd for $C_{38}H_{18}BF_{20}Fe$: C, 49.55; H, 1.97; N, 0.00. Found: C, 49.43; H, 1.97; N, 0.00. UV-vis [λ_{max}, nm (ε_{max}, $M^{-1}cm^{-1}$)]: 471 (188), 556 (236), 630 (364) in MeTHF and 472 (162), 559 (226), 628 (380) in MeCN. FT-IR (solid; cm^{-1}): $\nu_{(Cp-H)}$ = 3128; $\nu_{(C-H):nBu}$ = 2960, 2934, 2876, 2865. (Figure 21). ^{1}H-NMR (acetone-d_6, 500

MHz; δ, ppm): 37.4 (vbr, 2H), 33.9 (vbr, 2H), 31.3 (vbr, 5H), 1.2 (s, br, 2H), –1.0 (s, 3H), –6.8 (s, 2H), –18.3 (s, br, 2H) (Figure 51). ^{19}F-NMR (acetone-d_6, 470 MHz; δ, ppm): –133.0, –164.3, –168.3 (Figure 62). ^{1}H-NMR (CD_2Cl_2, 500 MHz; δ, ppm): 38.6 (vbr, 2H), 35.5 (vbr, 2H), 32.1 (vbr, 5H), 1.0 (s, br, 2H), –1.1 (s, 3H), –7.4 (s, 2H), –16.7 (s, br, 2H) (Figure 52). ^{19}F-NMR (CD_2Cl_2, 470 MHz; δ, ppm): –135.0, –164.3, –167.0 (Figure 63).

Ferricenium BArF$_{20}$ (***Fc**BArF$_{20}$*): 921.5 mg (88.26% yield). Anal. calcd for $C_{34}H_{10}BF_{20}Fe$: C, 47.21; H, 1.17; N, 0.00. Found: C, 47.15; H, 1.26; N, 0.00. UV-vis [λ_{max}, nm (ε_{max}, $M^{-1}cm^{-1}$)]: 469 (141), 536 (181), 621 (441) in MeTHF and 469 (156), 535 (199), 618 (445) in MeCN. FT-IR (solid; cm^{-1}): $\nu_{(Cp\text{-}H)}$ = 3128 (Figure 22). ^{1}H-NMR (acetone-d_6, 500 MHz; δ, ppm): 33.2 (s, vbr, 10H) (Figure 30). ^{19}F-NMR (acetone-d_6, 470 MHz; δ, ppm): –133.0, –164.4, –168.4 (Figure 64).

The BArF$_{20}$ salts of a series of ferricenium derivatives bearing one electron-withdrawing substituents as well as the *1,1'*-dibromo substituted ferricenium were prepared following the general procedure described here. Those complexes include ^{Br}**Fc**BArF$_{20}$, ^{Ac}**Fc** BArF$_{20}$, ^{Bz}**Fc**BArF$_{20}$, and **Fc**BArF$_{20}$. Details are given for *1-bromoferricenium* BArF$_{20}$, as a representative case. *Note:* For both mono-ketone-substituted ferrocenes, the order of addition of reagents is reversed (i.e., the solution of substituted ferrocene is gradually added to the silver(I) solution). An alternative procedure for the preparation of ^{Bz}**Fc**[B(C_6F_5)$_4$] is also included.

*1-Bromoferricenium BArF$_{20}$ (^{Br}**Fc**BArF$_{20}$):* In the glove box, a solution of *1*-bromoferrocene (252.2 mg, 0.944 mmol) in DCM (5 mL) was added to the solution of [Ag(MeCN)$_4$][B(C_6F_5)$_4$] (808.4 mg, 0.850 mmol) in DCM (20 mL). The mixture was stirred for 1 h under reduced light at RT. The solution was filtered through Celite to remove the silver metal. The filtrate was evaporated, washed with hexanes to remove the unreacted *1*-bromoferrocene, and dried before it was crystallized from MeTHF/hexanes. After the crystallization, the solvent was decanted. Crystals were further washed with hexanes and were recrystallized from MeTHF/hexanes. The crystals were dark blue and suitable for X-ray structure determination (Figure 80). After vacuum drying, the crystals weighed 697.2

mg (86.89% yield). Anal. calcd for $C_{34}H_9BF_{20}BrFe$: C, 43.26; H, 0.96; N, 0.00. Found: C, 42.99; H, 1.07; N, 0.00. UV-vis [λ_{max}, nm (ε_{max}, $M^{-1}cm^{-1}$)]: 477 (205), 567 (237), 683 (365) in MeTHF and 476 (207), 563 (234), 676 (362) in MeCN. FT-IR (solid; cm^{-1}): $v_{(Cp\text{-}H)}$ = 3124, 3114, 3102 (Figure 23). ^{1}H-NMR (acetone-d_6, 500 MHz; δ, ppm): 34.0 (s, vbr, 5H), 32.0 (s, vbr, 2H), 28.8 (s, vbr, 2H) (Figure 53). ^{19}F-NMR (acetone-d_6, 470 MHz; δ, ppm): –133.0, –164.4, –168.4 (Figure 65). ^{1}H-NMR (CD_2Cl_2, 500 MHz; δ, ppm): 35.0 (s, vbr, 5H), 33.1 (s, vbr, 4H) (Figure 54). ^{19}F-NMR (CD_2Cl_2, 470 MHz; δ, ppm): –135.2, –164.2, –169.0 (Figure 66).

1-Acetylferricenium BArF$_{20}$ (*^{Ac}**Fc**BArF$_{20}$)*: In the glove box, a solution of *1*-acetylferrocene (175.4 mg, 0.746 mmol) in DCM (3 mL) was added to the solution of $[Ag(MeCN)_4][B(C_6F_5)_4]$ (354.7 mg, 0.373 mmol) in DCM (10 mL). The unreacted *1*-acetylferrocene was removed by washing the crude product with hexanes. The crystals were grown in DCM/hexanes. 278.4 mg (82.28% yield), see Figure 81 for the molecular packing. Anal. calcd for $C_{36}H_{12}BF_{20}FeO$: C, 47.67; H, 1.33; N, 0.00. Found: C, 47.43; H, 1.36; N, 0.00. UV-vis [λ_{max}, nm (ε_{max}, $M^{-1}cm^{-1}$)]: 475 (198), 550 (202), 638 (425) in MeTHF and 481 (188), 555 (216), 638 (463) in DCM. FT-IR (solid; cm^{-1}): $v_{(Cp\text{-}H)}$ = 3377; $v_{(C–H):Ac}$ = 3140, 3125, 3115, 3092; $v_{(C=O):Ac}$ = 1698 (Figure 24). ^{1}H-NMR (acetone-d_6, 500 MHz; δ, ppm): 36.3 (s, vbr, 5H), 31.8 (s, vbr, 2H), 27.5 (s, vbr, 2H), –15.9 (s, br, 3H) (Figure 55). ^{19}F-NMR (acetone-d_6, 470 MHz; δ, ppm): –133.0, –164.4, –168.4 (Figure 67). ^{1}H-NMR (CD_2Cl_2, 500 MHz; δ, ppm): 37.2 (s, vbr, 5H), 32.4 (s, vbr, 2H), 30.4 (s, vbr, 2H), –13.0 (s, br, 3H) (Figure 56). ^{19}F-NMR (CD_2Cl_2, 470 MHz; δ, ppm): –135.2, –164.1, –169.0 (Figure 68).

1-Benzoylferricenium BArF$_{20}$ (*^{Bz}**Fc**BArF$_{20}$)*: An additional filtration step was performed to remove any silver(I) salt impurity. As an alternative procedure, in the glove box, a solution of benzoylferrocene (111.0 mg, 0.375 mmol) and $K[B(C_6F_5)_4]$ (269.3 mg, 0.375 mmol) in DCM (10 mL) was slowly added to the solution of $Ag[SbF_6]$ (131.5 mg, 0.375 mmol) in DCM (3 mL). The reaction mixture was allowed to stir for 15 min under reduced light at RT. The solution was then filtered through Celite to remove the silver metal and insoluble $K[SbF_6]$. The solvent was removed under vacuum and the resulting solid product was washed with hexanes to remove the remaining, unreacted *1*-benzoylferrocene. Moss green crystals were grown from DCM/hexanes (296.1 mg, 81.47% yield), see Figure 82 for the molecular packing. Anal. calcd for $C_{41}H_{14}BF_{20}FeO$: C, 50.81; H, 1.46; N, 0.00. Found: C, 50.15; H, 1.45; N, 0.00. UV-vis [λ_{max}, nm (ε_{max}, $M^{-1}cm^{-1}$)]: 473 (239), 555 (231), 640 (448) in MeTHF and 476 (230), 572 (249), 638 (439) in DCM. FT-IR (solid; cm^{-1}): $\nu_{(Cp\text{-}H)/(C–H):\mathit{Bz}}$ = 3298, 3103, 3082, 2981, 2965; $\nu_{(C=O):\mathit{Bz}}$ = 1658 (Figure 25). ^{1}H-NMR (acetone-d_6, 500 MHz; δ, ppm): 35.4 (vbr, 5H), 31.3 (vbr, 2H), 27.6 (vbr, 2H), 7.5 (s, br, 2H), 6.3 (s, 2H), 6.2 (s, H) (Figure 57). ^{19}F-NMR (acetone-d_6, 470 MHz; δ, ppm): –133.0, –164.3, –168.3 (Figure 69). ^{1}H-NMR (CD_2Cl_2, 500 MHz; δ, ppm): 36.0 (vbr, 5H), 30.5 (vbr, 4H), 12.4 (s, br, 2H), 7.3 (s, 2H), 6.7 (s, H) (Figure 58). ^{19}F-NMR (CD_2Cl_2, 470 MHz; δ, ppm): –134.9, –164.4, –168.5 (Figure 70).

1,1'-Dibromoferricenium BArF$_{20}$ (^{Br2}***Fc****BArF$_{20}$)*: 542.1 mg (88.62% yield). See Figure 83 for the molecular packing. Anal. calcd for $C_{34}H_8BF_{20}Br_2Fe$: C, 39.92; H, 0.79; N, 0.00. Found: C, 39.94; H, 0.86; N, 0.00. UV-vis [λ_{max}, nm (ε_{max}, $M^{-1}cm^{-1}$)]: 487 (280), 594 (282), 716 (411) in MeTHF and 486 (257), 599 (256), 708 (389) in MeCN. FT-IR (solid; cm^{-1}): $\nu_{(Cp\text{-}H)}$ = 3133, 3124, 3101 (Figure 26). ^{1}H-NMR (acetone-d_6, 400 MHz; δ, ppm): 34.2 (s, br, 4H), 29.6 (s, br, 4H) (Figure 47). ^{19}F-NMR (acetone-d_6, 376 MHz; δ, ppm): –133.0, –164.2, –168.4 (Figure 71). ^{1}H-NMR (CD_2Cl_2, 500 MHz; δ, ppm): 34.5 (s, br, 4H), 32.7 (s, br, 4H) (Figure 48). ^{19}F-NMR (CD_2Cl_2, 470 MHz; δ, ppm): –135.4, –164.3, –169.1 (Figure 72).

*1,1'-Diacetylferricenium BArF$_{20}$ (^{Ac2}**Fc**BArF$_{20}$)*: ^{Ac2}**Fc**BArF$_{20}$ can be prepared following a similar procedure as ^{Bz2}**Fc**[SbF_6] *(vide infra*), followed by an additional metathesis step using $K[B(C_6F_5)_4]$ in *1,2*-difluorobenzene. Alternatively, a more facile procedure is also described here. In the glove box, the solution of *1,1'*-diacetylferrocene (100.0 mg, 0.359 mmol) and $K[B(C_6F_5)_4]$ (257.8 mg, 0.359 mmol) in DCM (20 mL) was slowly added to the solution of $Ag[SbF_6]$ (125.9 mg, 0.359 mmol) in DCM (3 mL). The reaction mixture was allowed to stir for 5 mins under reduced light at RT. The solution was then filtered through Celite to remove the silver metal and insoluble $K[SbF_6]$. The filtrate was evaporated and washed with benzene to remove the remaining, unreacted *1,1'*-diacetylferrocene. Then it was dried and crystallized from DCM/hexanes. After the crystallization, the solvent was decanted, and crystals were further washed with hexanes. Dark green crystals, suitable for X-ray structure determination, were obtained with further recrystallization with DCM/hexanes (Figure 84). 279.3 mg (81.96 % yield). Anal. calcd for $C_{38}H_{14}BF_{20}FeO_2$: C, 48.09; H, 1.49; N, 0.00. Found: C, 48.23; H, 1.48; N, 0.00. UV-vis [λ_{max}, nm (ε_{max}, $M^{-1}cm^{-1}$)]: 476 (283), 602 (278), 652 (422) in *1,2*-difluorobenzene and 476 (295), 602 (298), 654 (439) in DCM. FT-IR (solid; cm^{-1}): $\nu_{(Cp\text{-}H)}$ = 3377; $\nu_{(Cp\text{-}H):Ac}$ = 3117, 3104; $\nu_{(C=O):Ac}$ = 1697 (Figure 27). ^{1}H-NMR (CD_2Cl_2, 500 MHz; δ, ppm): 30.69 (vbr, 8H), –9.43 (s, br, 6H) (Figure 49). ^{19}F-NMR (CD_2Cl_2, 470 MHz; δ, ppm): –134.7, –163.8, –168.5 (Figure 73).

1,1'-Dibenzoylferricenium SbF₆ (^{Bz2}***Fc****[SbF₆])*: In the glove box, a solution of *1,1'*-dibenzoylferrocene (499.7 mg, 1.268 mmol) in DCM (10 mL) was added to a solution of Ag[SbF_6] (444.6 mg, 1.268 mmol) in DCM (12 mL). The mixture was stirred for 1 h under reduced light at RT. The reaction mixture was then filtered through Celite to remove the silver metal. The filtrate was dried under vacuum, and the complex was crystallized from DCM/hexanes. After the crystallization, the solvent was decanted, and crystals were further washed with hexanes. Dark green crystals, suitable for X-ray structure determination, were grown through the slow diffusion of hexanes into the concentrated solution of the ^{Bz2}**Fc**[SbF_6] in DCM (Figure 85). After vacuum drying, the crystals weighed 679.6 mg (85.07% yield). Anal. calcd for $C_{24}H_{18}F_6FeO_2Sb$: C, 45.76; H, 2.88; N, 0.00. Found: C, 45.53; H, 2.79; N, 0.00. UV-vis [λ_{max}, nm (ε_{max}, $M^{-1}cm^{-1}$)]: 492 (650), 650 (545) in *1,2*-difluorobenzene and 493 (588), 587 (474), 653 (564) in DCM. FT-IR (solid; cm^{-1}): $\nu_{(Cp\text{-}H)}$ = 3308; $\nu_{(C-H):Bz}$ = 3123, 3112, 3100, 3068; $\nu_{(C=O):Bz}$ = 1665; $\nu_{(SbF6)}$= 651 (Figure 28). ^{1}H-NMR (CD_2Cl_2, 500 MHz; δ, ppm): 30.2 (s, vbr, 8H), 10.3 (s, br, 4H), δ 7.0 (s, 4H), δ 6.7 (s, 2H) (Figure 50). ^{19}F-NMR (CD_2Cl_2, 470 MHz; δ, ppm): –133.2 ($^1J(^{19}F\text{-}^{121}Sb)$ ≈ 2 kHz) (Figure 74).

Tetra-n-butylammonium BArF₂₀ ([(nBu)₄N][B(C₆F₅)₄]): A solutions of [(*n*Bu)$_4$N]Cl (4.50 g, 16.2 mmol) in dry MeCN (50 mL) was added into a solution of K[$B(C_6F_5)_4$] (11.66 g, 16.2 mmol) in dry MeCN (900 mL), in a 3-neck 1-liter round bottom flask under dry argon. Upon mixing, a white precipitate was observed, and the mixture was stirred for 2 h to ensure complete precipitation of KCl, followed by filtration. The solvent was removed under a vacuum. The resulting clear oil was further dried under vacuum overnight to yield a white solid. This solid was then dissolved in DCM and layered with hexanes for crystallization. Clear crystals were collected, dried and recrystallized using the same conditions. After drying the crystals, these were ground up to produce a fine white powder that was dried for an additional day under vacuum. The $[(n\text{Bu})_4\text{N}][\text{B}(\text{C}_6\text{F}_5)_4]$ powder was then stored under dry argon or in the glove box (12.89 g, 86.34% yield). Anal. calcd for $C_{40}H_{36}NBF_{20}$: C, 52.14; H, 3.94; N, 1.52. Found: C, 52.28; H, 3.80; N, 1.51. FT-IR (solid; cm^{-1}): $\nu_{(\text{C–H}):nBu}$ = 2980, 2969, 2944, 2880 (Figure 154). ^{1}H-NMR (acetone-d_6, 500 MHz; δ, ppm): 0.98 (t, 12H), 1.44 (sextet, 8H), 1.84 (q, 8H), 3.46 (m, 8H) (Figure 155). ^{19}F-NMR (acetone-d_6, 470 MHz; δ, ppm): –133.0, –164.3, –168.2 (Figure 156).

CRYSTALLOGRAPHIC STUDIES

Suitable X-ray quality single crystals were grown in the glovebox by layering hexanes onto the solution of the ferricenium derivatives in either MeTHF or DCM in 5 mm glass tubes at RT. The complexes ^{Me10}**Fc**BArF$_{20}$, ^{Me2}**Fc**BArF$_{20}$, ^{nBu}**Fc**BArF$_{20}$ and ^{Br2}**Fc**BArF$_{20}$ were crystallized from MeTHF/hexanes while all other ferricenium derivatives were crystallized using DCM/hexanes. All reflection intensities were measured at 100(2) K using a Gemini R diffractometer (equipped with Atlas detector) with Mo Kα radiation (λ = 0.71073 Å) under the program CrysAlisPro (Version CrysAlisPro 1.171.38.43f, Rigaku OD, 2015). The same program (but a different version viz. CrysAlisPro 1.171.40.53, Rigaku OD, 2019) was used to refine the cell dimensions and for data reduction. The structures were solved with the program SHELXT-2018/2 and were refined on F2 by full-matrix least-squares technique using the SHELXL-2018/3 program package.[60] Numerical absorption correction based on gaussian integration was applied using a multifaceted crystal model by CrysAlisPro. Non-hydrogen atoms were refined anisotropically. In the refinement, hydrogen was treated as riding atoms using SHELXL default parameters.

ELECTROCHEMICAL MEASUREMENTS

A three-electrode setup was used for all voltammetry experiments with a 3.0-mm glassy carbon disk working electrode, a carbon rod counter electrode, and a leak-free Ag/AgCl reference electrode inside an inert atmosphere box. Three separate 2.0-mm diameter reference electrodes were filled with 3.4 M KCl aqueous solutions (i.e., LF2) from Innovative Instruments, Inc. The electrodes were stored in either a 0.05 M H_2SO_4 aqueous solution or a saturated KCl aqueous solution between experiments. All potentials were referenced to the leak-free Ag/AgCl electrode by measuring the ferrocene/ferricenium couple under identical conditions. The electrodes were cleaned with acetone and ultrapure water. The solvents used were MeCN, DCM, and MeTHF. The electrolytes, $[(n\mathrm{Bu})_4\mathrm{N}][\mathrm{B}(\mathrm{C}_6\mathrm{F}_5)_4]$ and $[(n\mathrm{Bu})_4\mathrm{N}][\mathrm{PF}_6]$, were further purified by recrystallization from MeCN and ethanol, respectively. The solutions (1 or 2 mM analyte, 100 mM electrolyte) were scanned anodically then cathodically within a 1.5–2 V potential range at varying scan rates. (For further details, see Supporting Information).

Supporting Information

SPECTROSCOPIC DATA FOR CHARACTERIZATION OF VARIOUS COMPOUNDS

NMR symbols for residual deuterated and protic solvents include the following: water (**+**), hexanes (^), acetone (*****), dichloromethane (Δ), chloroform (‡), acetonitrile (ϕ).

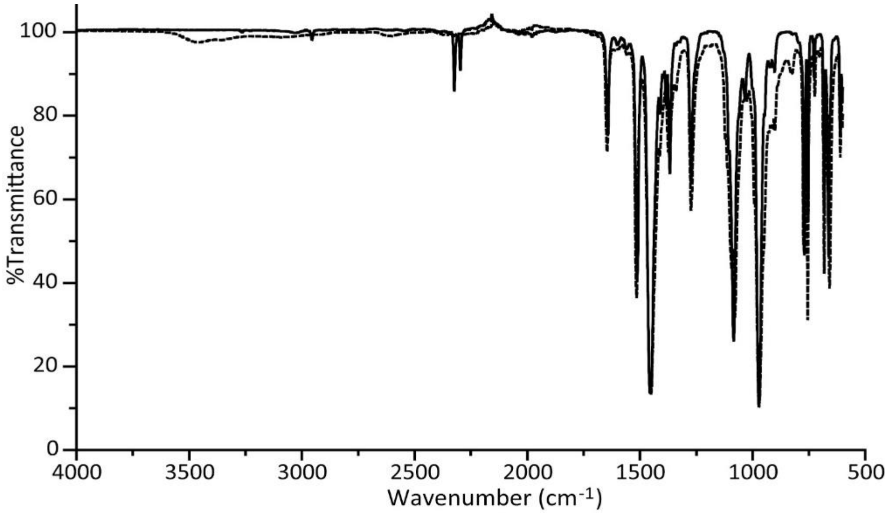

Figure 16. IR spectra comparison between K[B(C_6F_5)$_4$] (dotted line) and [Ag(MeCN)$_4$][B(C_6F_5)$_4$] (solid line).

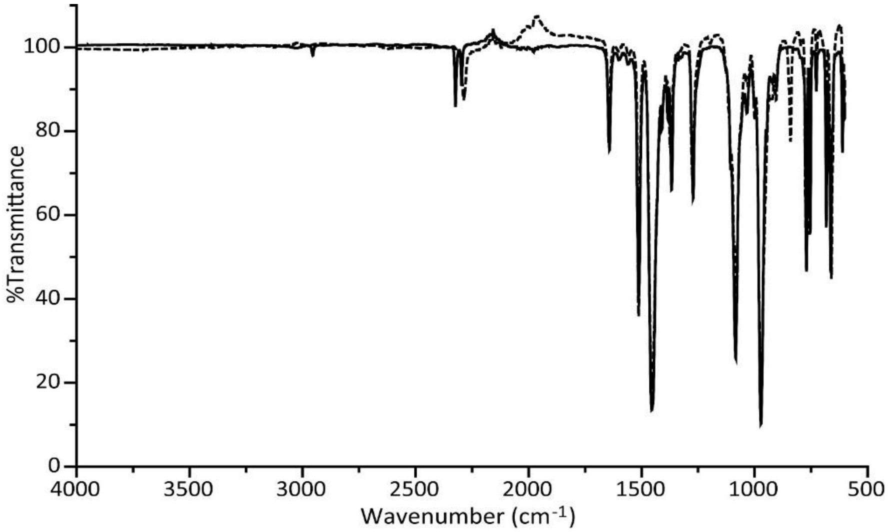

Figure 17. IR spectra comparison between [Ag(CD_3CN)$_4$][B(C_6F_5)$_4$] (dotted line) and [Ag(MeCN)$_4$][B(C_6F_5)$_4$] (solid line).

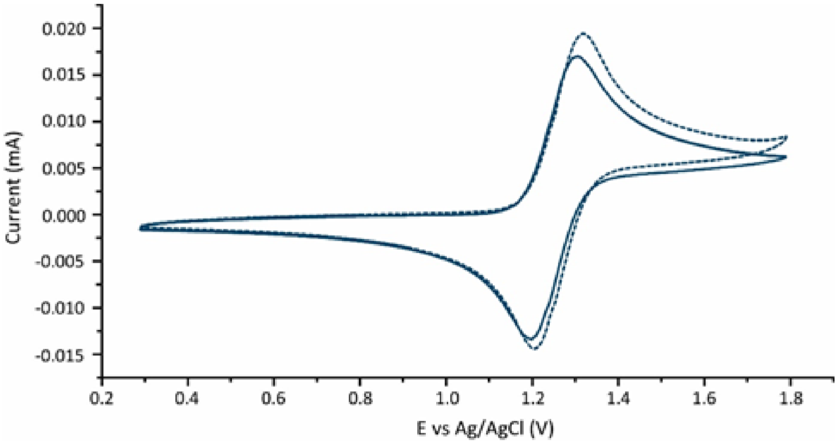

Figure 18. Cyclic voltammograms at 100 mV/s of 1 mM tris(4-bromophenyl)amine in DCM with 100 mM of either [(*n*Bu)$_4$N][B(C$_6$F$_5$)$_4$] (solid line, E$_{1/2}$ = 1.252 V) or [(*n*Bu)$_4$N][PF$_6$] (dashed line, E$_{1/2}$ = 1.267 V) as the supporting electrolyte. The potentials were collected vs a leak-free Ag/AgCl reference electrode. The working electrode was glassy carbon and the counter electrode was a carbon rod.

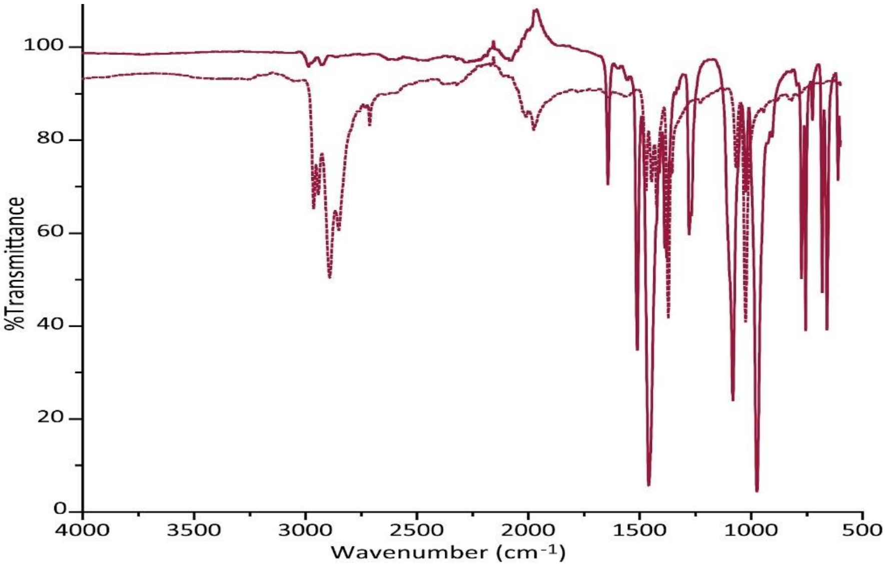

Figure 19. IR spectra comparison between ^{Me10}**Fc** (dotted line) and ^{Me10}**Fc**BArF$_{20}$ (solid line).

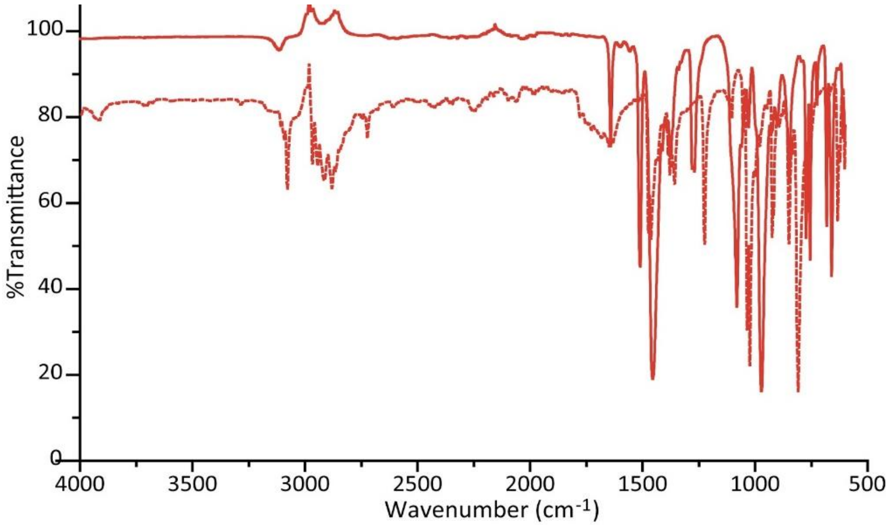

Figure 20. IR spectra comparison between ^{Me2}**Fc** (dotted line) and ^{Me2}**Fc**BArF$_{20}$ (solid line).

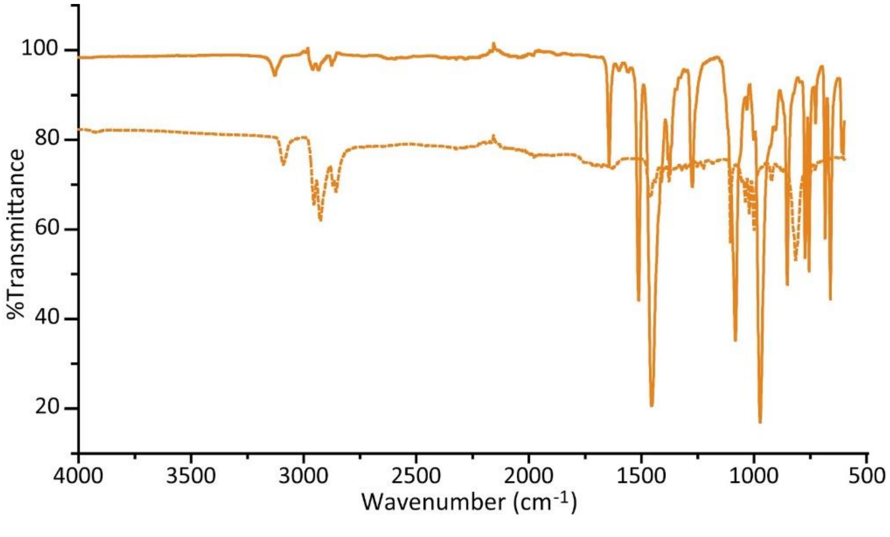

Figure 21. IR spectra comparison between ^{nBu}**Fc** (dotted line) and ^{nBu}**Fc**BArF$_{20}$ (solid line).

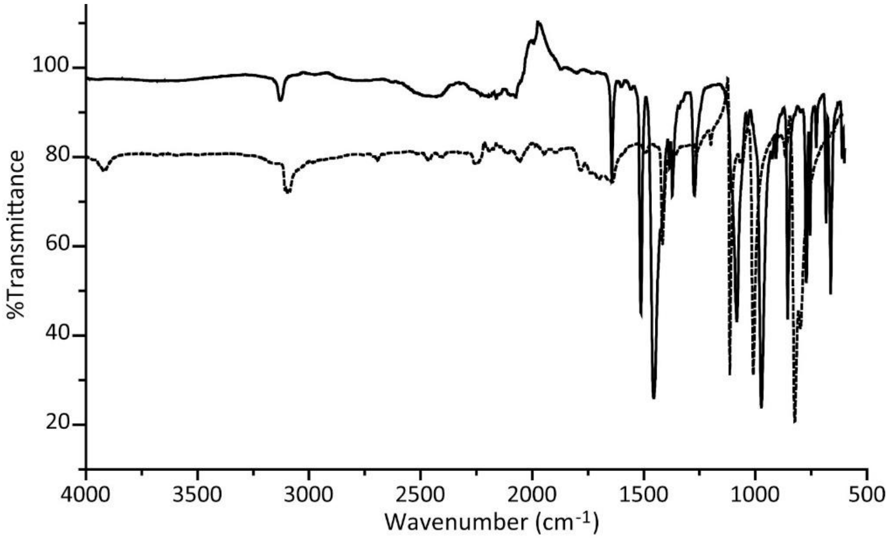

Figure 22. IR spectra comparison between **Fc** (dotted line) and **Fc**BArF$_{20}$ (solid line).

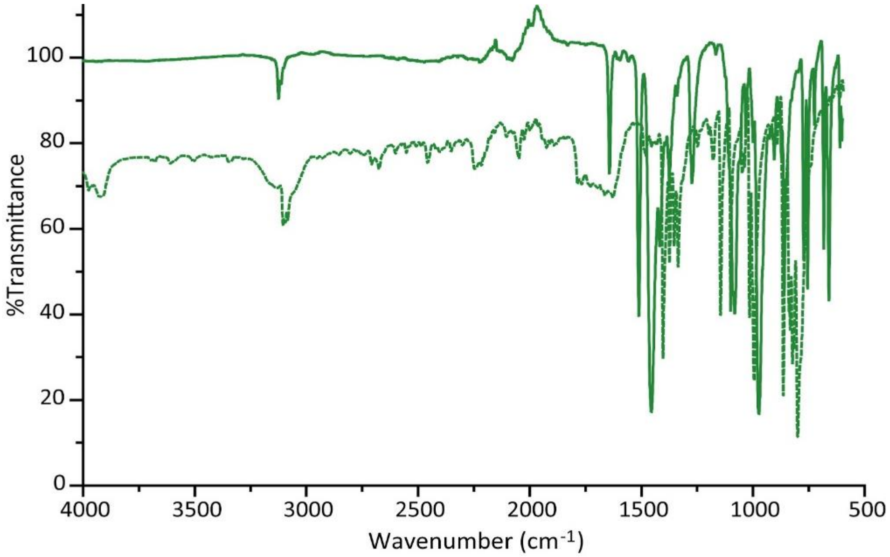

Figure 23. IR spectra comparison between ^{Br}**Fc** (dotted line) and ^{Br}**Fc**BArF$_{20}$ (solid line).

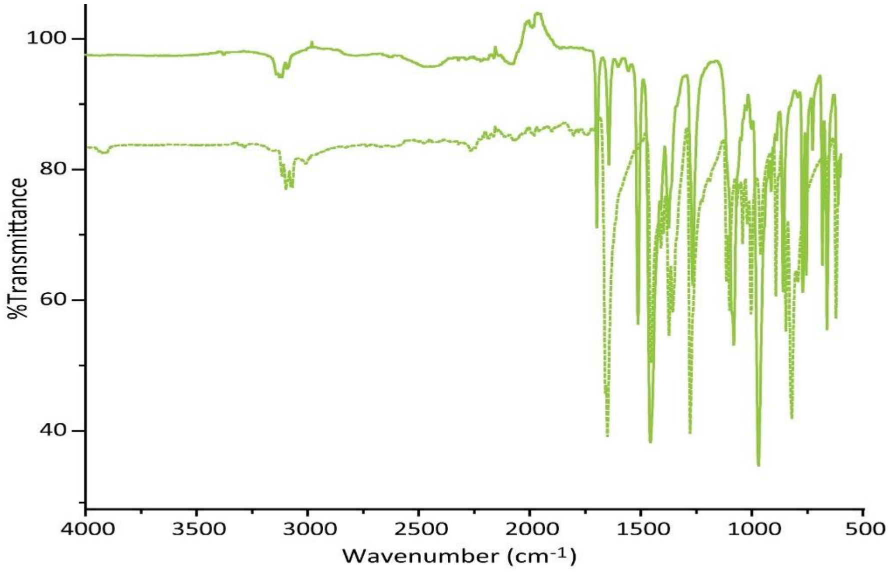

Figure 24. IR spectra comparison between ^{Ac}**Fc** (dotted line) and ^{Ac}**Fc**BArF$_{20}$ (solid line).

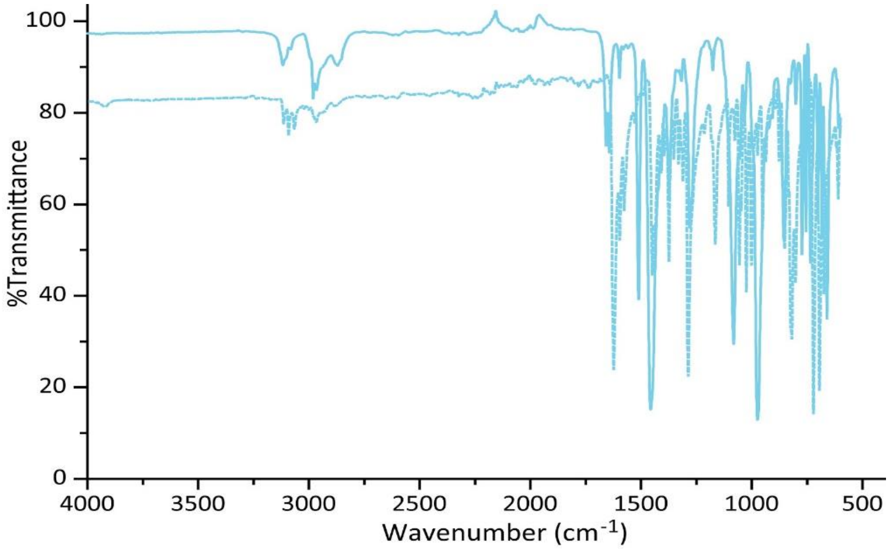

Figure 25. IR spectra comparison between ^{Bz}**Fc** (dotted line) and ^{Bz}**Fc**BArF$_{20}$ (solid line).

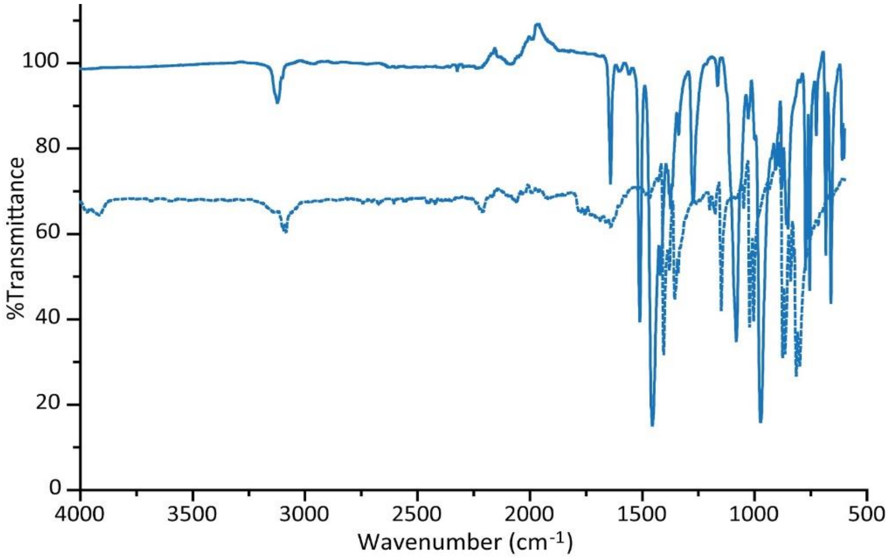

Figure 26. IR spectra comparison between ^{Br2}**Fc** (dotted line) and ^{Br2}**Fc**BArF$_{20}$ (solid line).

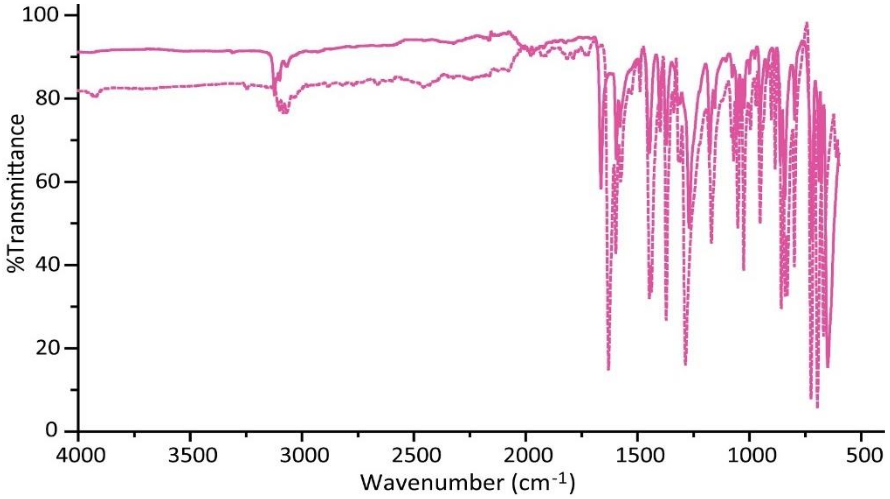

Figure 27. IR spectra comparison between ^{Ac2}**Fc** (dotted line) and ^{Ac2}**Fc**BArF$_{20}$ (solid line).

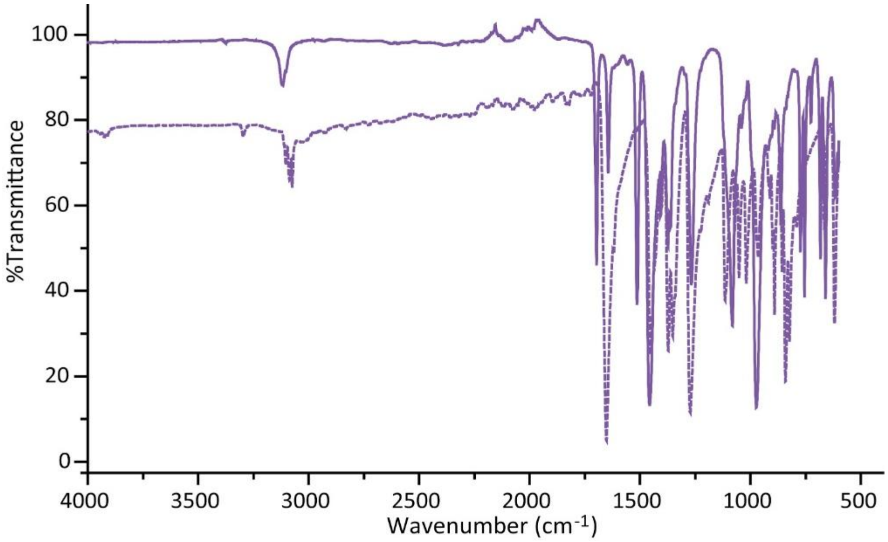

Figure 28. IR spectra comparison between ^{Bz2}**Fc** (dotted line) and ^{Bz2}**Fc**[SbF$_6$] (solid line).

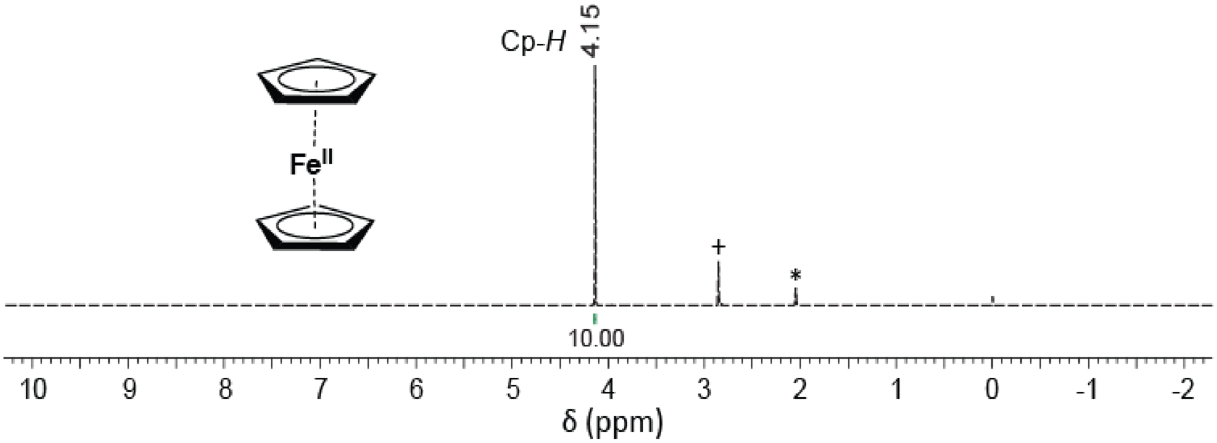

Figure 29. ^{1}H-NMR spectrum of **Fc** recorded in acetone-d_6 (500 MHz) at room temperature.

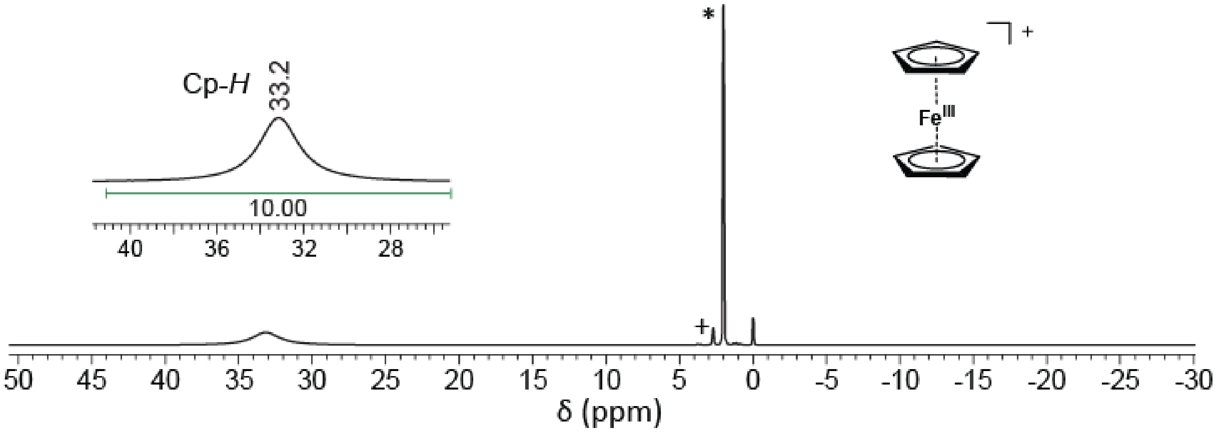

Figure 30. ^{1}H-NMR spectrum of **Fc**BArF$_{20}$ recorded in acetone-d_6 (500 MHz) at room temperature.

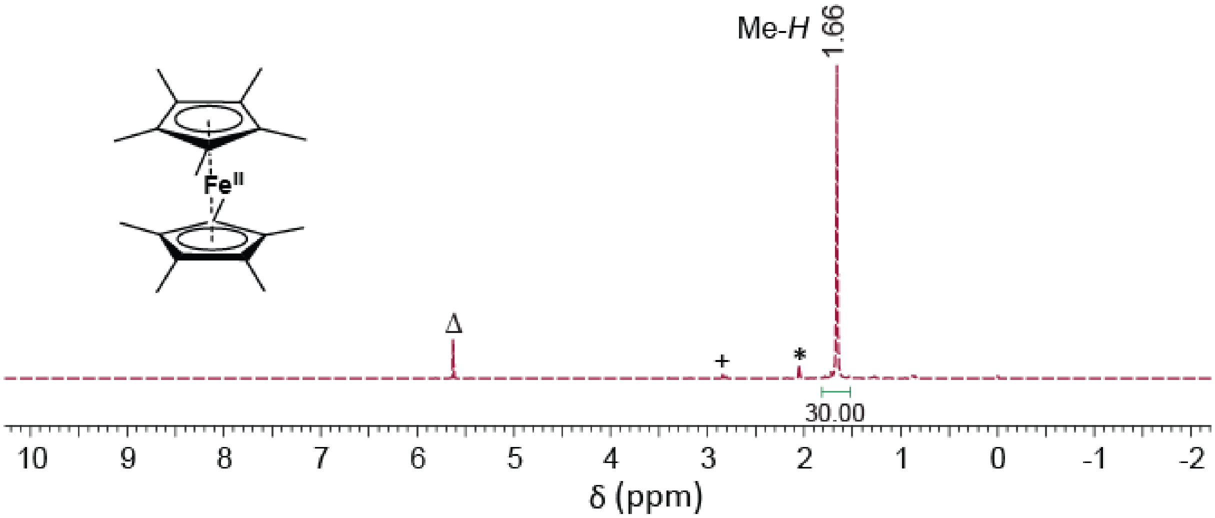

Figure 31. ^{1}H-NMR spectrum of ^{Me10}**Fc** recorded in acetone-d_6 (500 MHz) at room temperature.

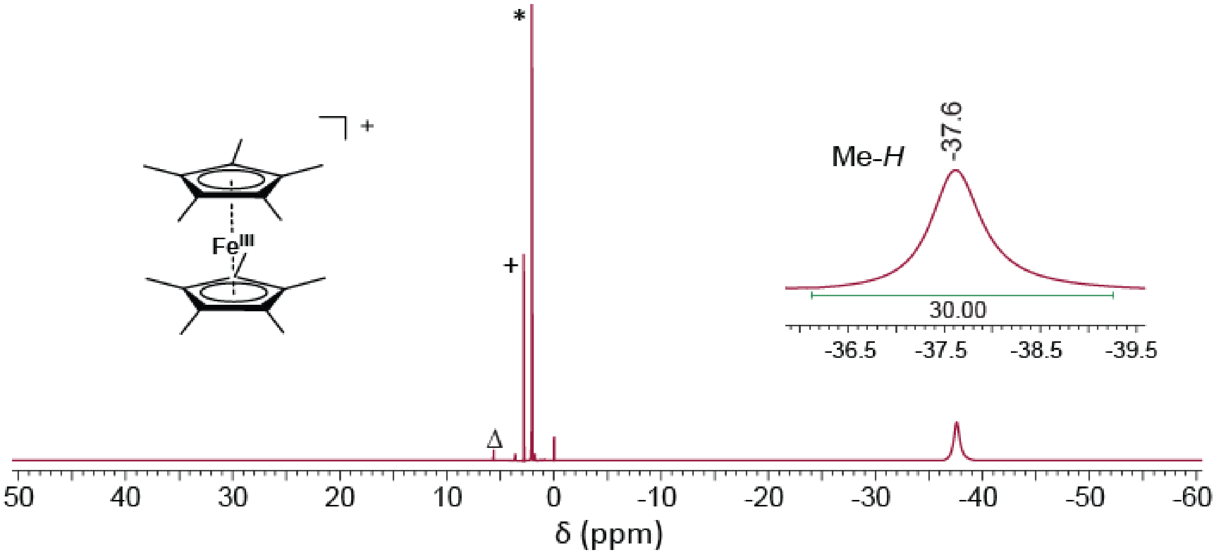

Figure 32. ^{1}H-NMR spectrum of ^{Me10}**Fc**BArF$_{20}$ recorded in acetone-d_6 (500 MHz) at room temperature.

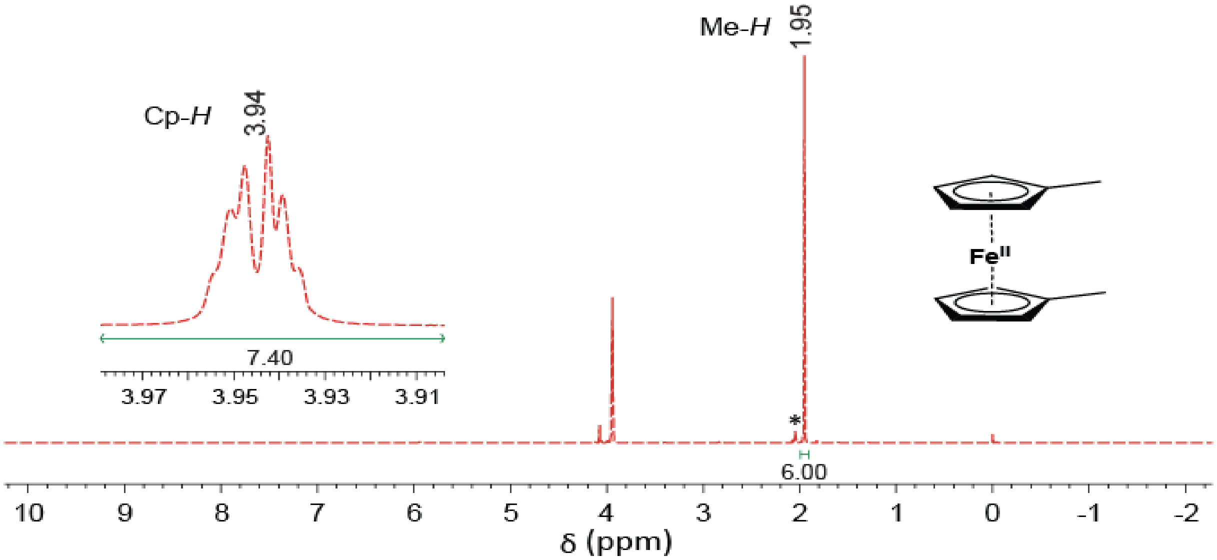

Figure 33. ^{1}H-NMR spectrum of ^{Me2}**Fc** recorded in acetone-d_6 (500 MHz) at room temperature.

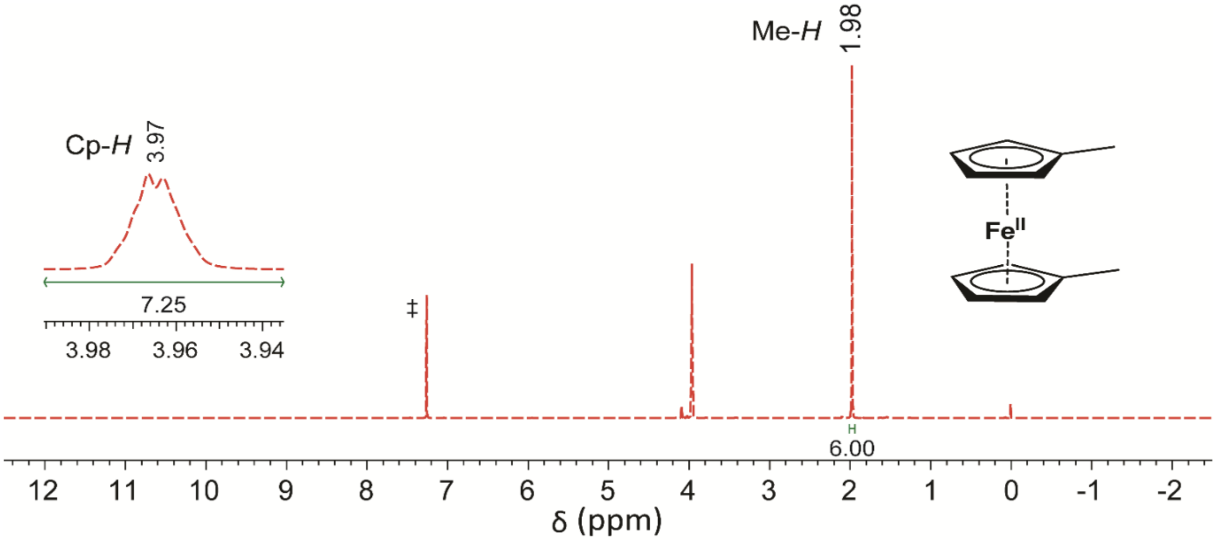

Figure 34. ^{1}H-NMR spectrum of ^{Me2}**Fc** recorded in $CDCl_3$ (500 MHz) at room temperature.

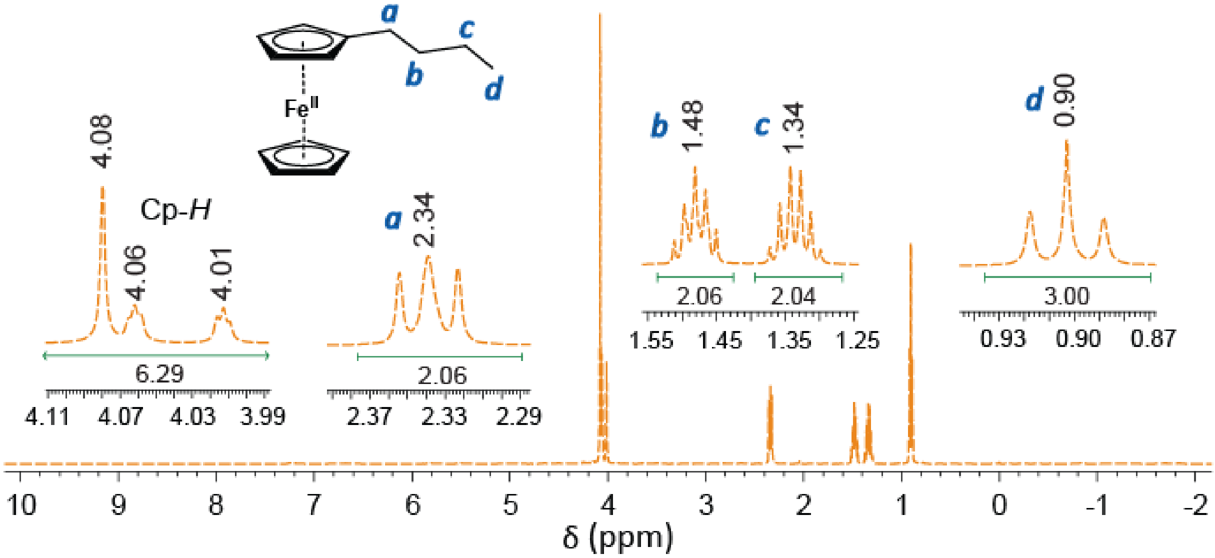

Figure 35. ^{1}H-NMR spectrum of ^{nBu}**Fc** recorded in acetone-d_6 (500 MHz) at room temperature.

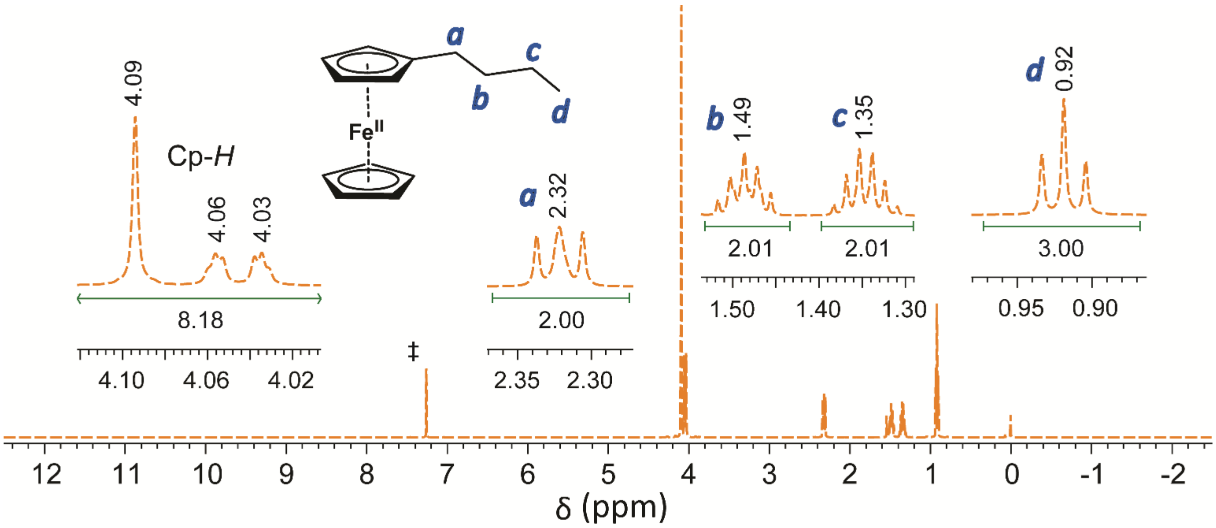

Figure 36. ^{1}H-NMR spectrum of ^{nBu}**Fc** recorded in CDCl$_3$ (500 MHz) at room temperature.

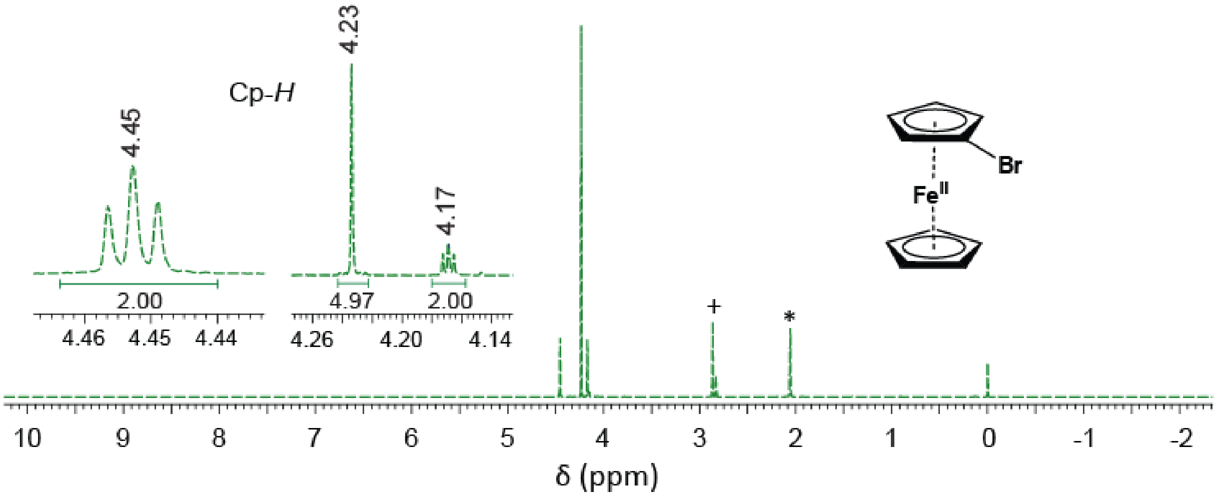

Figure 37. ^{1}H-NMR spectrum of ^{Br}**Fc** recorded in acetone-d_6 (500 MHz) at room temperature.

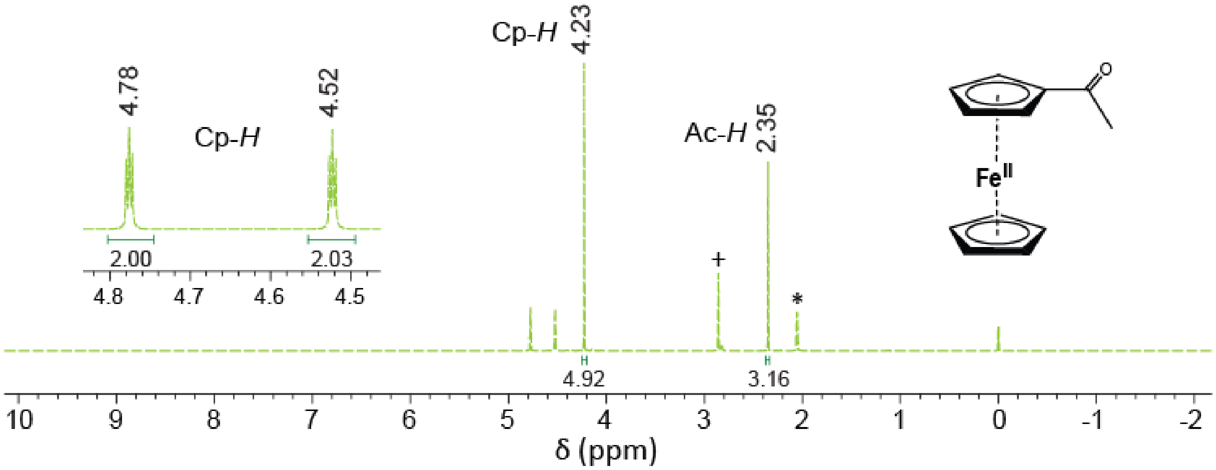

Figure 38. ^{1}H-NMR spectrum of ^{Ac}**Fc** recorded in acetone-d_6 (500 MHz) at room temperature.

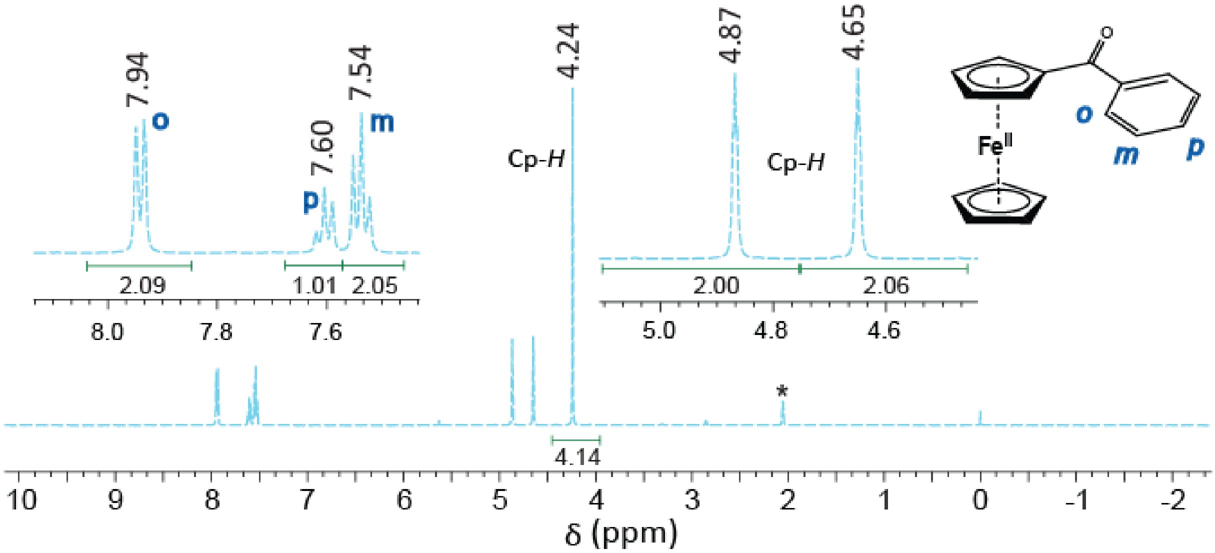

Figure 39. ^{1}H-NMR spectrum of ^{Bz}**Fc** recorded in acetone-d_6 (500 MHz) at room temperature.

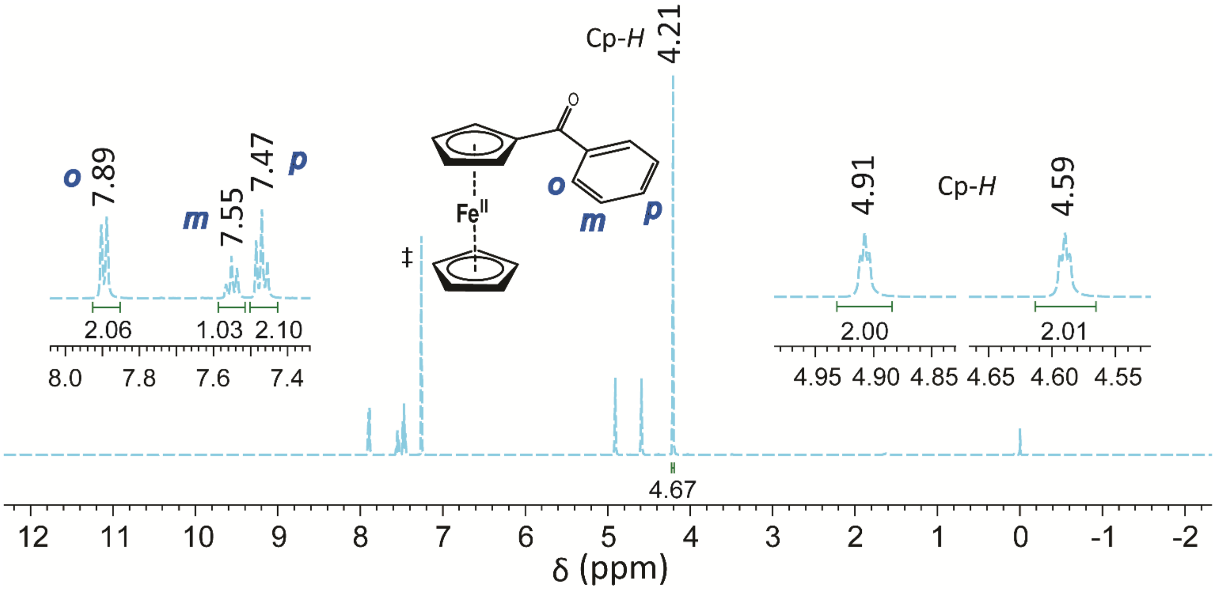

Figure 40. ^{1}H-NMR spectrum of ^{Bz}**Fc** recorded in CDCl$_3$ (500 MHz) at room temperature.

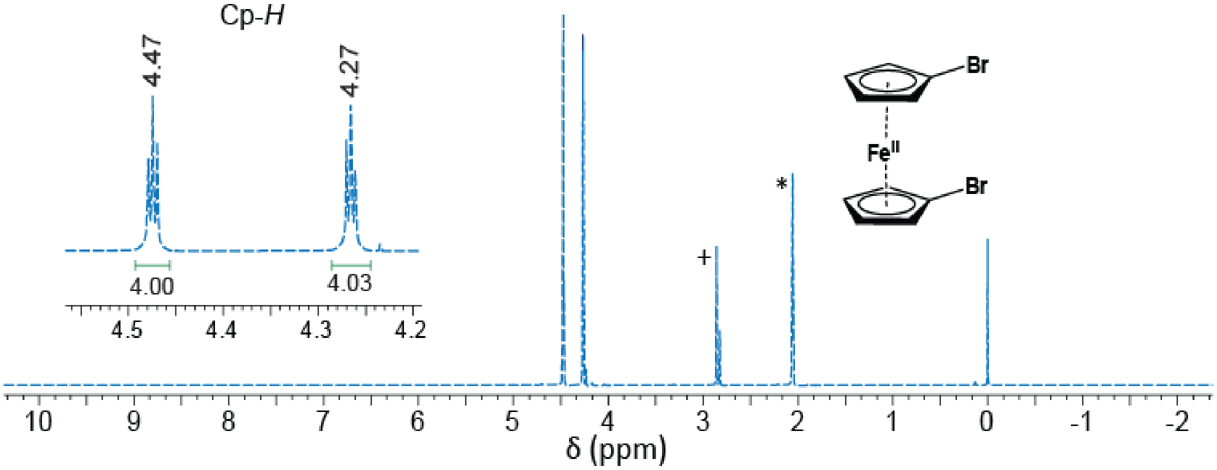

Figure 41. ^{1}H-NMR spectrum of ^{Br2}**Fc** recorded in acetone-d_6 (400 MHz) at room temperature.

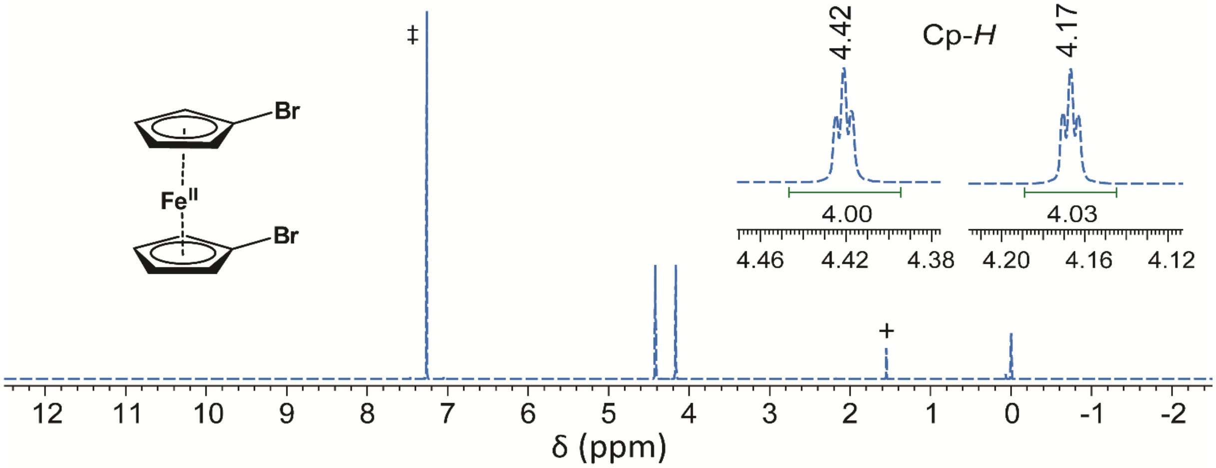

Figure 42.^{1}H-NMR spectrum of ^{Br2}**Fc** recorded in $CDCl_3$ (500 MHz) at room temperature.

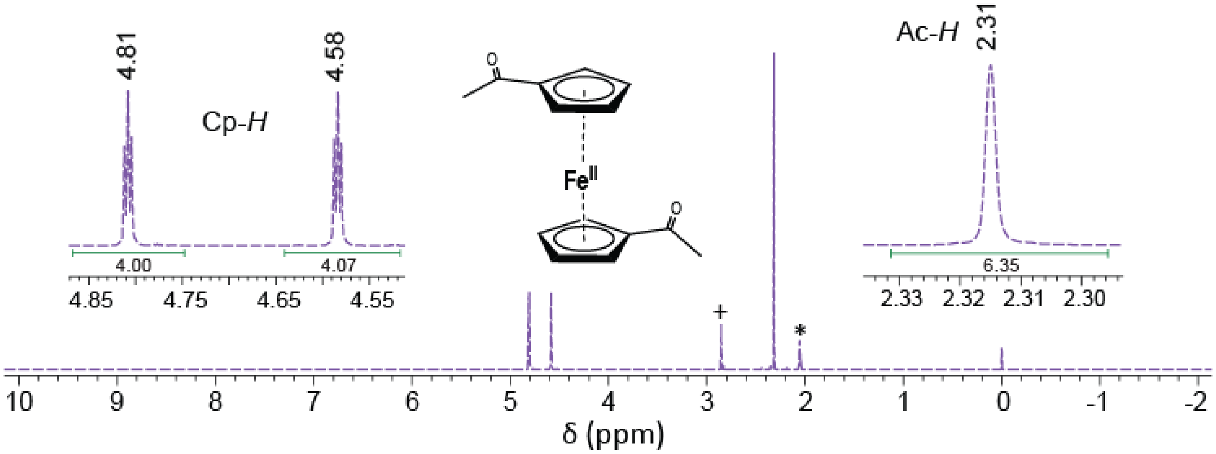

Figure 43. ^{1}H-NMR spectrum of ^{Ac2}**Fc** recorded in acetone-d_6 (500 MHz) at room temperature.

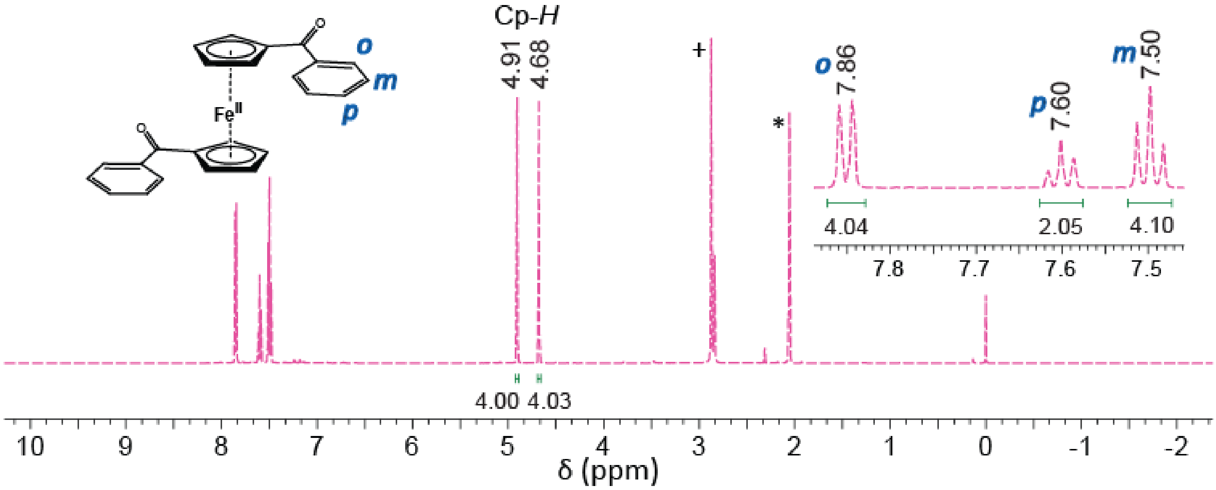

Figure 44. ^{1}H-NMR spectrum of ^{Bz2}**Fc** recorded in acetone-d_6 (500 MHz) at room temperature.

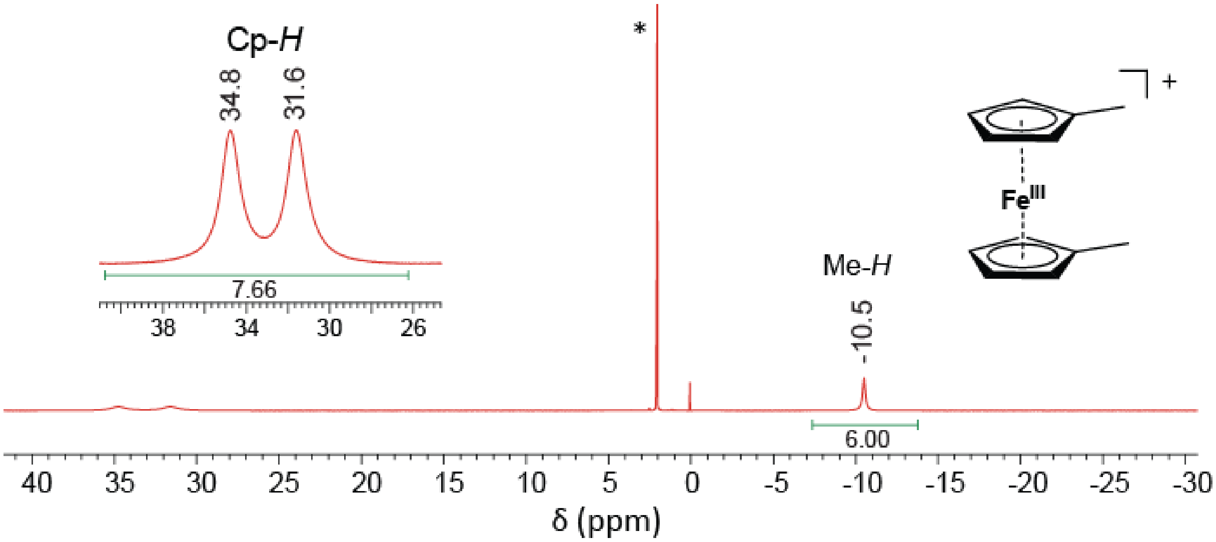

Figure 45. ^{1}H-NMR spectrum of ^{Me2}**Fc**BArF$_{20}$ recorded in acetone-d_6 (500 MHz) at room temperature.

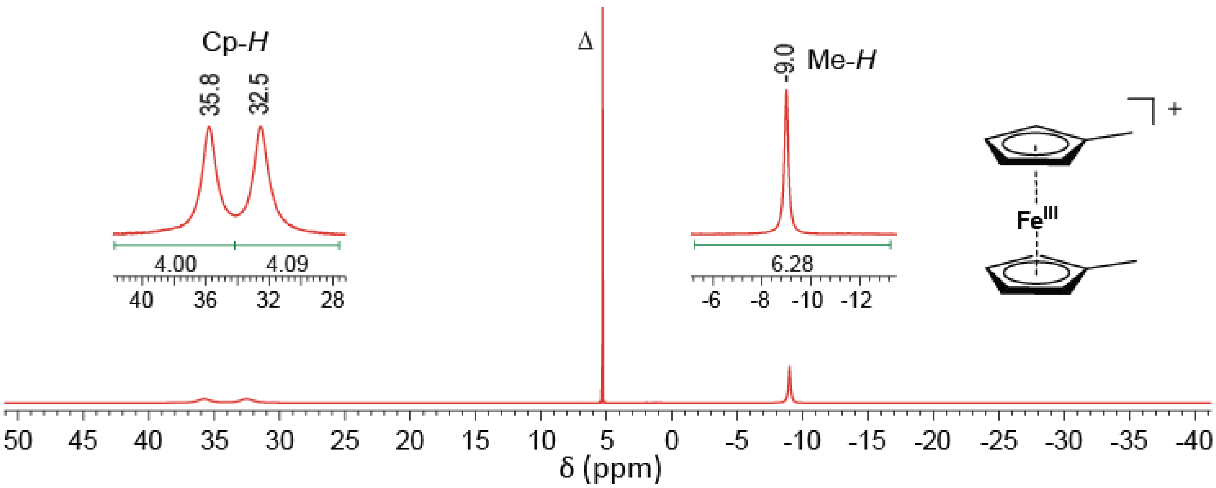

Figure 46. ^{1}H-NMR spectrum of ^{Me2}**Fc**BArF$_{20}$ recorded in CD_2Cl_2 (500 MHz) at room temperature.

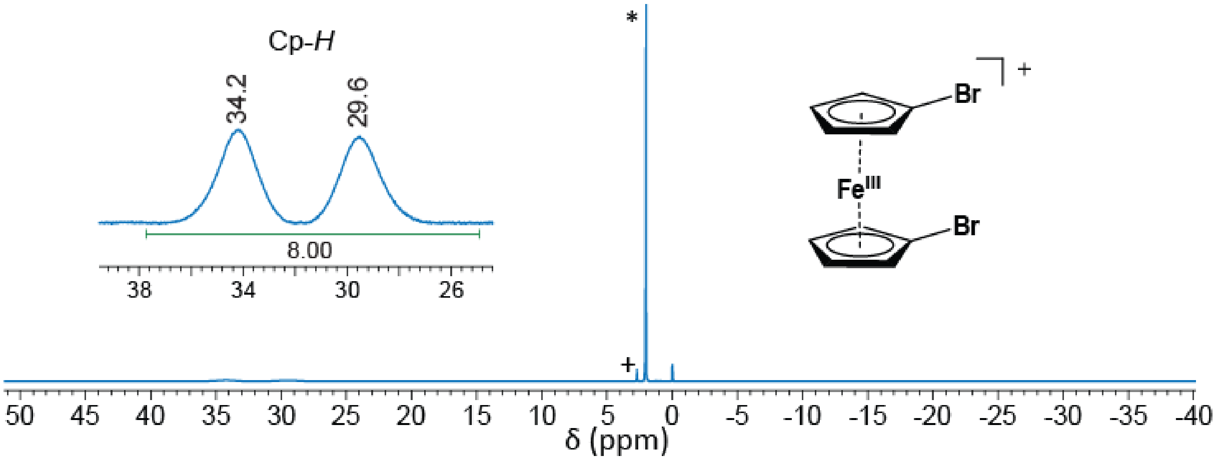

Figure 47. ^{1}H-NMR spectrum of ^{Br2}**Fc**BArF$_{20}$ recorded in acetone-d_6 (400 MHz) at room temperature.

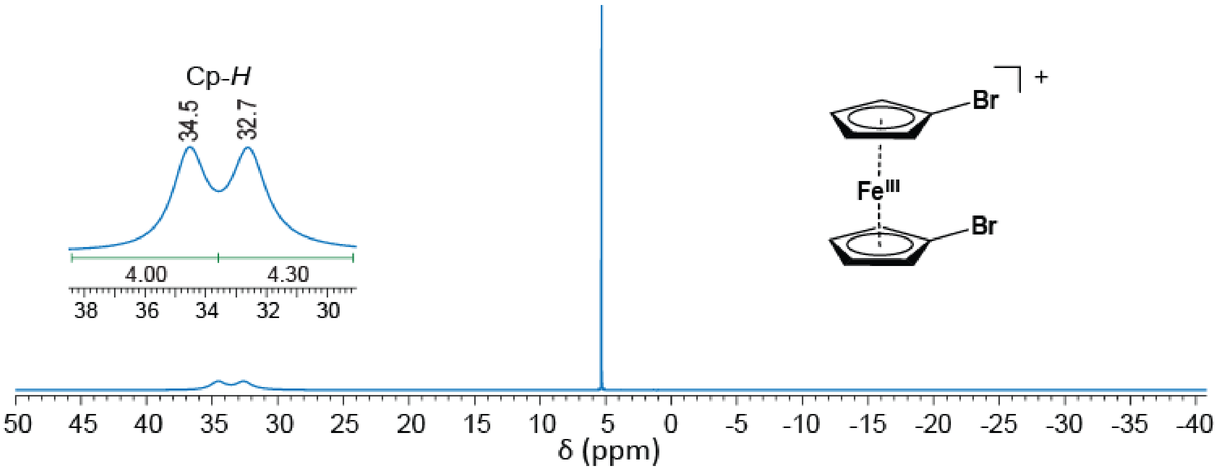

Figure 48. ^{1}H-NMR spectrum of ^{Br2}**Fc**BArF$_{20}$ recorded in CD$_2$Cl$_2$ (500 MHz) at room temperature.

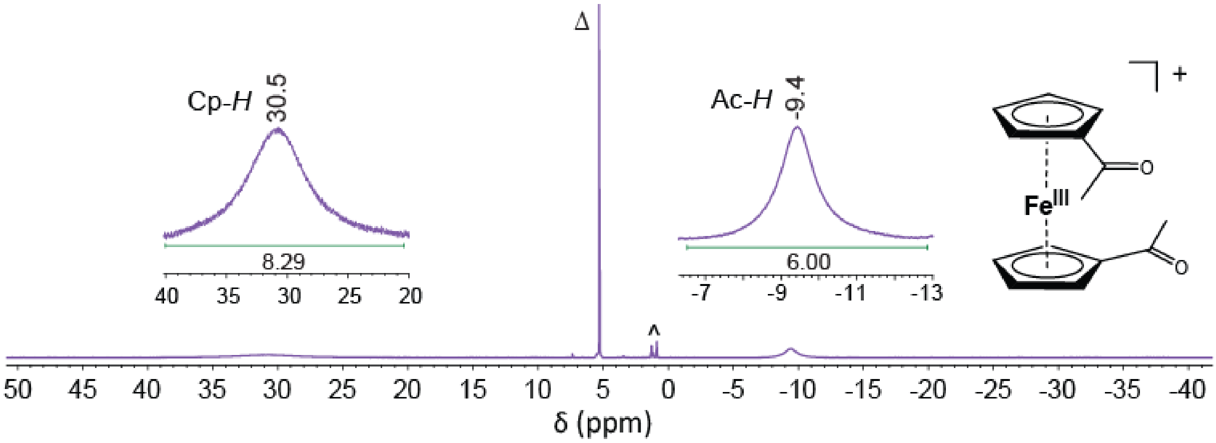

Figure 49. ^{1}H-NMR spectrum of ^{Ac2}**Fc**BArF$_{20}$ recorded in CD$_2$Cl$_2$ (500 MHz) at room temperature.

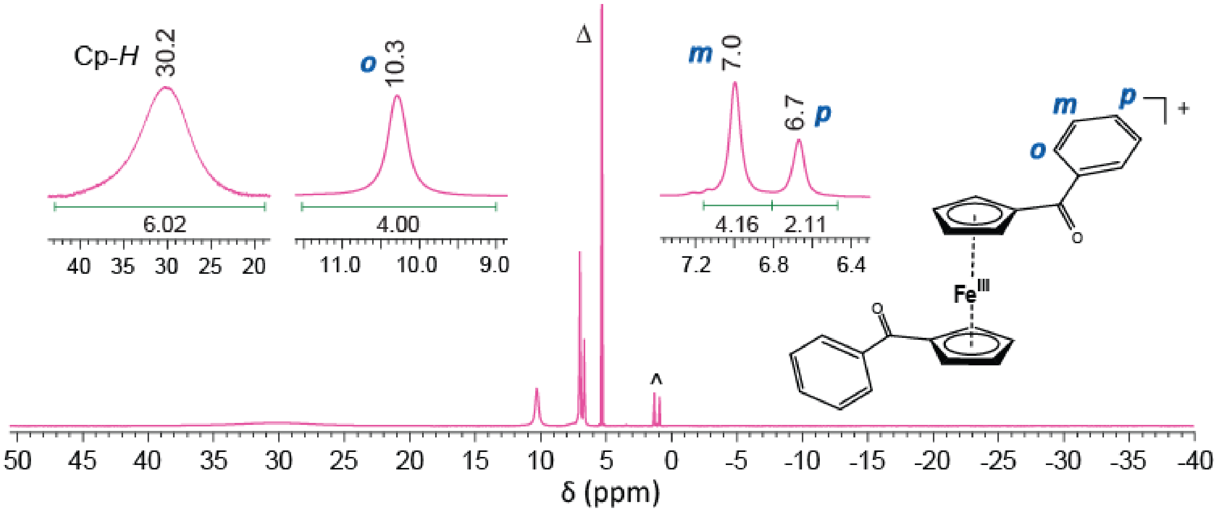

Figure 50. ^{1}H-NMR spectrum of ^{Bz2}**Fc**[SbF$_6$] recorded in CD_2Cl_2 (500 MHz) at room temperature.

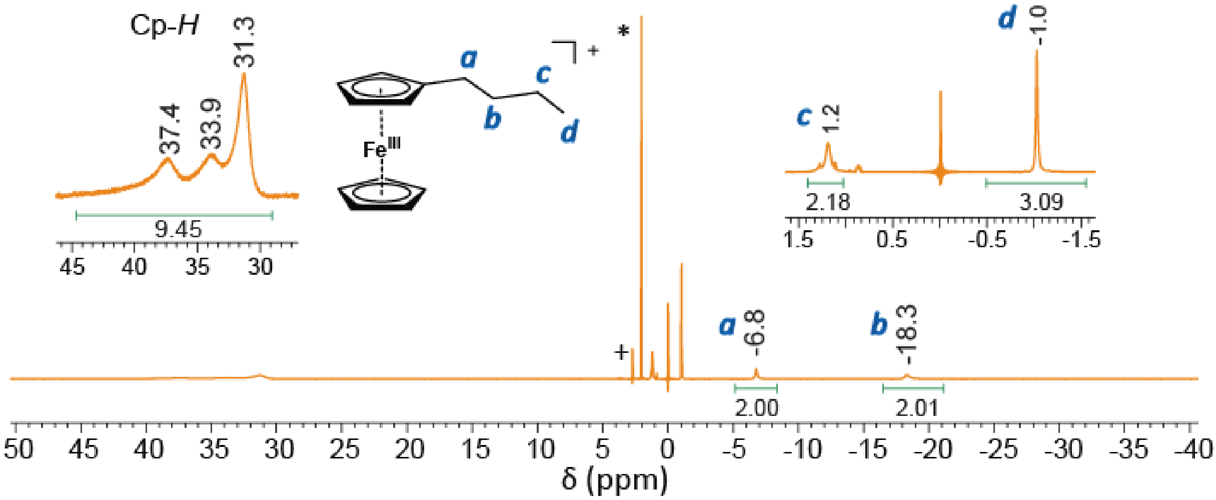

Figure 51. ^{1}H-NMR spectrum of ^{nBu}**Fc**BArF$_{20}$ recorded in acetone-d_6 (500 MHz) at room temperature.

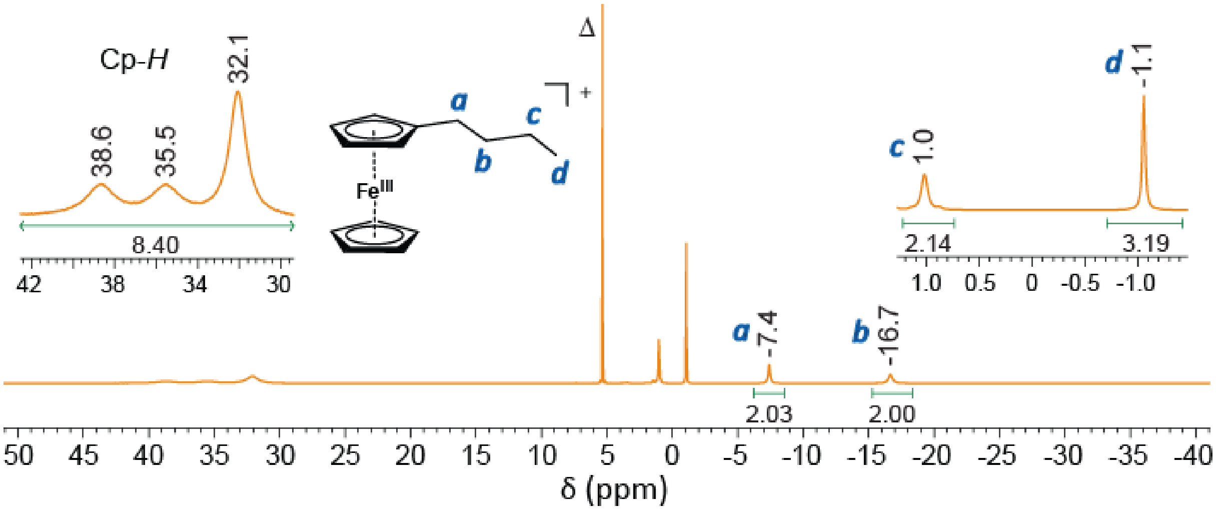

Figure 52. ^{1}H-NMR spectrum of ^{nBu}**Fc**BArF$_{20}$ recorded in CD$_2$Cl$_2$ (500 MHz) at room temperature.

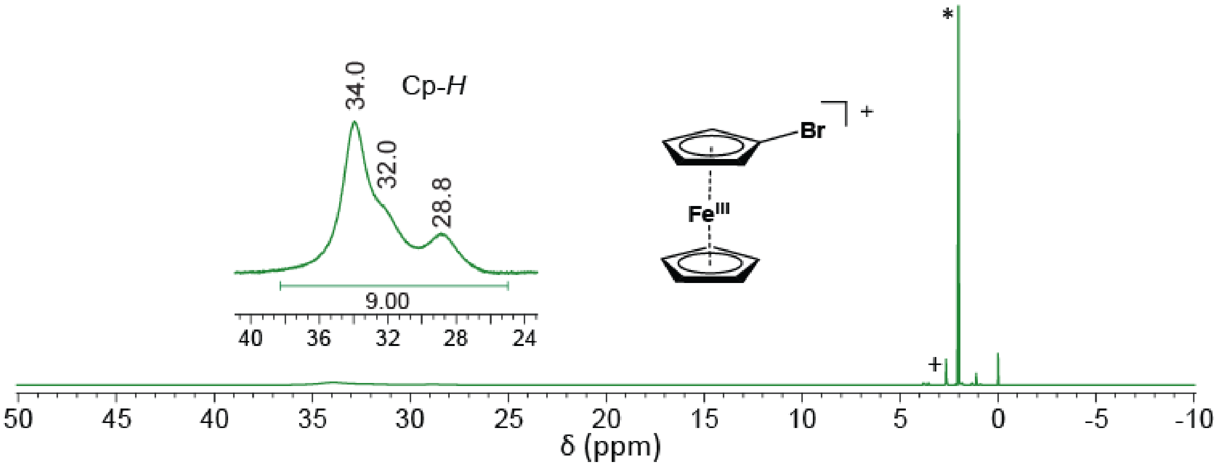

Figure 53. ^{1}H-NMR spectrum of ^{Br}**Fc**BArF$_{20}$ recorded in acetone-d_6 (500 MHz) at room temperature.

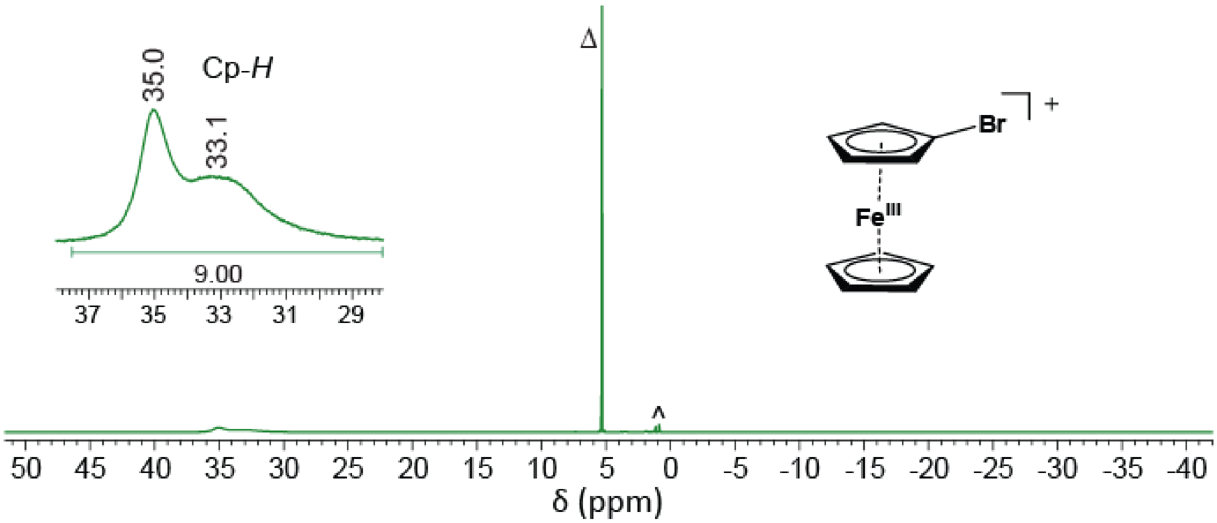

Figure 54. ^{1}H-NMR spectrum of ^{Br}**Fc**BArF$_{20}$ recorded in CD_2Cl_2 (500 MHz) at room temperature.

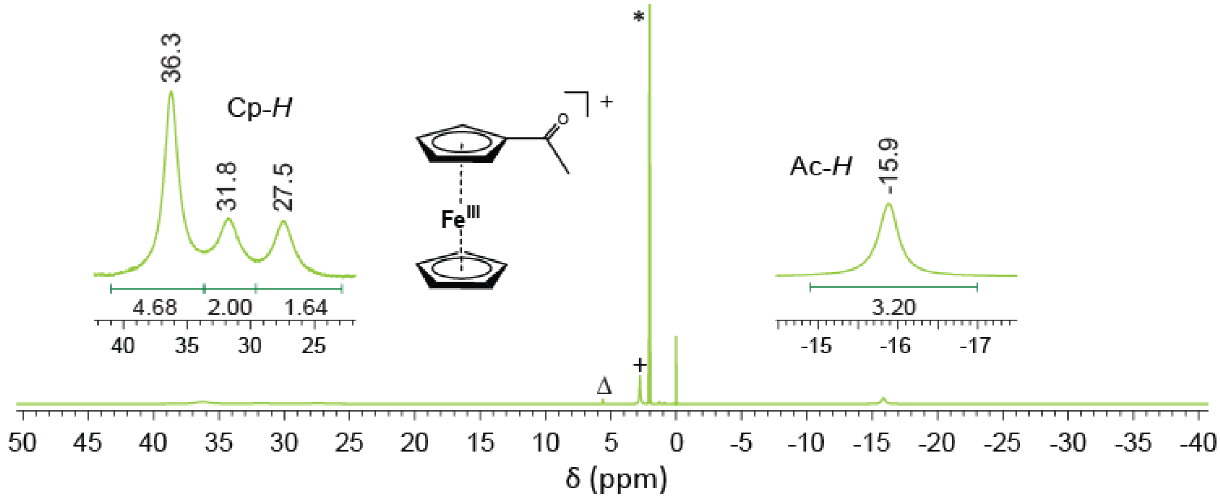

Figure 55. ^{1}H-NMR spectrum of ^{Ac}**Fc**BArF$_{20}$ recorded in acetone-d_6 (500 MHz) at room temperature.

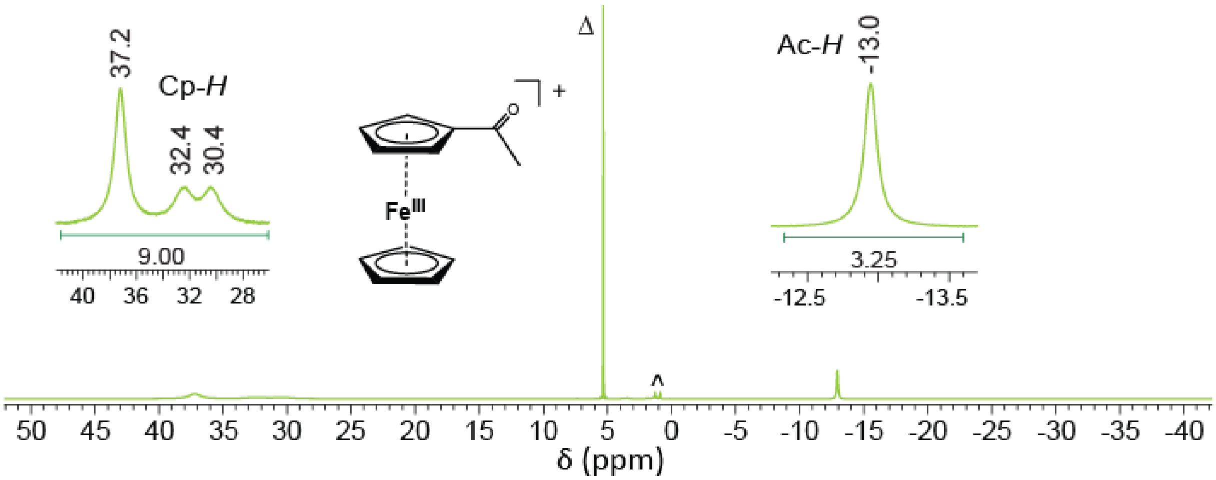

Figure 56. ^{1}H-NMR spectrum of ^{Ac}**Fc**BArF$_{20}$ recorded in CD$_2$Cl$_2$ (500 MHz) at room temperature.

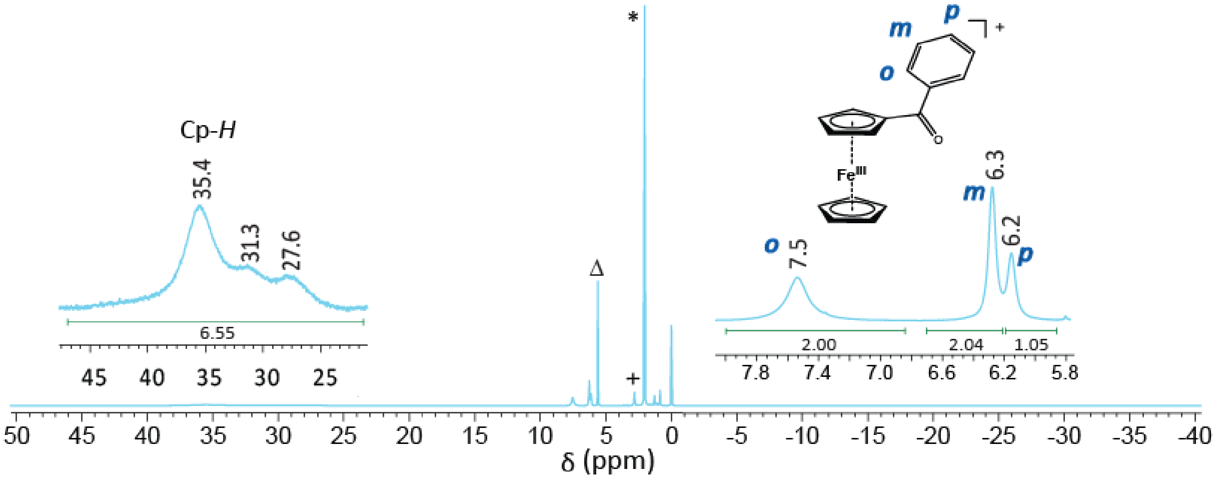

Figure 57. ^{1}H-NMR spectrum of ^{Bz}**Fc**BArF$_{20}$ recorded in acetone-d_6 (500 MHz) at room temperature.

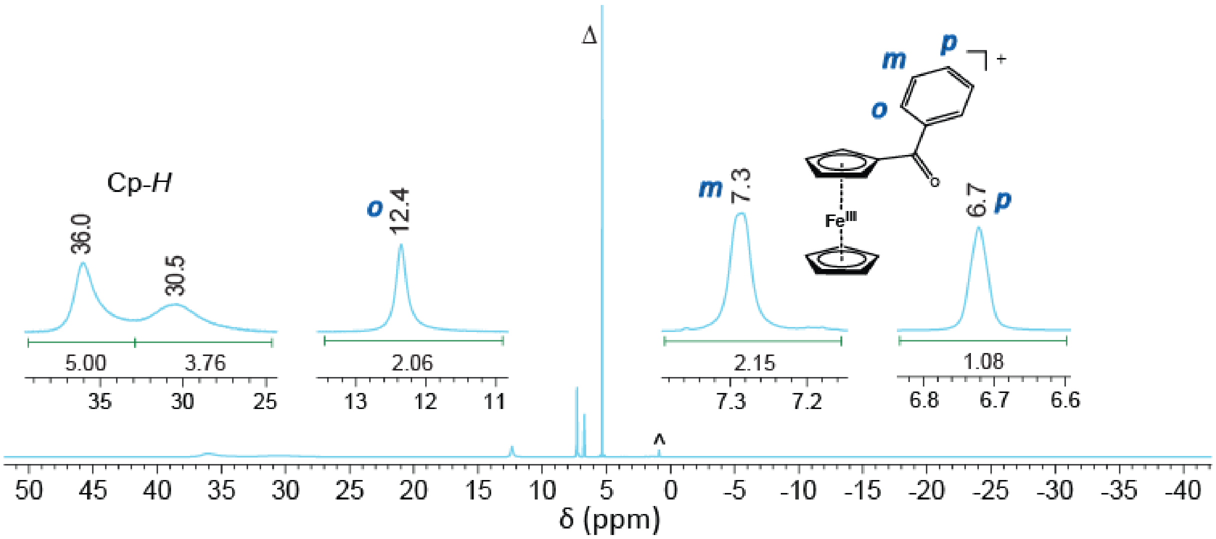

Figure 58. ^{1}H-NMR spectrum of ^{Bz}**Fc**BArF$_{20}$ recorded in CD_2Cl_2 (500 MHz) at room temperature.

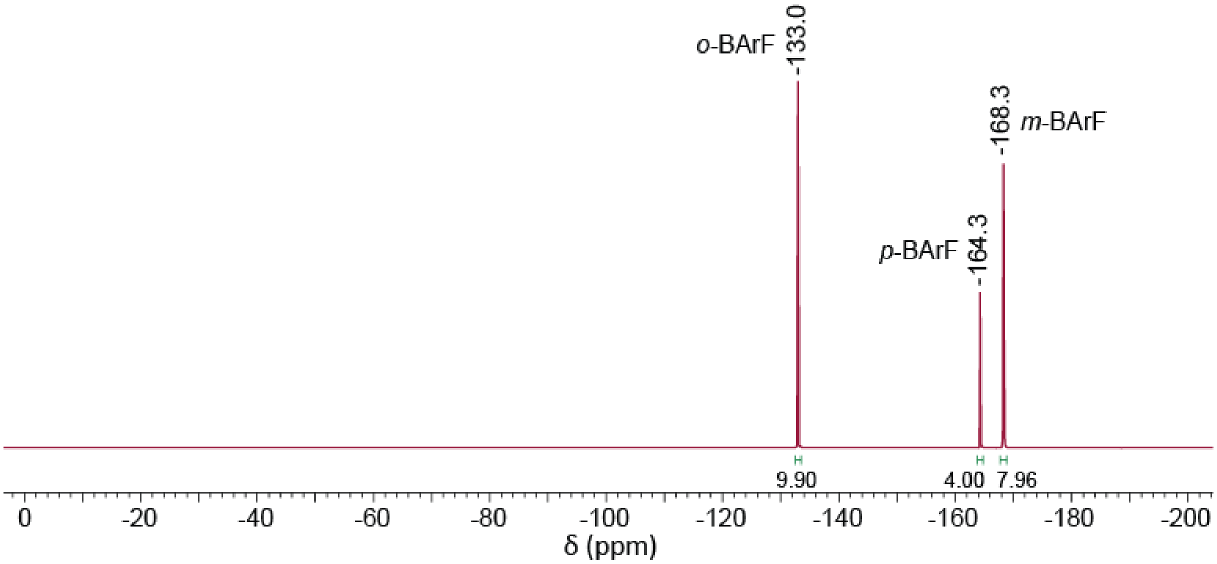

Figure 59. ^{19}F-NMR spectrum of ^{Me10}**Fc**BArF$_{20}$ recorded in acetone-d_6 (470 MHz) at room temperature.

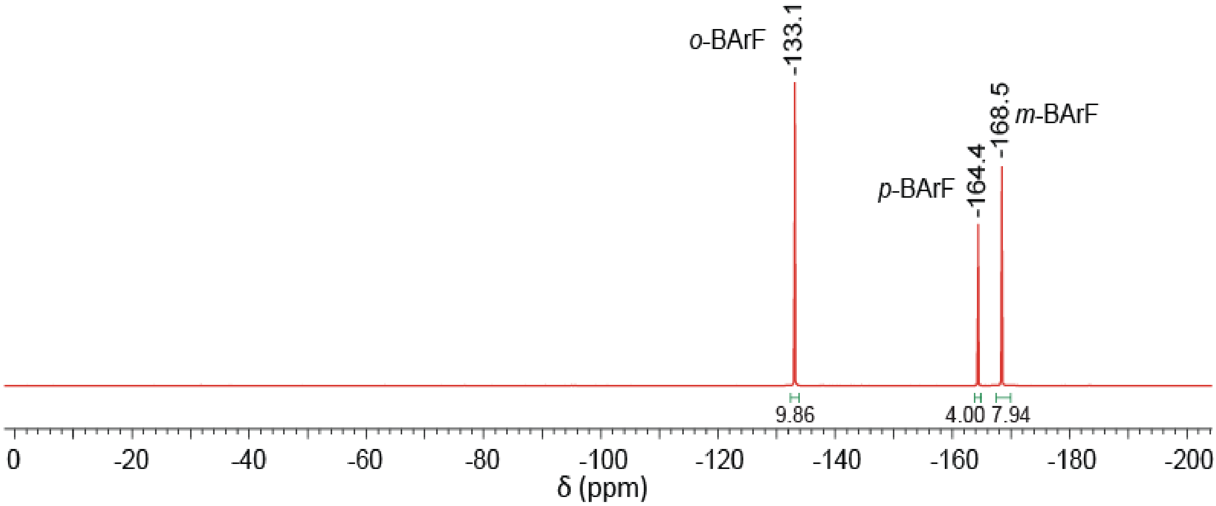

Figure 60. ^{19}F-NMR spectrum of ^{Me2}**Fc**BArF$_{20}$ recorded in acetone-*d*$_6$ (470 MHz) at room temperature.

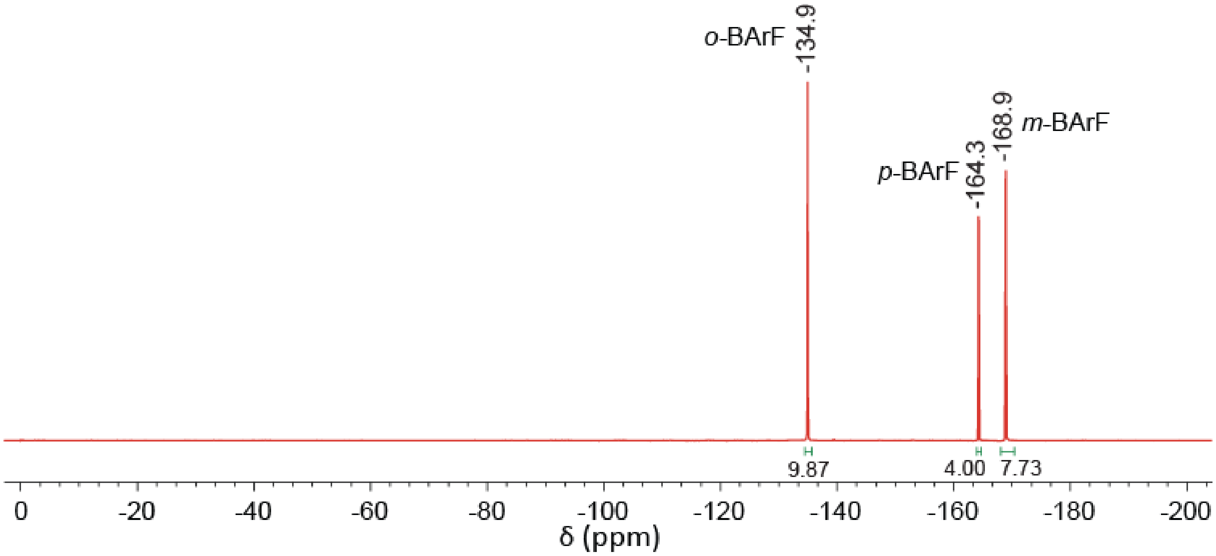

Figure 61. ^{19}F-NMR spectrum of ^{Me2}**Fc**BArF$_{20}$ recorded in CD_2Cl_2 (470 MHz) at room temperature.

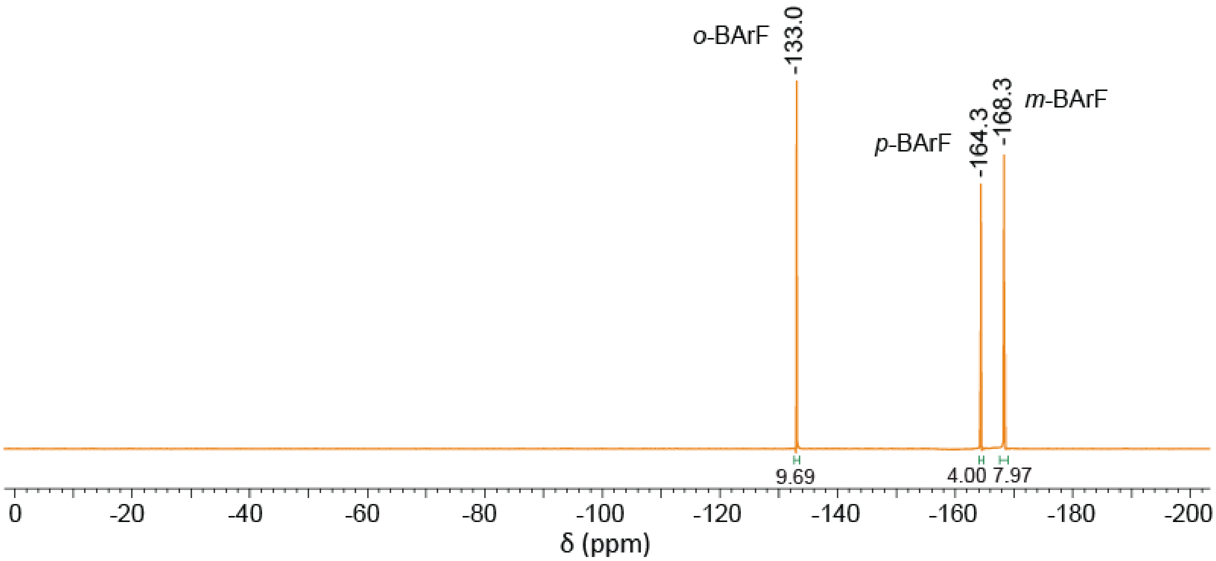

Figure 62. ^{19}F-NMR spectrum of ^{nBu}**Fc**BArF$_{20}$ recorded in acetone-d_6 (470 MHz) at room temperature.

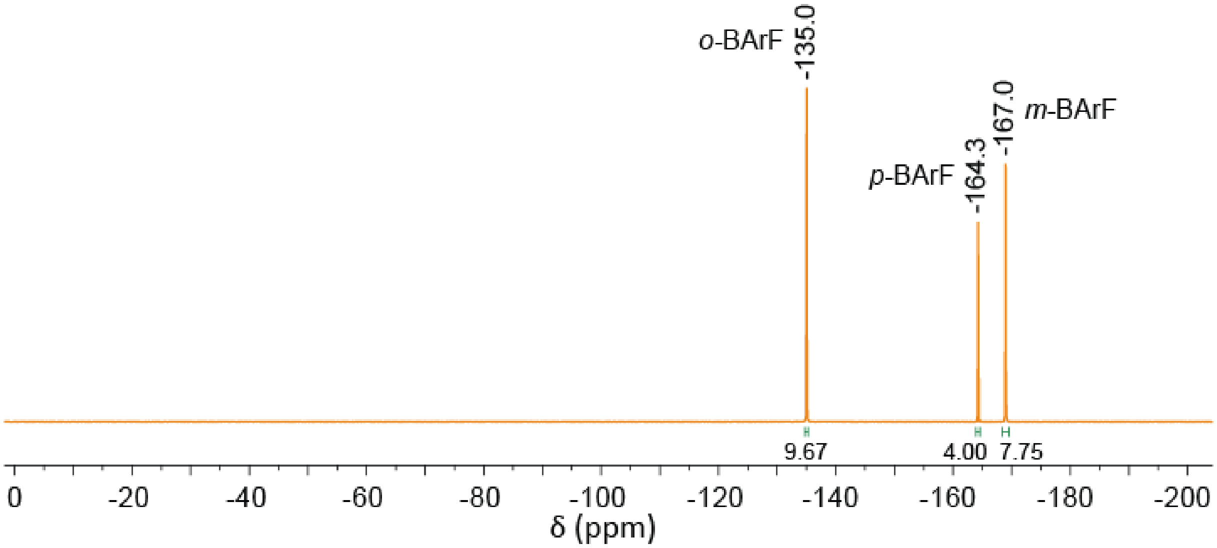

Figure 63. ^{19}F-NMR spectrum of ^{nBu}**Fc**BArF$_{20}$ recorded in CD_2Cl_2 (470 MHz) at room temperature.

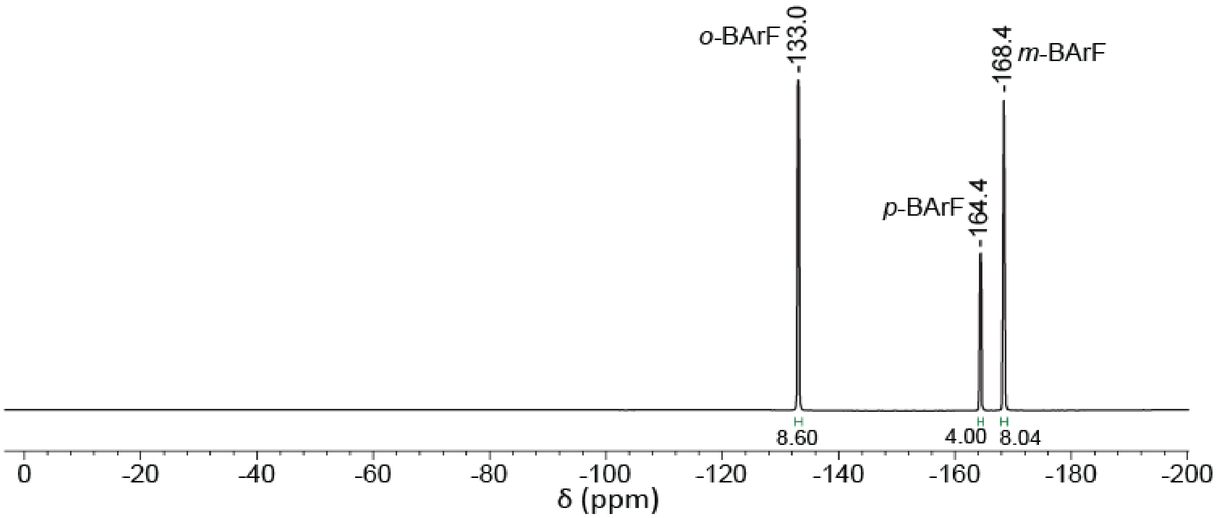

Figure 64. ^{19}F-NMR spectrum of **Fc**BArF$_{20}$ recorded in acetone-d_6 (470 MHz) at room temperature.

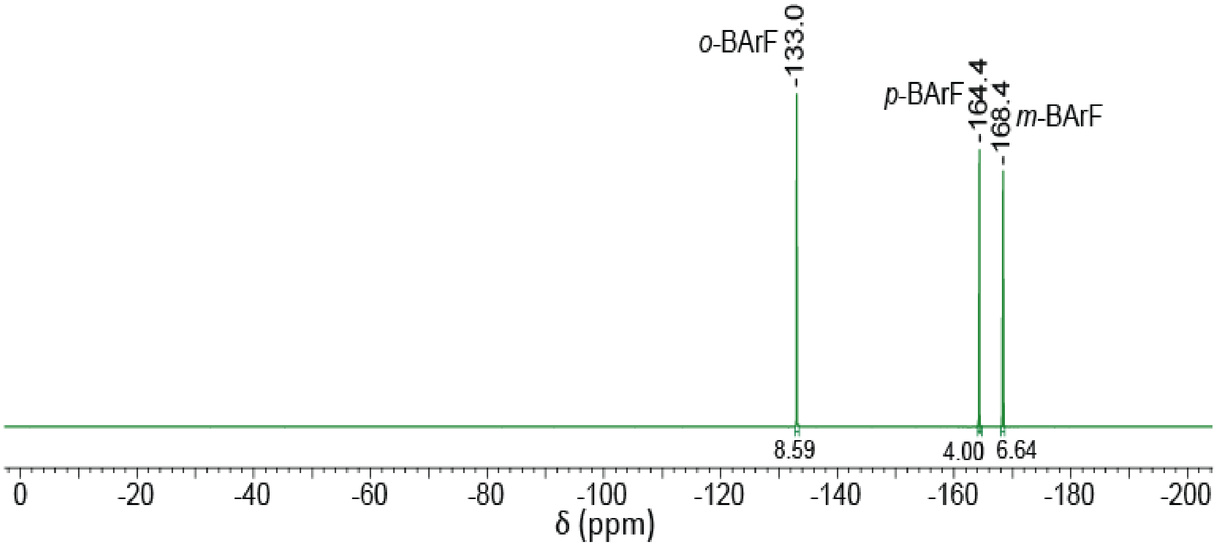

Figure 65. ^{19}F-NMR spectrum of ^{Br}**Fc**BArF$_{20}$ recorded in acetone-d_6 (470 MHz) at room temperature.

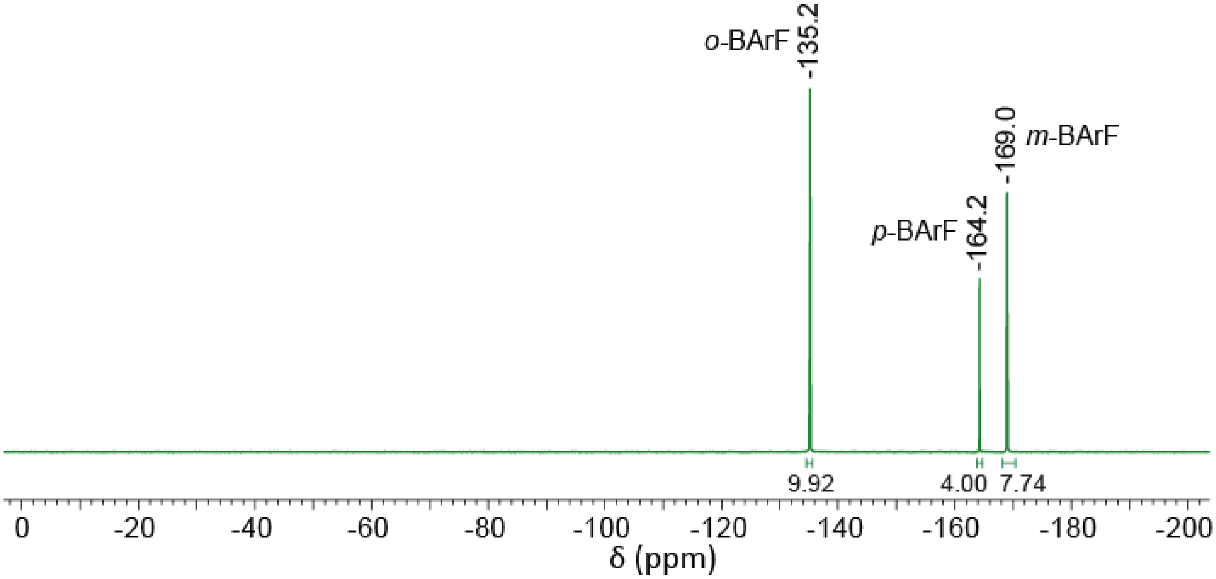

Figure 66. ^{19}F-NMR spectrum of ^{Br}**Fc**BArF$_{20}$ recorded in CD_2Cl_2 (470 MHz) at room temperature.

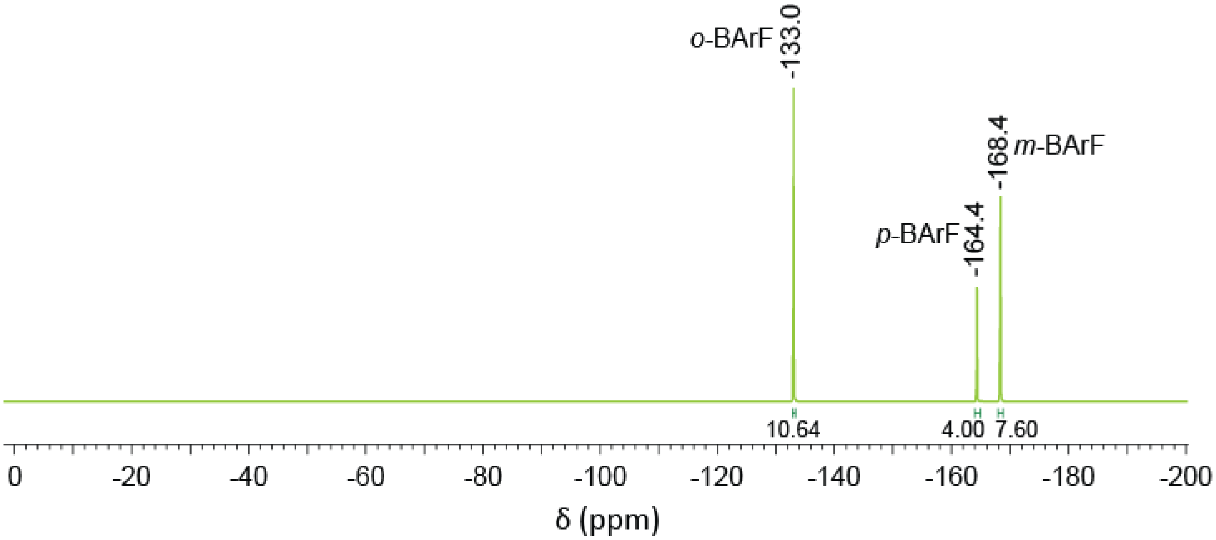

Figure 67. ^{19}F-NMR spectrum of ^{Ac}**Fc**BArF$_{20}$ recorded in acetone-d_6 (470 MHz) at room temperature.

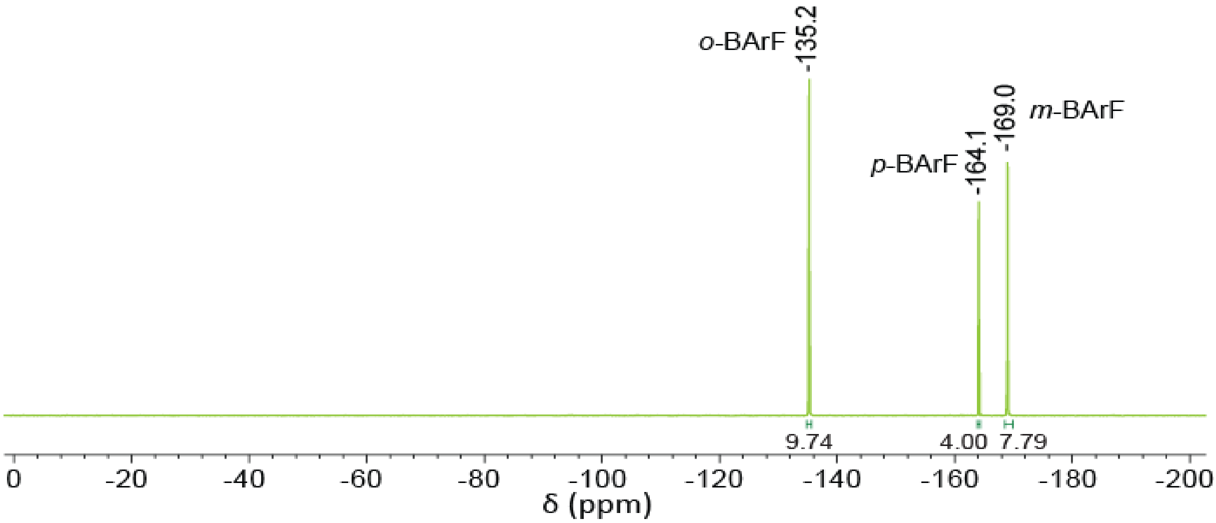

Figure 68. ^{19}F-NMR spectrum of ^{Ac}**Fc**BArF$_{20}$ recorded in CD_2Cl_2 (470 MHz) at room temperature.

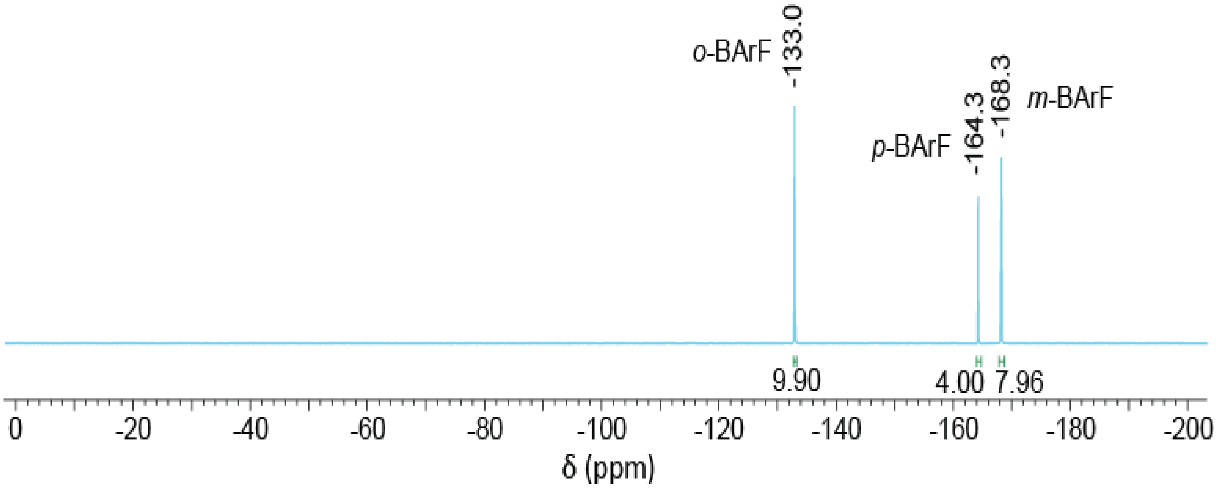

Figure 69. ^{19}F-NMR spectrum of ^{Bz}**Fc**BArF$_{20}$ recorded in acetone-d_6 (470 MHz) at room temperature.

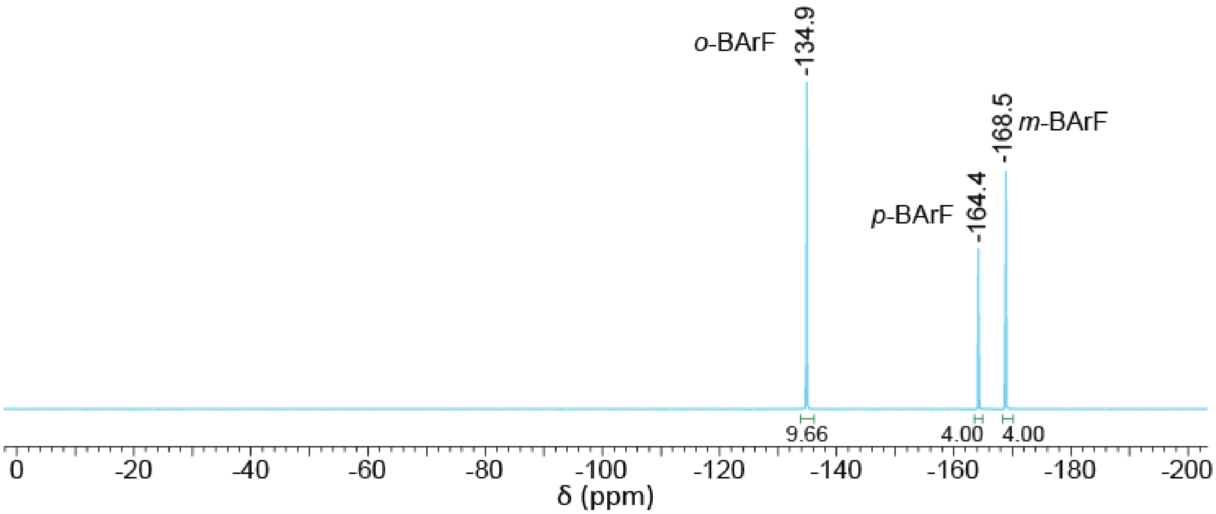

Figure 70. ^{19}F-NMR spectrum of ^{Bz}**Fc**BArF$_{20}$ recorded in CD_2Cl_2 (470 MHz) at room temperature.

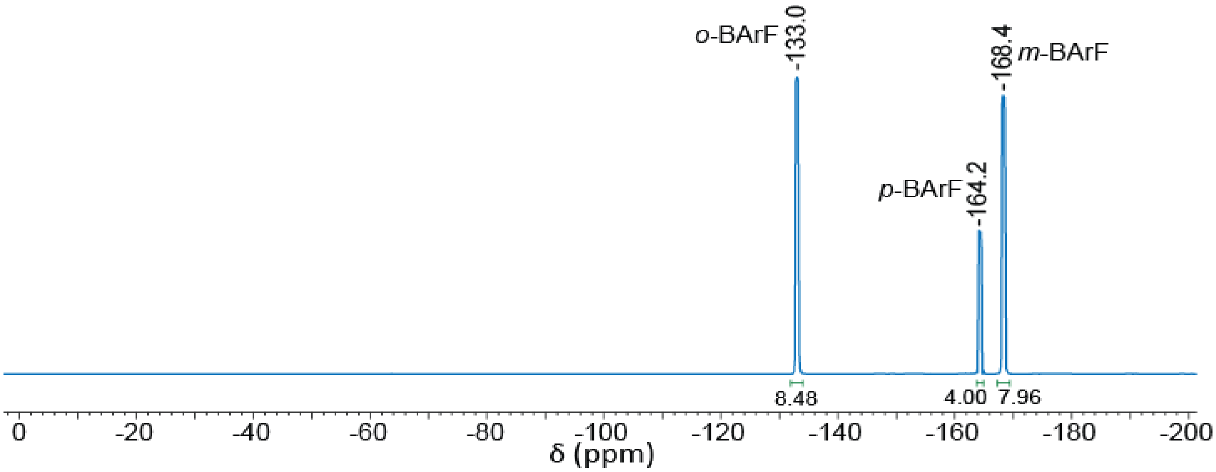

Figure 71. ^{19}F-NMR spectrum of ^{Br2}**Fc**BArF$_{20}$ recorded in acetone-d_6 (376 MHz) at room temperature.

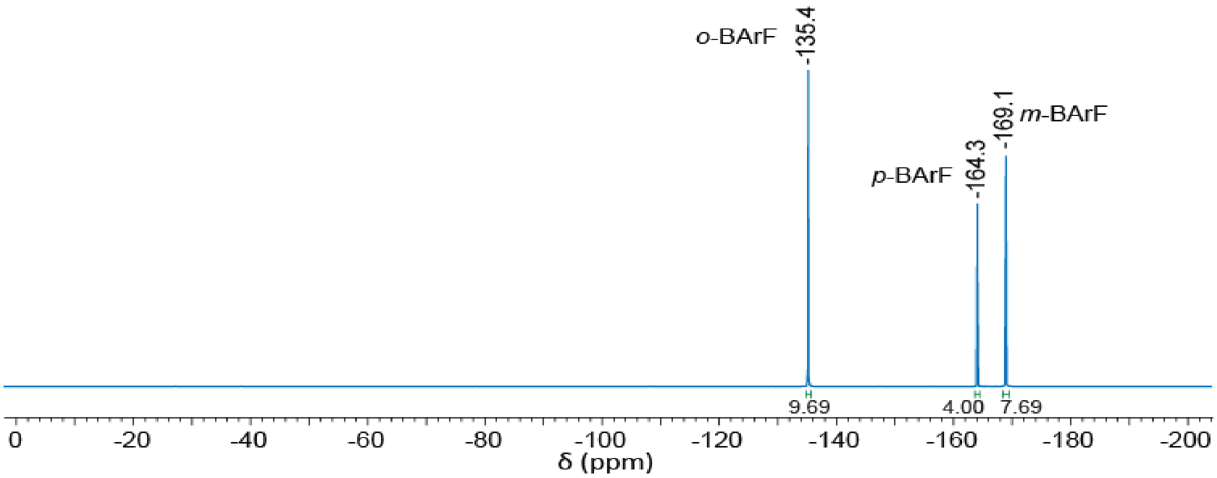

Figure 72. ^{19}F-NMR spectrum of ^{Br2}**Fc**BArF$_{20}$ recorded in CD_2Cl_2 (470 MHz) at room temperature.

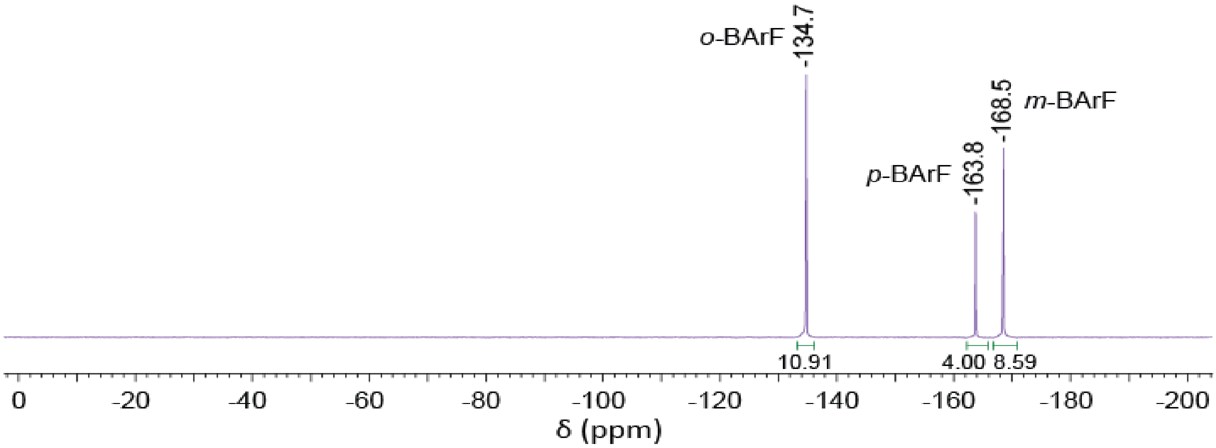

Figure 73. ^{19}F-NMR spectrum of ^{Ac2}**Fc**BArF$_{20}$ recorded in CD_2Cl_2 (470 MHz) at room temperature.

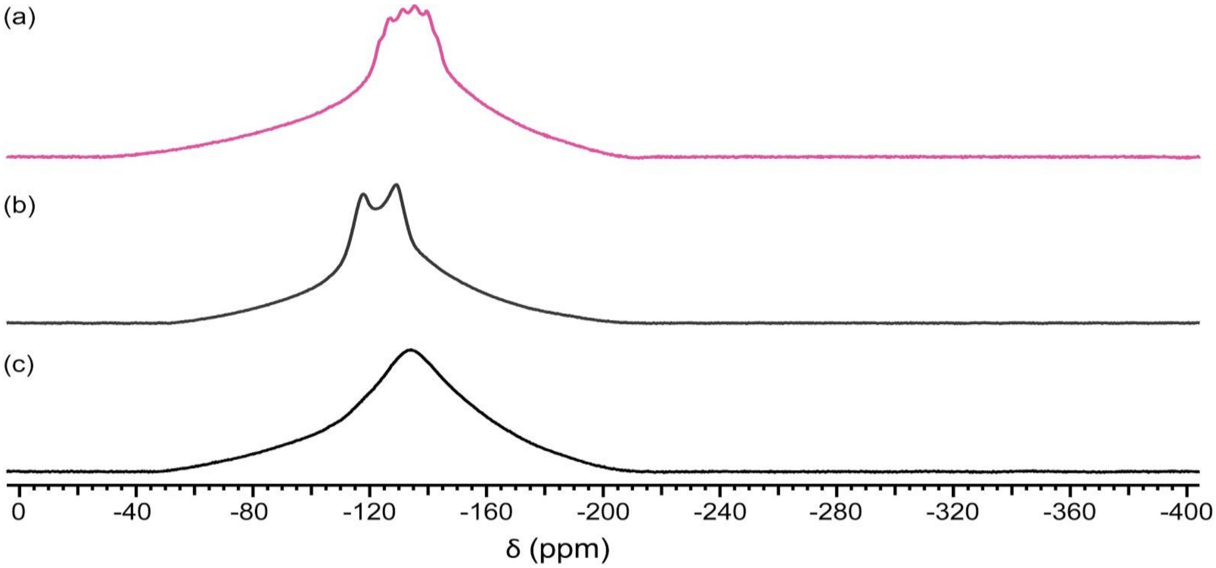

Figure 74. ^{19}F-NMR spectra of (a) ^{Bz2}**Fc**[SbF_6], (b) $AgSbF_6$, and (c) ^{Bz2}**Fc**[SbF_6] in the presence of $AgSbF_6$ recorded in CD_2Cl_2 (470 MHz) at room temperature.

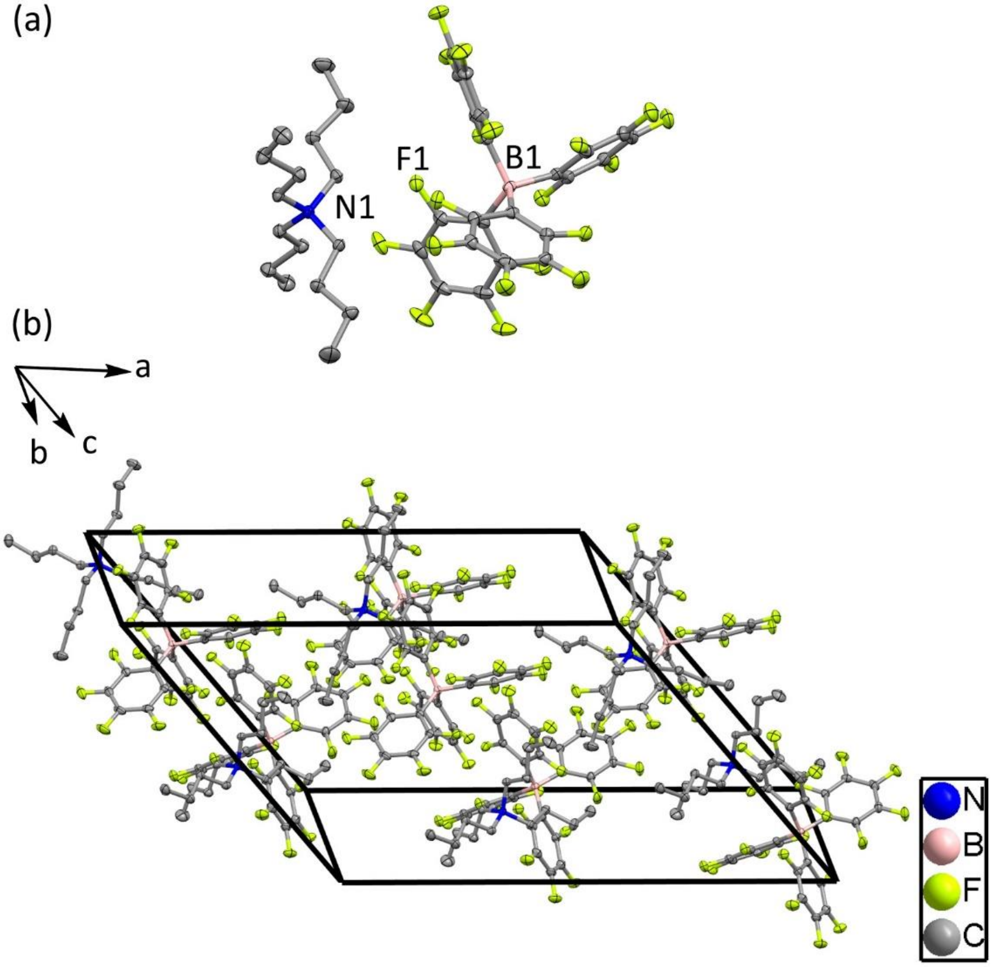

Figure 75. (a) Perspective view of $[(n\mathrm{Bu})_4\mathrm{N}][\mathrm{B}(\mathrm{C}_6\mathrm{F}_5)_4]$ showing 50% thermal contours for all non-hydrogen atoms, and (b) diagram illustrating the molecular packing of $[(n\mathrm{Bu})_4\mathrm{N}][\mathrm{B}(\mathrm{C}_6\mathrm{F}_5)_4]$ at 100 K (hydrogen atoms have been omitted for clarity). Selected bond lengths [Å] and angles [°]: N(1)-C(1), 1.517(2); N(1)-C(5), 1.525(2); N(1)-C(9), 1.521(2); N(1)-C(13), 1.521(2); B(1)-C(17), 1.654(3); B(1)-C(23), 1.651(3); B(1)-C(29), 1.663(3); B(1)-C(35), 1.649(3); C(1)-N(1)-C(9), 105.65(13); C(1)-N(1)-C(13), 111.46(14); C(9)-N(1)-C(13), 111.32(13); C(1)-N(1)-C(5), 111.28(13); C(9)-N(1)-C(5), 110.78(13); C(13)-N(1)-C(5), 106.43(13); C(17)-B(1)-C(29), 113.94(15); C(23)-B(1)-C(17), 112.52(14); C(35)-B(1)-C(23), 115.06(15); C(35)-B(1)-C(17), 101.60(14); C(35)-B(1)-C(29), 113.57(14); C(23)-B(1)-C(29), 100.74(13).

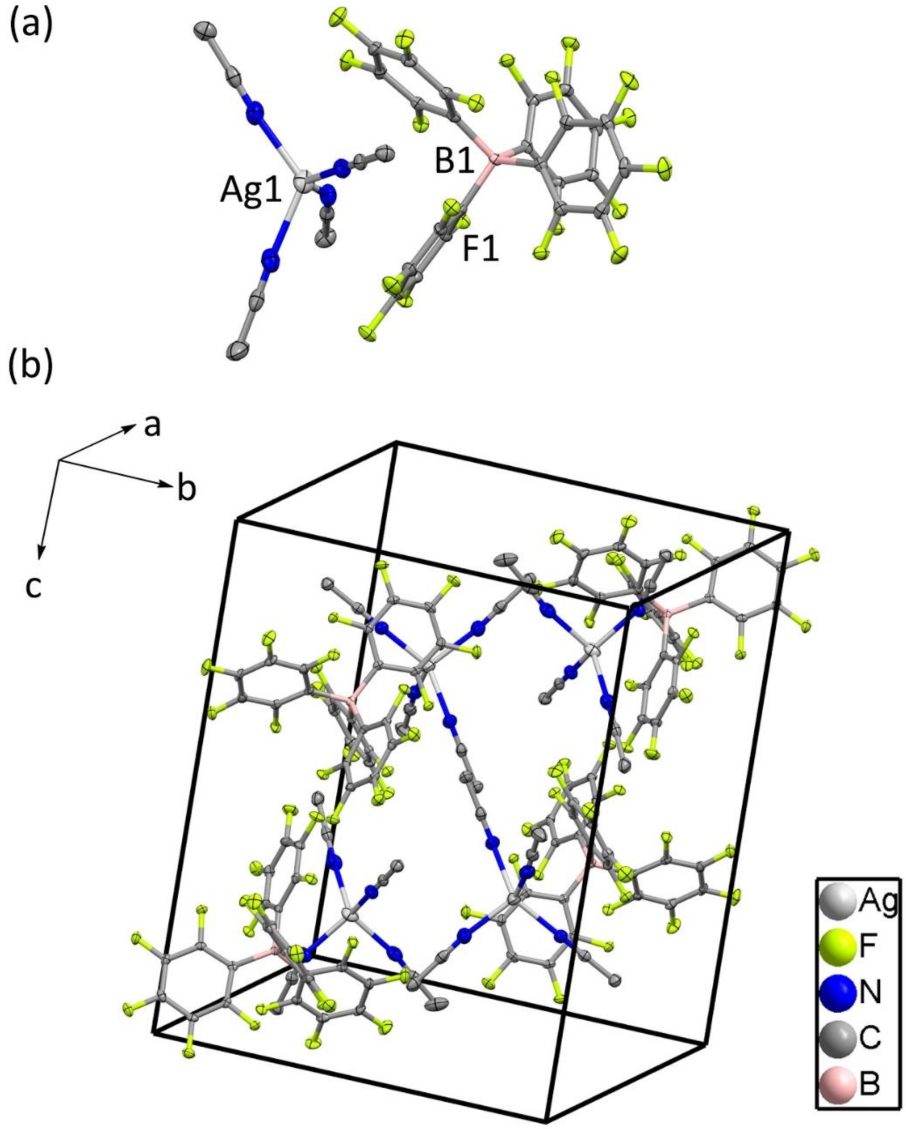

Figure 76. (a) Perspective view of $[Ag(MeCN)_4][B(C_6F_5)_4]$ showing 50% thermal contours for all non-hydrogen atoms, and (b) diagram illustrating the molecular packing of $[Ag(MeCN)_4][B(C_6F_5)_4]$ at 100 K (hydrogen atoms have been omitted for clarity). Selected bond lengths [Å] and angles [°]: Ag(1)-N(1), 2.242(2); Ag(1)-N(2), 2.283(2); Ag(1)-N(3), 2.313(2); Ag(1)-N(4), 2.314(2); B(1)-C(9), 1.648(3); B(1)-C(15), 1.652(3); B(1)-C(21), 1.654(3); B(1)-C(27), 1.656(3); N(1)-Ag(1)-N(2), 102.37(7); N(1)-Ag(1)-N(3), 106.30(7); N(2)-Ag(1)-N(3), 121.47(8); N(1)-Ag(1)-N(4), 136.27(7); N(2)-Ag(1)-N(4), 101.95(8); N(3)-Ag(1)-N(4), 90.89(7); C(9)-B(1)-C(15), 101.98(16); C(9)-B(1)-C(21), 114.80(16); C(15)-B(1)-C(21), 113.40(16); C(9)-B(1)-C(27), 112.50(16); C(15)-B(1)-C(27), 114.20(16); C(21)-B(1)-C(27), 100.54(15).

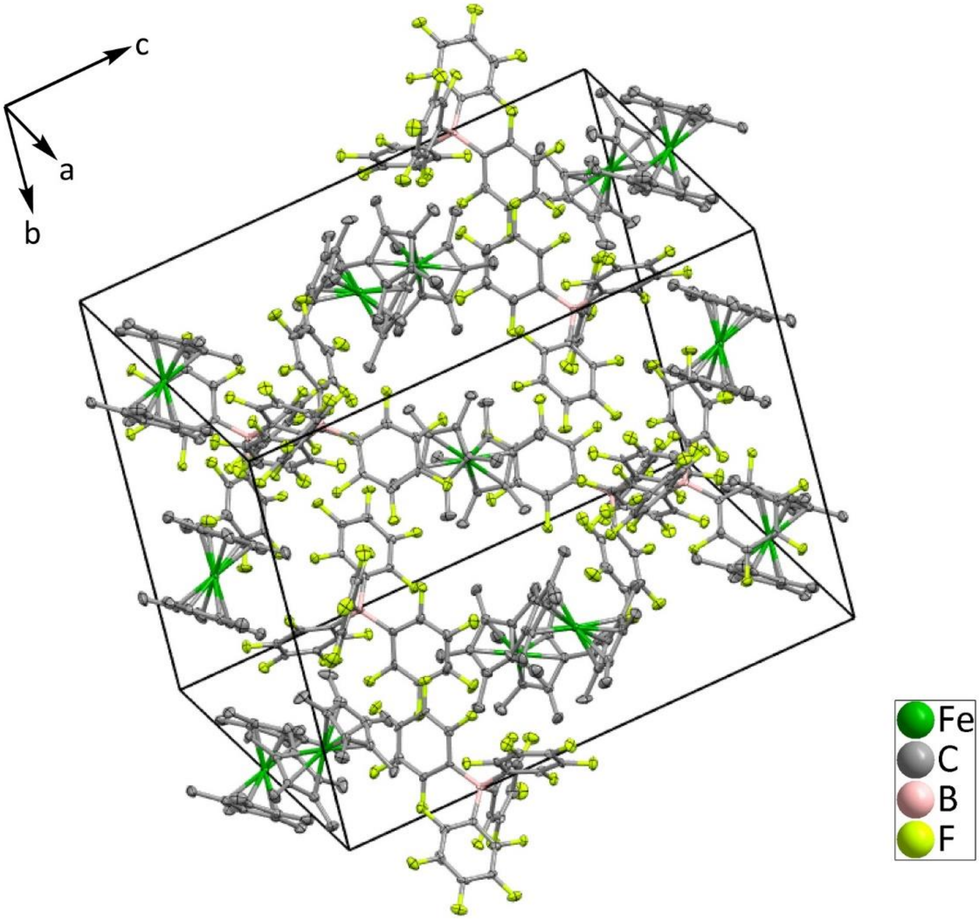

Figure 77. Diagram illustrating the molecular packing of ^{Me10}**Fc**BArF$_{20}$ at 100 K (hydrogen atoms have been omitted for clarity).

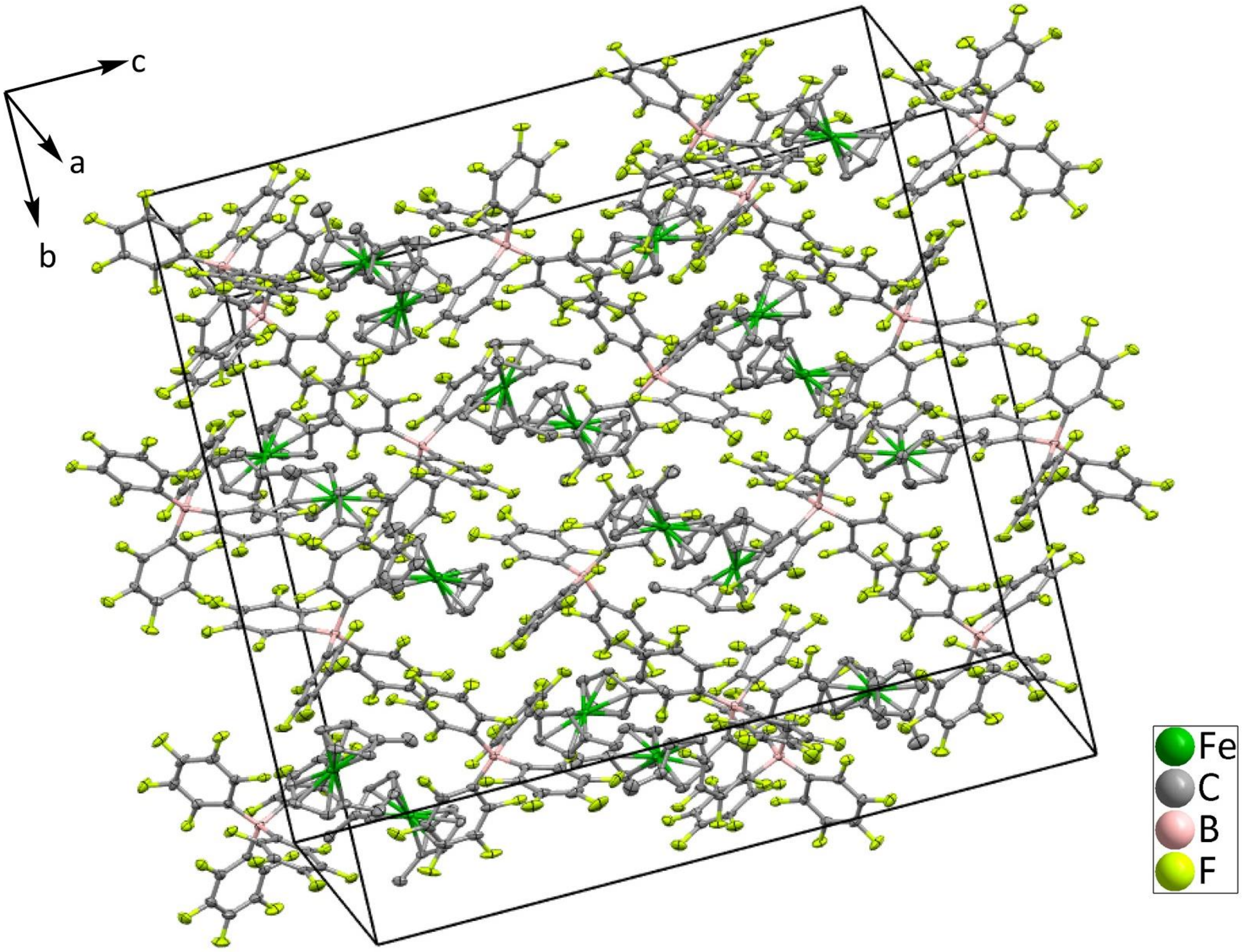

Figure 78. Diagram illustrating the molecular packing of ^{Me2}**Fc**BArF$_{20}$ at 100 K (hydrogen atoms have been omitted for clarity).

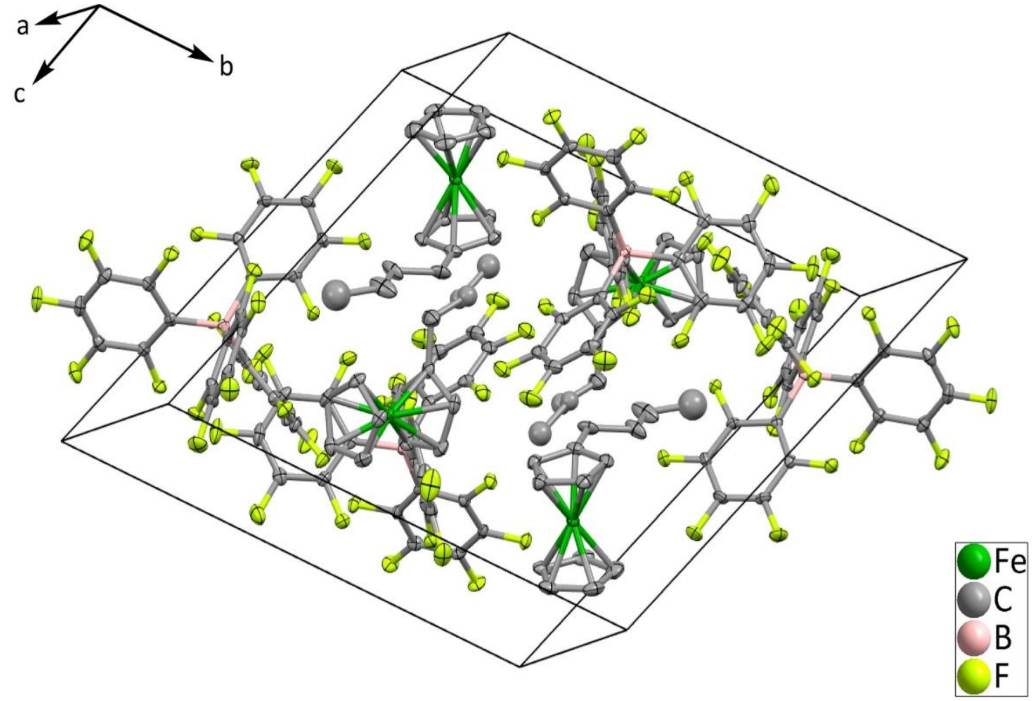

Figure 79. Diagram illustrating the molecular packing of ^{nBu}**Fc**BArF$_{20}$ at 100 K (hydrogen atoms have been omitted for clarity).

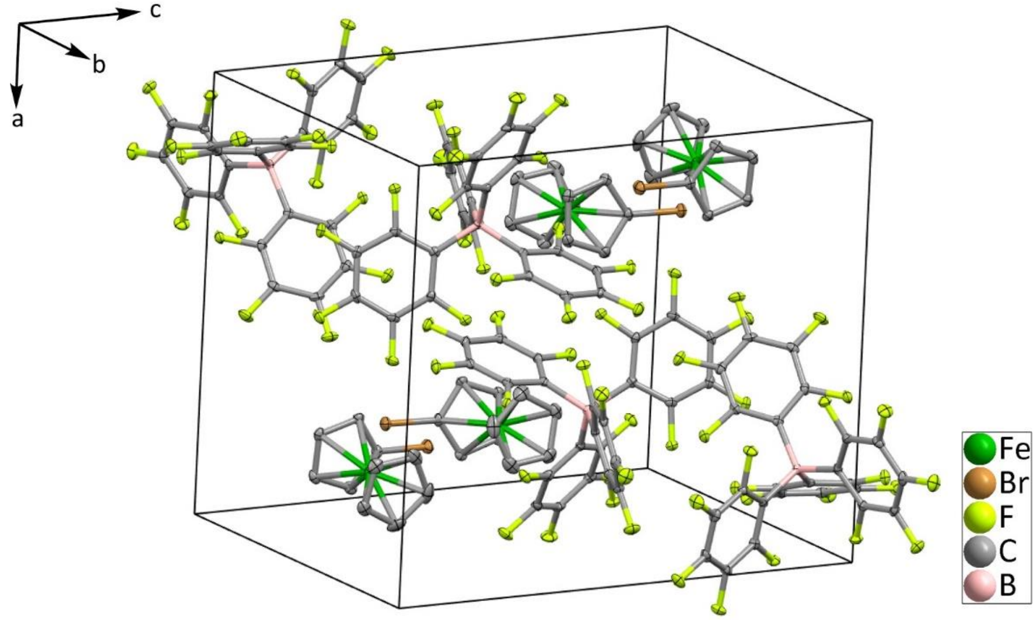

Figure 80. Diagram illustrating the molecular packing of ^{Br}**Fc**BArF$_{20}$ at 100 K (hydrogen atoms have been omitted for clarity).

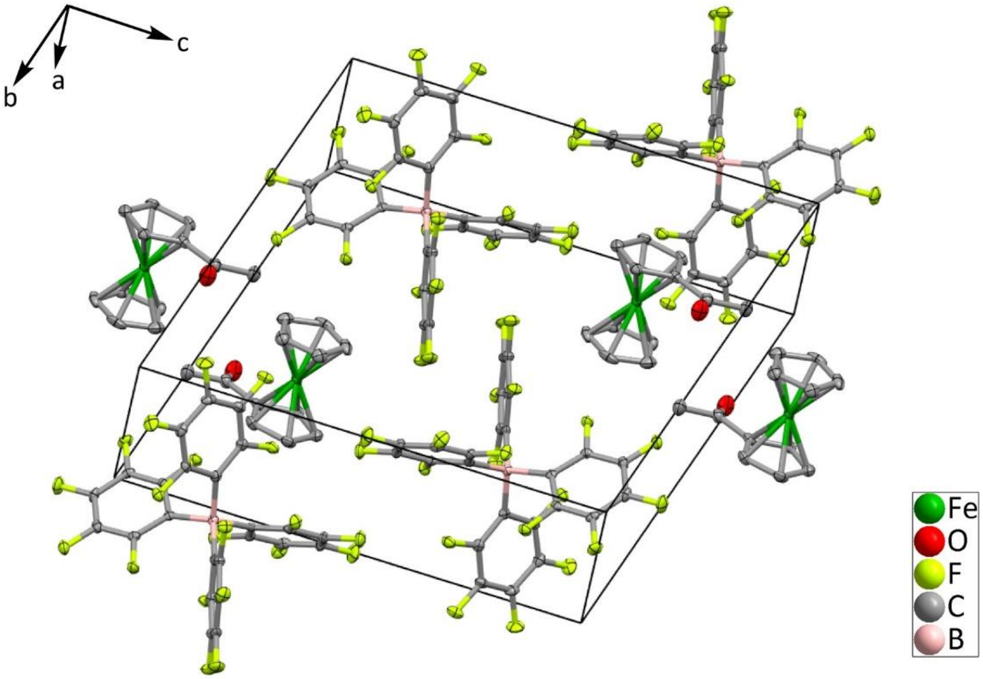

Figure 81. Diagram illustrating the molecular packing of ^{Ac}**Fc**BArF$_{20}$ at 100 K (hydrogen atoms have been omitted for clarity).

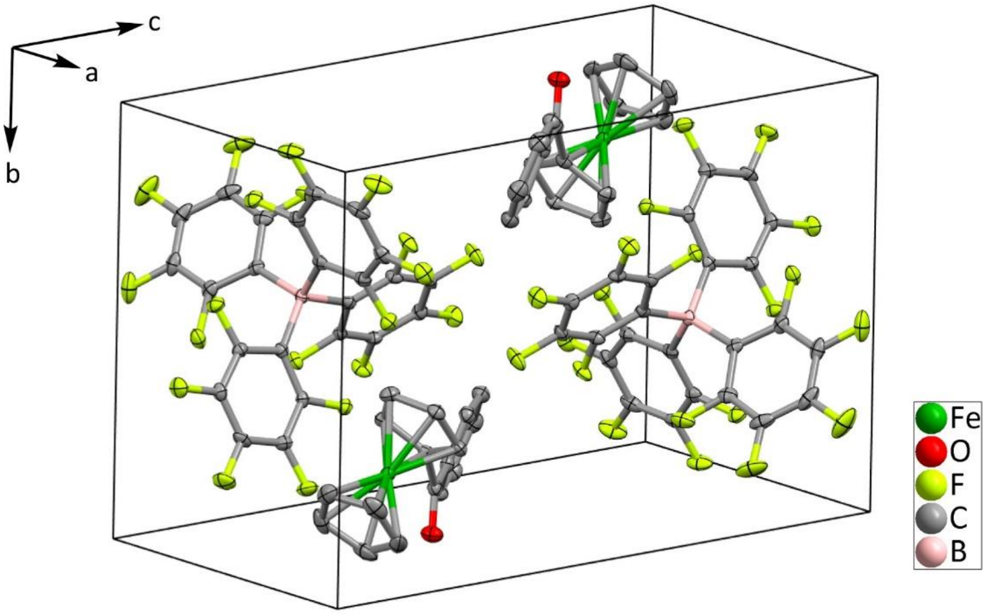

Figure 82. Diagram illustrating the molecular packing of ^{Bz}**Fc**BArF$_{20}$ at 100 K (hydrogen atoms have been omitted for clarity).

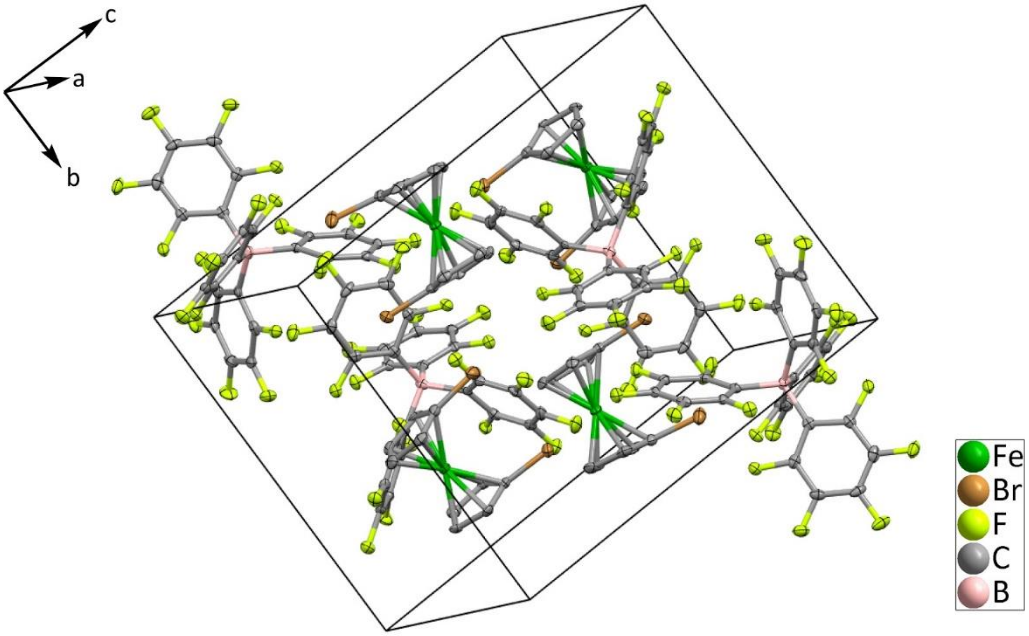

Figure 83. Diagram illustrating the molecular packing of ^{Br2}**Fc**BArF$_{20}$ at 100 K (hydrogen atoms have been omitted for clarity).

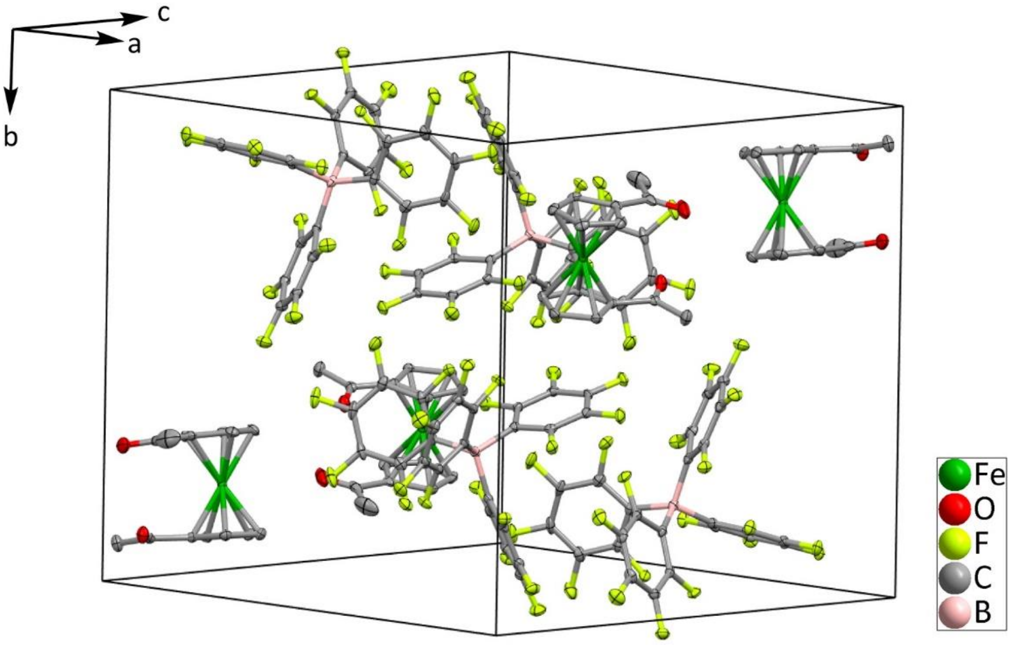

Figure 84. Diagram illustrating the molecular packing of ^{Ac2}**Fc**BArF$_{20}$ at 100 K (hydrogen atoms have been omitted for clarity).

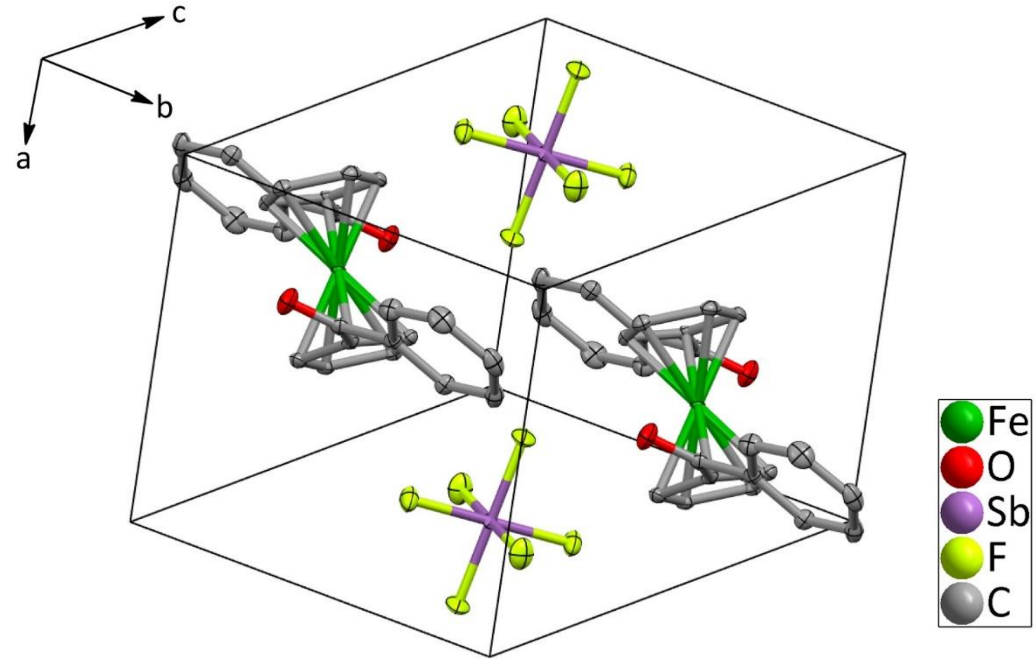

Figure 85. Diagram illustrating the molecular packing of ^{Bz2}**Fc[**SbF$_6$] at 100 K (hydrogen atoms have been omitted for clarity).

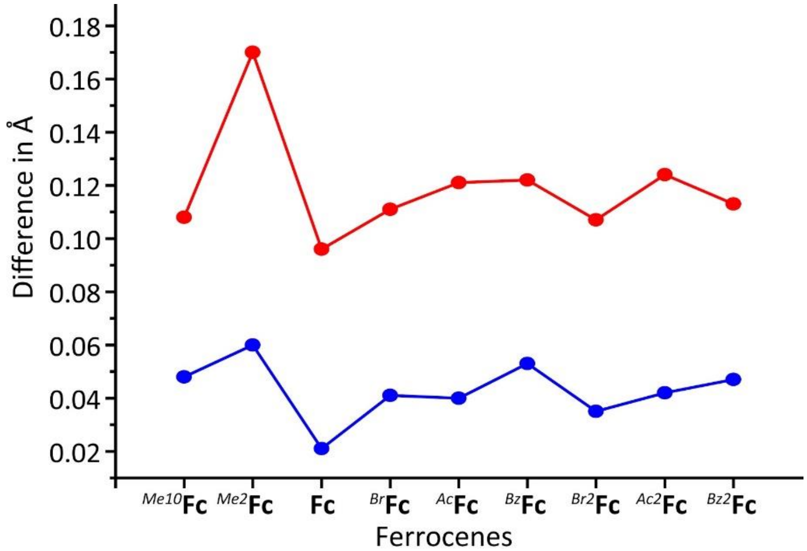

Figure 86. Plot showing the changes in the Ct⋯Ct distances (red) and in the Fe–C$_{avg}$ distances (blue) upon one electron oxidation of the ferrocene derivatives discussed in this study.

Tables for IR Spectroscopy and X-Ray Crystallography Data

a. Comparison of IR Data

Table 6. IR spectral data (cm^{-1}) for the ferrocene and ferricenium derivatives studied.

	^{Me10}**Fc**	^{Me10}**Fc**BArF$_{20}$	^{Me2}**Fc**	^{Me2}**Fc**BArF$_{20}$	^{nBu}**Fc**	^{nBu}**Fc**BArF$_{20}$	**Fc**	**Fc**BArF$_{20}$
v(C-H): C_5H_5	-	-	3077	3115	3091	3128	3105 3093 3093	3128
v(C-H): CH_3	2964 2944 2882 2850	2987 2978 2925	2968 2944 2916 2880	2934 2919 2895 2877	2956 2926 2870 2856	2960 2934 2876 2865	-	-

Table 7. IR spectral data (cm^{-1}) for the ferrocene and ferricenium derivatives studied.

	^{Br}**Fc**	^{Br}**Fc**BArF$_{20}$	^{Ac}**Fc**	^{Ac}**Fc**BArF$_{20}$	^{Br2}**Fc**	^{Br2}**Fc**BArF$_{20}$	^{Ac2}**Fc**	^{Ac2}**Fc**BArF$_{20}$
v(C-H): C_5H_5	3107 3096 3085	3124 3114 3102	3287 3308	3377	3102 3094 3085	3133 3124 3101	3295	3377
v(C-H): CH_3	-	-	3116 3097 3077 3068	3140 3125 3115 3092	-	-	3104 3087 3074	3117 3104

v(C-H): C_6H_5	-	-	-	-	-	-	-	-
v(C=O)	-	-	1650	1698	-	-	1650	1697

Table 8. IR spectral data (cm^{-1}) for the ferrocene and ferricenium derivatives studied.

	^{Bz}**Fc**	^{Bz}**Fc**BArF$_{20}$	^{Bz2}**Fc**	^{Bz2}**Fc[**SbF$_6$]
v(C-H): C_6H_5/C_5H_5	3239	3298	3247	3308
	3114	3103	3109	3123
	3092	3082	3100	3112
	3066	2981	3084	3100
	2967	2965	3070	3068
v(C=O)	1624	1659	1630	1665
v(SbF_6)	-	-	-	651

Table 9. Average J-values calculated for ferrocene and its derivatives from the two proton signals (triplets) of the substituted Cp rings.

Compound	Avg. Cp J-value (Hz)	NMR Magnet Strength (MHz)
^{Bz2}**Fc**	1.84	500
^{Ac2}**Fc**	1.94	500
^{Br2}**Fc**	1.85	400
^{Bz}**Fc**	1.75	500
^{Ac}**Fc**	1.95	500

^{Br}Fc	1.88	500
Fc	---	500
^{nBu}Fc	1.83	500
^{Me2}Fc	1.63	500
^{Me10}Fc	---	500

b. Crystallography Data and Data Collection Parameters

Table 10. Crystallographic Data and Data Collection Parameters.

	$[(n\text{Bu})_4\text{N}][\text{B}(\text{C}_6\text{F}_5)_4]$	$[\text{Ag}(\text{MeCN})_4][\text{B}(\text{C}_6\text{F}_5)_4]$
Formula	$C_{40}H_{36}BF_{20}N$	$C_{32}H_{12}AgBF_{20}N_4$
T (K)	100(2)	100(2)
Formula weight	921.51	951.14
Crystal system	Monoclinic	Monoclinic
Space group	Cc	$P\ 2_1/c$
a, Å	23.9161(5)	10.9055(6)
b, Å	12.8024(3)	16.9646(4)
c, Å	17.3043(4)	19.0513(15)
α , deg	90	90
β, deg	130.542(2)	104.764(9)
γ, deg	90	90
V, Å3	4026.33(18)	3408.3(4)
Z	4	4
Radiation (λ, Å)	Mo Kα (0.71073)	Mo Kα (0.71073)
$d$calcd, g•cm^{-3}	1.520	1.854
F(000)	1872	1856

Crystal size (mm^3)	0.565 x 0.523 x 0.320	0.406 x 0.184 x 0.116
Theta range for data collection	2.365 to 27.500°	2.274 to 25.499°
μ, mm^{-1}	0.153	0.734
No of unique data	9127	6352
Completeness to theta	99.9%	99.9%
No. of restraints	2	0
No. of params. refined	563	527
GOF on F^2	1.036	1.030
$R1^{a}$ $^{[I > 2\sigma(I)]}$	0.0247	0.0278
$R1^{a}$ (all data)	0.0265	0.0368
$wR2^{b}$ (all data)	0.0621	0.0676
Largest diff. peak and hole	0.192 and -0.163 e.Å^{-3}	0.488 and -0.720 e.Å^{-3}

$$^{a}R1= \frac{\Sigma||F_o|-|F_c||}{\Sigma|F_o|};\ ^{b}wR2= \sqrt{\frac{\Sigma\left[w\left(F_o{}^2-F_c{}^2\right)^2\right]}{\Sigma\left[w\left(F_o{}^2\right)^2\right]}}$$

Table 11. Crystallographic Data and Data Collection Parameters.

	^{Me10}**Fc**BArF$_{20}$	^{Me2}**Fc**BArF$_{20}$	^{nBu}**Fc**BArF$_{20}$
Formula	$C_{44}H_{30}BF_{20}Fe$	$C_{36}H_{14}BF_{20}Fe$	$C_{38}H_{18}BF_{20}Fe$
T (K)	100(2)	100(2)	100(2)
Formula weight	1005.34	893.13	921.18
Crystal system	Monoclinic	Orthorhombic	Triclinic
Space group	$P\ 2_1/c$	P bcn	P -1
a, A	16.5730(4)	20.9252(4)	15.4902(6)
b, A	19.8456(5)	29.1241(4)	15.5939(6)
c, A	24.3129(5)	31.8841(4)	16.4411(5)

α , deg	90	90	107.224(3)
β, deg	90.297	90	102.664(3)°
γ, deg	90	90	101.494(4)°
V, A3	7996.4(3)	19431.0(5)	3549.2(2)
Z	8	24	4
Radiation (λ, A)	Mo Kα (0.71073)	Mo Kα (0.71073)	Mo Kα (0.71073)
$d$calcd, g•cm–3	1.670	1.832	1.724
F(000)	4040	10584	1828
Crystal size (mm^3)	0.29 x 0.25 x 0.14	0.351 x 0.272 x 0.107	0.285 x 0.109 x 0.075
Theta range for data collection	2.217 to 24.999°	1.751 to 25.500°	2.226 to 27.500°
μ, mm^{-1}	0.505	0.611	0.561
No of unique data	14294	17808	16303
Completeness to theta	99.9%	98.7%	99.9%
No. of restraints	24	54	0
No. of params. refined	1213	1694	1109
GOF on F^2	0.973	1.113	1.007
$R1^{a}$ $^{[I> 2\sigma(I)]}$	0.0463	0.0531	0.0458
$R1^{a}$ (all data)	0.0750	0.0707	0.0917
$wR2^{b}$ (all data)	0.1102	0.1346	0.0979
Largest diff. peak and hole	0.526 and -0.383 e.Å^{-3}	2.017 and -0.777 e.Å^{-3}	0.669 and -0.485 e.Å^{-3}

$$^{a}R1= \frac{\sum\left||F_o|-|F_c|\right|}{\sum|F_o|};\ ^{b}wR2= \sqrt{\frac{\sum\left[w\left(F_o{}^2-F_c{}^2\right)^2\right]}{\sum\left[w\left(F_o{}^2\right)^2\right]}}$$

Table 12. Crystallographic Data and Data Collection Parameters.

	^{Br}**Fc**BArF$_{20}$	^{Ac}**Fc**BArF$_{20}$	^{Bz}**Fc**BArF$_{20}$
Formula	$C_{34}H_9BBrF_{20}Fe$	$C_{36}H_{12}BF_{20}FeO$	$C_{41}H_{14}BF_{20}FeO$

T (K)	100(2)	100(2)	100(2)
Formula weight	943.98	907.12	969.18
Crystal system	Monoclinic	Triclinic	Triclinic
Space group	$P\ 2_1/n$	*P* -1	*P* -1
a, Å	14.3172(3)	8.5444(3)	11.5342(4)
b, Å	13.0057(3)	12.5527(5)	12.1297(6)
c, Å	16.3446(3)	16.3063(6)	15.3574(7)
α , deg	90	73.244(3)°	108.024(4)
β, deg	90.457(2)	88.652(3)°	94.966(3)
γ, deg	90	73.301(4)°	115.789(4)
V, Å3	3043.35(11)	1600.70(11)	1777.22(15)
Z	4	2	2
Radiation (*λ*, Å)	Mo Kα (0.71073)	Mo Kα (0.71073)	Mo Kα (0.71073)
*d*calcd, g•cm–3	2.060	1.882	1.811
F(000)	1836	894	958
Crystal size (mm^3)	0.293 x 0.107 x 0.097	0.158 x 0.137 x 0.120	0.276 x 0.218 x 0.116
Theta range for data collection	2.450 to 27.496°	2.492 to 25.497°	2.355 to 25.498°
μ, mm^{-1}	1.961	0.622	0.567
No of unique data	6969	5955	6611
Completeness to theta	99.9%	99.9%	99.9%
No. of restraints	0	0	0
No. of params. refined	514	533	577
GOF on F^2	1.024	1.052	1.030
$R1^{a\ [I>2\sigma(I)]}$	0.0256	0.0341	0.0288
$R1^{a}$ (all data)	0.0346	0.0521	0.0382

*wR*2^{b} (all data)	0.0586	0.0718	0.0656
Largest diff. peak and hole	0.413 and -0.349 e.Å^{-3}	0.328 and -0.309 e.Å^{-3}	0.336 and -0.369 e.Å^{-3}

$$^{a}R1=\frac{\Sigma||F_o|-|F_c||}{\Sigma|F_o|};\ ^{b}wR2=\sqrt{\frac{\Sigma\left[w\left(F_o{}^2-F_c{}^2\right)^2\right]}{\Sigma\left[w\left(F_o{}^2\right)^2\right]}}$$

Table 13. Crystallographic Data and Data Collection Parameters.

	^{Br2}**Fc**BArF$_{20}$	^{Ac2}**Fc**BArF$_{20}$	^{Bz2}**Fc[**SbF$_6$]
Formula	$C_{34}H_8BBr_2F_{20}Fe$	$C_{38}H_{14}BF_{20}FeO_2$	$C_{24}H_{18}F_6FeO_2Sb$
T (K)	100(2)	100(2)	100(2)
Formula weight	1022.88	949.15	629.98
Crystal system	Monoclinic	Monoclinic	Triclinic
Space group	*P* 2_1/n	*P* 2_1/c	*P* -1
a, Å	15.4399(13)	15.4200(8)	7.7836(4)
b, Å	13.3339(7)	16.6840(5)	8.1200(5)
c, Å	15.7029(10)	15.1965(8)	9.8619(7)
α , deg	90	90	112.789(6)
β, deg	91.482(6)	119.448(7)	101.780(5)
γ, deg	90	90	96.453(5)
V, Å3	3231.7(4)	3404.5(3)	549.74(6)
Z	4	4	1
Radiation (*λ*, Å)	Mo Kα (0.71073)	Mo Kα (0.71073)	Mo Kα (0.71073)
*d*calcd, g•cm–3	2.102	1.852	1.903
F(000)	1972	1876	309

Crystal size (mm^3)	0.141 x 0.095 x 0.073	0.270 x 0.125 x 0.111	0.290 x 0.195 x 0.190
Theta range for data collection	2.418 to 25.497°	2.442 to 27.500°	2.735 to 27.497°
μ, mm^{-1}	3.085	0.592	1.949
No of unique data	6002	7816	2511
Completeness to theta	99.8%	99.9%	99.5%
No. of restraints	0	0	0
No. of params. refined	523	561	157
GOF on F^2	1.011	1.015	1.056
$R1^{a}$ $^{[I>2\sigma(I)]}$	0.0438	0.0355	0.0176
$R1^{a}$ (all data)	0.0958	0.0542	0.0180
$wR2^{b}$ (all data)	0.0803	0.0786	0.0453
Largest diff. peak and hole	0.473 and -0.581 e.Å^{-3}	0.390 and -0.424 e.Å^{-3}	0.388 d -0.434 e.Å^{-3}

$$^{a}R1= \frac{\Sigma||F_o|-|F_c||}{\Sigma|F_o|};\ ^{b}wR2= \sqrt{\frac{\Sigma\left[w\left(F_o{}^2-F_c{}^2\right)^2\right]}{\Sigma\left[w\left(F_o{}^2\right)^2\right]}}$$

c. Selected Structural Parameters for All the Ferrocene and Ferricenium Derivatives Described in This Study

Table 14. Selected structural parameters of the neutral and oxidized complexes.

Complex	C–C^{a} (Å) (T)	C–C^{a} (Å) (B)	Fe–C$_{avg}$^{b} (Å) (T)	Fe–C$_{avg}$^{b} (Å) (B)	Ct⋯Fe^{c} (Å) (T)	Ct⋯Fe^{c} (Å) (B)	Ct⋯Ct^{d} (Å)	Reference
^{Me10}**Fc**	1.434	1.434	2.053	2.053	1.651	1.651	3.305	61

$^{Me10}\mathbf{Fc}^{+}$	1.432	1.430	2.095	2.098	1.706	1.711	3.413	this work
$^{Me2}\mathbf{Fc}$	1.430	1.428	2.047	2.047	1.646	1.647	3.293	61
$^{Me2}\mathbf{Fc}^{+}$	1.416	1.412	2.104	2.109	1.730	1.733	3.463	this work
$^{R}\mathbf{Fc}^{+e}$	1.424	1.414	2.045	2.041	1.648	1.650	3.297	62
$^{nBu}\mathbf{Fc}^{+}$	1.412	1.410	2.083	2.083	1.702	1.703	3.404	this work
Fc	1.427	1.425	2.046	2.046	1.648	1.649	3.296	63
$\mathbf{Fc}^{+}$	1.394	1.391	2.079	2.075	1.708	1.705	3.412	64
$^{Br}\mathbf{Fc}$	1.424	1.420	2.041	2.048	1.642	1.654	3.296	65
$^{Br}\mathbf{Fc}^{+}$	1.417	1.410	2.089	2.082	1.706	1.701	3.407	this work
$^{Ac}\mathbf{Fc}$	1.429	1.426	2.045	2.048	1.645	1.651	3.294	66
$^{Ac}\mathbf{Fc}^{+}$	1.417	1.408	2.092	2.084	1.711	1.705	3.415	this work
$^{Bz}\mathbf{Fc}$	1.423	1.408	2.043	2.043	1.646	1.655	3.301	67
$^{Bz}\mathbf{Fc}^{+}$	1.418	1.401	2.094	2.085	1.712	1.711	3.423	this work
$^{Br2}\mathbf{Fc}$	1.429	1.427	2.048	2.049	1.648	1.650	3.298	68
$^{Br2}\mathbf{Fc}^{+}$	1.415	1.411	2.088	2.080	1.706	1.700	3.405	this work
$^{Ac2}\mathbf{Fc}$	1.431	1.432	2.049	2.050	1.649	1.649	3.293	61
$^{Ac2}\mathbf{Fc}^{+}$	1.420	1.417	2.092	2.091	1.708	1.709	3.417	this work
$^{Bz2}\mathbf{Fc}$	1.417	1.417	2.040	2.044	1.646	1.650	3.296	69
$^{Bz2}\mathbf{Fc}^{+}$	1.420	1.420	2.089	2.089	1.705	1.705	3.409	this work

T and *B* correspond to the top and bottom Cp rings in all complexes, respectively. The Top ring is the substituted ring in the monosubstituted complexes. [a]Average of the C–C bond lengths for each Cp ring. [b]Average of the Fe–C(Cp) bond lengths with each Cp ligand. [c]Distance between the centroid of the Cp ring and Fe center. [d]Separation between the centroids of two Cp rings. [e]The data corresponds to average for the two closely related ferrocene derivatives, $^{nC14}\mathbf{Fc}$ and **Fc**-(CH_2)$_8$-**Fc**.

Table 15. Selected structural and geometrical parameters of the neutral and oxidized complexes.

Complex	Ct–Fe–Ct, ∠α (°)	Ring tilt, ∠β (*T*) (°)	Ring tilt, ∠β (*B*) (°)	Torsion, ∠φ (°)	Sub. out of plane ∠γ (T) (°)[a]	Sub. out of plane ∠γ (B) (°)[a]	Reference
^{Me10}**Fc**	180.0	90.0	90.0	36.0	−1.78	−1.78	61
^{Me10}**Fc**$^{+}$	179.7	89.6	90.5	16.9/35.9	−1.62	−1.17	this work
^{Me2}**Fc**	178.4	90.2	90.4	−3.6	−2.63	−2.27	61
^{Me2}**Fc**$^{+}$	179.1	96.4	85.5	13.6/−14.9/−1.9	+0.45	−0.90	this work
^{R}**Fc**$^{+b}$	179.5	90.3	89.6	−3.8	−2.6	—	62
^{nBu}**Fc**$^{+}$	178.9	91.2	90.7	7.94/−1.18	+1.19	—	this work
Fc	179.7	90.0	90.0	−8.8/9.0	—	—	63
Fc^{+}	179.1	90.0	90.0	−8.4	—	—	4
^{Br}**Fc**	179.3	89.0	89.7	2.6/28.57	−2.06	—	65
^{Br}**Fc**$^{+}$	178.8	90.8	90.0	9.1	−2.31	—	this work
^{Ac}**Fc**	178.2	89.1	90.2	0.1/1.0	+3.52	—	66
^{Ac}**Fc**$^{+}$	178.2	88.7	88.9	−3.4	+0.78	—	this work
^{Bz}**Fc**	177.6	89.4	90.3	6.3	−0.10	—	67
^{Bz}**Fc**$^{+}$	178.5	90.2	90.7	−1.3	+1.85	—	this work
^{Br2}**Fc**	177.7	90.0	89.8	0.6	−2.67	−4.07	68
^{Br2}**Fc**$^{+}$	177.0	92.5	93.1	3.5	+1.27	+1.06	this work
^{Ac2}**Fc**	178.9	89.1	88.9	139.6	+4.37	−2.97	61
^{Ac2}**Fc**$^{+}$	179.2	88.3	88.0	−26.4	+2.86	+2.18	this work
^{Bz2}**Fc**	179.4	89.1	89.3	130.4	+5.06	−3.46	69
^{Bz2}**Fc**$^{+}$	180.0	88.4	88.4	180.0	+2.33	+2.33	this work

[a] For substituent out of plane deviation, "+" denotes towards the Fe center, while "–" denotes away from the Fe center. [b] The data corresponds to average for the two closely related ferrocene derivatives, ^{nC14}**Fc** and **Fc**-(CH_2)$_8$-**Fc**.

Table 16. Selected bond lengths (Å) for the ferricenium complexes containing electron donating substituents.

	^{Me10}**Fc**BArF$_{20}$	^{Me2}**Fc**BArF$_{20}$	^{nBu}**Fc**BArF$_{20}$
Fe(1)-C(1A)	2.101(5)	2.028(3)	2.115(3)
Fe(1)-C(2A)	2.099(5)	2.000(3)	2.068(3)
Fe(1)-C(3A)	2.097(5)	2.214(4)	2.055(3)
Fe(1)-C(4A)	2.107(5)	2.176(4)	2.071(3)
Fe(1)-C(5A)	2.110(5)	2.078(4)	2.098(3)
Fe(1)-C(6A)	2.107(5)	2.295(4)	2.097(3)
Fe(1)-C(7A)	2.100(5)	2.170(4)	2.073(3)
Fe(1)-C(8A)	2.083(5)	2.047(4)	2.070(3)
Fe(1)-C(9A)	2.101(5)	1.937(4)	2.084(3)
Fe(1)-C(10A)	2.099(5)	2.053(4)	2.096(3)
Fe(2)-C(1B)	2.115(5)	2.264(5)	2.113(3)
Fe(2)-C(2B)	2.087(5)	2.015(4)	2.104(3)
Fe(2)-C(3B)	2.079(5)	1.965(4)	2.068(3)
Fe(2)-C(4B)	2.081(5)	2.069(4)	2.058(3)
Fe(2)-C(5B)	2.096(5)	2.200(4)	2.081(3)
Fe(2)-C(6B)	-	2.063(4)	2.099(3)
Fe(2)-C(7B)	-	2.116(4)	2.091(3)
Fe(2)-C(8B)	-	2.216(4)	2.078(3)
Fe(2)-C(9B)	-	2.178(4)	2.066(3)
Fe(2)-C(10B)	-	1.980(4)	2.079(3)
Fe(3)-C(1C)	-	2.173(8)	-
Fe(3)-C(2C)	-	2.225(8)	-
Fe(3)-C(3C)	-	2.196(8)	-
Fe(3)-C(4C)	-	1.951(7)	-

Fe(3)-C(5C)	-	2.036(6)	-
Fe(3)-C(6C)	-	2.030(9)	-
Fe(3)-C(7C)	-	2.099(9)	-
Fe(3)-C(8C)	-	2.172(8)	-
Fe(3)-C(9C)	-	2.220(9)	-
Fe(3)-C(10C)	-	2.039(7)	-

Table 17. Selected bond lengths (Å) for the ferricenium complexes containing mildly electron withdrawing substituents.

	^{Br}**Fc**BArF$_{20}$	^{Ac}**Fc**BArF$_{20}$	^{Bz}**Fc**BArF$_{20}$	^{Br2}**Fc**BArF$_{20}$	^{Ac2}**Fc**BArF$_{20}$	^{Bz2}**Fc[**SbF$_6$]
Fe(1)-C(1A)	2.0962(18)	2.073(2)	2.0979(17)	2.116(4)	2.0634(19)	2.0643(16)
Fe(1)-C(2A)	2.0886(18)	2.091(2)	2.0697(18)	2.084(5)	2.0648(18)	2.0938(14)
Fe(1)-C(3A)	2.0843(18)	2.112(2)	2.0718(19)	2.055(5)	2.1010(19)	2.1162(14)
Fe(1)-C(4A)	2.0835(18)	2.107(2)	2.1053(19)	2.068(4)	2.1223(19)	2.1059(14)
Fe(1)-C(5A)	2.0924(18)	2.081(2)	2.1246(18)	2.115(4)	2.105(2)	2.0659(15)
Fe(1)-C(6A)	2.081(2)	2.067(2)	2.096(2)	2.126(4)	2.0593(18)	-
Fe(1)-C(7A)	2.086(2)	2.078(2)	2.070(2)	2.085(4)	2.1003(18)	-
Fe(1)-C(8A)	2.0863(19)	2.096(2)	2.065(2)	2.036(5)	2.136(2)	-
Fe(1)-C(9A)	2.0794(19)	2.097(2)	2.0867(19)	2.050(5)	2.0985(19)	-
Fe(1)-C(10A)	2.075(2)	2.082(2)	2.110(2)	2.105(5)	2.0664(18)	-
Br(1)-C(1)	1.8666(18)	-	-	1.872(5)	-	-
Br(2)-C(6)	-	-	-	1.855(5)	-	-
C(11)-C(1)	-	1.500(3)	1.508(3)	-	1.503(3)	1.500(2)
C(13)-C(6)	-	-	-	-	1.494(3)	-
O(1)-C(11)	-	1.209(3)	1.215(2)	-	1.209(3)	1.2149(19)

O(2)-C(13)	-	-	-	-	1.210(2)	-

ELECTROCHEMISTRY

a. Uncompensated Resistance and Impedance Measurements

The uncompensated resistance (R_u) was measured using potentio electrochemical impedance spectroscopy (PEIS) to correct for internal resistance drop of voltage in the electrolyte solution. A three-electrode setup was employed using the same electrolyte/solvent combinations as were used in the ferrocene cyclic voltammetry (CV) experiments. The frequency was scanned from 1 MHz to 100 mHz and the "real impedance" value observed at 1MHz was considered the uncompensated resistance value for that solution. This was corrected 85% in the cyclic voltammetry experiments.

Table 18. R_u Values for Each Solvent/Electrolyte Combination Used in Ferrocene Cyclic Voltammetry Experiments.

Solvent/Electrolyte Solution	**R_u Value (Ohm)**
MeCN, $[(n\text{Bu})_4\text{N}][\text{B}(\text{C}_6\text{F}_5)_4]$	67
MeCN, $[(n\text{Bu})_4\text{N}][\text{PF}_6]$	62
DCM, $[(n\text{Bu})_4\text{N}][\text{B}(\text{C}_6\text{F}_5)_4]$	237
DCM, $[(n\text{Bu})_4\text{N}][\text{PF}_6]$	410
MeTHF, $[(n\text{Bu})_4\text{N}][\text{B}(\text{C}_6\text{F}_5)_4]$	351

The Ag/AgCl reference electrodes were stored in 0.05 M H_2SO_4 overnight and then in saturated KCl solution immediately prior to testing. Before performing experiments on the ferrocene samples in organic solutions, the impedance of the Ag/AgCl reference electrodes was measured in a 100 mM aqueous KCl solution using impedance spectroscopy in a 2-electrode setup between the counter and reference electrodes. The frequency was scanned from 200 kHz to 1 Hz and the real impedance value observed at

200 kHz was considered the impedance for that particular Ag/AgCl electrode. An impedance under 20,000 Ohm was considered suitable for use. Additionally, CV measurements of ferrocene carboxylate in 100 mM aqueous KCl solution were performed and the measured potential vs Ag/AgCl was compared to the potential observed using a saturated calomel electrode (SCE). A potential difference of approximately 32-44 mV was considered satisfactory for use.[70] If the Ag/AgCl electrode satisfied both of these conditions, it was used in the experiments.

b. Cyclic Voltammograms of All Ferrocenes Discussed in Each Solvent

Each sample solution contained 2 mM of the corresponding ferrocene and 100 mM of the supporting electrolyte. The potentials were collected vs a leak-free Ag/AgCl reference electrode. The working electrode was glassy carbon and the counter electrode was a carbon rod. Scan rates were varied as follows (in mV/s): 1000, 500, 250, 100, 50, 25. Exceptions to this procedure were ^{Me10}**Fc**; ^{Bz2}**Fc**; and ^{Ac2}**Fc** in MeCN, as discussed in the main text.

i. DCM

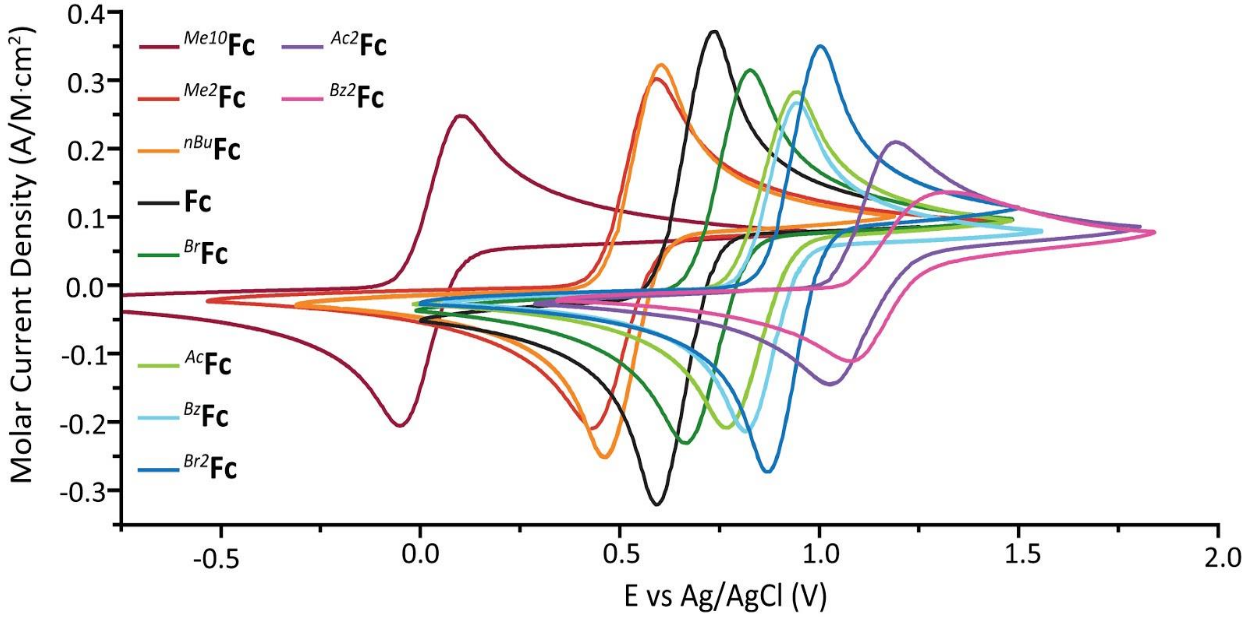

Figure 87. Cyclic voltammograms at 100 mV/s of various ferrocene derivatives collected in DCM using $[(n\text{Bu})_4\text{N}][\text{B}(\text{C}_6\text{F}_5)_4]$ as the supporting electrolyte.

ii. MeCN

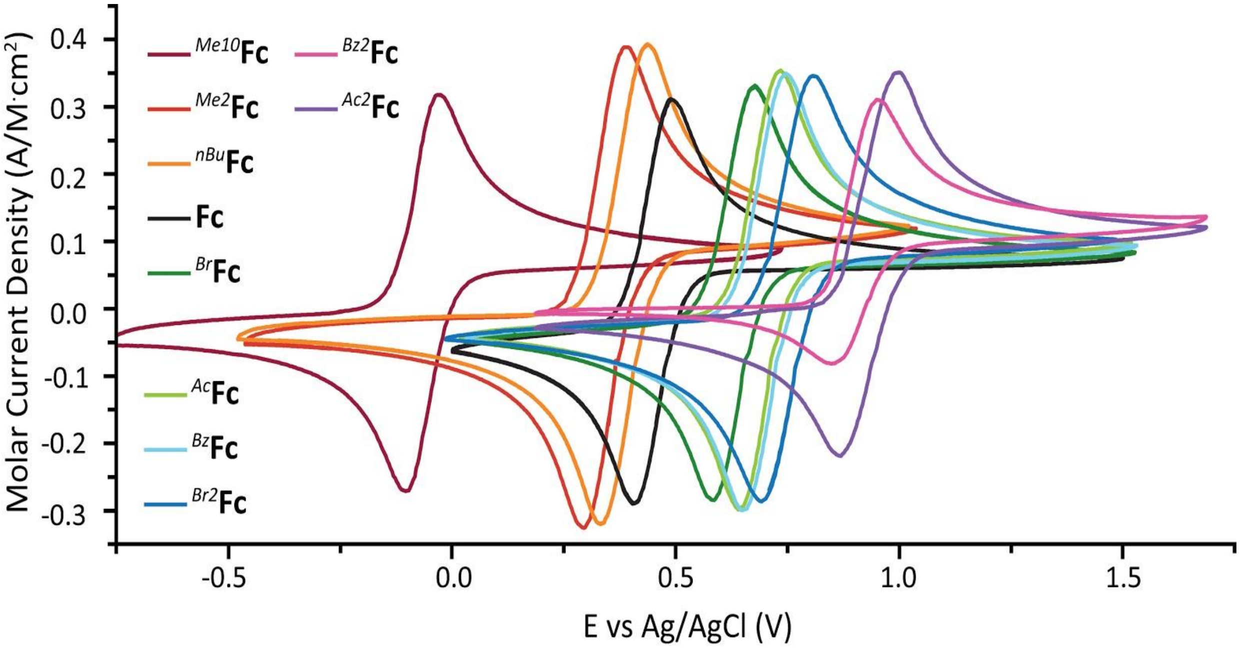

Figure 88. Cyclic voltammograms at 100 mV/s of various ferrocene derivatives collected in MeCN using $[(nBu)_4N][B(C_6F_5)_4]$ as the supporting electrolyte.

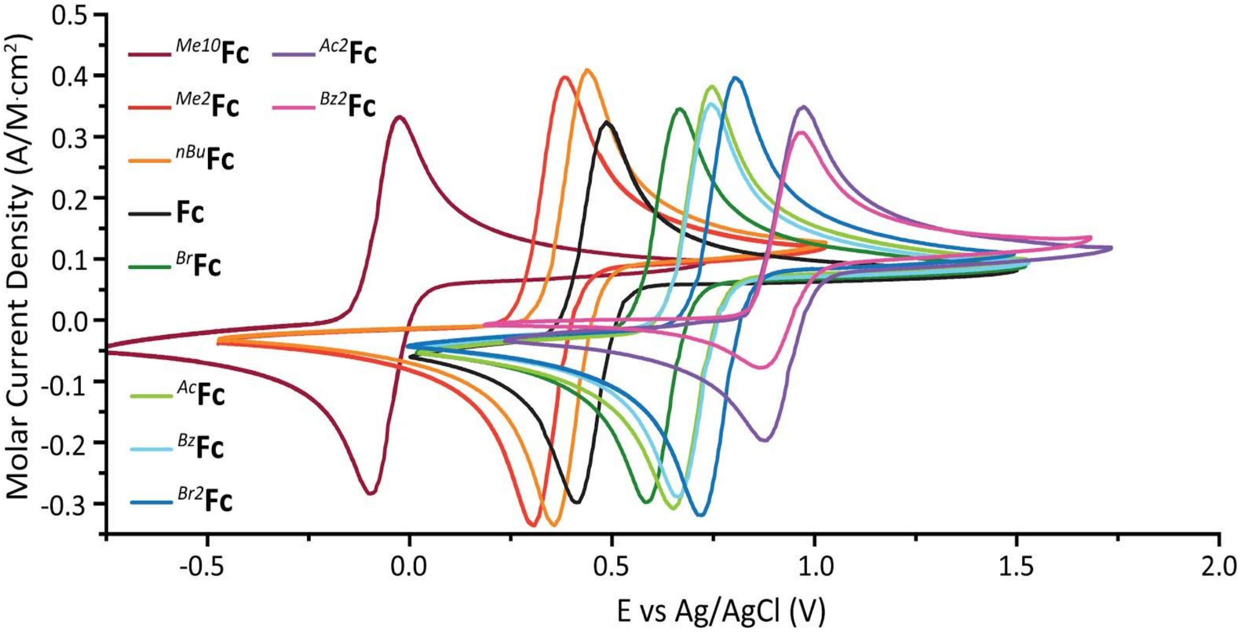

Figure 89. Cyclic voltammograms at 100 mV/s of various ferrocene derivatives collected in MeCN using $[(nBu)_4N][PF_6]$ as the supporting electrolyte.

iii. MeTHF

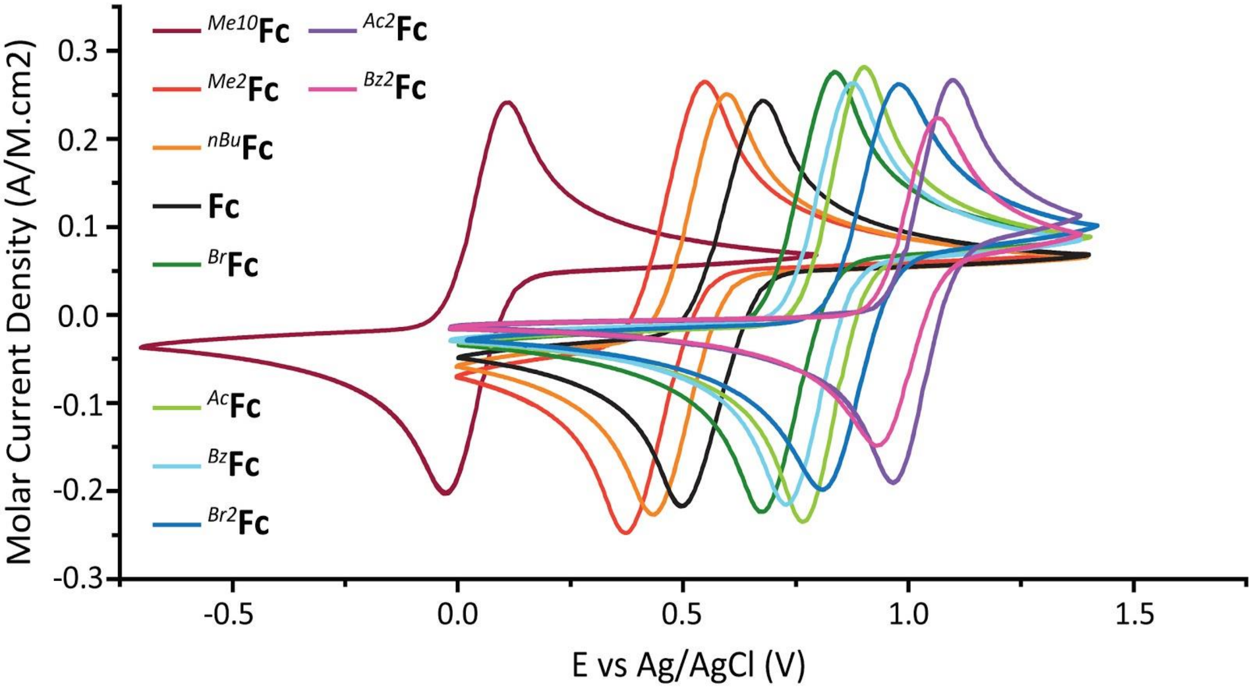

Figure 90. Cyclic voltammograms at 100 mV/s of various ferrocene derivatives collected in MeTHF using $[(n\mathrm{Bu})_4\mathrm{N}][\mathrm{B}(\mathrm{C}_6\mathrm{F}_5)_4]$ as the supporting electrolyte.

c. Cyclic Voltammograms of Each Ferrocene Derivative with Their Corresponding Randles-Sevcik Plots

i. Decamethylferrocene

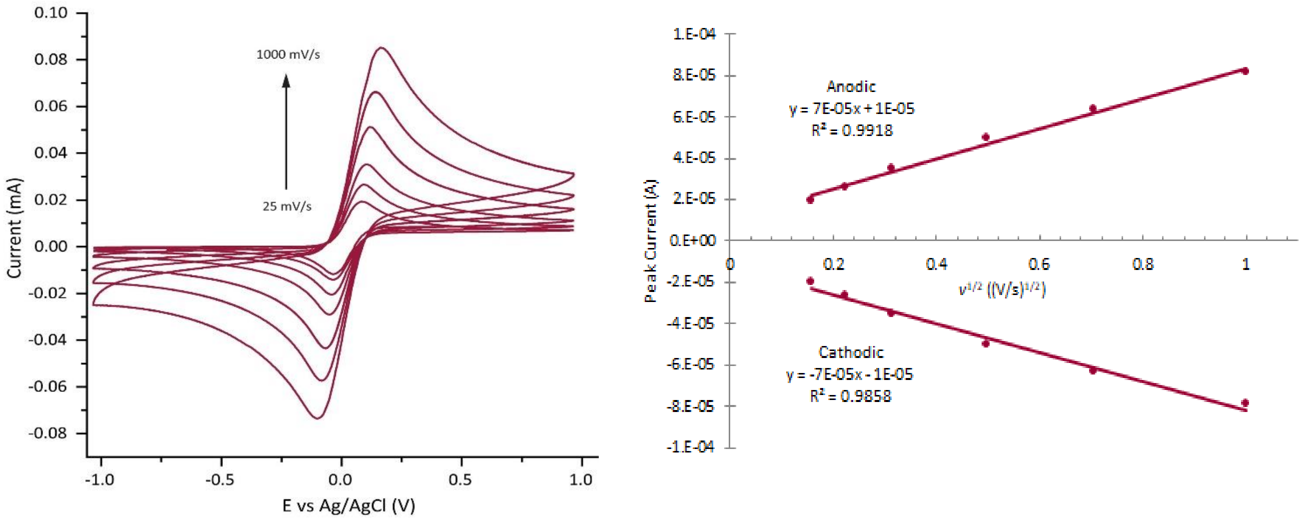

Figure 91. (Left) Cyclic voltammograms of 2 mM ^{Me10}**Fc** in DCM with 100 mM $[(n\text{Bu})_4\text{N}][\text{B}(\text{C}_6\text{F}_5)_4]$ as the supporting electrolyte at different scan rates. (Right) Randles-Sevcik plot of the CV data.

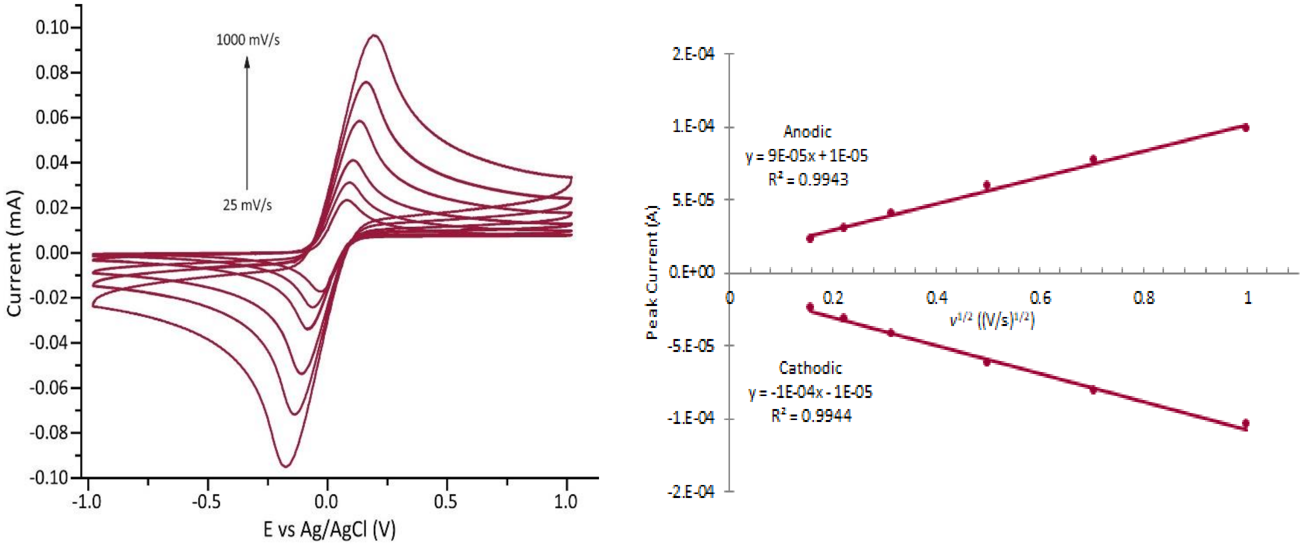

Figure 92. (Left) Cyclic voltammograms of 2 mM ^{Me10}**Fc** in DCM with 100 mM $[(n\text{Bu})_4\text{N}][\text{PF}_6]$ as the supporting electrolyte at different scan rates. (Right) Randles-Sevcik plot of the CV data.

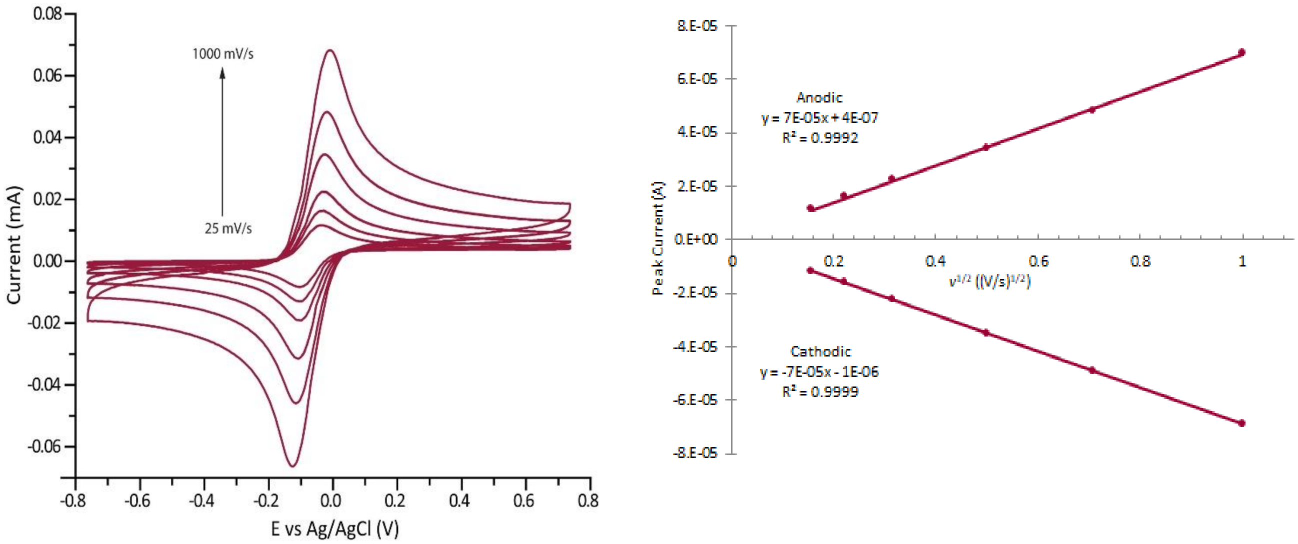

Figure 93. (Left) Cyclic voltammograms of 1 mM ^{Me10}**Fc** in MeCN with 100 mM [(*n*Bu)$_4$N][B(C$_6$F$_5$)$_4$] as the supporting electrolyte at different scan rates. (Right) Randles-Sevcik plot of the CV data.

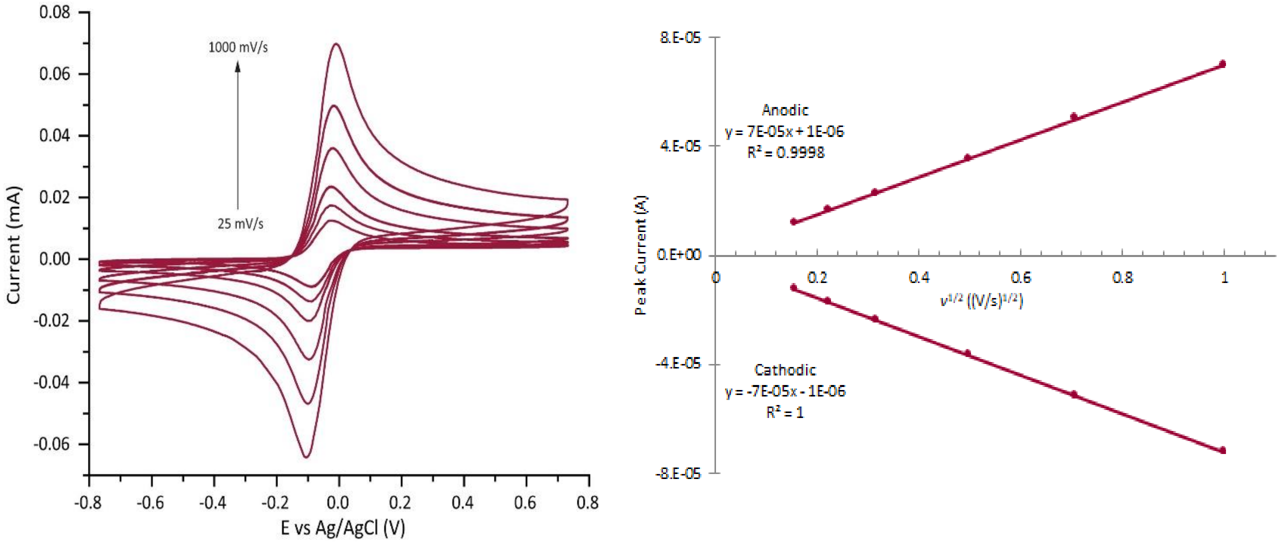

Figure 94. (Left) Cyclic voltammograms of 1 mM ^{Me10}**Fc** in MeCN with 100 mM [(*n*Bu)$_4$N][PF$_6$] as the supporting electrolyte at different scan rates. (Right) Randles-Sevcik plot of the CV data.

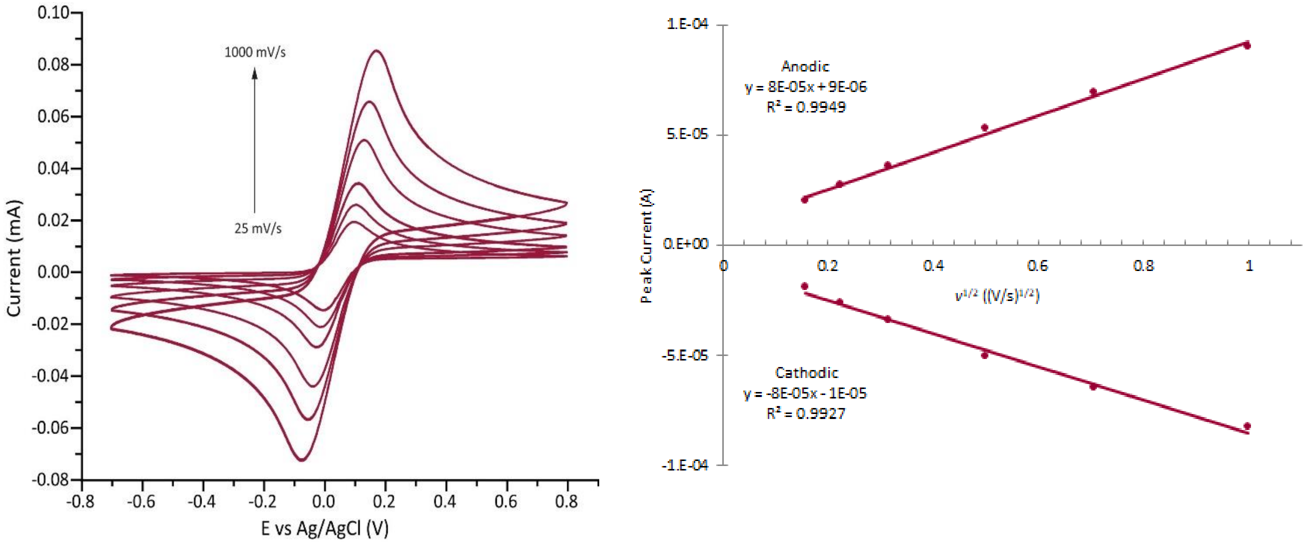

Figure 95. (Left) Cyclic voltammograms of 2 mM ^{Me10}**Fc** in MeTHF with 100 mM $[(n\mathrm{Bu})_4\mathrm{N}][\mathrm{B}(\mathrm{C}_6\mathrm{F}_5)_4]$ as the supporting electrolyte at different scan rates. (Right) Randles-Sevcik plot of the CV data.

ii. *1,1’*-Dimethylferrocene

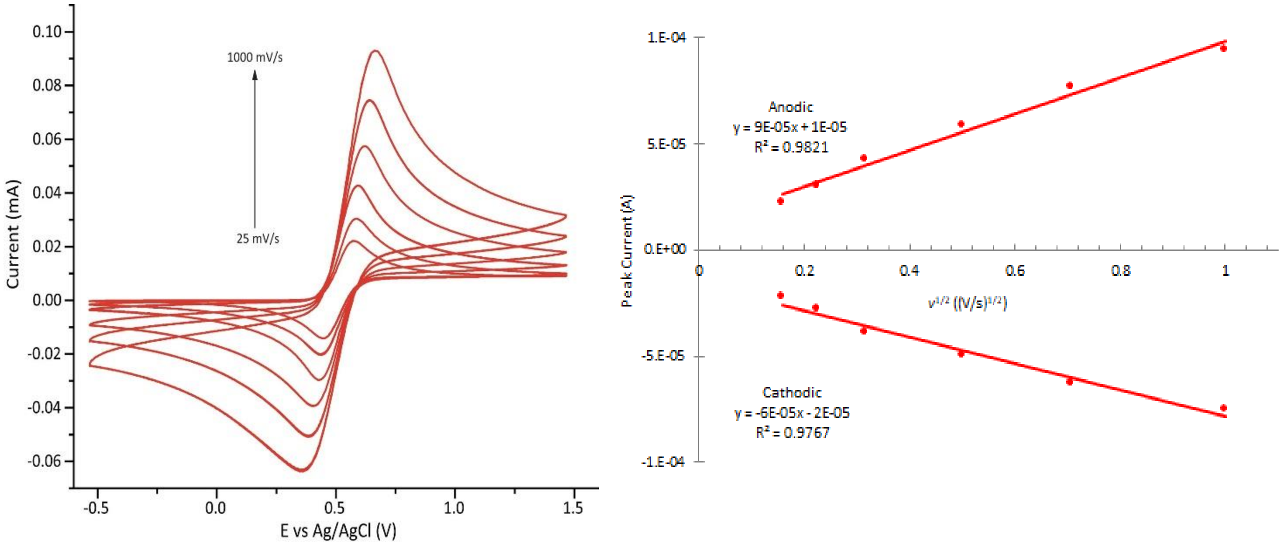

Figure 96. (Left) Cyclic voltammograms of 2 mM ^{Me2}**Fc** in DCM with 100 mM $[(n\mathrm{Bu})_4\mathrm{N}][\mathrm{B}(\mathrm{C}_6\mathrm{F}_5)_4]$ as the supporting electrolyte at different scan rates. (Right) Randles-Sevcik plot of the CV data.

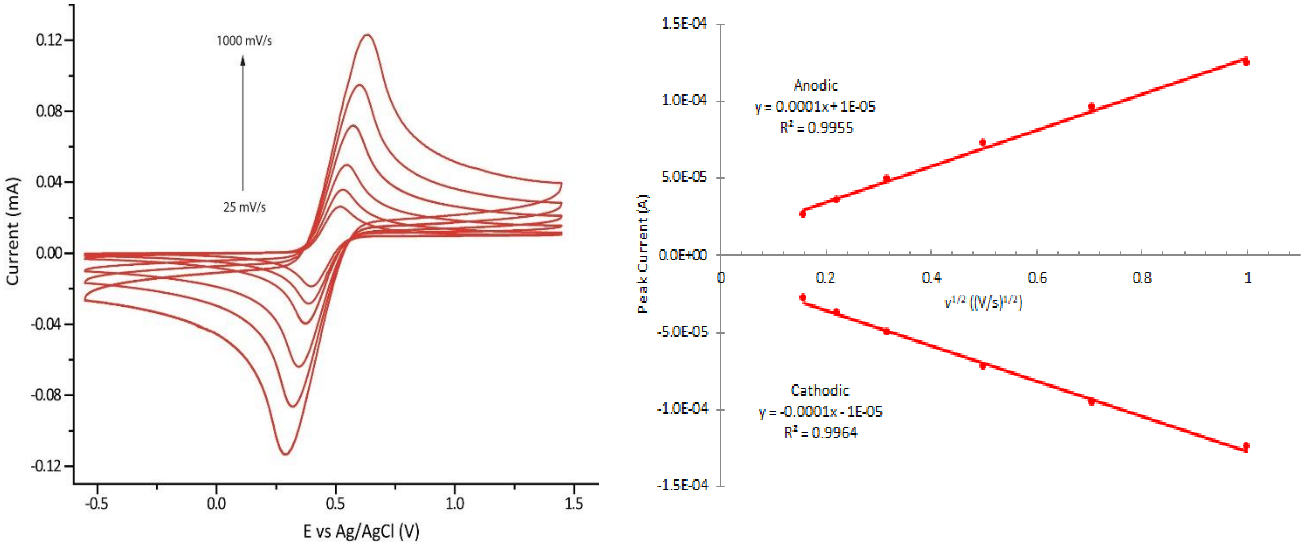

Figure 97. (Left) Cyclic voltammograms of 2 mM ^{Me2}**Fc** in DCM with 100 mM [(nBu)$_4$N][PF$_6$] as the supporting electrolyte at different scan rates. (Right) Randles-Sevcik plot of the CV data.

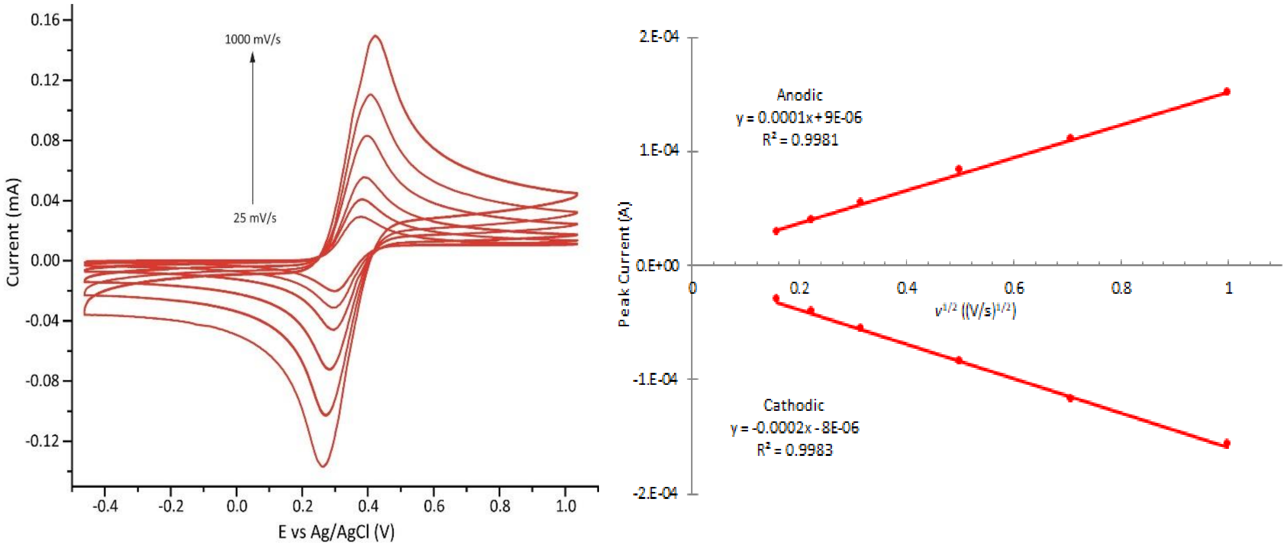

Figure 98. (A) Cyclic voltammograms of 2 mM ^{Me2}**Fc** in MeCN with 100 mM [(nBu)$_4$N][B(C$_6$F$_5$)$_4$] as the supporting electrolyte at different scan rates. (B) Randles-Sevcik plot of the CV data.

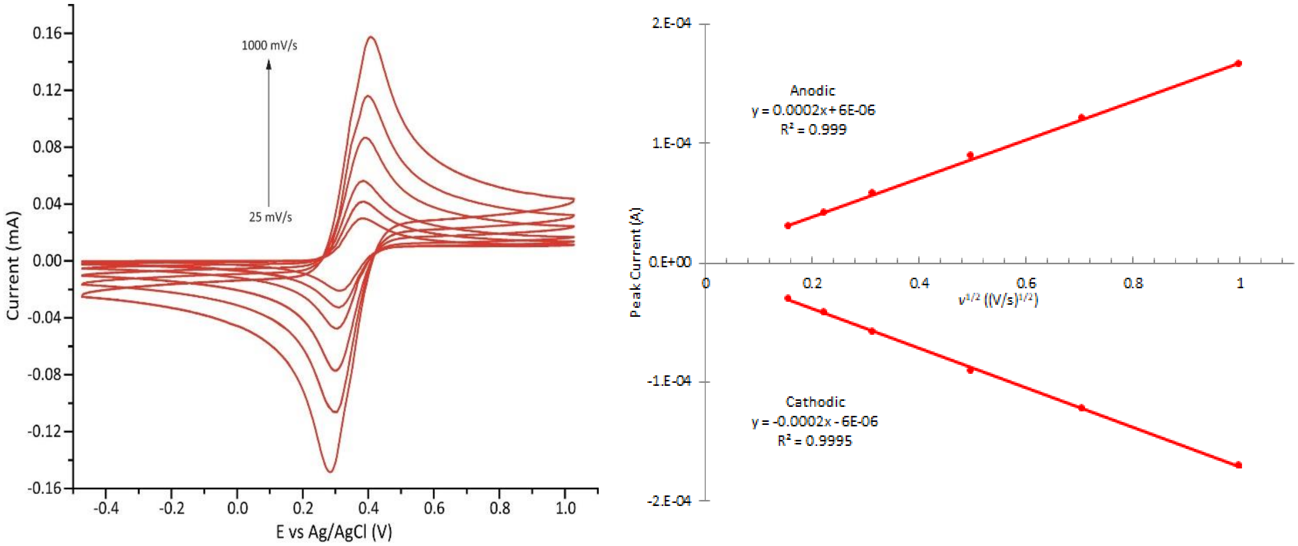

Figure 99. (Left) Cyclic voltammograms of 2 mM ^{Me2}**Fc** in MeCN with 100 mM $[(n\text{Bu})_4\text{N}][\text{PF}_6]$ as the supporting electrolyte at different scan rates. (Right) Randles-Sevcik plot of the CV data.

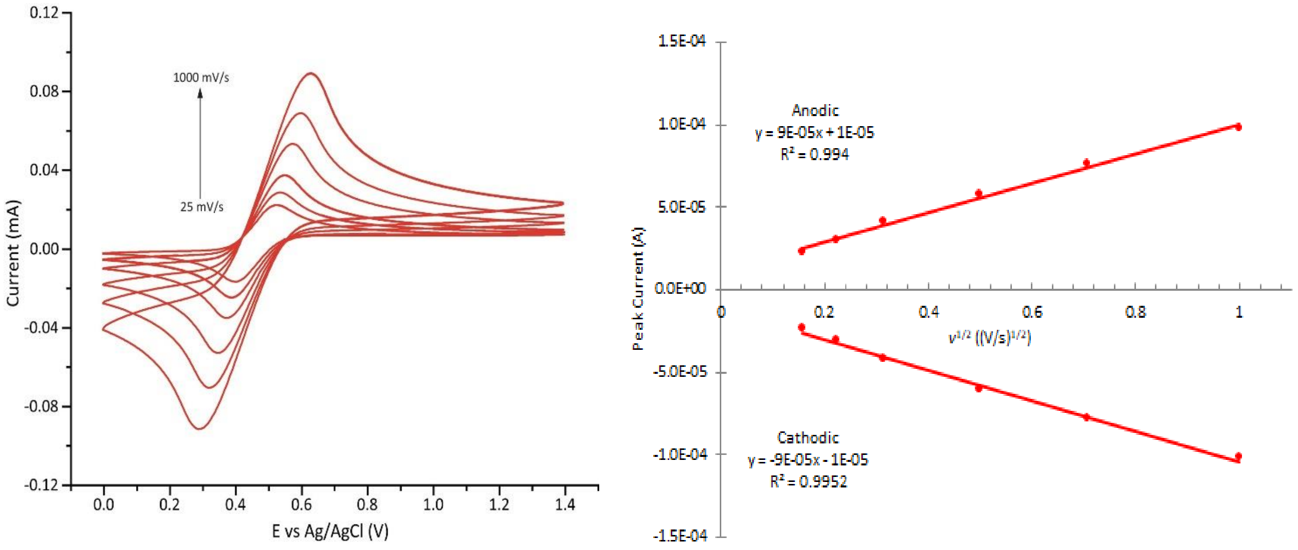

Figure 100. (Left) Cyclic voltammograms of 2 mM ^{Me2}**Fc** in MeTHF with 100 mM $[(n\text{Bu})_4\text{N}][\text{B}(\text{C}_6\text{F}_5)_4]$ as the supporting electrolyte at different scan rates. (Right) Randles-Sevcik plot of the CV data.

iii. *n*-Butylferrocene

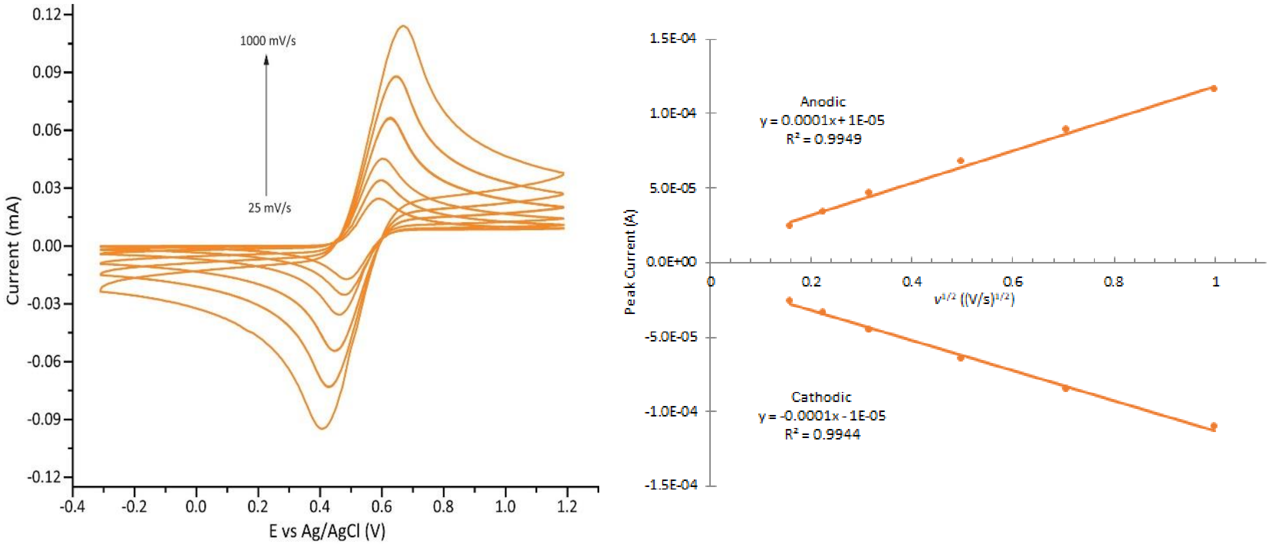

Figure 101. (Left) Cyclic voltammograms of 2 mM ^{nBu}**Fc** in DCM with 100 mM $[(n\text{Bu})_4\text{N}][\text{B}(\text{C}_6\text{F}_5)_4]$ as the supporting electrolyte at different scan rates. (Right) Randles-Sevcik plot of the CV data.

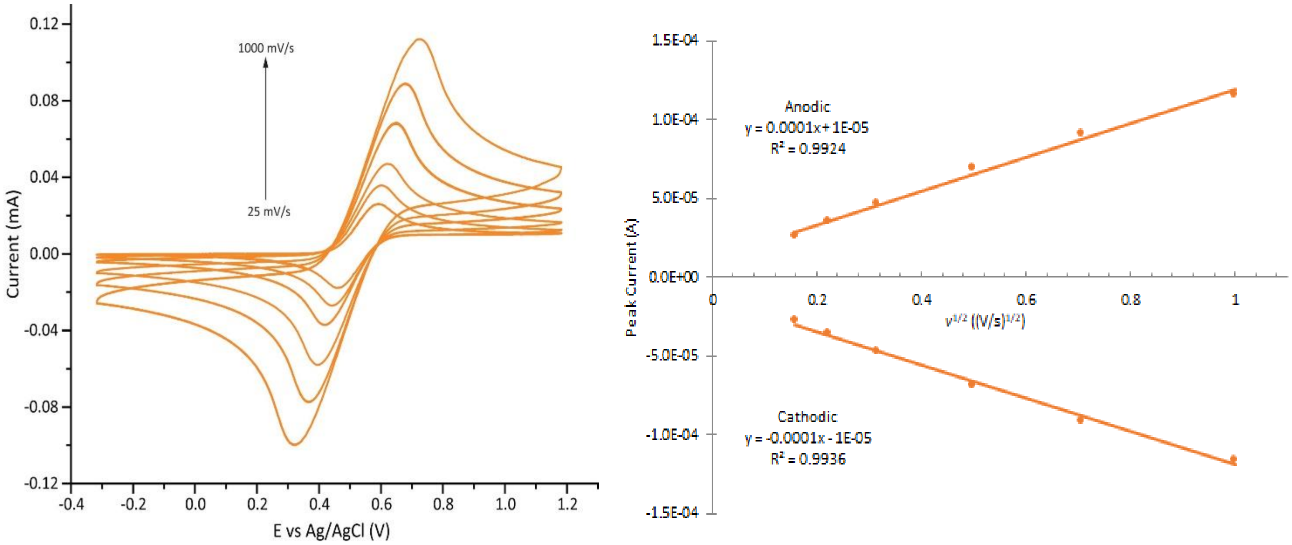

Figure 102. (Left) Cyclic voltammograms of 2 mM ^{nBu}**Fc** in DCM with 100 mM $[(n\text{Bu})_4\text{N}][\text{PF}_6]$ as the supporting electrolyte at different scan rates. (Right) Randles-Sevcik plot of the CV data.

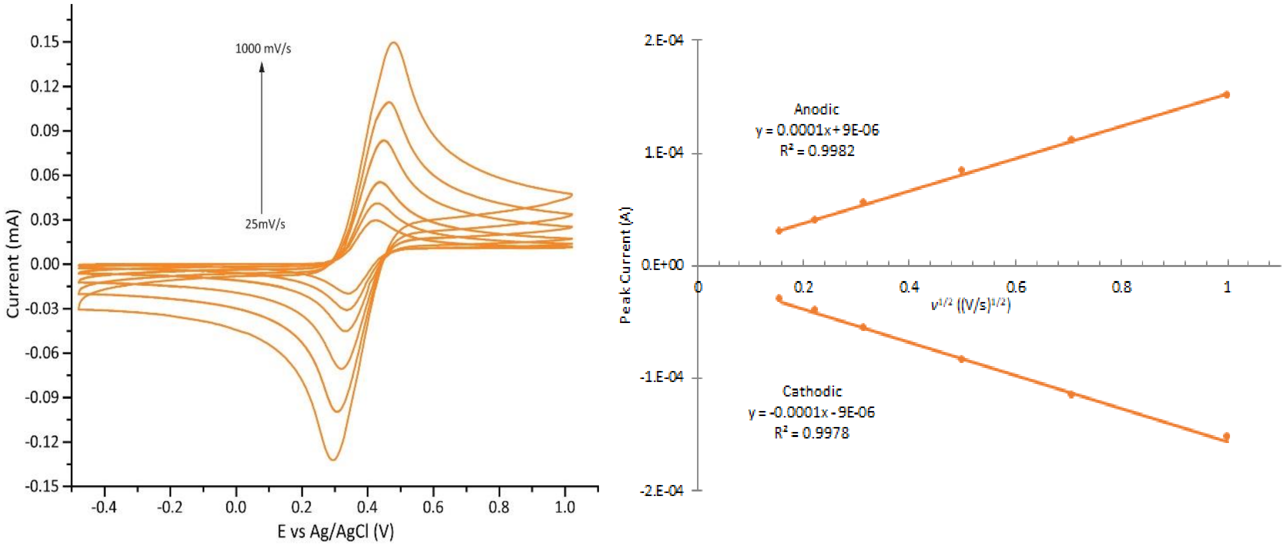

Figure 103. (Left) Cyclic voltammograms of 2 mM ^{nBu}**Fc** in MeCN with 100 mM $[(n\text{Bu})_4\text{N}][\text{B}(\text{C}_6\text{F}_5)_4]$ as the supporting electrolyte at different scan rates. (Right) Randles-Sevcik plot of the CV data.

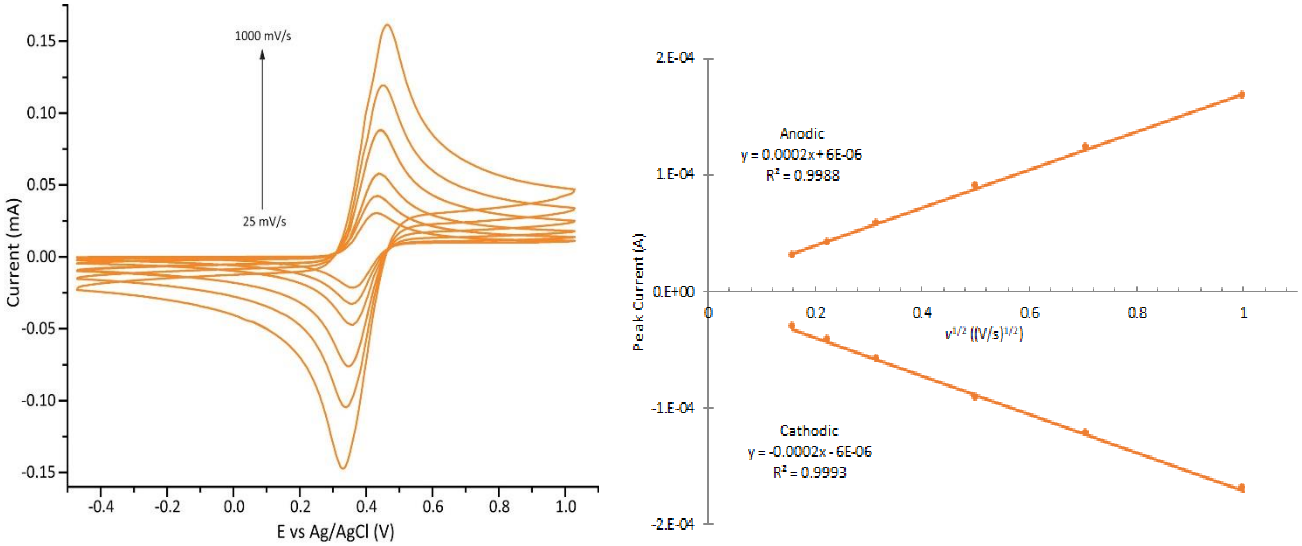

Figure 104. (Left) Cyclic voltammograms of 2 mM ^{nBu}**Fc** in MeCN with 100 mM $[(n\text{Bu})_4\text{N}][\text{PF}_6]$ as the supporting electrolyte at different scan rates. (Right) Randles-Sevcik plot of the CV data.

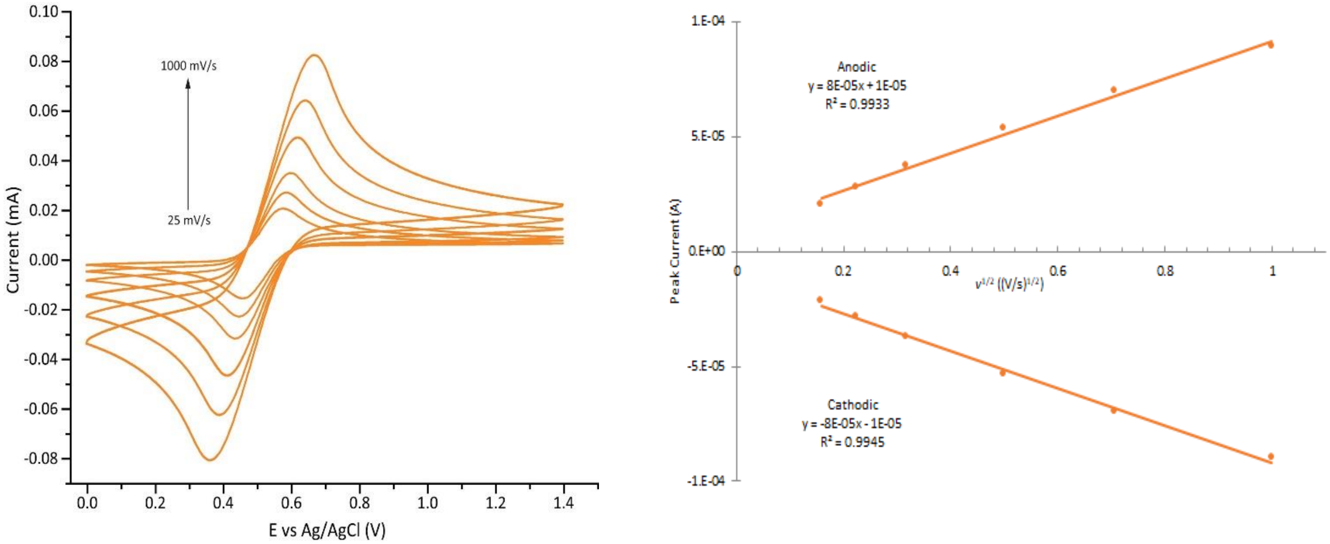

Figure 105. (Left) Cyclic voltammograms of 2 mM ^{nBu}**Fc** in MeTHF with 100 mM [(*n*Bu)$_4$N][B(C$_6$F$_5$)$_4$] as the supporting electrolyte at different scan rates. (Right) Randles-Sevcik plot of the CV data.

iv. Ferrocene

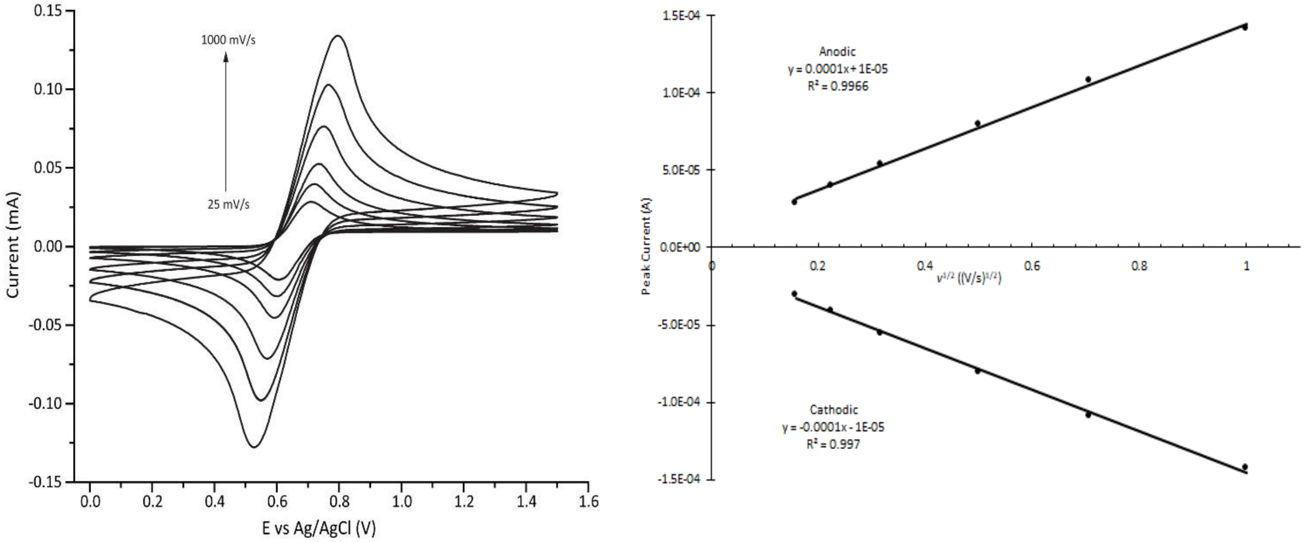

Figure 106. (Left) Cyclic voltammograms of 2 mM **Fc** in DCM with 100 mM [(*n*Bu)$_4$N][B(C$_6$F$_5$)$_4$] as the supporting electrolyte at different scan rates. (Right) Randles-Sevcik plot of the CV data.

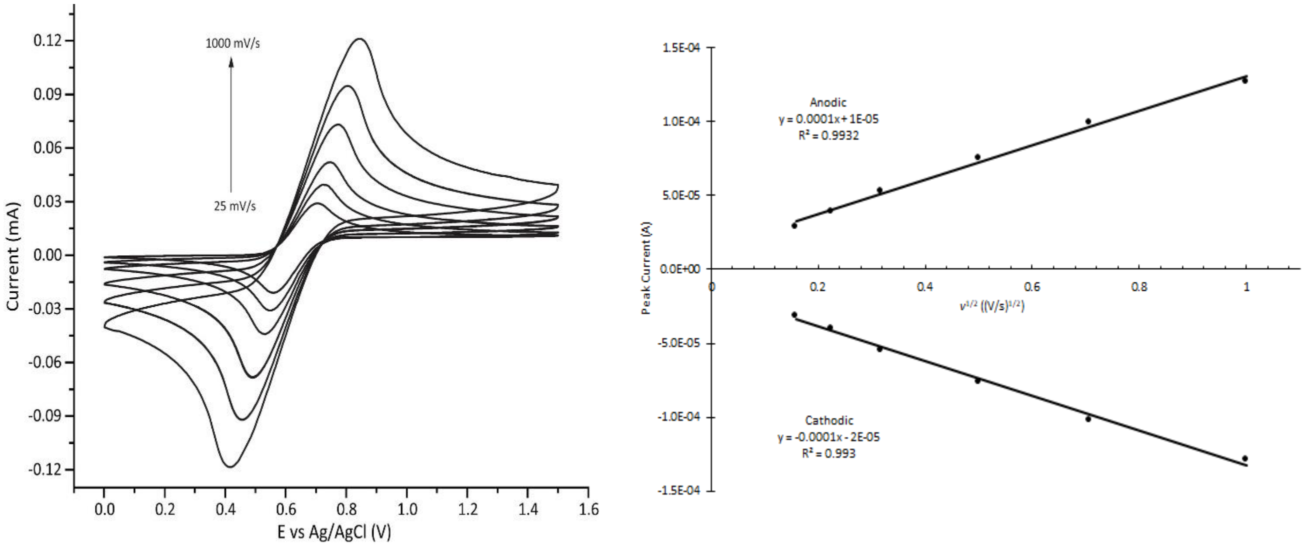

Figure 107. (Left) Cyclic voltammograms of 2 mM **Fc** in DCM with 100 mM $[(n\mathrm{Bu})_4\mathrm{N}][\mathrm{PF}_6]$ as the supporting electrolyte at different scan rates. (Right) Randles-Sevcik plot of the CV data.

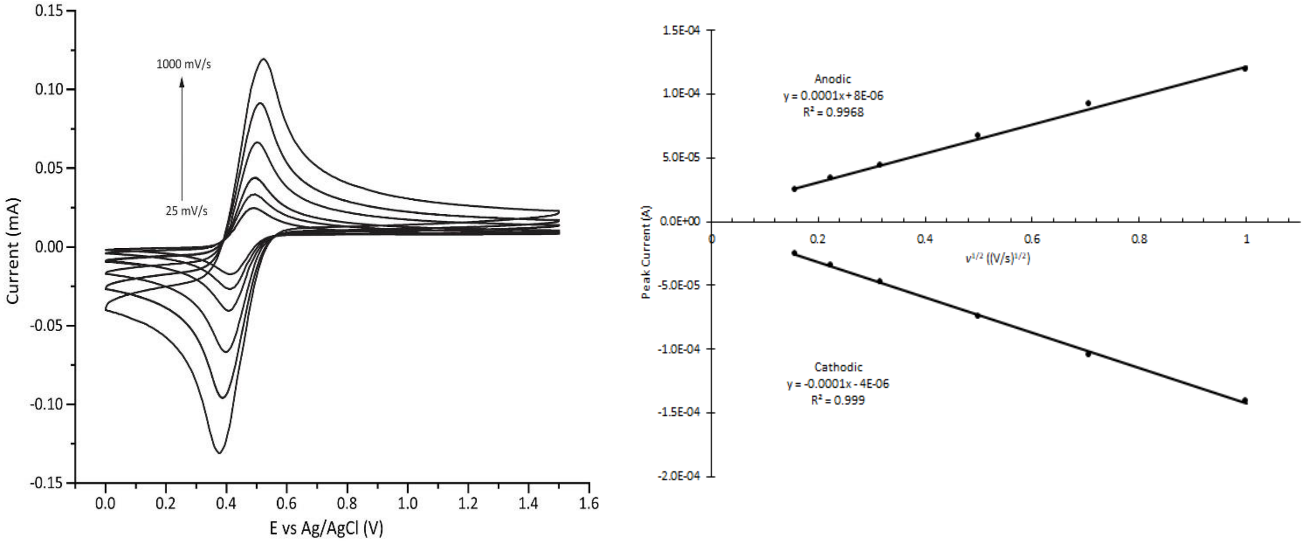

Figure 108. (Left) Cyclic voltammograms of 2 mM **Fc** in MeCN with 100 mM $[(n\mathrm{Bu})_4\mathrm{N}][\mathrm{B}(\mathrm{C}_6\mathrm{F}_5)_4]$ as the supporting electrolyte at different scan rates. (Right) Randles-Sevcik plot of the CV data.

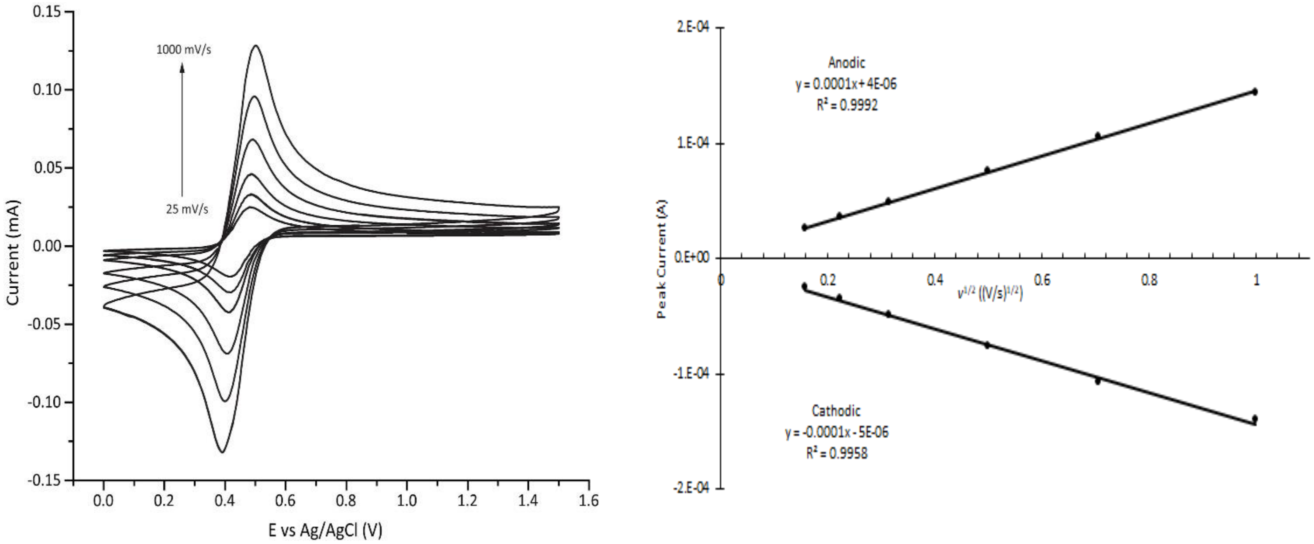

Figure 109. (Left) Cyclic voltammograms of 2 mM **Fc** in MeCN with 100 mM $[(n\text{Bu})_4\text{N}][\text{PF}_6]$ as the supporting electrolyte at different scan rates. (Right) Randles-Sevcik plot of the CV data.

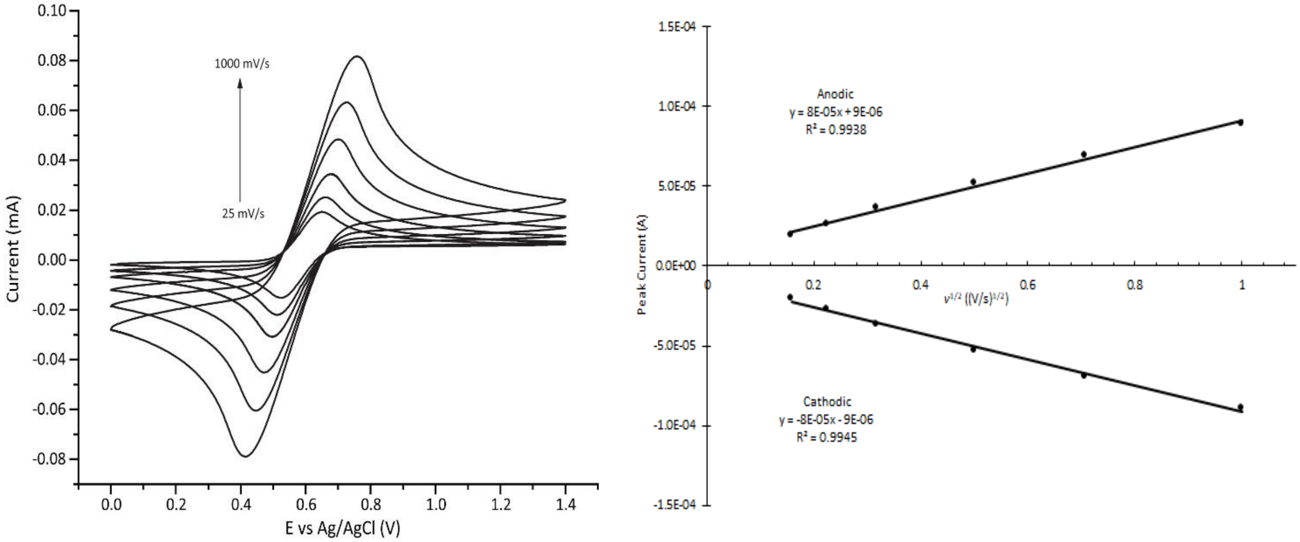

Figure 110. (Left) Cyclic voltammograms of 2 mM **Fc** in MeTHF with 100 mM $[(n\text{Bu})_4\text{N}][\text{B}(\text{C}_6\text{F}_5)_4]$ as the supporting electrolyte at different scan rates. (Right) Randles-Sevcik plot of the CV data.

v. *1*-Bromoferrocene

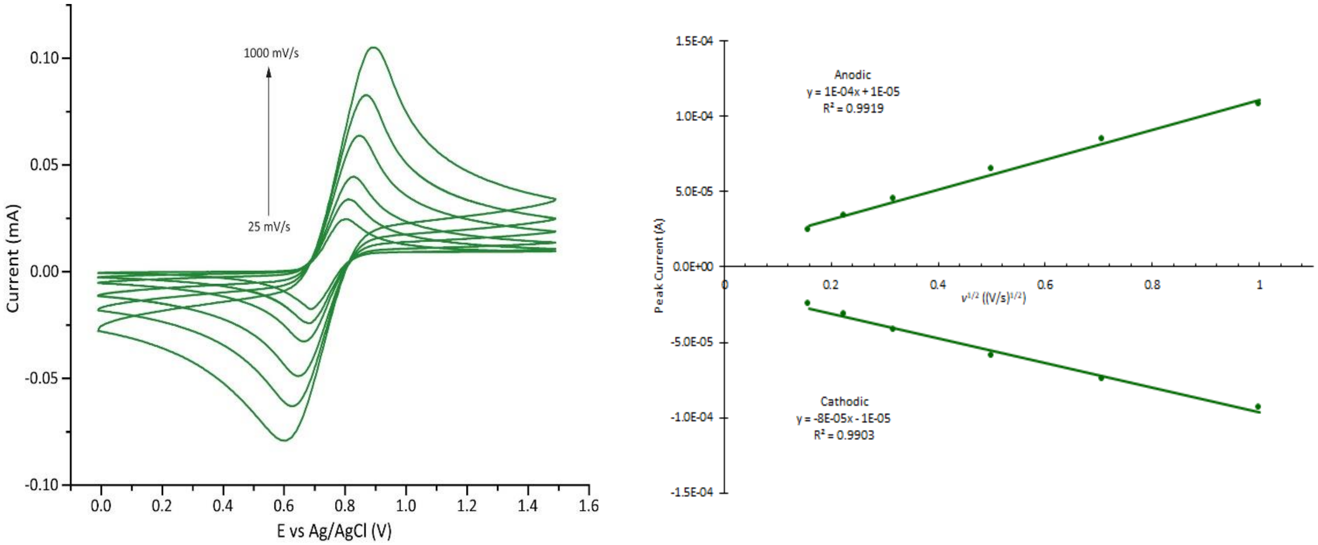

Figure 111. (Left) Cyclic voltammograms of 2 mM ^{Br}**Fc** in DCM with 100 mM $[(n\text{Bu})_4\text{N}][\text{B}(\text{C}_6\text{F}_5)_4]$ as the supporting electrolyte at different scan rates. (Right) Randles-Sevcik plot of the CV data.

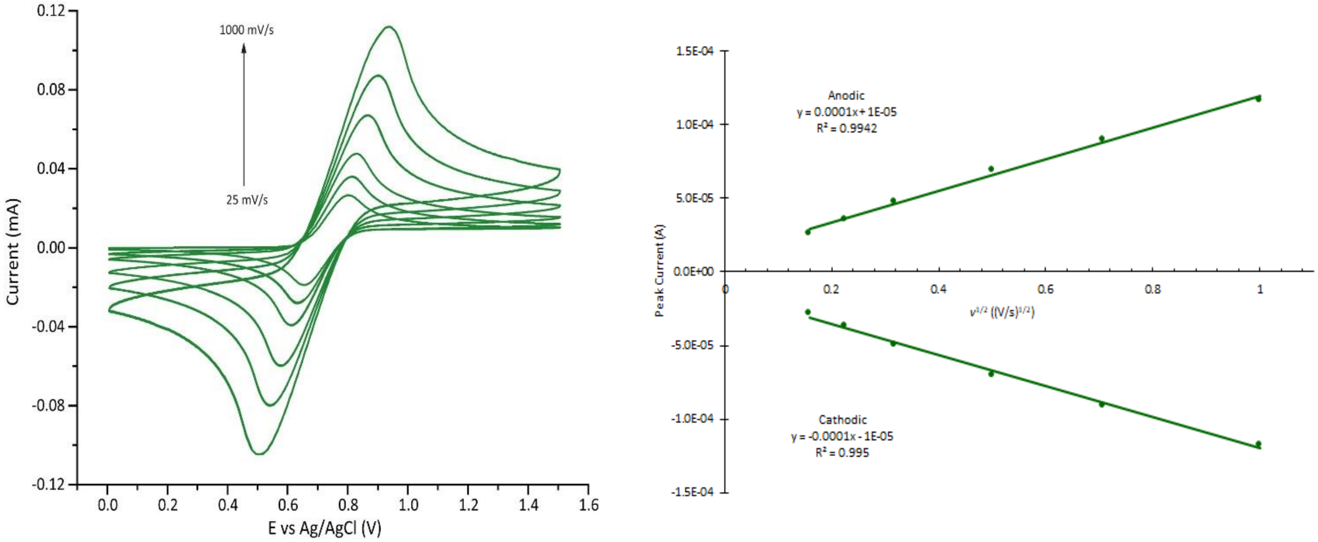

Figure 112. (Left) Cyclic voltammograms of 2 mM ^{Br}**Fc** in DCM with 100 mM $[(n\text{Bu})_4\text{N}][\text{PF}_6]$ as the supporting electrolyte at different scan rates. (Right) Randles-Sevcik plot of the CV data.

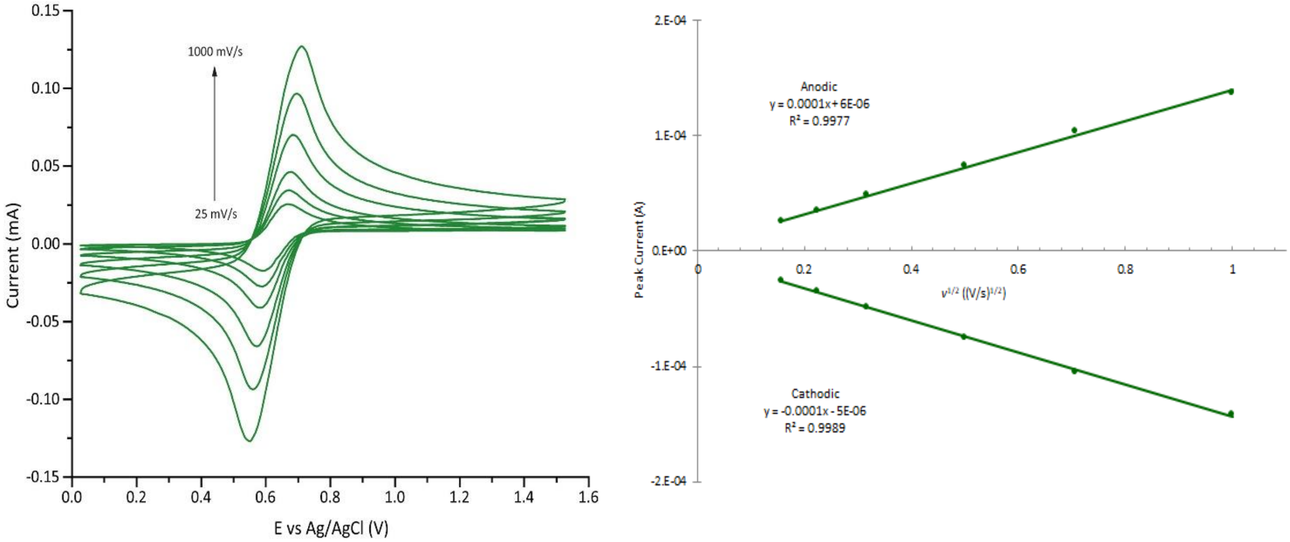

Figure 113. (Left) Cyclic voltammograms of 2 mM ^{Br}**Fc** in MeCN with 100 mM $[(n\mathrm{Bu})_4\mathrm{N}][\mathrm{B}(\mathrm{C}_6\mathrm{F}_5)_4]$ as the supporting electrolyte at different scan rates. (Right) Randles-Sevcik plot of the CV data.

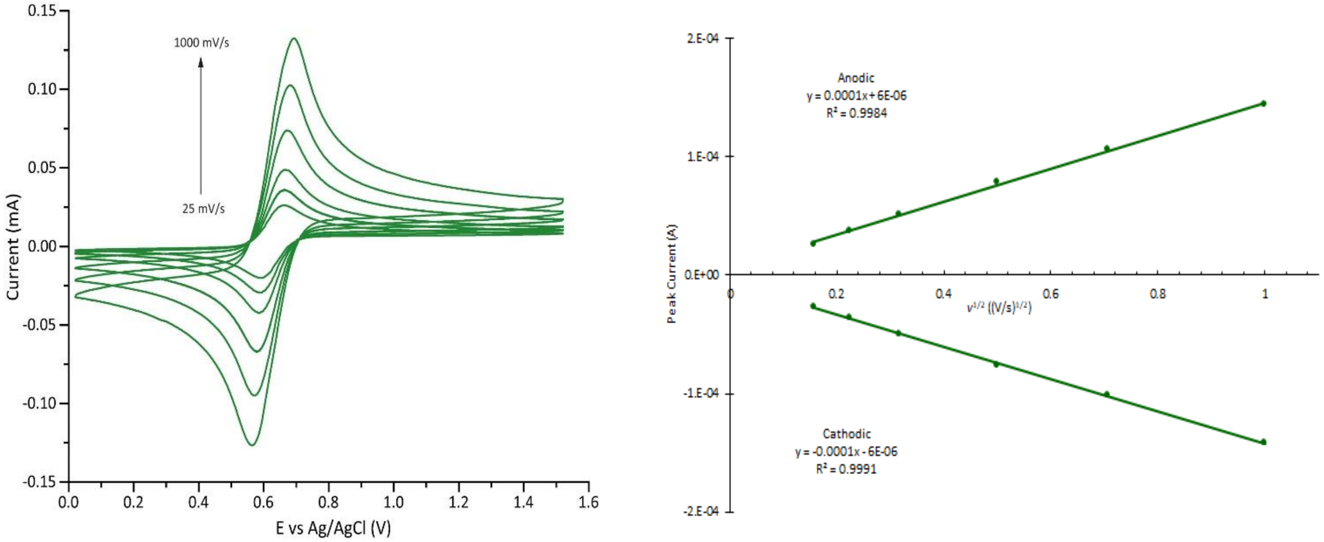

Figure 114. (Left) Cyclic voltammograms of 2 mM ^{Br}**Fc** in MeCN with 100 mM $[(n\mathrm{Bu})_4\mathrm{N}][\mathrm{PF}_6]$ as the supporting electrolyte at different scan rates. (Right) Randles-Sevcik plot of the CV data.

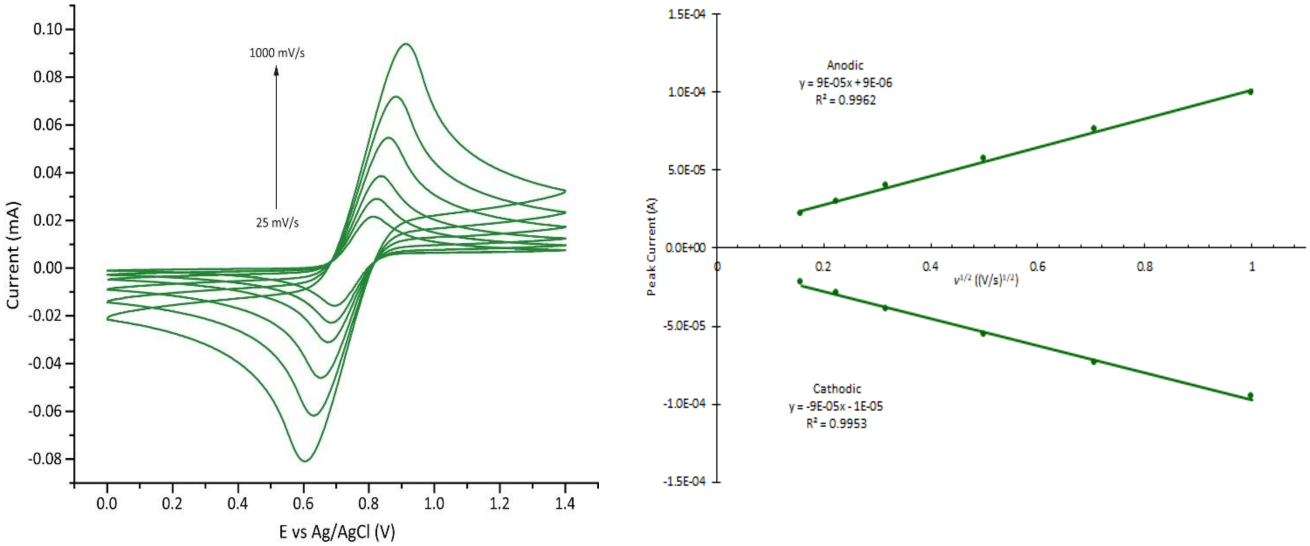

Figure 115. (Left) Cyclic voltammograms of 2 mM ^{Br}**Fc** in MeTHF with 100 mM $[(n\text{Bu})_4\text{N}][\text{B}(\text{C}_6\text{F}_5)_4]$ as the supporting electrolyte at different scan rates. (Right) Randles-Sevcik plot of the CV data.

vi. *1*-Acetylferrocene

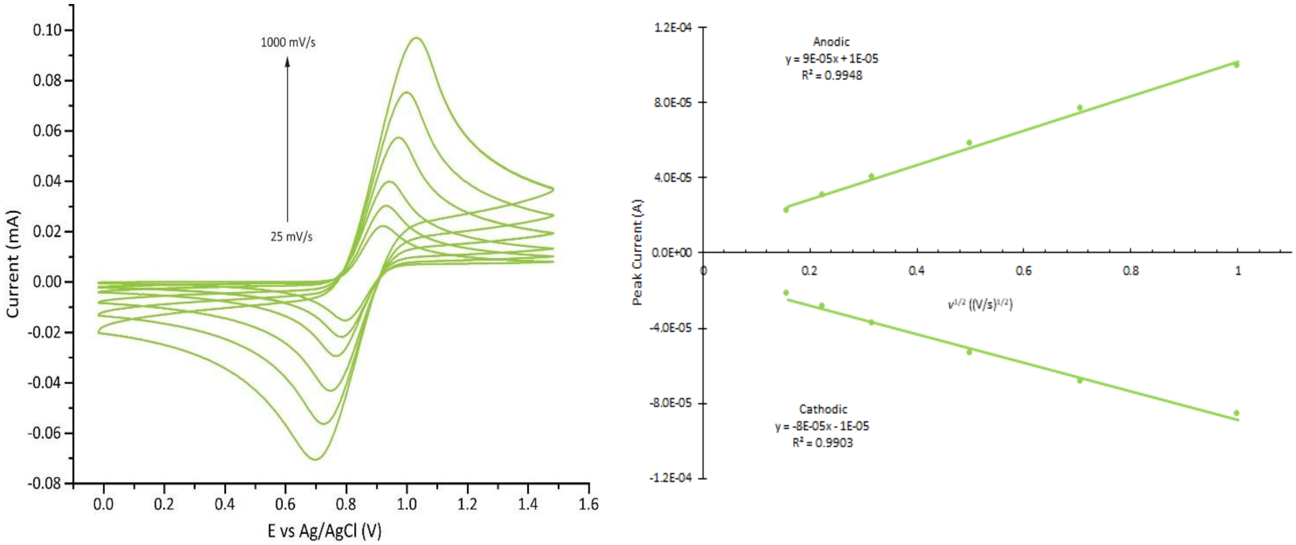

Figure 116. (Left) Cyclic voltammograms of 2 mM ^{Ac}**Fc** in DCM with 100 mM $[(n\text{Bu})_4\text{N}][\text{B}(\text{C}_6\text{F}_5)_4]$ as the supporting electrolyte at different scan rates. (Right) Randles-Sevcik plot of the CV data.

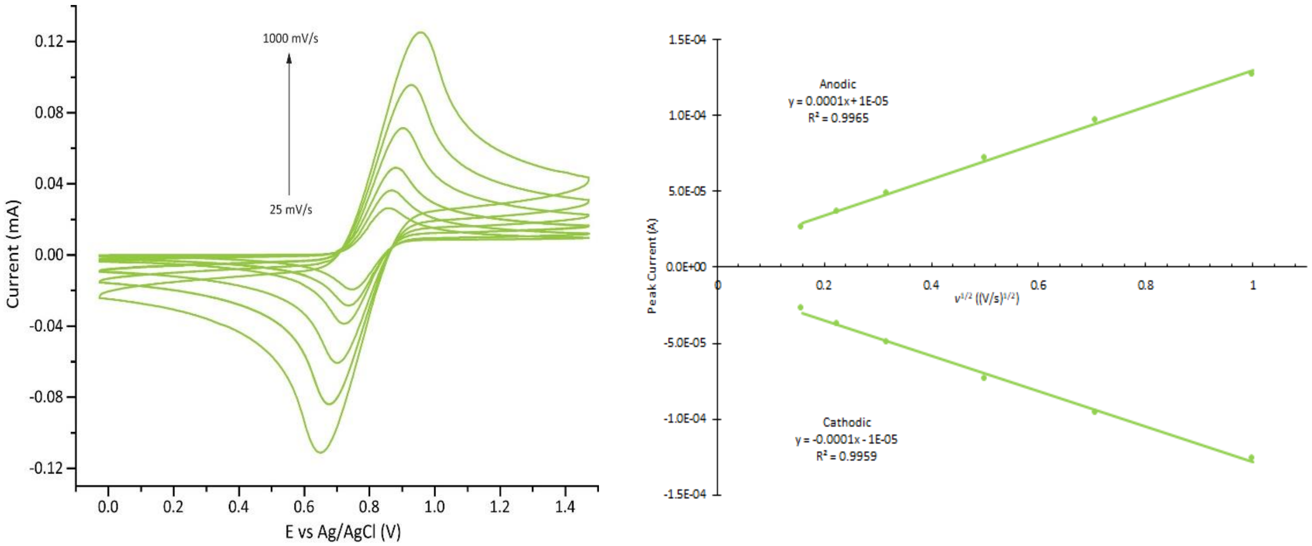

Figure 117. (Left) Cyclic voltammograms of 2 mM ^{Ac}**Fc** in DCM with 100 mM [(*n*Bu)$_4$N][PF$_6$] as the supporting electrolyte at different scan rates. (Right) Randles-Sevcik plot of the CV data.

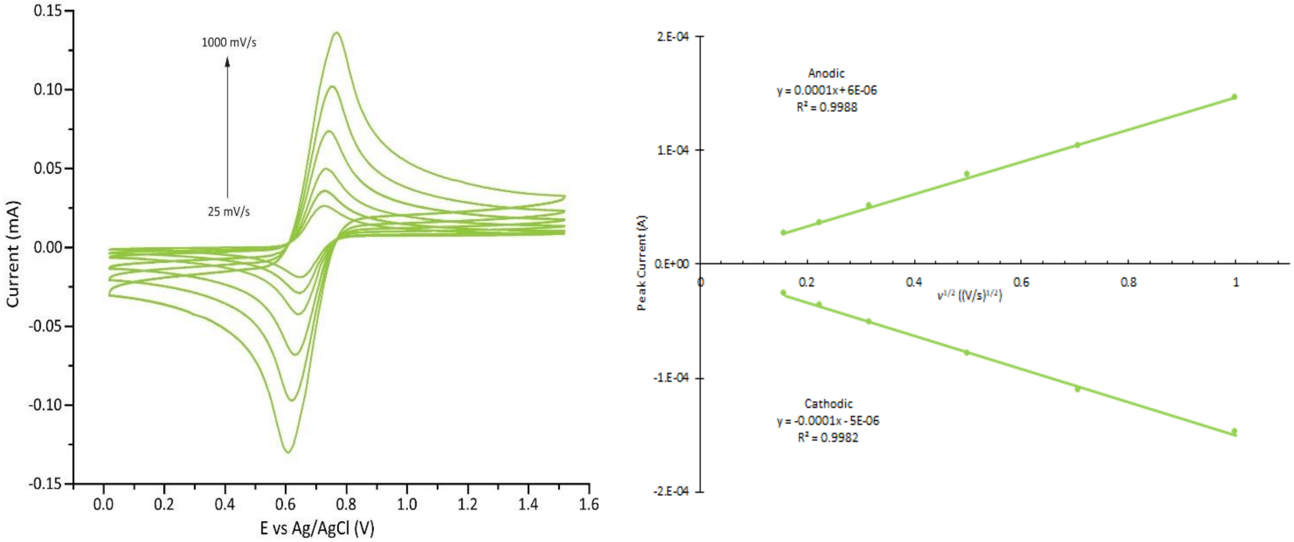

Figure 118. (Left) Cyclic voltammograms of 2 mM ^{Ac}**Fc** in MeCN with 100 mM [(*n*Bu)$_4$N][B(C$_6$F$_5$)$_4$] as the supporting electrolyte at different scan rates. (Right) Randles-Sevcik plot of the CV data.

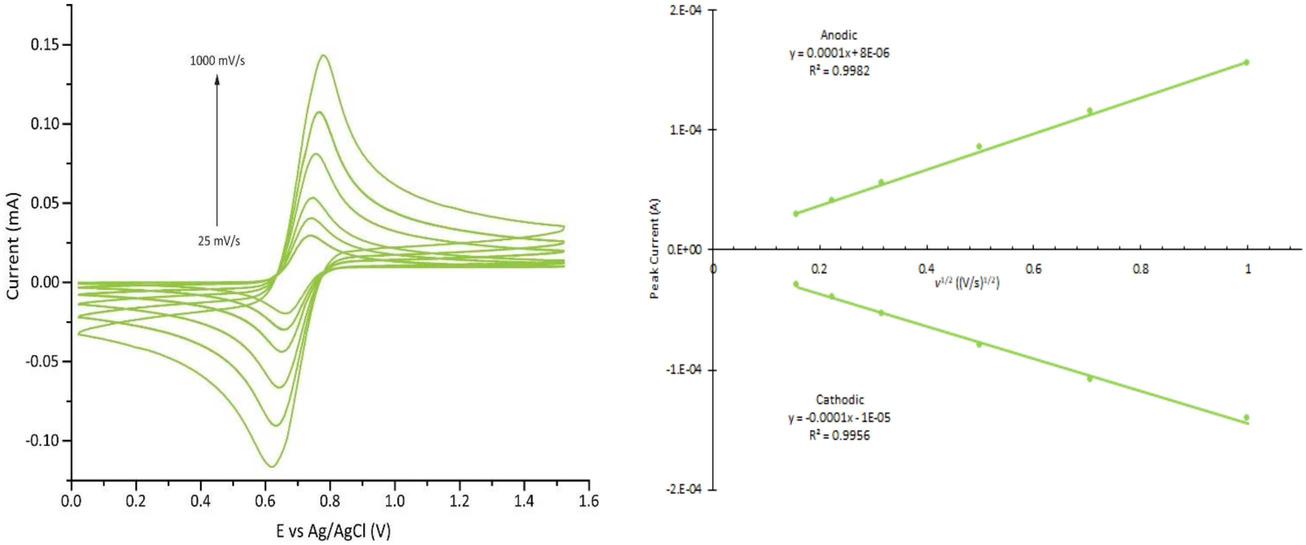

Figure 119. (Left) Cyclic voltammograms of 2 mM ^{Ac}**Fc** in MeCN with 100 mM $[(n\mathrm{Bu})_4\mathrm{N}][\mathrm{PF}_6]$ as the supporting electrolyte at different scan rates. (Right) Randles-Sevcik plot of the CV data.

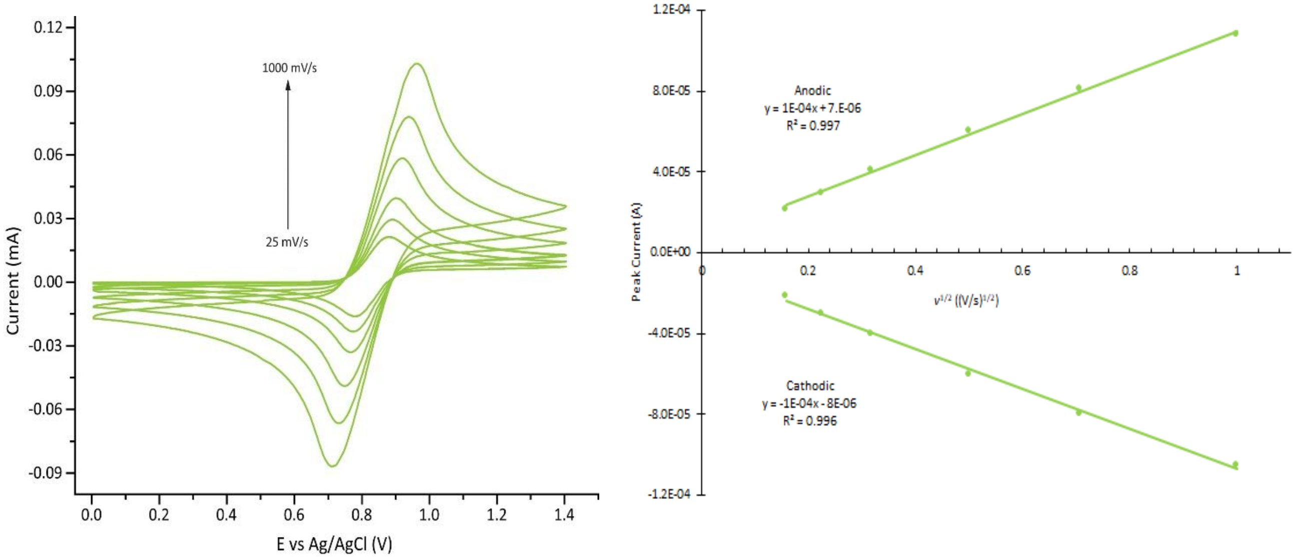

Figure 120. (Left) Cyclic voltammograms of 2 mM ^{Ac}**Fc** in MeTHF with 100 mM $[(n\mathrm{Bu})_4\mathrm{N}][\mathrm{B}(\mathrm{C}_6\mathrm{F}_5)_4]$ as the supporting electrolyte at different scan rates. (Right) Randles-Sevcik plot of the CV data.

vii. *1*-Benzoylferrocene

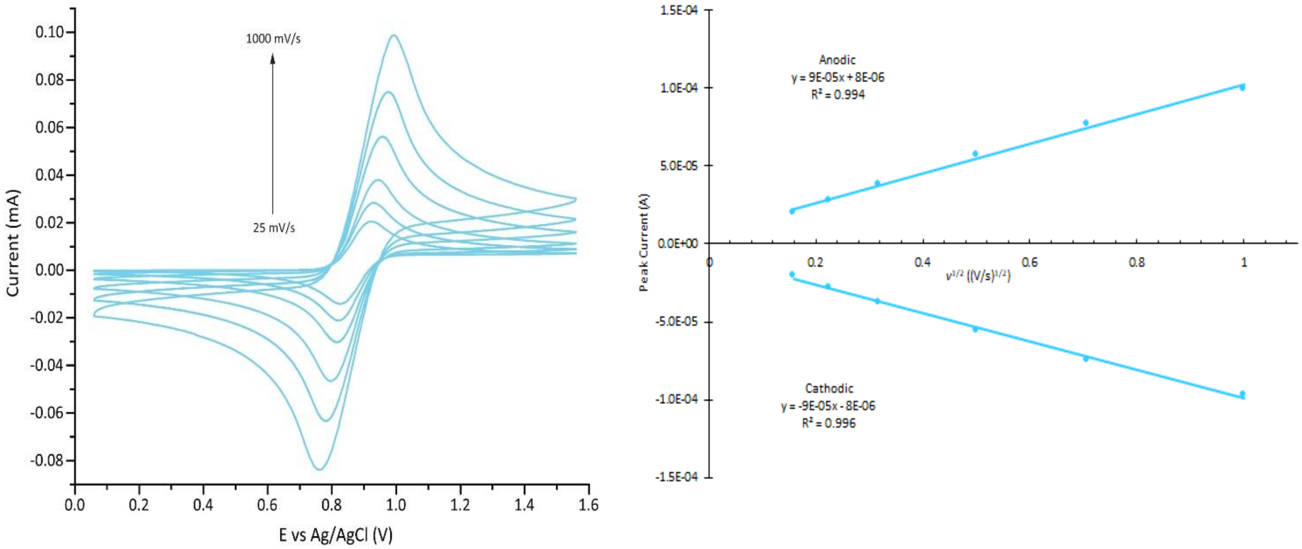

Figure 121. (Left) Cyclic voltammograms of 2 mM ^{Bz}**Fc** in DCM with 100 mM $[(n\mathrm{Bu})_4\mathrm{N}][\mathrm{B}(\mathrm{C}_6\mathrm{F}_5)_4]$ as the supporting electrolyte at different scan rates. (Right) Randles-Sevcik plot of the CV data.

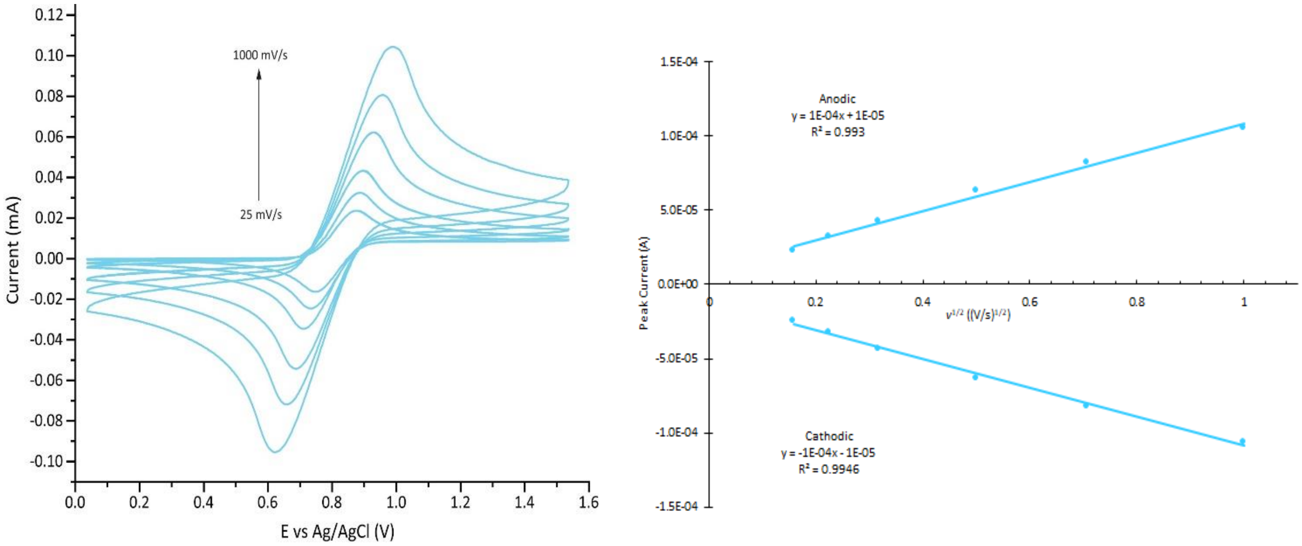

Figure 122. (Left) Cyclic voltammograms of 2 mM ^{Bz}**Fc** in DCM with 100 mM $[(n\mathrm{Bu})_4\mathrm{N}][\mathrm{PF}_6]$ as the supporting electrolyte at different scan rates. (Right) Randles-Sevcik plot of the CV data.

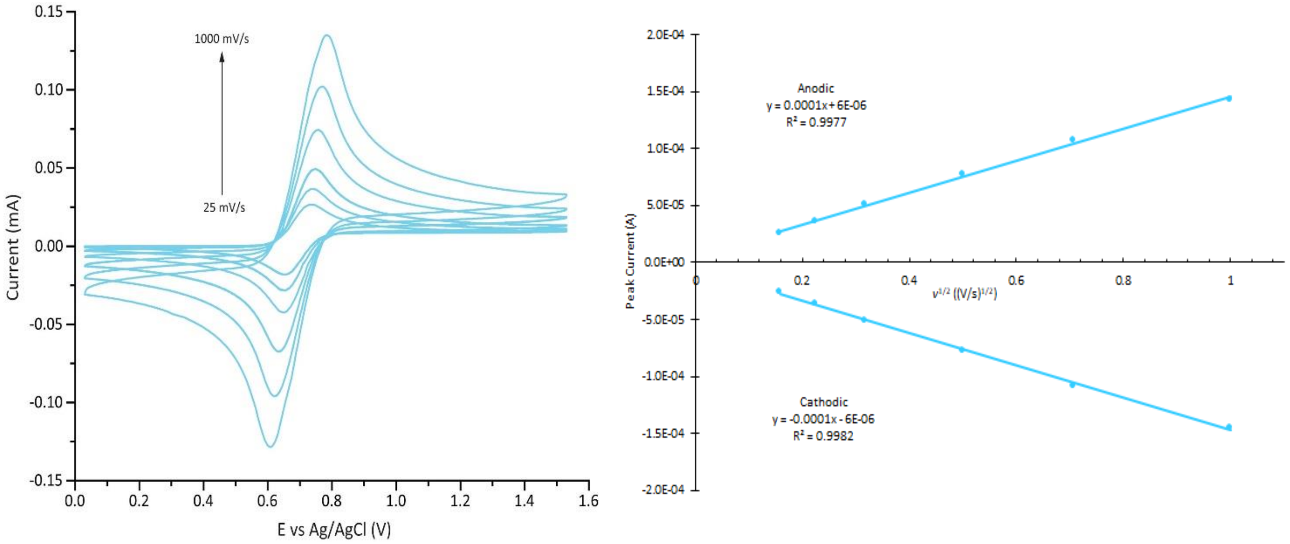

Figure 123. (Left) Cyclic voltammograms of 2 mM ^{Bz}**Fc** in MeCN with 100 mM $[(n\text{Bu})_4\text{N}][\text{B}(\text{C}_6\text{F}_5)_4]$ as the supporting electrolyte at different scan rates. (Right) Randles-Sevcik plot of the CV data.

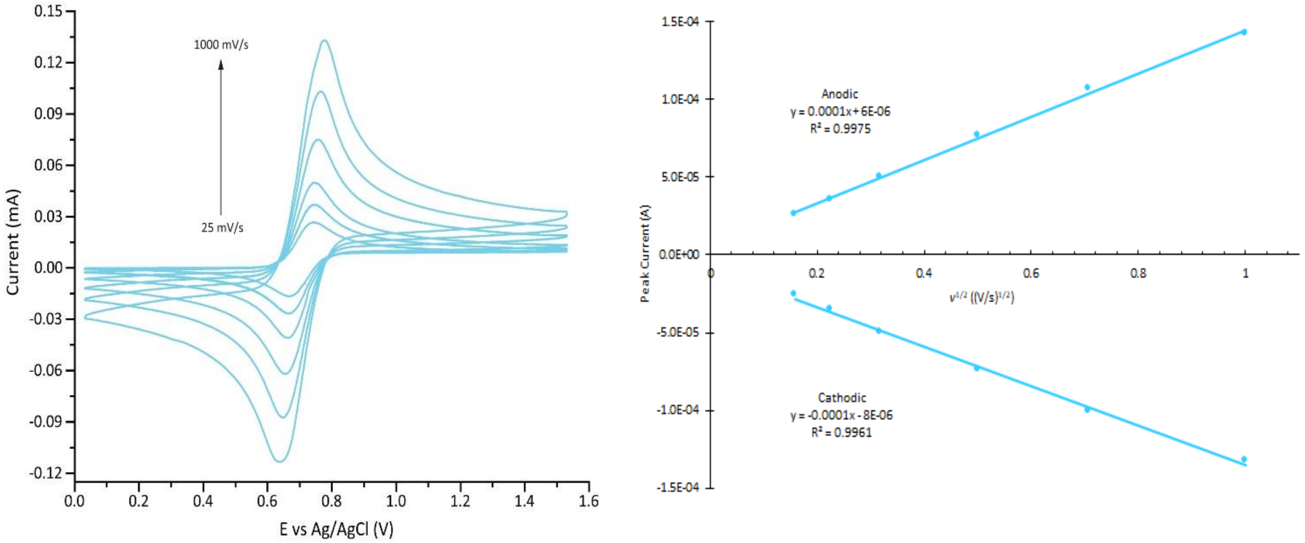

Figure 124. (Left) Cyclic voltammograms of 2 mM ^{Bz}**Fc** in MeCN with 100 mM $[(n\text{Bu})_4\text{N}][\text{PF}_6]$ as the supporting electrolyte at different scan rates. (Right) Randles-Sevcik plot of the CV data.

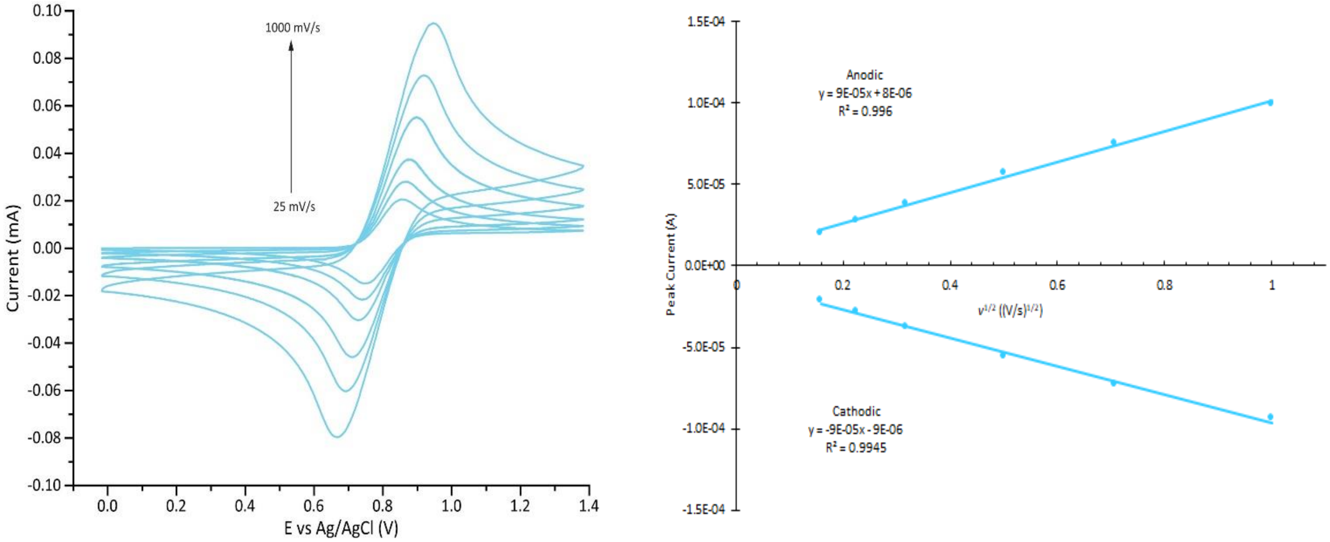

Figure 125. (Left) Cyclic voltammograms of 2 mM ^{Bz}**Fc** in MeTHF with 100 mM [(*n*Bu)$_4$N][B(C$_6$F$_5$)$_4$] as the supporting electrolyte at different scan rates. (Right) Randles-Sevcik plot of the CV data.

viii. *1,1'*-Dibromoferrocene

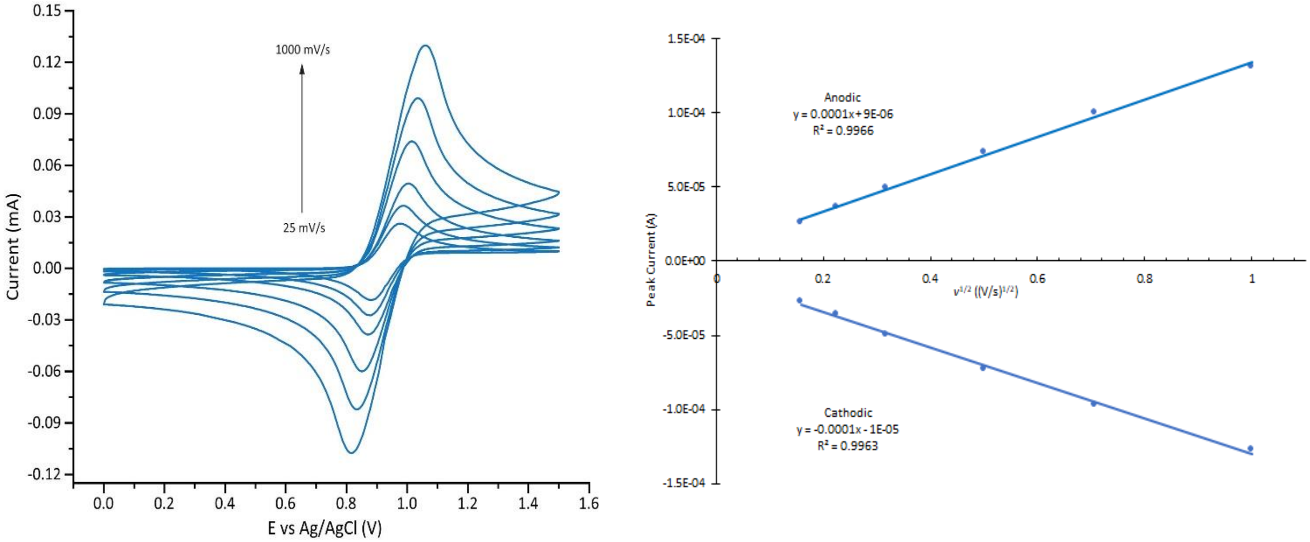

Figure 126. (Left) Cyclic voltammograms of 2 mM ^{Br2}**Fc** in DCM with 100 mM [(*n*Bu)$_4$N][B(C$_6$F$_5$)$_4$] as the supporting electrolyte at different scan rates. (Right) Randles-Sevcik plot of the CV data.

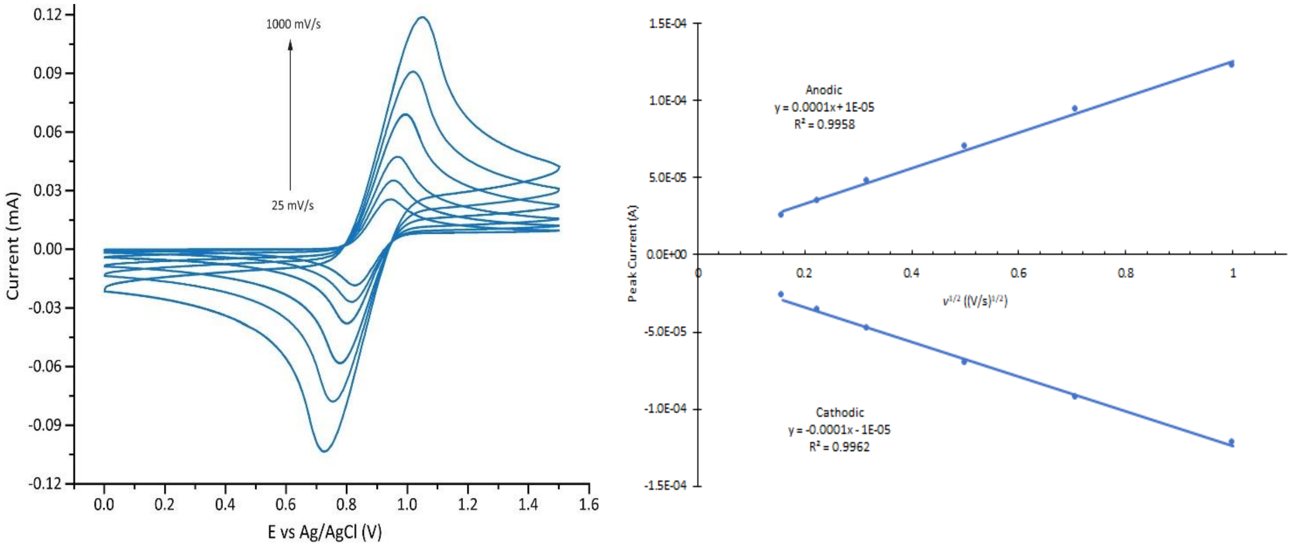

Figure 127. (Left) Cyclic voltammograms of 2 mM ^{Br2}**Fc** in DCM with 100 mM [(*n*Bu)$_4$N][PF$_6$] as the supporting electrolyte at different scan rates. (Right) Randles-Sevcik plot of the CV data.

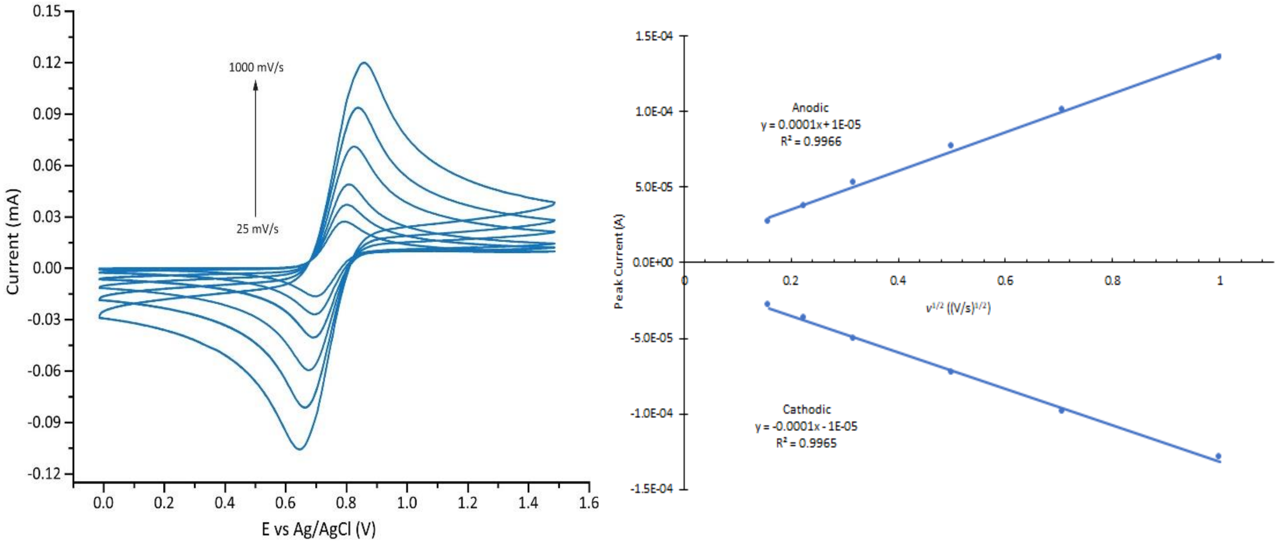

Figure 128. (Left) Cyclic voltammograms of 2 mM ^{Br2}**Fc** in MeCN with 100 mM [(*n*Bu)$_4$N][B(C$_6$F$_5$)$_4$] as the supporting electrolyte at different scan rates. (Right) Randles-Sevcik plot of the CV data.

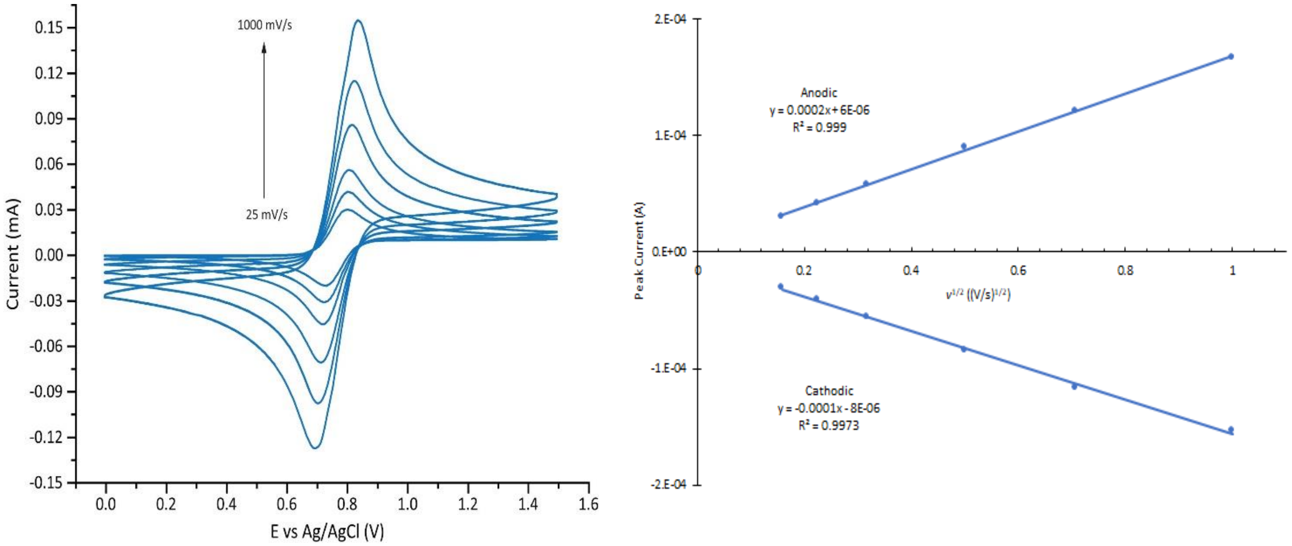

Figure 129. (Left) Cyclic voltammograms of 2 mM ^{Br2}**Fc** in MeCN with 100 mM [(*n*Bu)$_4$N][PF$_6$] as the supporting electrolyte at different scan rates. (Right) Randles-Sevcik plot of the CV data.

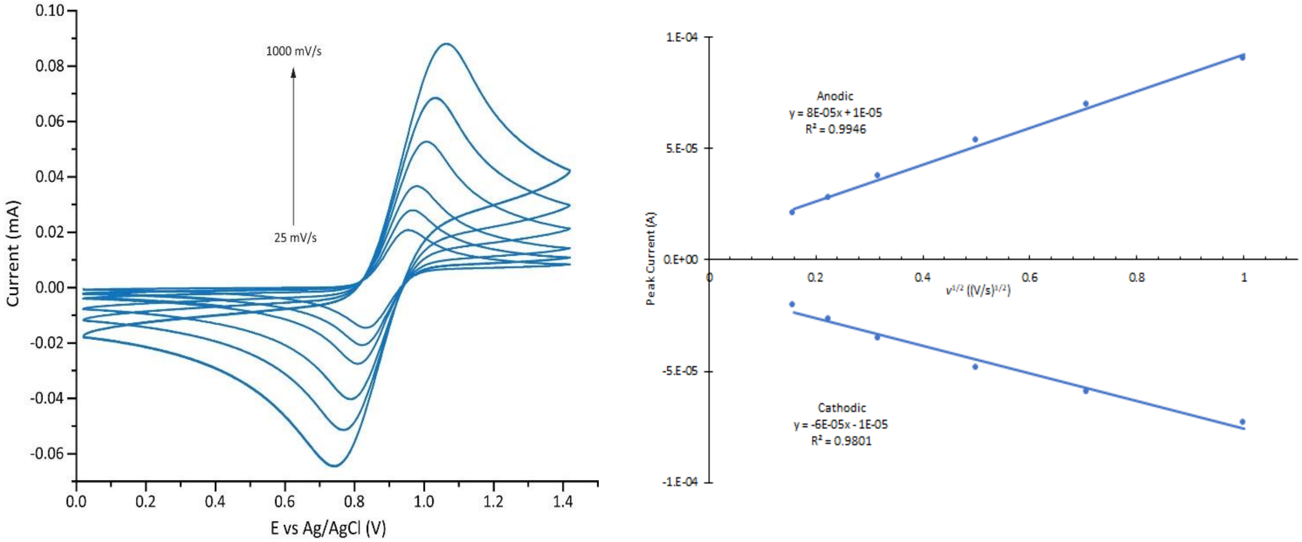

Figure 130. (Left) Cyclic voltammograms of 2 mM ^{Br2}**Fc** in MeTHF with 100 mM [(*n*Bu)$_4$N][B(C$_6$F$_5$)$_4$] as the supporting electrolyte at different scan rates. (Right) Randles-Sevcik plot of the CV data.

ix. *1,1'*-Diacetylferrocene

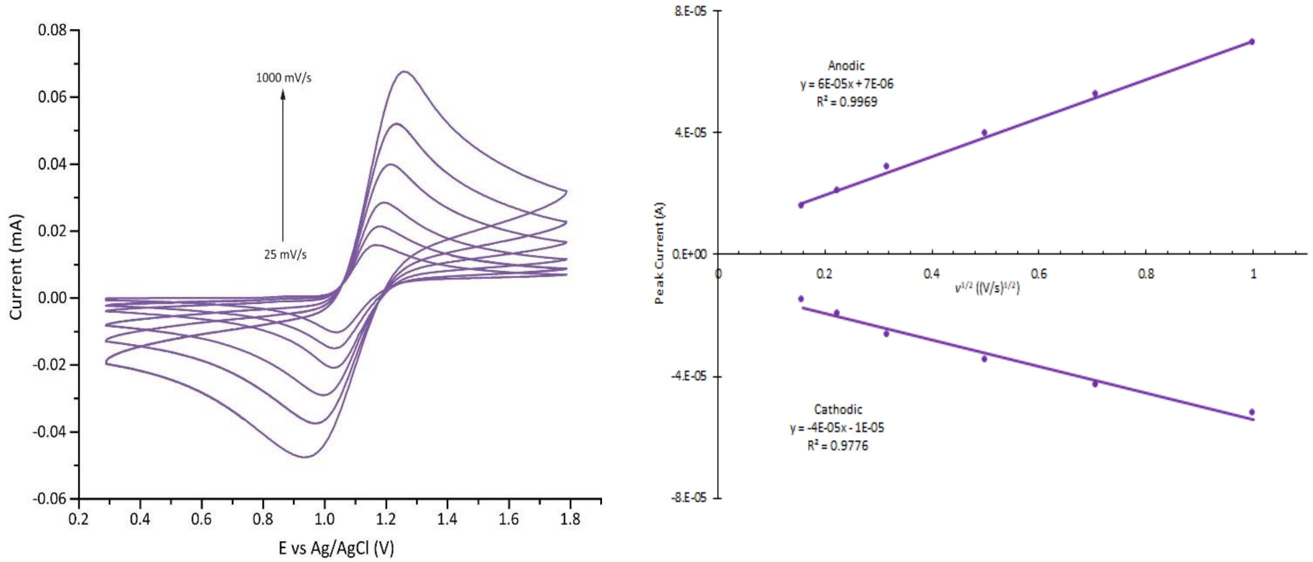

Figure 131. (Left) Cyclic voltammograms of 2 mM ^{Ac2}**Fc** in DCM with 100 mM [(nBu)$_4$N][B(C$_6$F$_5$)$_4$] as the supporting electrolyte at different scan rates. (Right) Randles-Sevcik plot of the CV data.

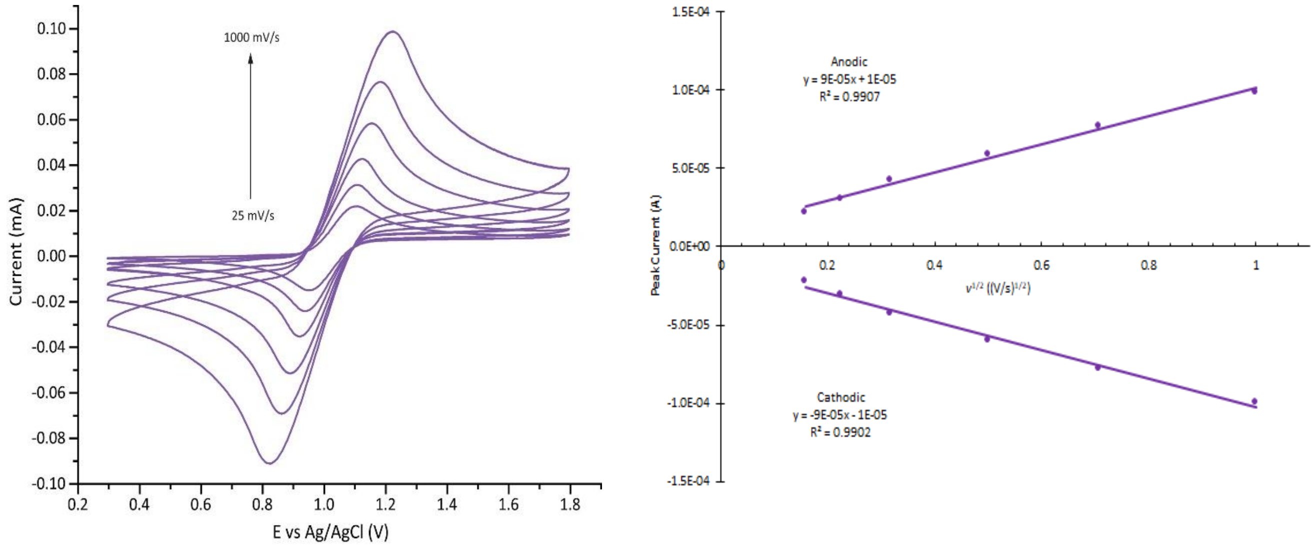

Figure 132. (Left) Cyclic voltammograms of 2 mM ^{Ac2}**Fc** in DCM with 100 mM [(nBu)$_4$N][PF$_6$] as the supporting electrolyte at different scan rates. (Right) Randles-Sevcik plot of the CV data.

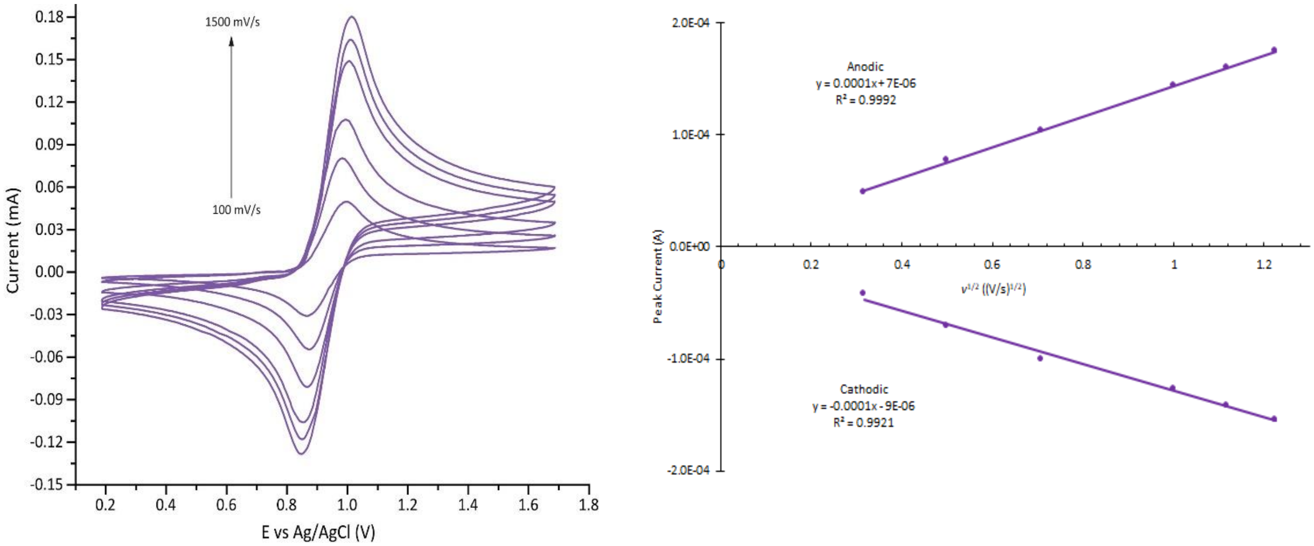

Figure 133. (Left) Cyclic voltammograms of 2 mM ^{Ac2}**Fc** in MeCN with 100 mM $[(n\text{Bu})_4\text{N}][\text{B}(\text{C}_6\text{F}_5)_4]$ as the supporting electrolyte at different scan rates. (Right) Randles-Sevcik plot of the CV data.

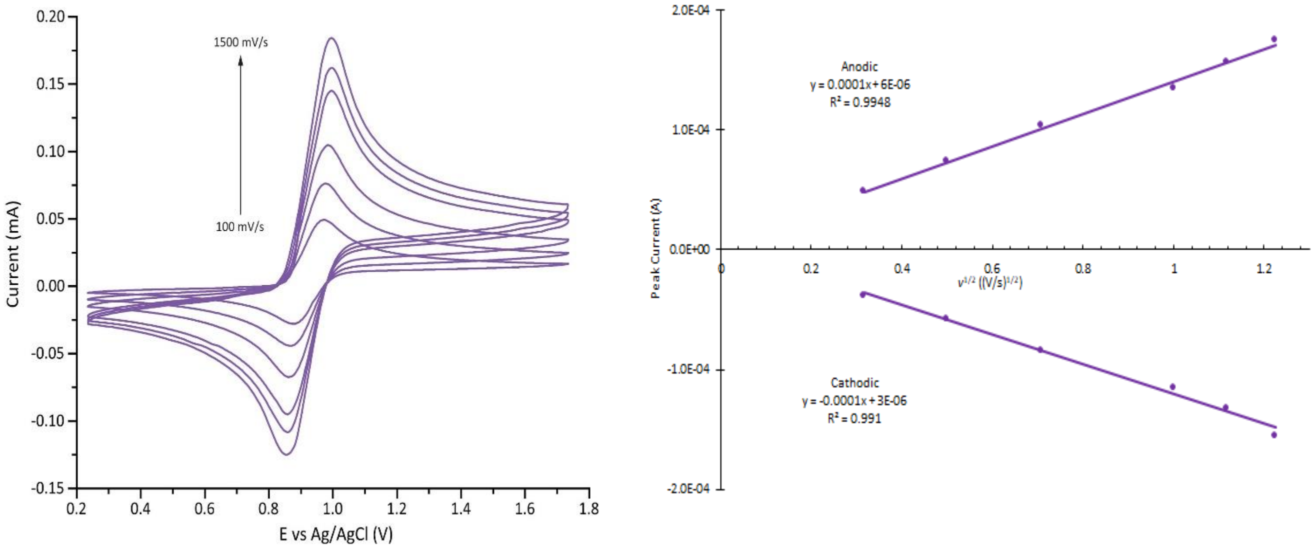

Figure 134. (Left) Cyclic voltammograms of 2 mM ^{Ac2}**Fc** in MeCN with 100 mM $[(n\text{Bu})_4\text{N}][\text{PF}_6]$ as the supporting electrolyte at different scan rates. (Right) Randles-Sevcik plot of the CV data.

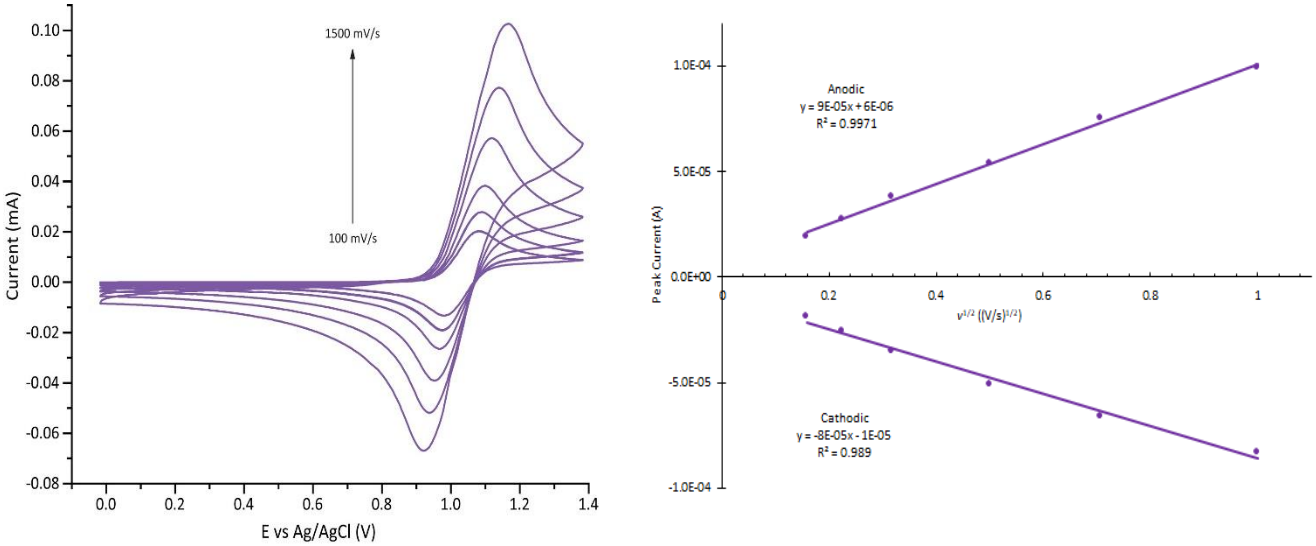

Figure 135. (Left) Cyclic voltammograms of 2 mM ^{Ac2}**Fc** in MeTHF with 100 mM $[(n\text{Bu})_4\text{N}][\text{B}(\text{C}_6\text{F}_5)_4]$ as the supporting electrolyte at different scan rates. (Right) Randles-Sevcik plot of the CV data.

x. *1,1'*-Dibenzoylferrocene

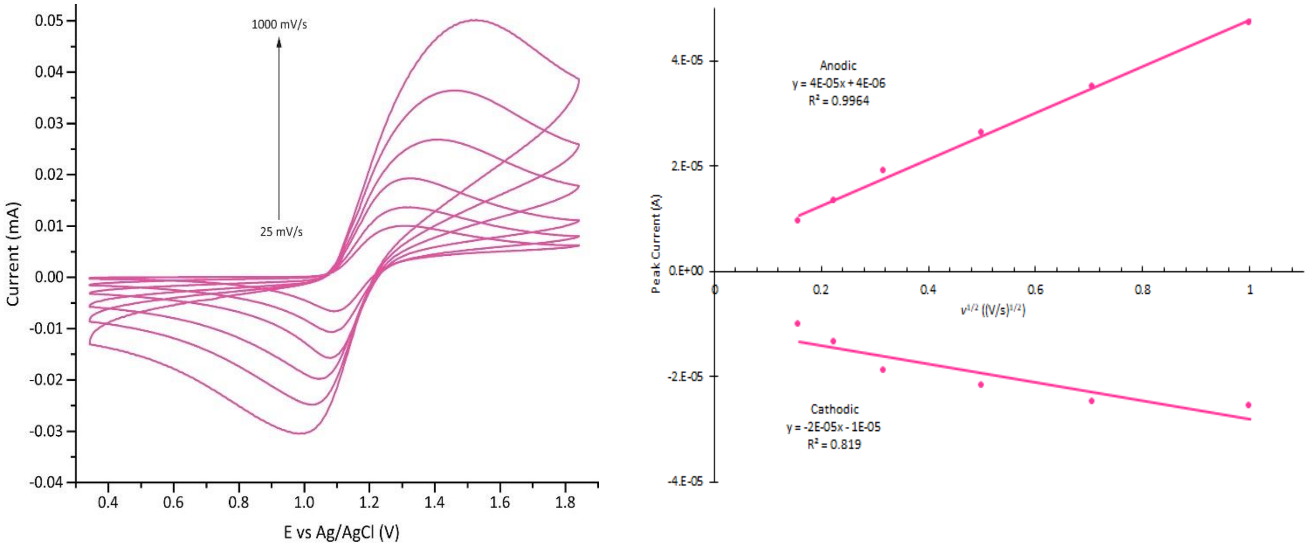

Figure 136. (Left) Cyclic voltammograms of 2 mM ^{Bz2}**Fc** in DCM with 100 mM $[(n\text{Bu})_4\text{N}][\text{B}(\text{C}_6\text{F}_5)_4]$ as the supporting electrolyte at different scan rates. (Right) Randles-Sevcik plot of the CV data.

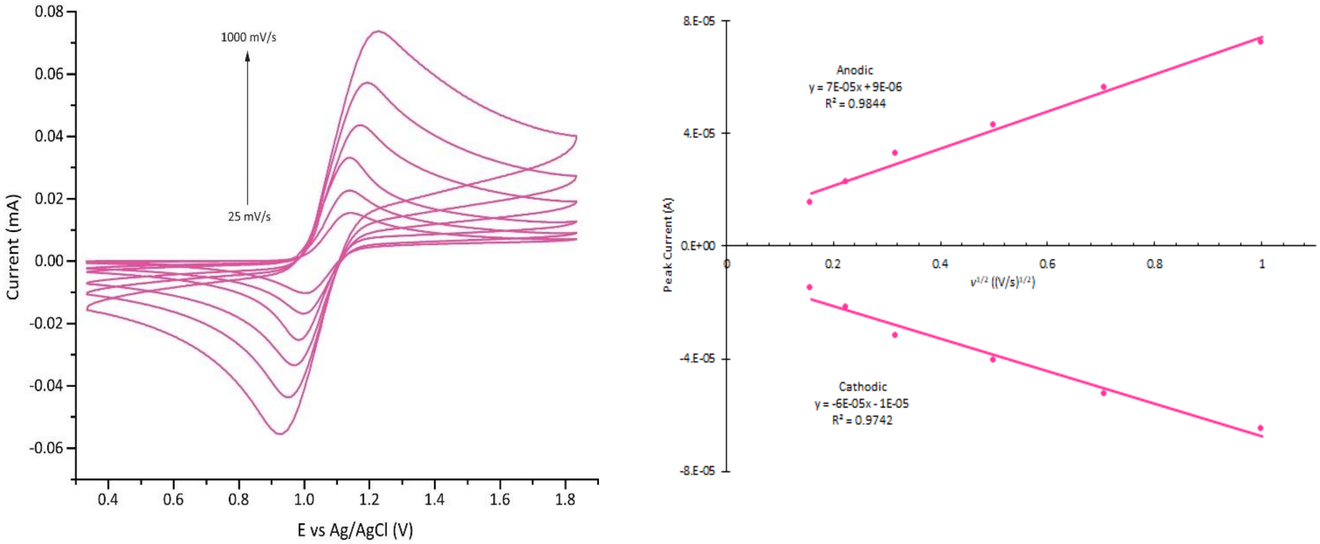

Figure 137. (Left) Cyclic voltammograms of 2 mM ^{Bz2}**Fc** in DCM with 100 mM $[(n\mathrm{Bu})_4\mathrm{N}][\mathrm{PF}_6]$ as the supporting electrolyte at different scan rates. (Right) Randles-Sevcik plot of the CV data.

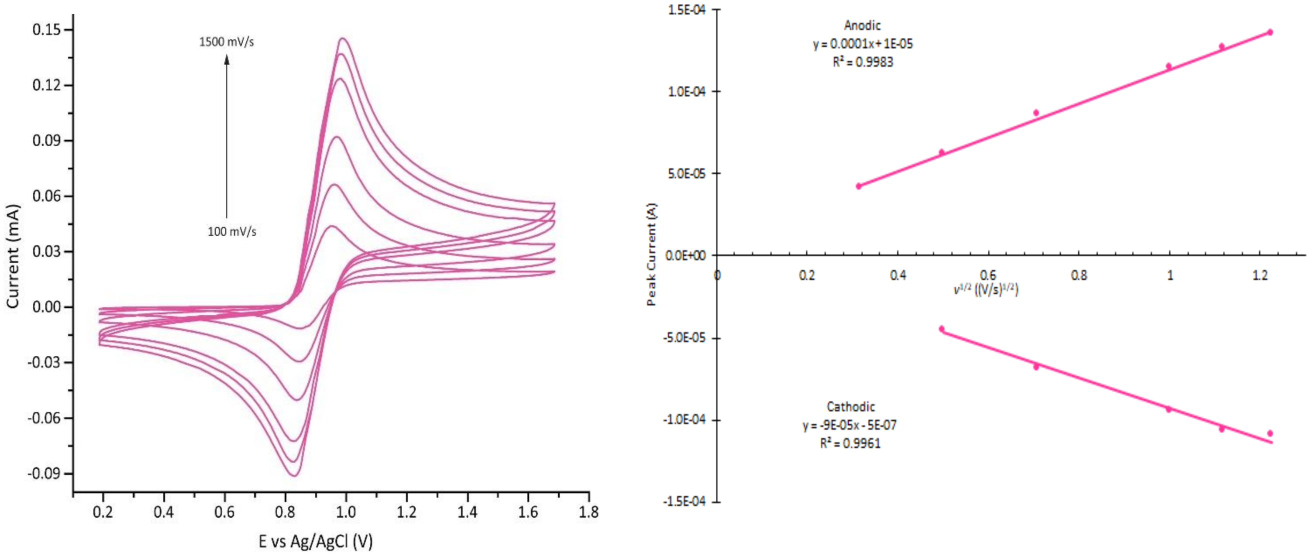

Figure 138. (Left) Cyclic voltammograms of 2 mM ^{Bz2}**Fc** in MeCN with 100 mM $[(n\mathrm{Bu})_4\mathrm{N}][\mathrm{B}(\mathrm{C}_6\mathrm{F}_5)_4]$ as the supporting electrolyte at different scan rates. (Right) Randles-Sevcik plot of the CV data. We were unable to determine a cathodic peak at 100 mV/s.

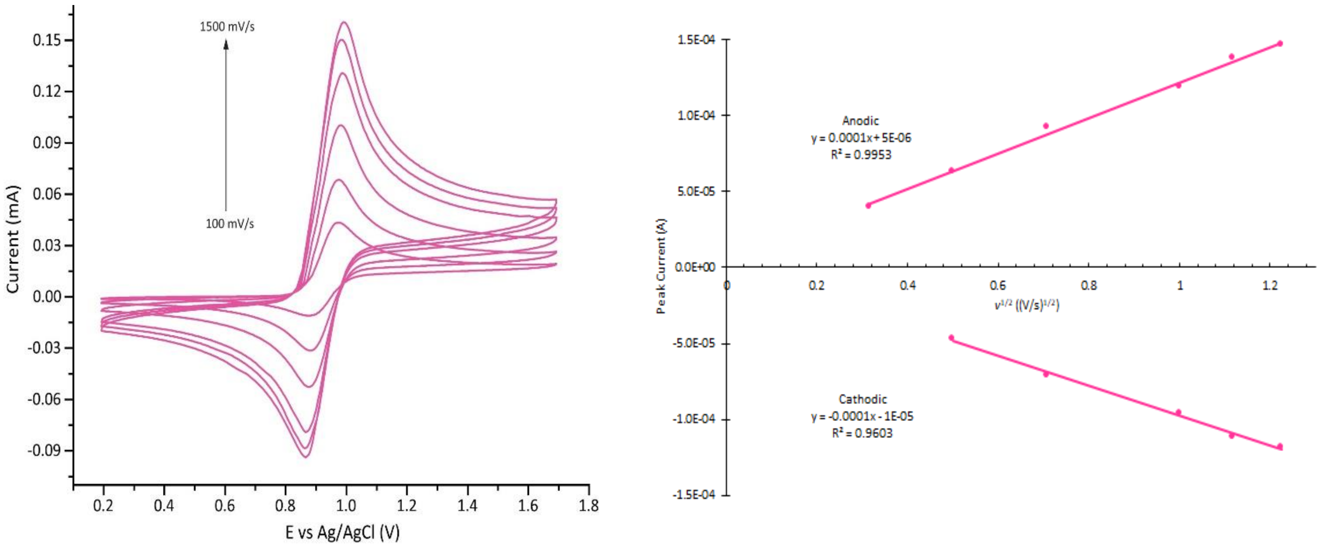

Figure 139. (Left) Cyclic voltammograms of 2 mM ^{Bz2}**Fc** in MeCN with 100 mM [(nBu)$_4$N][PF$_6$] as the supporting electrolyte at different scan rates. (Right) Randles-Sevcik plot of the CV data. We were unable to determine a cathodic peak at 100 mV/s.

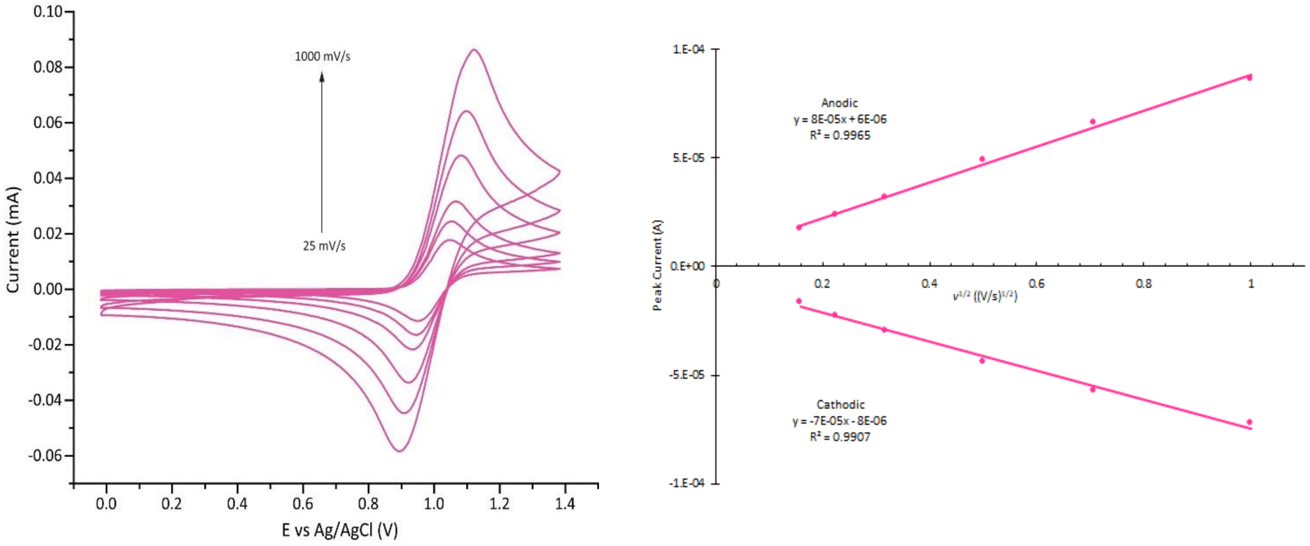

Figure 140. (Left) Cyclic voltammograms of 2 mM ^{Bz2}**Fc** in MeTHF with 100 mM [(nBu)$_4$N][B(C$_6$F$_5$)$_4$] as the supporting electrolyte at different scan rates. (Right) Randles-Sevcik plot of the CV data.

d. Reversibility Data

i. Plots of ΔE½ vs Scan Rate for Each Ferrocene Derivative in Various Media

Overall, in most cases the smallest and largest $\Delta E_{½}$ values were found in MeCN and DCM, respectively, both with [(*n*Bu)$_4$N][PF$_6$] as the supporting electrolyte. Also, the scan rate has the least influence on the $\Delta E_{½}$ values of different ferrocene derivatives in acetonitrile, see below. In general, in low polarity solvents the increased currents, due to the faster scan rates, lead to greater peak-to-peak separations due to larger incomplete *iR* compensation.

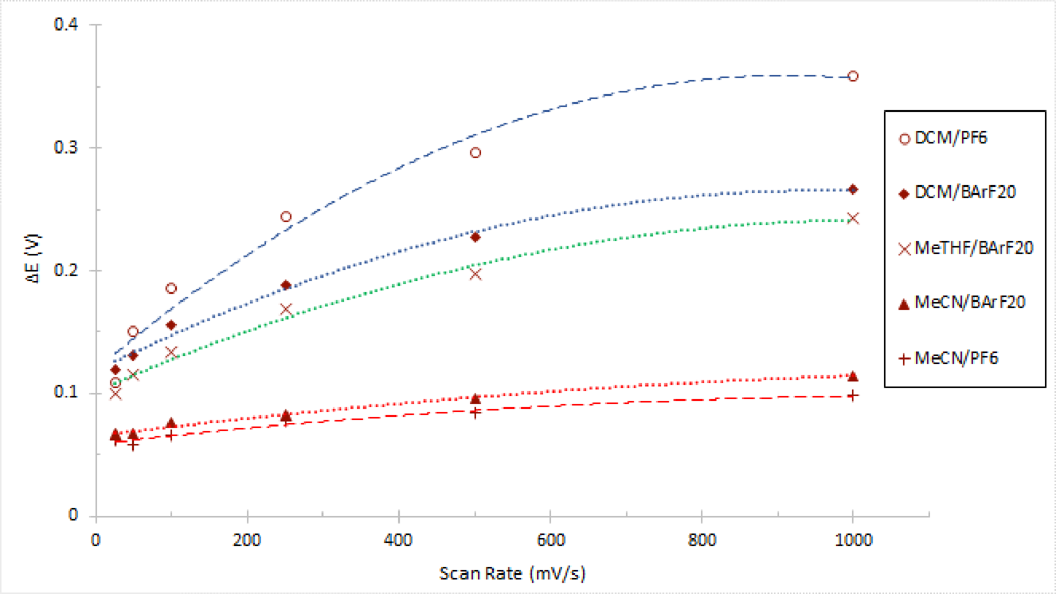

Figure 141. Plots of ΔE½ vs scan rate for cyclic voltammograms of ^{Me10}**Fc** measured in various solvent/electrolyte conditions.

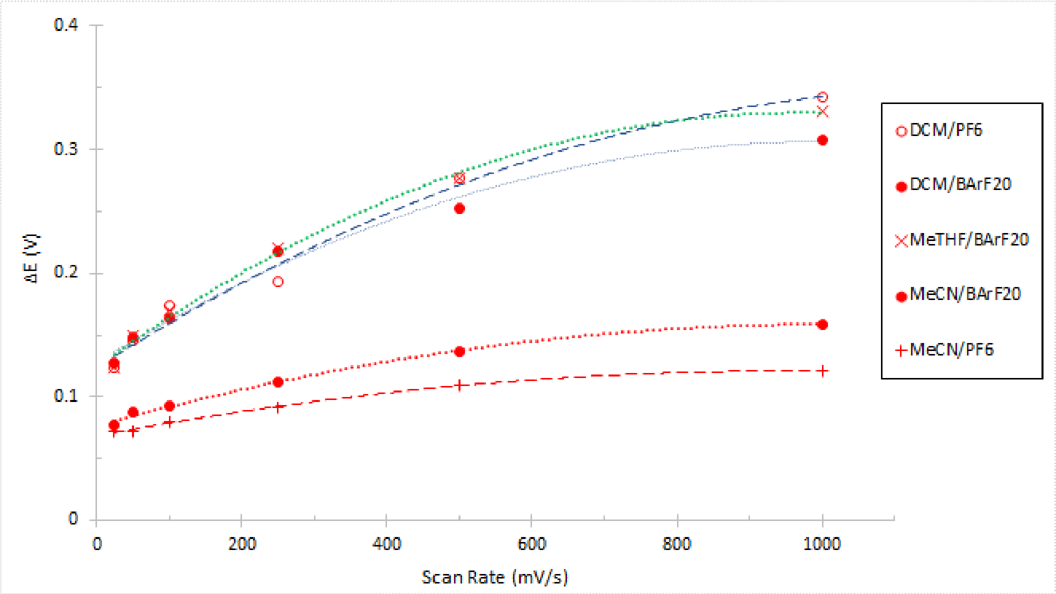

Figure 142. Plots of $\Delta E_{½}$ vs scan rate for cyclic voltammograms of ^{Me2}**Fc** measured in various solvent/electrolyte conditions.

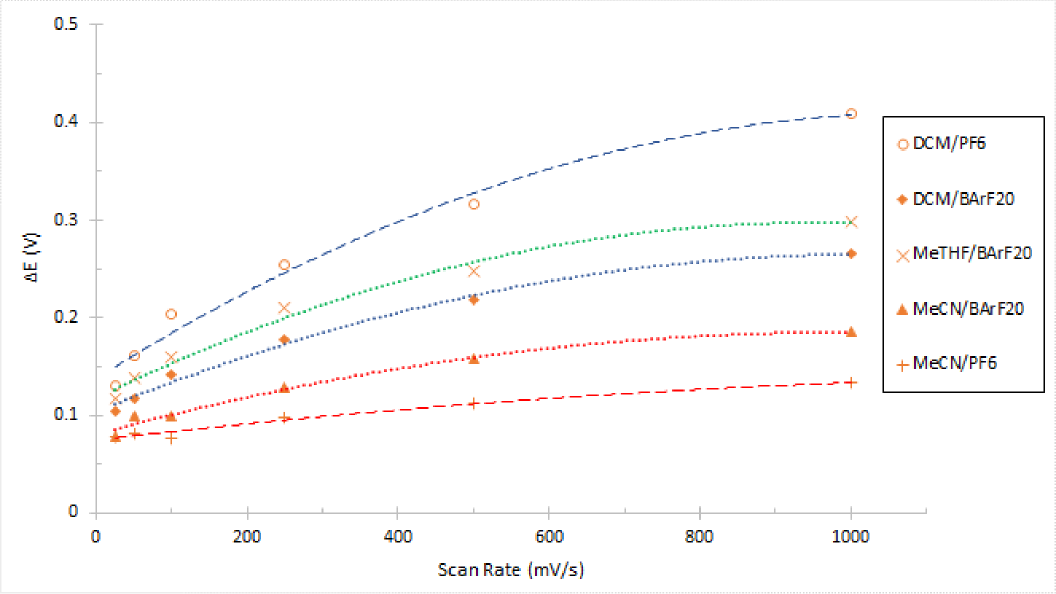

Figure 143. Plots of $\Delta E_{½}$ vs scan rate for cyclic voltammograms of ^{nBu}**Fc** measured in various solvent/electrolyte conditions.

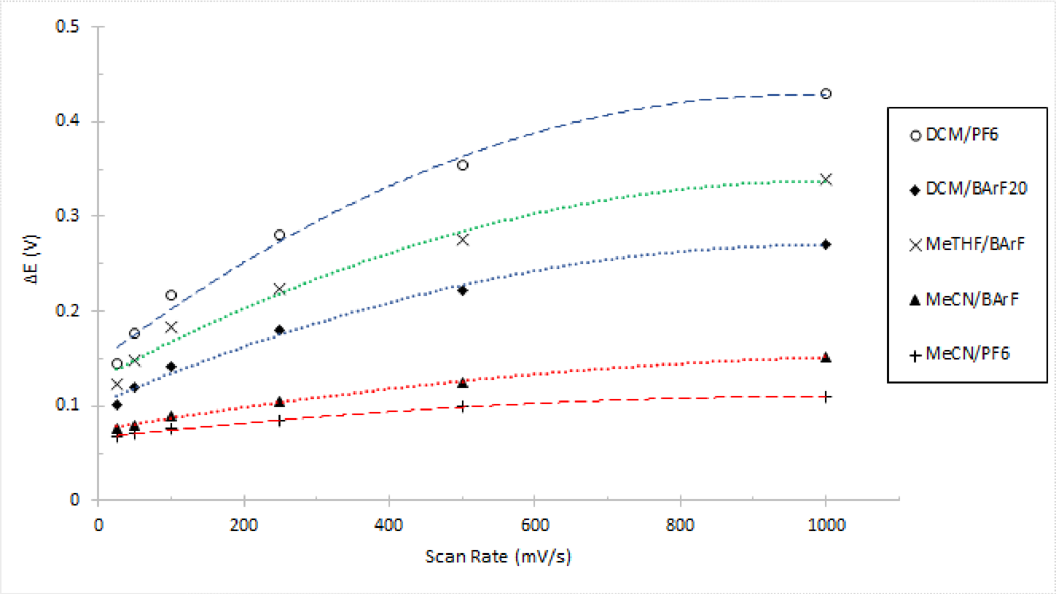

Figure 144. Plots of ΔE½ vs scan rate for cyclic voltammograms of **Fc** measured in various solvent/electrolyte conditions.

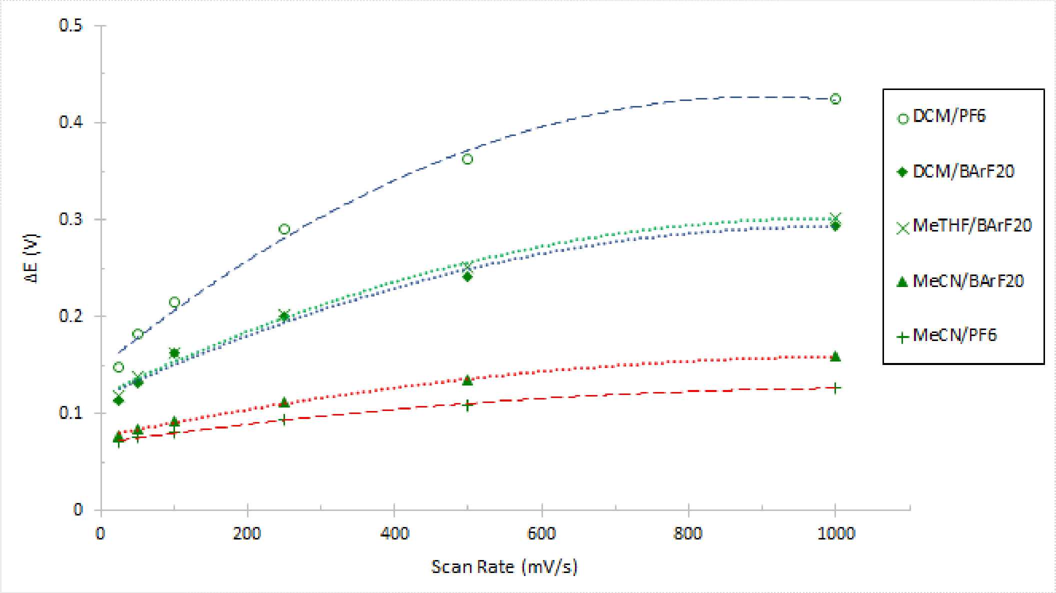

Figure 145. Plots of ΔE½ vs scan rate for cyclic voltammograms of ^{Br}**Fc** measured in various solvent/electrolyte conditions.

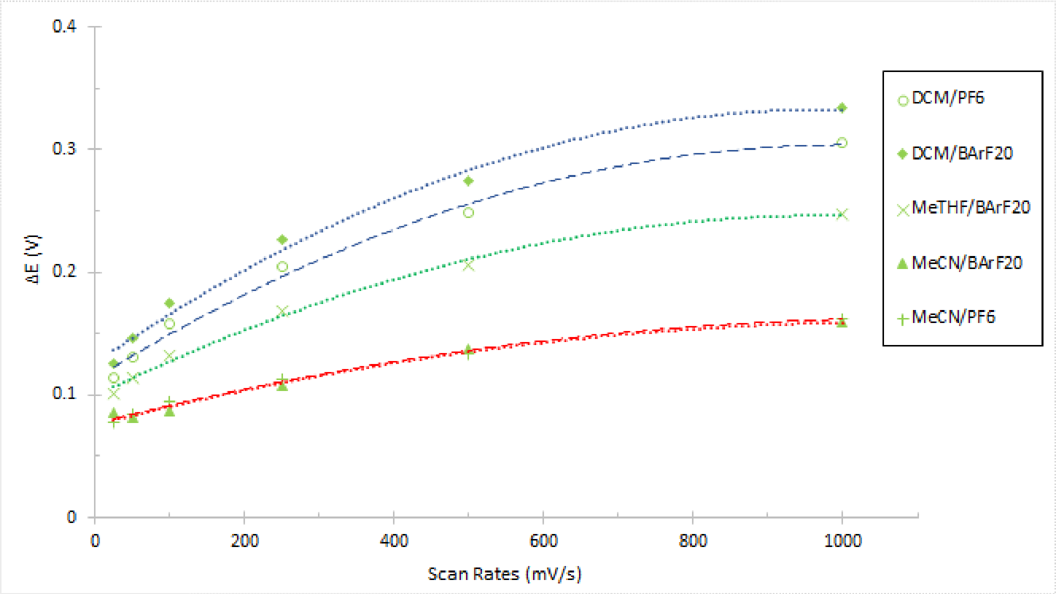

Figure 146. Plots of ΔE½ vs scan rate for cyclic voltammograms of ^{Ac}**Fc** measured in various solvent/electrolyte conditions.

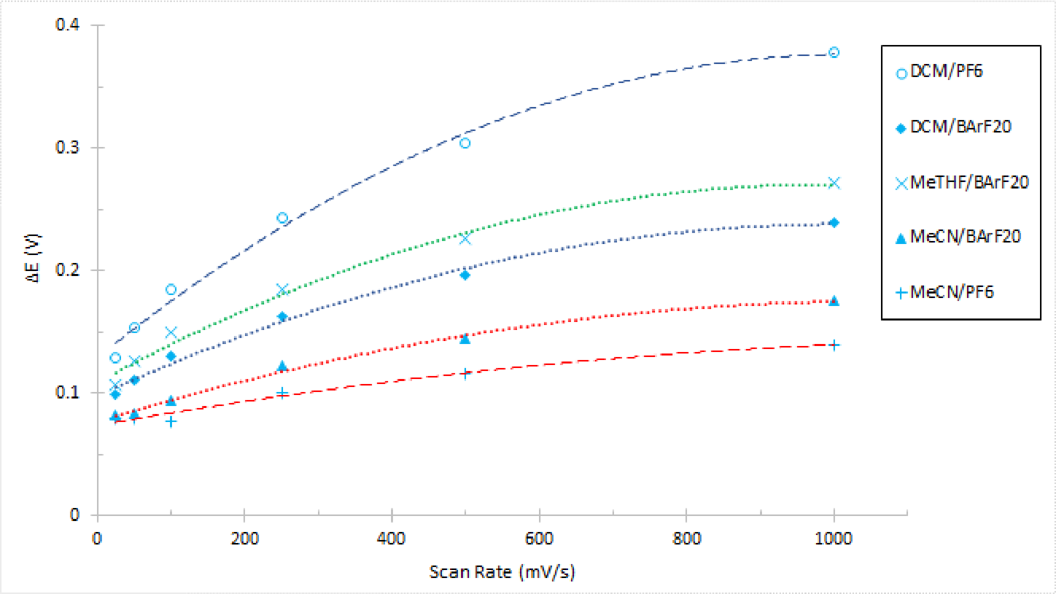

Figure 147. Plots of ΔE½ vs scan rate for cyclic voltammograms of ^{Bz}**Fc** measured in various solvent/electrolyte conditions.

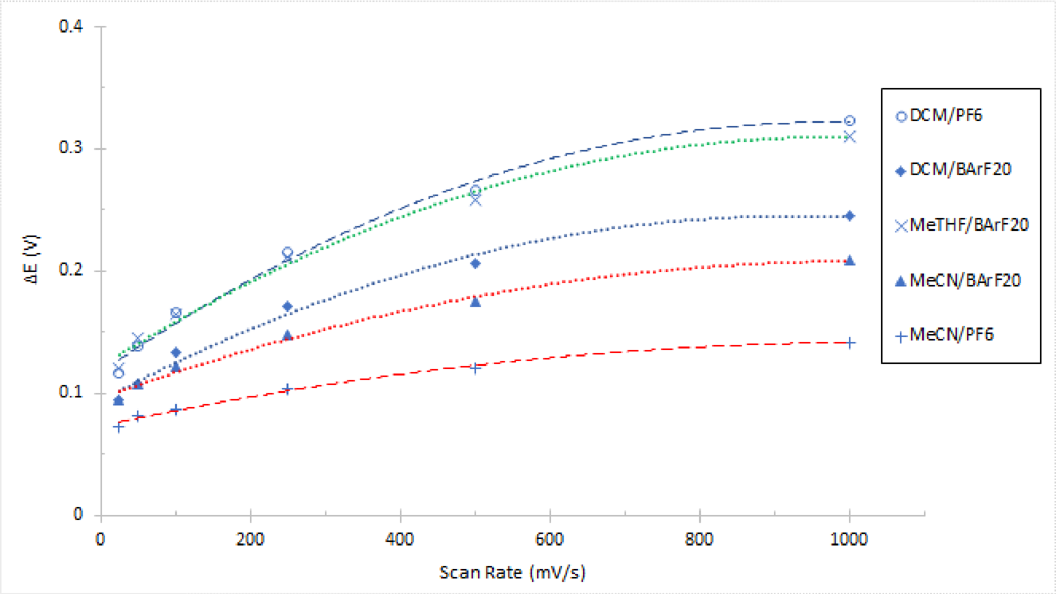

Figure 148. Plots of ΔE½ vs scan rate for cyclic voltammograms of ^{Br2}**Fc** measured in various solvent/electrolyte conditions.

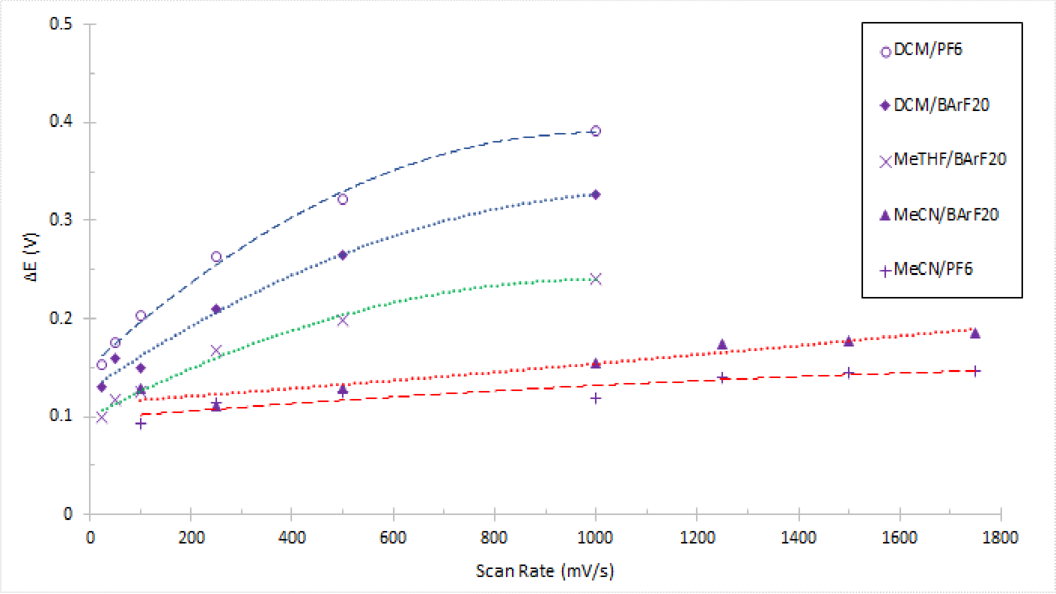

Figure 149. Plots of ΔE½ vs scan rate for cyclic voltammograms of ^{Ac2}**Fc** measured in various solvent/electrolyte conditions.

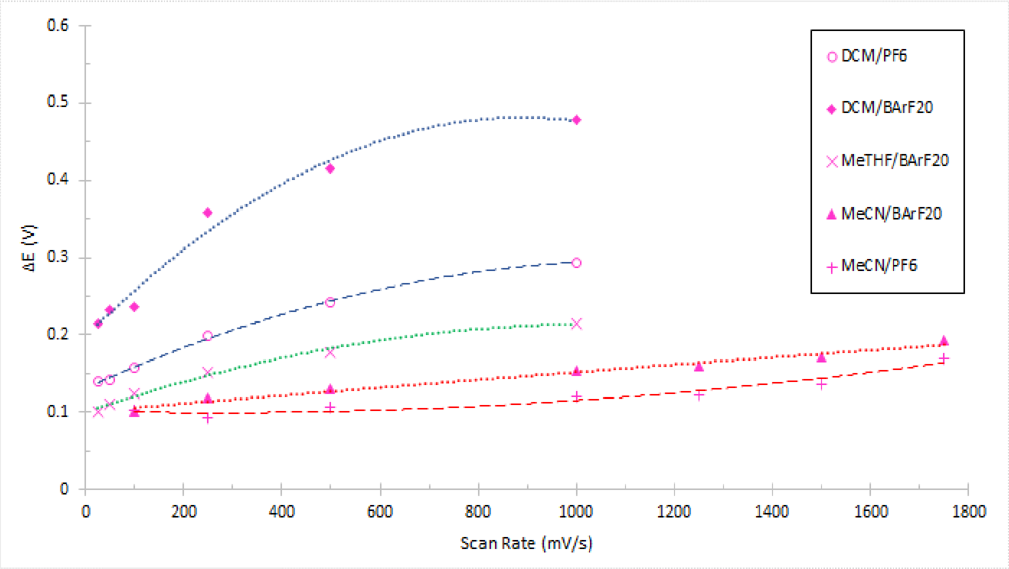

Figure 150. Plots of $\Delta E_{1/2}$ vs scan rate for cyclic voltammograms of ^{Bz2}**Fc** measured in various solvent/electrolyte conditions.

ii. Peak Current Ratios (i_{pa}/i_{pc})

Table 19. i_{pa}/i_{pc} values of various ferrocene analogs at 100 mV/s. We were unable to measure a cathodic peak height for ^{Bz2}**Fc** in MeCN at 100 mV/s; therefore, a ratio of peak heights was not possible. The value in the parentheses corresponds to the most ideal ratio found when the scan rate was increased to 500, [a] 1500,[b] or 1250 mV/s.[c]

	i_{pa}/i_{pc} in DCM		**i_{pa}/i_{pc} in MeCN**		**i_{pa}/i_{pc} in MeTHF**
Ferrocene Derivatives	$[(n\mathrm{Bu})_4\mathrm{N}][\mathrm{B}(\mathrm{C_6F_5})_4]$	$[(n\mathrm{Bu})_4\mathrm{N}][\mathrm{PF_6}]$	$[(n\mathrm{Bu})_4\mathrm{N}][\mathrm{B}(\mathrm{C_6F_5})_4]$	$[(n\mathrm{Bu})_4\mathrm{N}][\mathrm{PF_6}]$	$[(n\mathrm{Bu})_4\mathrm{N}][\mathrm{B}(\mathrm{C_6F_5})_4]$
^{Me10}**Fc**	0.99	0.96	0.98	0.97	1.04
^{Me2}**Fc**	1.10	0.97	0.99	0.99	0.97
^{nBu}**Fc**	1.01	0.99	1.00	1.00	1.00
Fc	0.98	0.98	0.97	0.98	0.99
^{Br}**Fc**	1.07	0.98	0.99	1.01	1.02
^{Ac}**Fc**	1.07	0.98	1.00	1.04	1.01
^{Bz}**Fc**	1.02	0.99	1.00	1.02	1.02
^{Br2}**Fc**	1.01	1.00	1.05	1.04	1.07
^{Ac2}**Fc**	1.08	1.00	1.14 (1.04)[a]	1.29 (1.13)[b]	1.07
^{Bz2}**Fc**	1.00	1.03	N/A (1.19)[c]	N/A (1.24)[b]	1.09

e. Diffusion Coefficient Data for the Various Ferrocene Derivatives in This Study

i. Influence of Molecular Weight on the Diffusion Coefficient

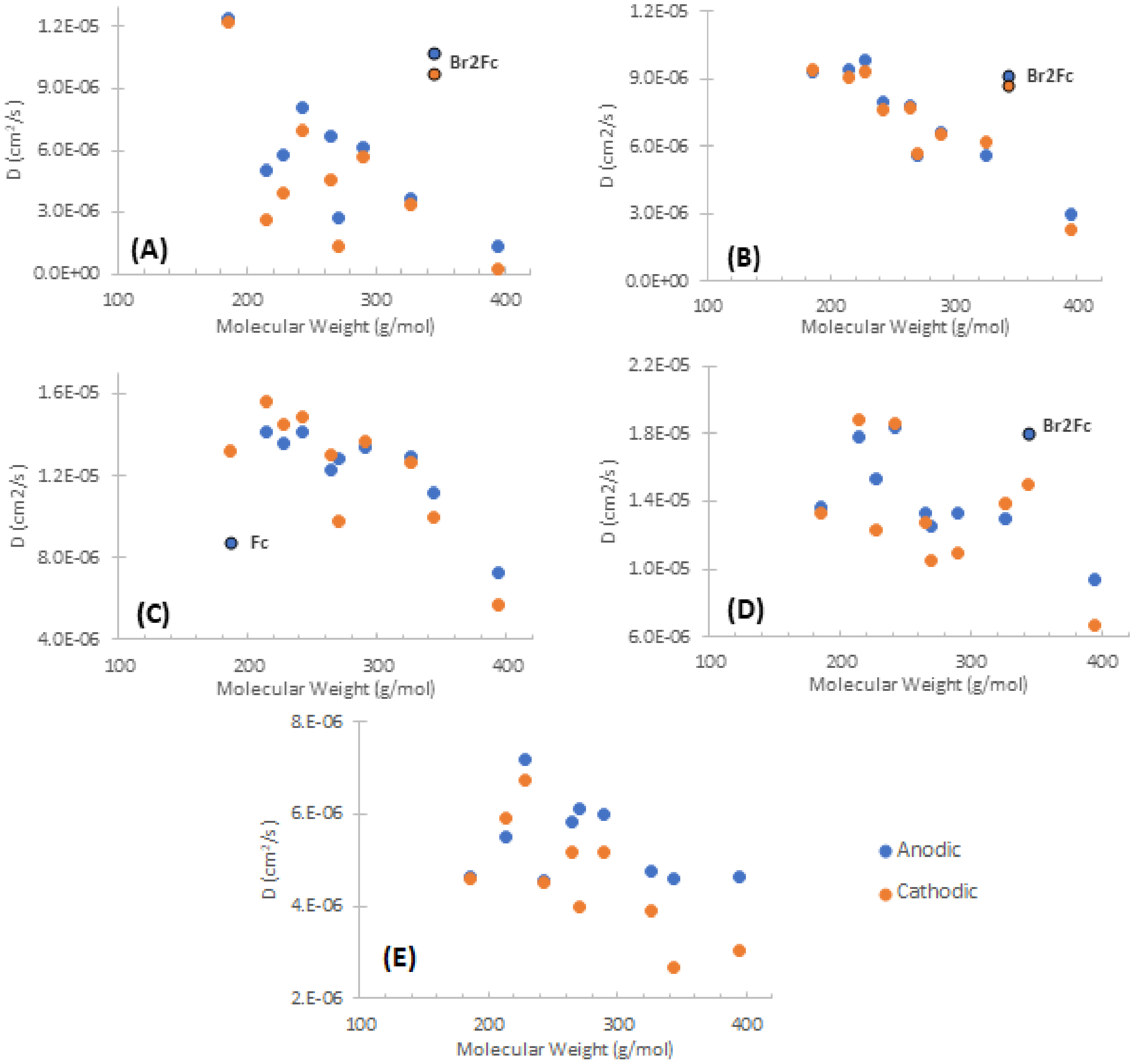

Figure 151. Correlations between the molecular weight of the ferrocene derivatives and the calculated diffusion coefficients of the neutral (blue) and oxidized (orange) species in A) DCM with 100 mM [(*n*Bu)$_4$N][B(C$_6$F$_5$)$_4$], B) DCM with 100 mM [(*n*Bu)$_4$N][PF$_6$], C) MeCN with 100 mM [(*n*Bu)$_4$N][B(C$_6$F$_5$)$_4$], D) MeCN with 100 mM [(*n*Bu)$_4$N][PF$_6$], and E) MeTHF with 100 mM [(*n*Bu)$_4$N][B(C$_6$F$_5$)$_4$] as the supporting electrolyte. The molecular weight of the counter anions was omitted for simplification purposes.

ii. Effect of Moisture on Diffusion Coefficients

Using the solution of ferrocene (2 mM) with [(*n*Bu)$_4$N][PF$_6$] (100mM) in acetonitrile, we studied the effect of moisture on the diffusion coefficient. First, the solution was made inside of the glovebox and subsequently brought outside. Under an argon flow, variable scan rate CV measurements were made. Then, nanopure water was added in increments and the same variable scan rate CV measurements were performed. The diffusion coefficient was again calculated for the brief exposure to the outside atmosphere and each subsequent addition of water. It was observed that upon the introduction of moisture into the solution, the diffusion coefficient increased, as shown in Table 20.

Table 20. Diffusion coefficient values for a ferrocene (2mM) and [(*n*Bu)$_4$N][PF$_6$] (100mM) solution upon increase of the water content under an Ar blanket.

Solution	**D_{Anodic}** ($cm^2.s^{-1}$)	**$D_{Cathodic}$** ($cm^2.s^{-1}$)
Fc + [(*n*Bu)$_4$N][PF$_6$] inside glove box	1.37×10^{-5}	1.33×10^{-5}
Fc + [(*n*Bu)$_4$N][PF$_6$] brief outside exposure	1.57×10^{-5}	1.64×10^{-5}
Fc + [(*n*Bu)$_4$N][PF$_6$] outside + 25 µL n.p. H_2O	1.77×10^{-5}	1.95×10^{-5}
Fc + [(*n*Bu)$_4$N][PF$_6$] + 75 µL n.p. H_2O	2.08×10^{-5}	2.22×10^{-5}

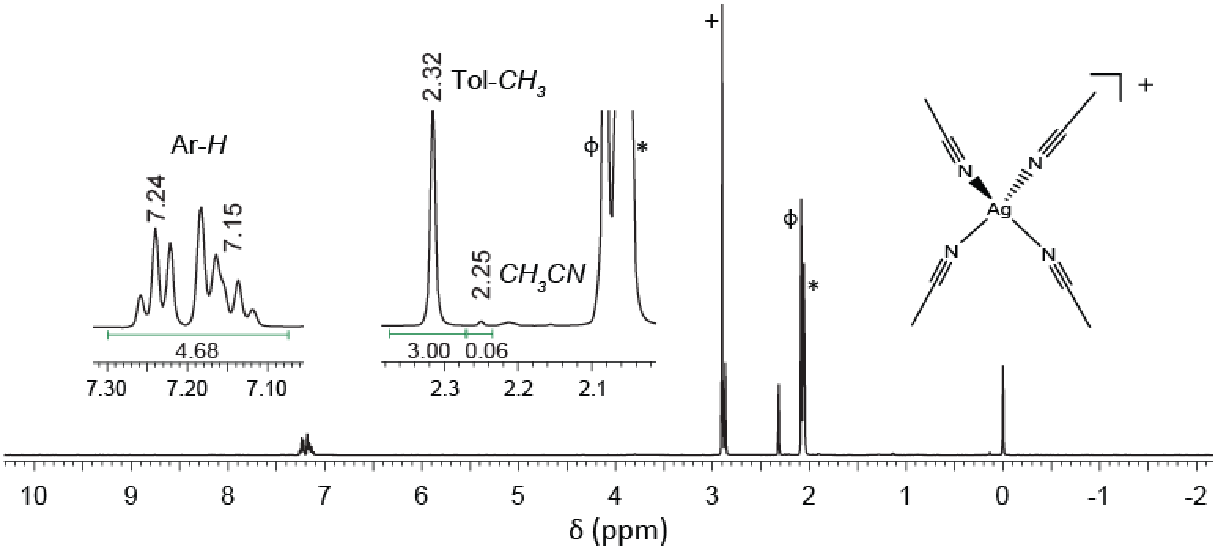

Figure 152. ^{1}H-NMR spectrum of [Ag(MeCN)$_4$][B(C$_6$F$_5$)$_4$] recorded in acetone-d_6 (500 MHz) at room temperature with an internal toluene standard. Quantification of the coordinating acetonitrile molecules was possible with the addition of 1 equivalent of toluene to the silver(I) salt NMR solution, as well as the use of the acetonitrile-CH$_3$ satellite peak (1/200th of the main acetonitrile signal) and its ratio to the toluene-CH$_3$ signal (i.e., four acetonitrile molecules per toluene molecule; 4:1).

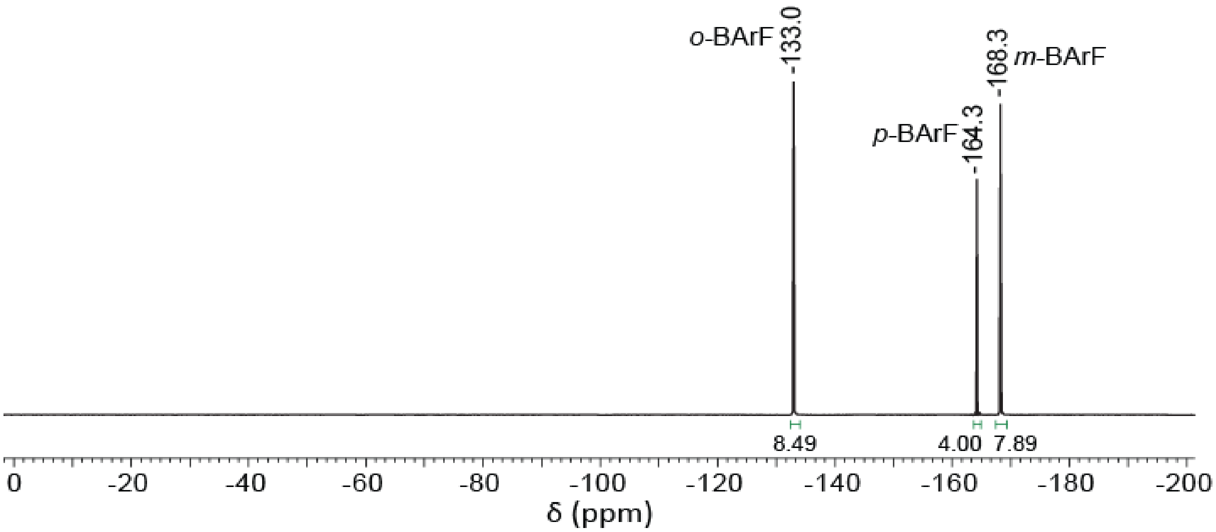

Figure 153. ^{19}F-NMR spectrum of [Ag(MeCN)$_4$][B(C$_6$F$_5$)$_4$] recorded in acetone-d_6 (470 MHz) at room temperature.

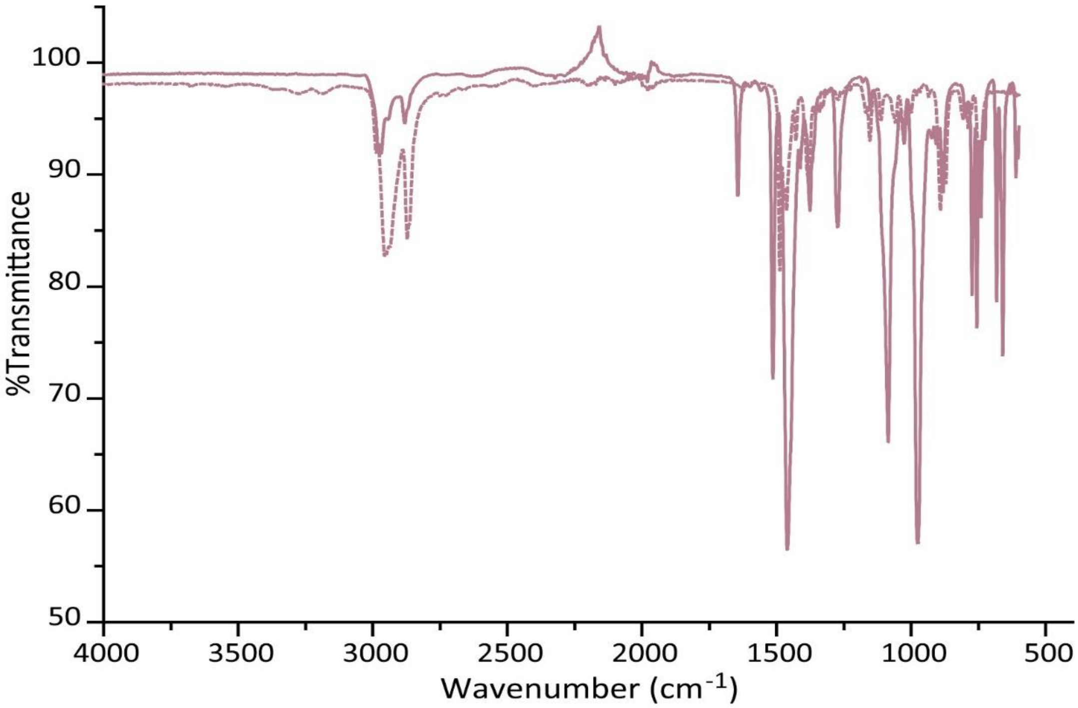

Figure 154. IR spectra comparison between [(nBu)$_4$N]Cl (dotted line) and [(nBu)$_4$N][B(C$_6$F$_5$)$_4$] (solid line).

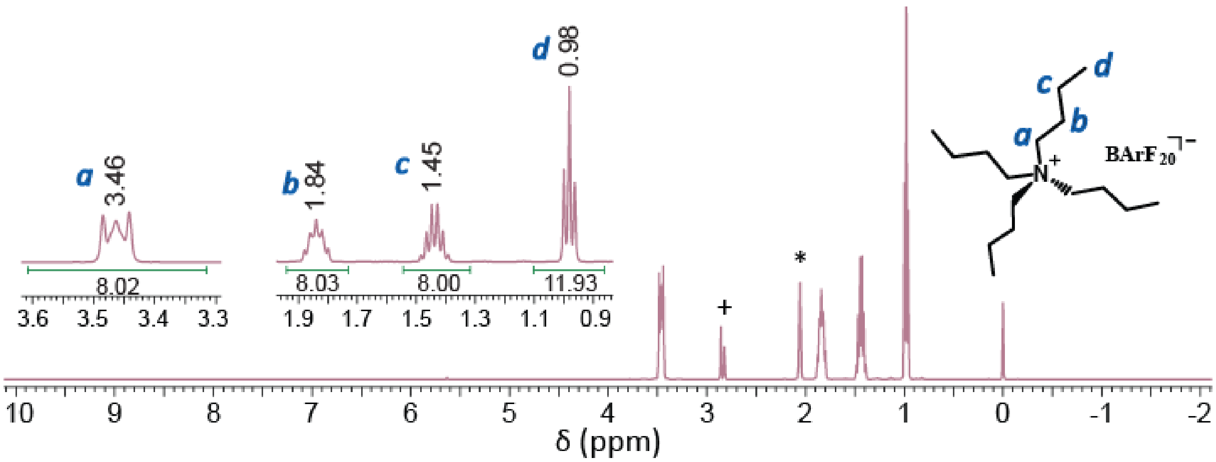

Figure 155. ^{1}H-NMR spectrum of [(nBu)$_4$N][B(C$_6$F$_5$)$_4$] recorded in acetone-d_6 (500 MHz) at room temperature.

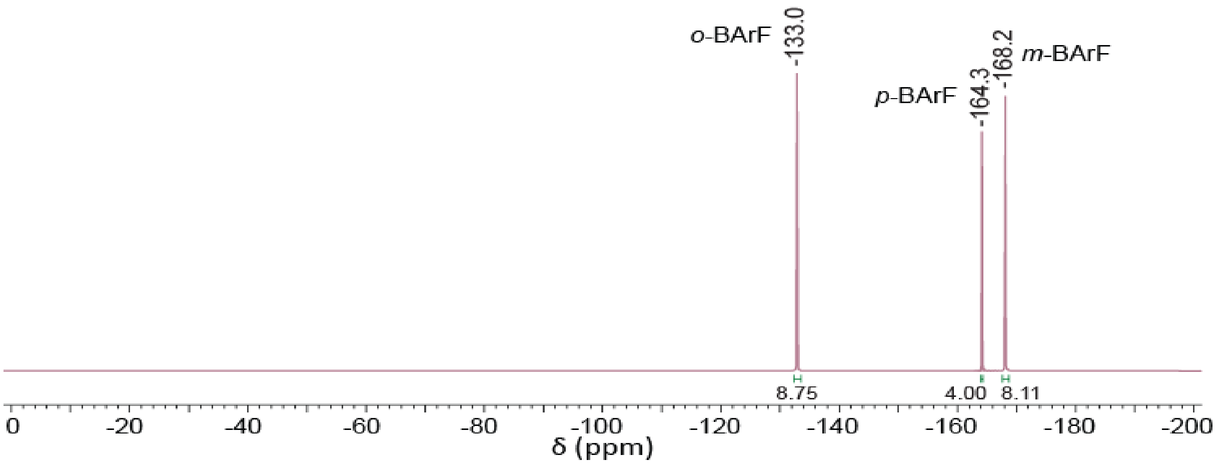

Figure 156. ^{19}F-NMR spectrum of $[(n\text{Bu})_4\text{N}][\text{B}(\text{C}_6\text{F}_5)_4]$ recorded in acetone-d_6 (470 MHz) at room temperature.

CHAPTER II: ELECTROCATALYTIC ANAEROBIC OXIDATION OF BENZYLIC AMINES MEDIATED BY *1,1'*-DIBROMOFERROCENE

Abstract

The generation and functionalization of carbon- or nitrogen centered radicals are of great interest for their potential synthetic utility. Here, we report the anaerobic electrocatalytic oxidation of two primary benzylic amines, benzylamine and 2-picolylamine, in the presence of an electron deficient ferrocene derivative as a redox mediator. The use of the appropriate redox mediator prevented fouling of the electrode surface which is dominant during the direct electrochemical oxidation as well as decreased the potential at which the catalytic oxidation reaction occurred. Cyclic voltammetry studies revealed an E_rC_i' catalytic process between the ferrocene derivative and both substrates. Through anaerobic controlled-potential electrolysis, we have demonstrated a method that utilized 90% of electrons removed from the system towards forming the desired coupled imine product of benzylamine oxidation while avoiding an excess of problematic hydrolysis and other side reactions. The products obtained from bulk electrolysis experiments were characterized through IR, ^{1}H- and ^{13}C-NMR spectroscopies and proposed mechanistic steps were laid out for the electrocatalytic process. Our results can guide the development of new electrocatalytic systems aimed at oxidizing and transforming simple compounds into chemicals of higher complexity and value.

Introduction

Carbon- or nitrogen-centered radical species are attractive intermediates involved in a variety of chemical transformations and can be generated through numerous synthetic methods to functionalize molecules in organic synthesis and form C–C and C–N bonds. This bond formation transforms simple compounds into chemicals of higher complexity and value.[71] However, traditional methods for these types of reactions typically involve undesirable reaction conditions, including high temperatures and the need to use large amounts of oxidants and expensive catalysts. Electrochemistry can offer a mild and versatile alternative and provides a powerful approach to access the radical intermediates due to its precise control over redox processes. For this reason, electrochemistry has become more recognized as a powerful tool to develop new synthetic methods for sustainable chemical reactions over the recent years.[72-74] There are many examples of electrochemical oxidation involving net two-electron reactivity, while very few have employed one-electron pathways to selectively form and functionalize a radical species. In the latter case, the radical species most often reacts with dioxygen present to form the desired product,[75-77] and there are limited reports on anaerobic functionalization of the radical.[78, 79]

The electrochemical oxidation of amines, particularly primary amines, presents its own challenges, most notably the reactivity of the singly-oxidized species (i.e., radicals) towards the working electrode, causing surface fouling which shuts down the flow of electrons between the reaction solution and the electrode surface.[80] Additionally, primary amines are more difficult to oxidize than secondary or tertiary amines, and require higher overpotentials for oxidation, which can result in a greater chance of over oxidizing the amines and lead to substrate degradation or electrode surface fouling.

One way to overcome these challenges is through the use of a redox mediator, a compound that is continuously oxidized at the electrode surface and in turn reduced by the substrates in solution. This keeps the oxidized substrate away from the electrode surface, preventing passivation of the electrode and encouraging the desired reactions to occur instead. Effective mediators undergo reversible redox processes, at potentials less positive than the oxidation potential of the substrate, allowing the target reaction to occur at lower potentials than would be required without a mediator and thus preventing over oxidation. Redox mediators should include appropriate redox potentials, high stability of both oxidized and reduced forms in the reaction conditions, and fast electron-transfer kinetics.

Ferrocene (Fc) and its derivatives are attractive compounds for this purpose, due to its well-known reversible one-electron redox process between the ferrocene and ferricenium (Fc^+) states. In fact, there have been several reports documenting the efficacy of ferrocene and its derivatives as redox mediators for the electrocatalytic oxidation of various organic substrates, including amines. [79, 81-84] However, there have not been such studies done with benzylic amines, such as benzylamine, although the oxidation reaction for this compound resulting in a coupled imine product has been done through various methods, ranging from chemical[85-87] to photochemical oxidation reactions.[88, 89] More recently Deb *et. al.* have shown it possible to perform this reaction under very mild conditions using a ferricenium catalyst in water and air as the primary oxidant.[90] Most of the hypothesized mechanisms for benzylamine oxidation not only require the use of dioxygen (O_2) as the terminal oxidant to drive the reaction forward but also depict the role of O_2 as necessary in many catalytic steps involving formation of the hypothetical superoxide or hydroperoxide intermediates, which can lead to undesired products. In all the reports, due to the presence of water, hydrolysis of further oxidized products is also observed.[85, 89] This creates the need for anaerobic methods such as redox mediated electrocatalytic oxidation that can form and functionalize the radical species and selectively result in the desired product.

The results herein demonstrate the effectiveness of electron-deficient ferrocene derivatives to act as redox mediators in the anaerobic electrocatalytic oxidation of benzylic amines to selectively form coupled imine products. Cyclic voltammetry studies reflect the catalytic nature of the reaction conditions through an E_rC_i' mechanism which reduced the potential required for amine oxidation. Through controlled potential electrolysis, the desired product was formed with no evidence of hydrolysis, giving a new route to performing efficient amine oxidations that can be an impactful strategy for the future of electrochemical organic synthesis.

Results and Discussion

Cyclic Voltammetry

The cyclic voltammogram of the direct oxidation of benzylamine (BA) in an acetonitrile (MeCN) solution with 100 mM of $[(nBu)_4N][PF_6]$ as the supporting electrolyte revealed an irreversible oxidation peak at 1.55 V vs Ag/AgCl that passivated the surface of the working electrode over several cycles, as was evident by the loss of a peak shape and the current as the cycling continued (Figure 157, *left*). A similar surface fouling behavior was also observed for 2-picolylamine (PA), which displayed an irreversible peak at 1.62 V vs Ag/AgCl (Figure 157, *right*).

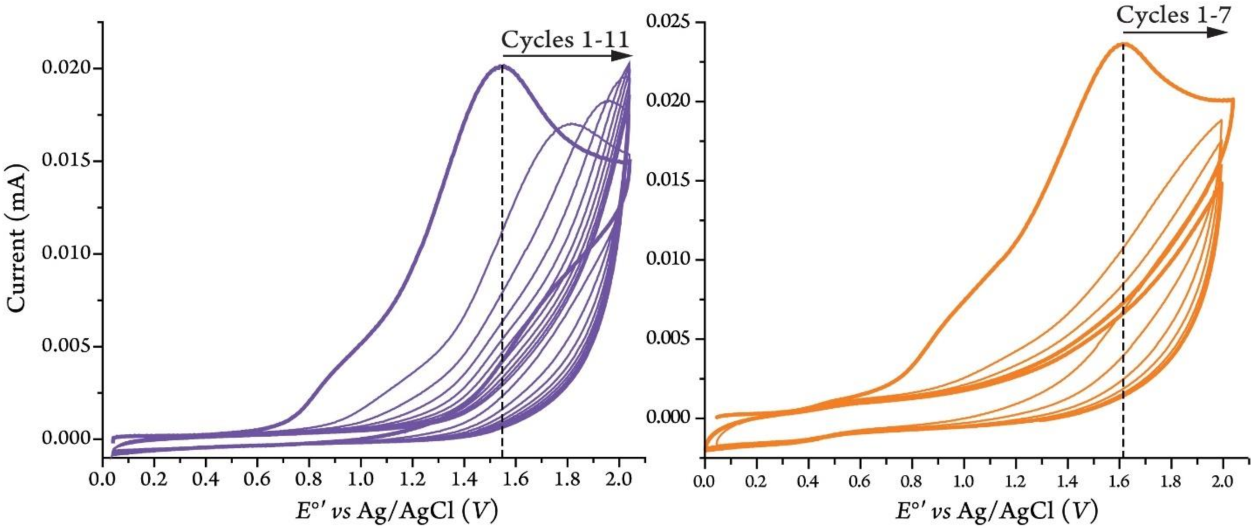

Figure 157. Cyclic voltammogram of the direct oxidation of 1 mM benzylamine (left) and 2-picolylamine (right) at 100 mVs^{-1} in MeCN with 100 mM $[(n\mathrm{Bu})_4N][PF_6]$ as the supporting electrolyte, showing passivation of the glassy carbon electrode as cycles continued.

This was expected, as primary amines are known to adhere to the surface of carbon electrodes upon electrochemical oxidation, specifically through the nitrogen radical cation intermediate that initially forms, as proposed first by Desarmot and Sanchez in 1990 (Scheme 2).[91] The maximum current observed in the first scans are similar for both amines, pointing to the comparable diffusion rates of the substrates in our experimental condition (Figure 157).

Scheme 2. Attachment of oxidized primary amine to a carbon electrode surface. Recreated with permission from [91]. Copyright 1990 IOP Publishing.

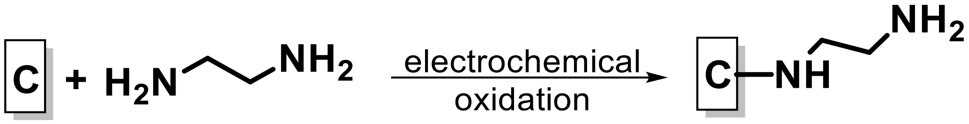

In order to overcome electrode surface fouling, we consider the use of ferrocene derivatives as single-electron electrochemical mediators due to their appropriate range of redox potentials. Two electron-deficient ferrocene derivatives (^{Br}Fc, ^{Br2}Fc) as well as the parent ferrocene complex were studied through cyclic voltammetry in various solvent/electrolyte conditions for the reversibility and redox potential of their one-electron redox processes. In an acetonitrile (MeCN) solution containing 100 mM $[(n\mathrm{Bu})_4\mathrm{N}][\mathrm{PF}_6]$ as the supporting electrolyte, the introduction of an electron-withdrawing bromo-substituent on one or both cyclopentadienyl ring(s), increases the redox potential by 178 mV or 313 mV in the mono- or *1,1'*-disubstitued analog, respectively, relative to that of the unsubstituted ferrocene (Figure 161). Their redox processes were quite reversible (i.e., $\Delta E_{1/2}$ ranging from 76 to 87 mV and anodic/cathodic peak current ratios (i_{pa}/i_{pc}) between 0.98 and 1.04, see Table 21), and all three complexes in both reduced and oxidized forms were freely diffusing through the solution, confirming that these derivatives can act as appropriate redox mediators for an electrocatalytic oxidation process.

1,1'-Dibromoferrocene (^{Br2}Fc) displayed the most suitable redox potential value for oxidation of benzylic amines among the derivatives that were studied. The one-electron redox process for $^{Br2}\mathrm{Fc}^+/^{Br2}\mathrm{Fc}$ at 0.763 V vs Ag/AgCl was reversible ($\Delta E_{1/2}$ = 87 mV and i_{pa}/i_{pc} = 1.04 at 100 mVs^{-1} scan rate), as shown in Figure 158. Interestingly, a Randles-Sevcik analysis of the peak current vs the square root of the scan rate revealed that ^{Br2}Fc, despite its higher molecular weight, shows relatively higher diffusion coefficient values for both oxidized and reduced species (1.5 and 1.81 x 10^{-7} cm^{2}s^{-1}) when compared to those of other ferrocene derivatives. These data demonstrate the ability of ^{Br2}Fc to serve as an effective redox mediator for electrocatalytic oxidation of benzylic amines.

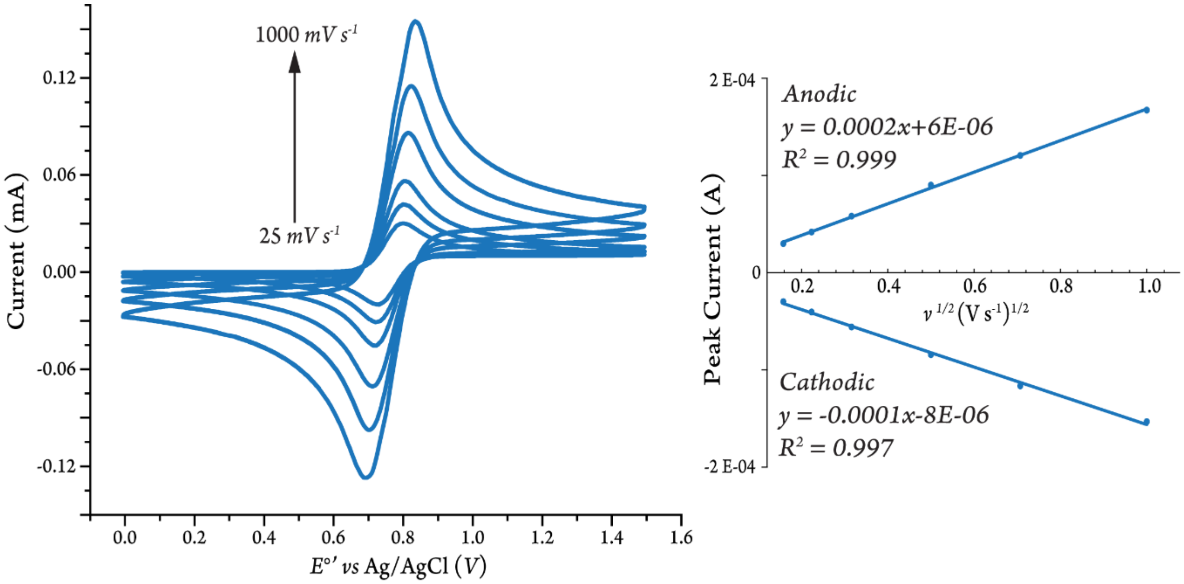

Figure 158. (Left) Cyclic voltammogram of the ^{Br2}Fc^{+}/^{Br2}Fc couple (2 mM) at various scan rates in MeCN with $[(n\text{Bu})_4\text{N}][\text{PF}_6]$ as the supporting electrolyte (100 mM). (Right) Randles-Sevcik plot of the CV data.

Cyclic voltammetry measurements of the three chosen ferrocene derivatives (Fc, ^{Br}Fc, ^{Br2}Fc) in the presence of increasing concentrations of BA and PA were measured to determine which ferrocene would act as the best mediator. The shape of the CV responses indicate whether or not catalytic activity is occurring, as described by Saveant.[92] As shown in figure 162, ferrocene did not act as a redox mediator in the presence of either amine, most likely due to its much lower redox potential as compared to the peak oxidation potential values of both BA and PA. ^{Br}Fc offered a slightly more catalytic response, but only in the highest concentrations of BA and PA. Figure 159 demonstrates the CV responses of ^{Br2}Fc obtained with increasing concentrations of BA and PA at 100 mVs^{-1}. Notably, electrode surface fouling was no longer observed when ^{Br2}Fc was present with each amine. Instead, the current increased from the current acquired with ^{Br2}Fc alone, representing a reversible electron transfer (from the amine to the electrochemically generated ferricenium) followed by an irreversible homogeneous chemical reaction, also known as an E_rC_i' catalytic mechanism, in which the redox mediator is regenerated on the timescale of the scan rate and is proportional to catalyst activity.[92, 93]

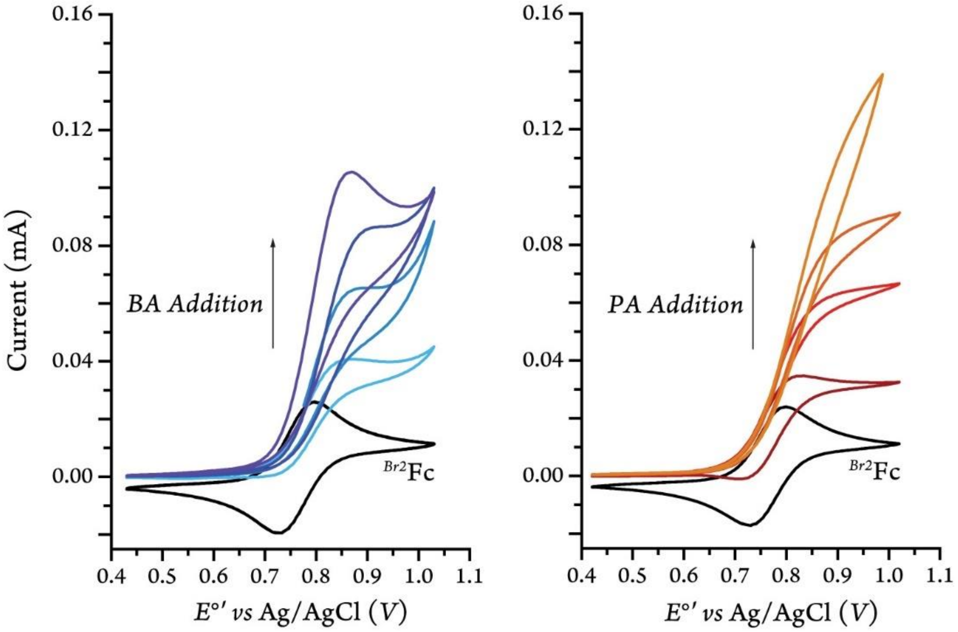

Figure 159. Cyclic voltammograms of 1 mM ^{Br2}Fc (black) in MeCN (100 mM $[(n\mathrm{Bu})_4\mathrm{N}][\mathrm{PF}_6]$) with the addition of 100, 250, 500, and 1000 mM of BA (left) and 10, 50, 100, and 500 mM of PA (right) at 100 mVs^{-1}.

Other important factors to note are the catalysis-initiating redox potential (E_{redox}), the potential necessary for catalysis (E_{cat}) and the half-wave potential ($E_{cat/2}$). E_{redox} is the redox potential of the mediator (^{Br2}Fc) without the amine which provides thermodynamic information about the reaction, and $E_{cat/2}$ is the potential at which half of the maximum catalytic current is measured and provides kinetic information. Determining $\mathrm{E}_{\mathrm{cat}}$ has not been consistent among reports, as some suggest that this is the potential at which the catalytic peak begins ("onset"), while others use the potential of the peak current. For this reason, it has been suggested by Dempsey and coworkers that the most effective way to study the effect of a redox mediator on catalysis is to look at the $E_{cat/2}$ value.[93] For our systems, both E_{cat} and $E_{cat/2}$ values are presented in Table 22, where we measured E_{cat} as the potential at the maximum current. It was found that the $\mathrm{E}_{\mathrm{cat/2}}$ value for both BA and

PA decreases by approximately 430 mV when the amines are oxidized with ${}^{Br2}Fc^+$ as a redox mediator as compared to their direct electrochemical oxidations. Additionally, both $E_{cat/2}$ values are very close to the E_{redox} of ^{Br2}Fc ($E_{cat/2}$ = 0.798 V, E_{redox} = 0.763 V), which is expected for an efficient catalytic system.

In the case of benzylamine, at 100 mVs^{-1} scan rate, the voltammogram was the most S-shaped at 100 mM, and then began to peak again at concentrations above 500 mM. This can be ascribed to competition between the substrate oxidation and the diffusion of new substrate towards the electrode.[92, 93] This can be avoided by increasing the scan rate, as seen in Figure 160, where the voltammogram became less peak-shaped as the scan rate increased. With 2-picolylamine, the S-shaped voltammograms appeared at much lower concentrations of the amine (10 mM) and did not form into a peaked-shape response even at a concentration of 500 mM. This demonstrates that the amine is at equal concentrations both in the bulk solution and at the electrode. Comparison between CV responses for both substrates in similar conditions (i.e., scan rate, substrate and mediator concentrations, and diffusion rates) infers that the electron transfer from the substrate to the ferricenium generated during catalysis is different for benzylamine and 2-picolylamine (as shown in the kinetic zone diagram illustrated by Dempsey *et al.*, see Figure 163 for more details). Studies are underway to determine the exact rate of electron transfer using CV simulation software.

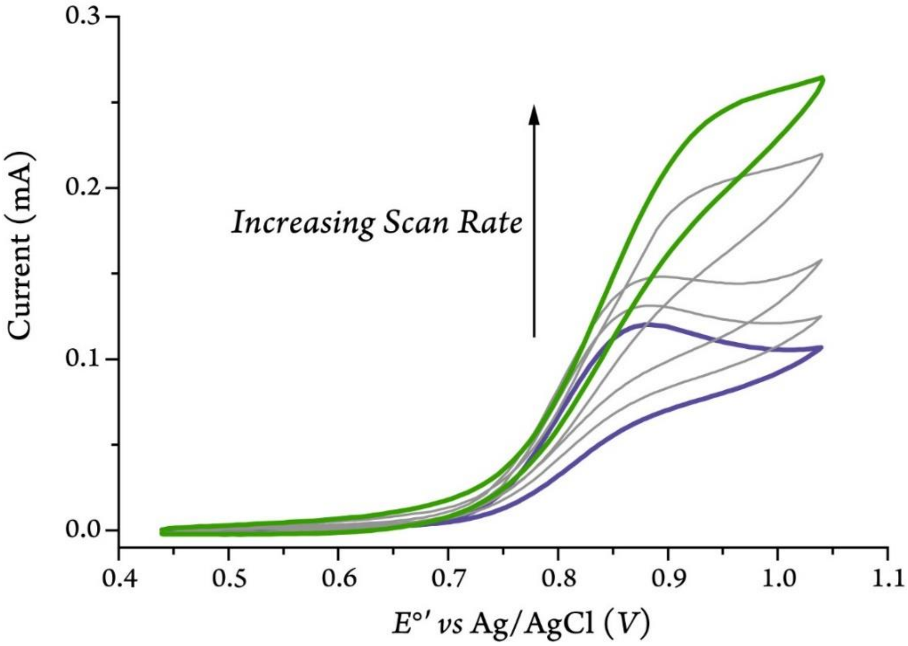

Figure 160. Cyclic voltammograms of ^{Br2}Fc (1 mM) in MeCN (100 mM [(*n*Bu)$_4$N][PF$_6$]) in the presence of 1 M benzylamine at scan rates of 100, 250, 500, and 3500 mVs^{-1}.

BENZYLAMINE ELECTROCATALYTIC OXIDATION

The utility of ^{Br2}Fc as the redox mediator for oxidation of BA was then probed under anaerobic controlled-potential electrolysis, see Supporting Information for details. After purification, we observed the coupled imine product, *N*-(benzylidene)benzylamine (**5**), as the major product of the reaction, with 90% of the electrons removed from the reaction mixture resulting in the formation of the desired product (calculated by Equation 1, where *z*, *n*, *F*, and *Q* are the electrons needed to form the product, the number of moles of the product that were obtained, Faraday's Constant, and the number of coulombs passed in the experiment). Our proposed mechanism for this reaction as well as some of the key product characterization details are shown in Scheme 3.

$$\text{Faradaic Efficiency} = \frac{z \text{ x } n \text{ x } F}{Q} \text{ x } 100 \qquad (1)$$

Scheme 3. Proposed mechanism for the electrocatalytic oxidation of benzylamine mediated by ^{Br2}Fc.*

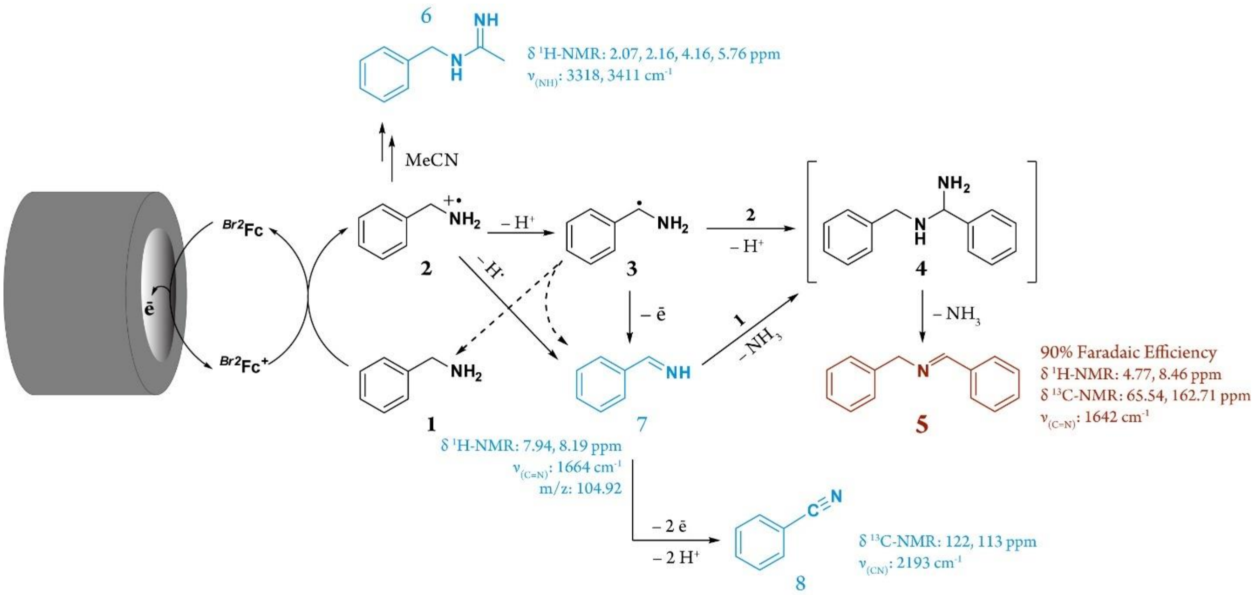

*The major product is shown in red and minor products formed during the electrocatalysis are displayed in blue.

Characterization data collected from the anaerobic electrochemical oxidation of benzylamine mediated by ^{Br2}Fc show the formation of the coupled imine product typically formed upon the oxidation of benzylamine under aerobic conditions (Figures 164-169). As is discussed in several studies of amine oxidation,[94-96] the first electron oxidation step forms a radical cation on the nitrogen (**2**). In our E_rC_i' mechanism, BA (**1**) transfers one electron to the electrochemically generated $^{Br2}Fc^+$ to regenerate ^{Br2}Fc in the rate-limiting step. That affords the radical cation (**2**) and results in a dramatic estimated acidification and significant weakening of the benzylic C−H bond.[97, 98] This radical cation intermediate can undergo various irreversible chemical reactions. The deprotonation of amine radical cation (**2**) at the α-position generates benzyl radical (**3**) which can couple to an amine radical cation (**2**) to form an intermediate species (**4**), which loses ammonia to form the coupled product (**5**). Additionally, the benzyl radical can either undergo disproportionation to form the original benzylamine (**1**) along with an aldimine (**7**), or a one-electron oxidation followed by deprotonation to form the aldimine (**7**), which with the addition of benzylamine can form the coupled product (**5**). Alternatively, a direct hydrogen atom transfer (HAT) from the weakened benzylic C–H bond of the amine radical cation followed by a deprotonation can generate the aldimine (**7**). Minor side reactions during the electrolysis can also include the amine radical cation reacting with acetonitrile/solvent to form an amidine species (**6**).[99, 100] Finally, the aldimine (**7**) can be further oxidized to form benzonitrile (**8)**.

It is important to note that hydrolysis of the imine to a benzaldehyde can also occur due to aerobic conditions during purification, however there was no evidence of such products prior to column chromatography. We have performed the electrocatalytic oxidation of 2-picolylamine in a similar manner as benzylamine, and studies are currently underway to characterize the products of that reaction.

Conclusion

Electrochemical oxidation of amines using a redox mediator presents many benefits. Most notably, fouling of the electrode surface is prevented, and the potential at which the catalytic oxidation reaction occurs ($E_{cat/2}$) is greatly reduced. We hypothesize that the rate limiting step of the E_rC_i mechanism, a one-electron transfer between the amine and ${}^{Br2}Fc^+$, is different for benzylamine and 2-picolylamine, demonstrated through cyclic voltammetry studies. Simulation data is being collected for these systems to determine the actual electron-transfer rates for these processes. Finally, we have established an anaerobic electrocatalytic oxidation method for the oxidation of benzylamine, which utilizes the electrons removed during the reaction at 90% efficiency for forming the desired coupled imine product while suppressing an excess of problematic side reactions such as hydrolysis or overoxidation of the substrate that can occur under aerobic conditions. These results should guide the development of electrocatalytic systems where the modes of reactivity can be controlled for the radicals formed to transform simple compounds into chemicals of higher complexity and value.

Experimental Section

GENERAL METHODS

All chemicals and solvents were of commercially available grade, unless otherwise noted. Acetonitrile (MeCN) and toluene were purchased from Sigma Aldrich. All solvents were further purified by passing through a 60 or 18 cm-long activation alumina column under argon using a solvent purification system (Innovative Technologies or Inert PureSolve Micro). Acetonitrile was then bubbled with argon for 45-60 minutes and stored in the glovebox over 3 Å molecular sieves for at least 72 hours prior to use.

Infrared (IR) spectra were obtained using a PerkinElmer Spectrum 65 Fourier Transform IR (FT-IR). All NMR spectra were recorded on a JEOL 400 or 500 MHz instrument. The chemical shifts were referenced against the CH_3 and C≡N shifts for the MeCN-d_3 solvent. LC-MS experiments were conducted using a Waters Acquity Ultra Performance Liquid Chromatography System (UPLC) coupled to a Thermo Scientific LTQ XL Linear Ion Trap Mass Spectrometer. Electrochemical data was collected using a Bio-Logic SP-200 potentiostat.

Benzylamine (>99.0%) and *1,1'*-dibromoferrocene (>98%) were purchased from Tokyo Chemical Industry (TCI). Silver nitrate (>99.9%) and potassium chloride (99%) were purchased from Alfa Aesar, as was the 0.180 mm thick Nafion N-117 membrane. 2-picolylamine/2-aminomethylpyridine (98%) and *tetra-n*-butylammonium hexafluorophosphate (98%) were purchased from Oakwood Chemicals.

Deuterated acetonitrile (MeCN-d_3, 99.8%) was purchased from Cambridge Isotope Laboratories. Distilled water was further purified by a PURELAB flex 1 Analytical Ultrapure Water System (ELGA) for a specific resistance of 18.2 MΩ·cm at 25°C.

ELECTROCHEMICAL MEASUREMENTS

Cyclic Voltammetry. A three-electrode setup was used for all voltammetry experiments with a 3.0-mm glassy carbon disk working electrode, a carbon rod counter electrode, and a leak-free Ag/AgCl reference electrode (3.4 M KCl). The reference electrodes were stored in either a 0.05 M H_2SO_4 aqueous solution or a saturated KCl aqueous solution between experiments. The potentials were referenced to the Ag/AgCl electrode by first measuring the potential of the ferrocene/ferricenium couple under identical solvent/electrolyte conditions. All electrodes were cleaned with acetone and nanopure water before and after use.

Bulk Electrolysis. Reactions were performed in an H-cell where the 1 mm thick glassy carbon plate working and Ag/$AgNO_3$ (0.01 M in MeCN) reference electrodes were separated from the Pt mesh counter electrode using a 0.180 mm thick Nafion N-117 membrane. The "counter solution" was comprised of only the electrolyte, $[(nBu)_4N][PF_6]$ (0.1 M) and the "working solution" was comprised of the electrolyte (0.1 M), ^{Br2}Fc (1 mM), and the substrate of interest (1 M benzylamine, 500 mM 2-picolylamine). The solutions (leaving out the amines) were made in the glovebox and brought out to fill each side of the cell, which was under argon. The substrate was then added to the working solution under argon. A unique bubbling system was used in which argon bubbled into the cell was first bubbled through MeCN to ensure that the solution would not evaporate during electrolysis. The potential was kept at 0.950 V vs Ag/AgCl, and the reaction continued until the resulting current was unchanging.

PURIFICATION AND CHARACTERIZATION OF THE PRODUCTS.

Benzylamine Oxidation. The first fraction collected from column chromatography, mostly the coupled product **5**, was collected as a pale-yellow oil and characterized. FT-IR (cm^{-1}): $\nu_{(C=N)}$ = 1642 (Figure 166). ^{1}H-NMR (MeCN-d_3, 500 MHz; δ, ppm): 4.77 (d, 2H), 8.46 (s, 1H), 7.27 (q, 1H), 7.35 (d, 4H), 7.45 (m, 3H), 7.78 (dd, 2H) (Figure 164). ^{13}C-NMR (MeCN-d_3, 500 MHz, δ, ppm): 65.54 (C−N), 127.83, 128.96 (d), 129.40, 129.65, 131.67, 137.46, 140.86, 162.71 (C=N) (Figure 165).

The second fraction contained a mixture of compounds as shown by the NMR spectra, including an amidine and nitrile. The evidence for the amidine is as follows: FT-IR (cm^{-1}):

$\nu_{(N-H)}$ = 3318, 3411 (sh); $\nu_{(C=N)}$ = 1598 (Figure 169). ^{1}H-NMR (MeCN-d_3, 500 MHz; δ, ppm): 2.07 (s, 3H), 4.16 (d, 2H), 5.76 (br. s, 1H) (Figure 167). ^{13}C-NMR (MeCN-d_3, 500 MHz; δ, ppm): 19.80 (CH3), 47.38 (CH2) (Figure 168). Evidence for the nitrile is as follows: FT-IR (cm^{-1}): ν(C≡N) = 2193 (Figure 169); ^{13}C-NMR (MeCN-d_3, 500 MHz; δ, ppm): 122, 113 (Figure 168). Evidence for the aldimine is as follows: ^{1}H-NMR (MeCN-d_3, 500 MHz; δ, ppm): 7.94 (t), 8.19 (br. s) (Figure 167); FT-IR (cm^{-1}): $\nu_{(C=N)}$ = 1664 (Figure 169); LC-MS: *m/z*: 104.92.

Supporting Information for Chapter 2

CYCLIC VOLTAMMETRY DATA

a. Ferrocene and electron-deficient derivatives

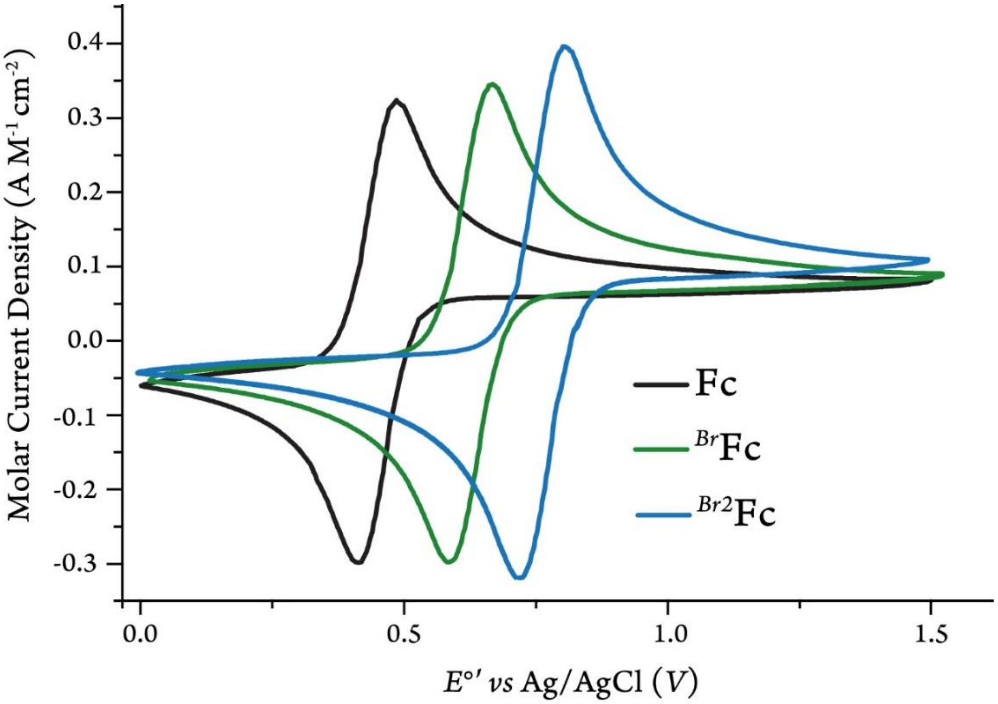

Figure 161. Cyclic voltammograms of ferrocene, 1-bromoferrocene, and *1,1'*-dibromoferrocene at 100 mVs^{-1} in MeCN with [(nBu)$_4$N][PF$_6$] as the supporting electrolyte (100 mM).

Table 21. $E_{1/2}$, $\Delta E_{1/2}$, and i_{pa}/i_{pc} values for ferrocene, 1-bromoferrocene, and *1,1'*-dibromoferrocene in MeCN with 100 mM of $[(n\text{Bu})_4\text{N}][\text{PF}_6]$ as the supporting electrolyte.

Ferrocene Derivative	**$E_{1/2}$**	**$\Delta E_{1/2}$***	**I_{PA}/I_{PC}***
Fc	0.450	0.076	0.98
^{Br}Fc	0.628	0.081	1.01
^{Br2}Fc	0.763	0.087	1.04

*These values were obtained at 100 $\text{mV}\cdot\text{s}^{-1}$ scan rate.

b. Benzylamine and 2-picolylamine redox mediated oxidation

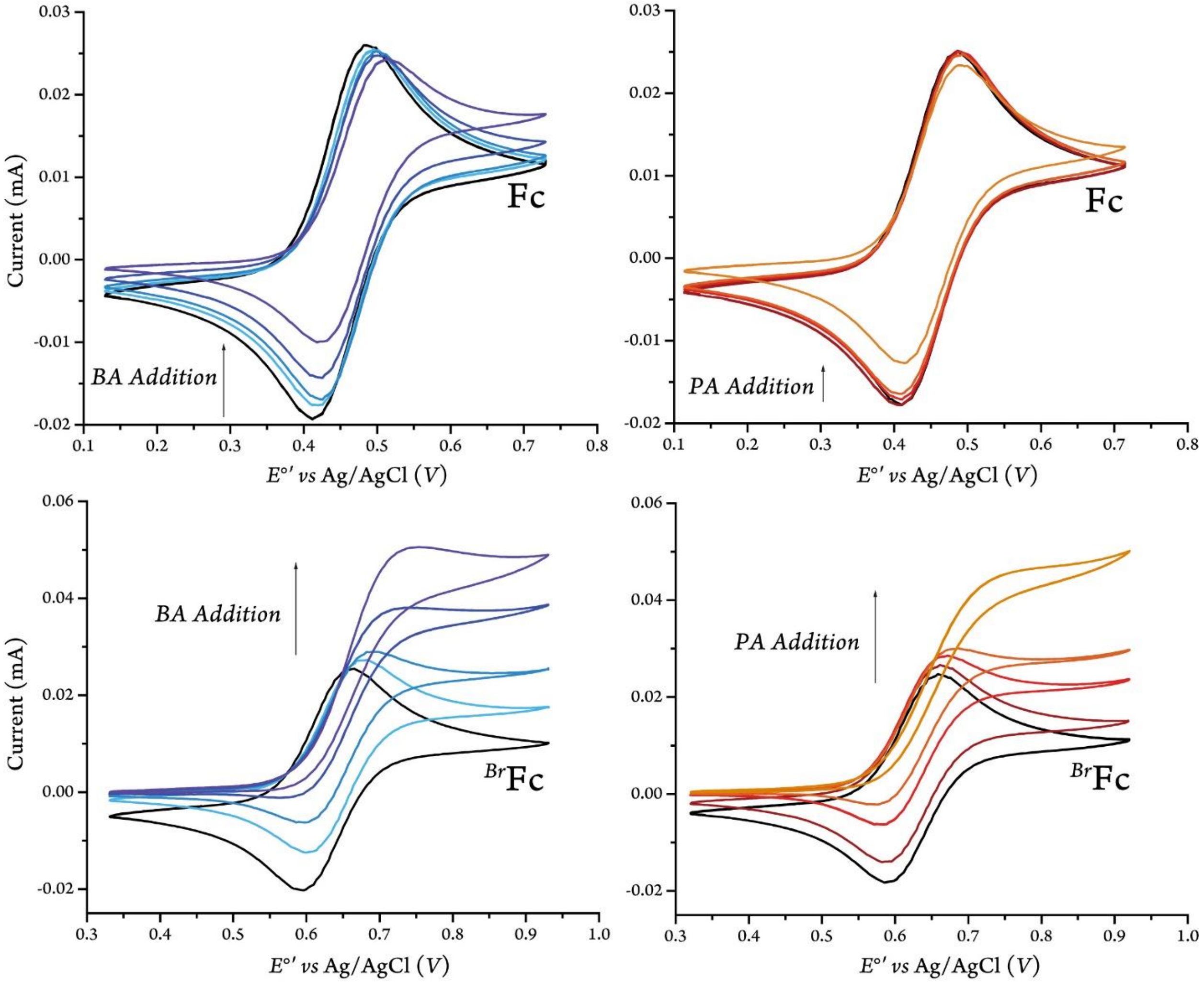

Figure 162. Cyclic voltammograms of (top) 1 mM Fc and (bottom) 1 mM ^{Br}Fc in MeCN (100 mM [(nBu)$_4$N][PF$_6$]) with the addition of 100, 250, 500, and 1000 mM of BA (left) and 10, 50, 100, and 500 mM of PA (right) at 100 mVs^{-1}.

Table 22. E_{cat} and $E_{cat/2}$ values for the direct and redox mediated oxidation of benzylamine and 2-picolylamine in MeCN with 100 mM of $[(n\text{Bu})_4\text{N}][\text{PF}_6]$ as the supporting electrolyte.

	Direct Oxidation		**^{Br2}Fc Mediated Oxidation**	
	E_{cat}	$E_{cat/2}$	E_{cat}	$E_{cat/2}$
Benzylamine	1.55	1.229	0.950	0.798
2-Picolylamine	1.62	1.234	0.950	0.789

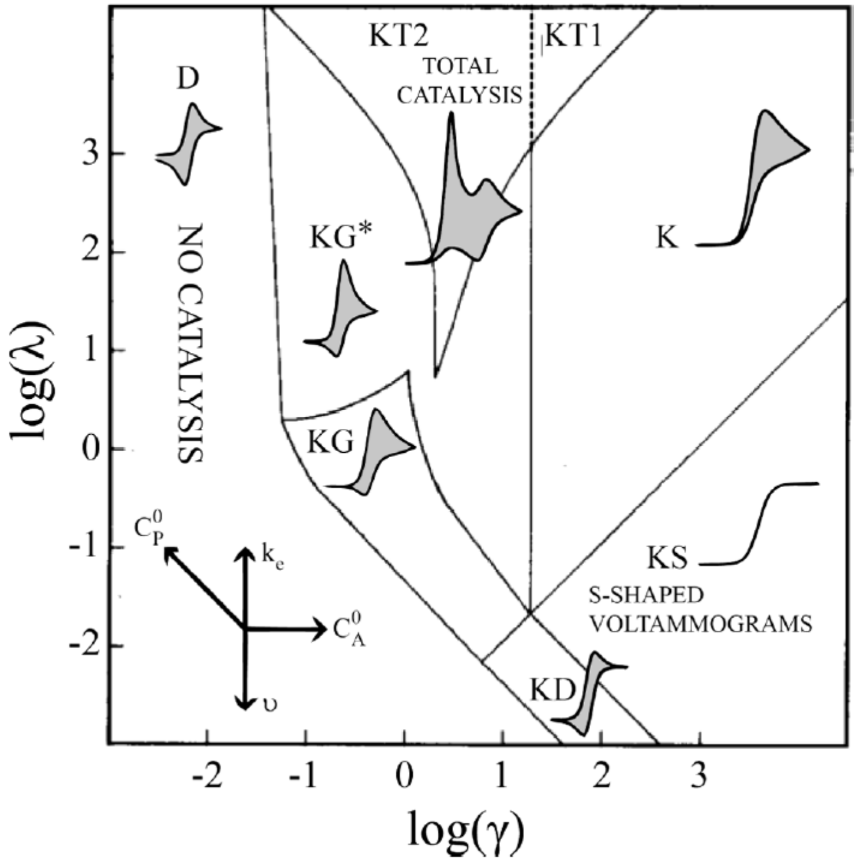

$$\lambda = \left(\frac{RT}{F}\right)\left(\frac{k_e C_P^0}{\upsilon}\right)$$

$$\gamma = \frac{C_A^0}{C_P^0}$$

Figure 163. Kinetic zone diagram for catalytic CV responses (left), based on the kinetic parameter λ and the excess factor γ (right). Reprinted with permission from [101]. Copyright 2014 American Chemical Society.

CHARACTERIZATION DATA FOR THE MAJOR AND MINOR PRODUCTS OF ELECTROCATALYTIC BENZYLAMINE OXIDATION MEDIATED BY ^{Br2}FC

Anaerobic controlled-potential electrolysis was performed in a separated “H-cell” in order to separate the processes at the working electrode from those at the counter. The ^{1}H-NMR spectra of the crude solution after electrolysis showed that some BA remained in the mixture, and there was another compound present whose shifts matched those expected of the coupled product **5**. The solvent, along with some of the benzylamine, was removed from the “working electrode” solution under vacuum. A minimal amount of toluene was added to the dark brown sludge and the mixture was filtered to separate the products from the electrolyte. The solvent was again removed under vacuum. Thin layer chromatography on alumina with a 60% hexanes/40% ethyl acetate mixture revealed two major fractions, besides benzylamine, which were separated through column chromatography of the same conditions. Through column chromatography we were able to separate the benzylamine from two other species present in the solution, as BA was no longer seen in the NMR spectra of the mixture after the column. The first fraction to elute from the column was the major coupled product. The second fraction contained a mixture of minor products. Following is the characterization data of both fractions.

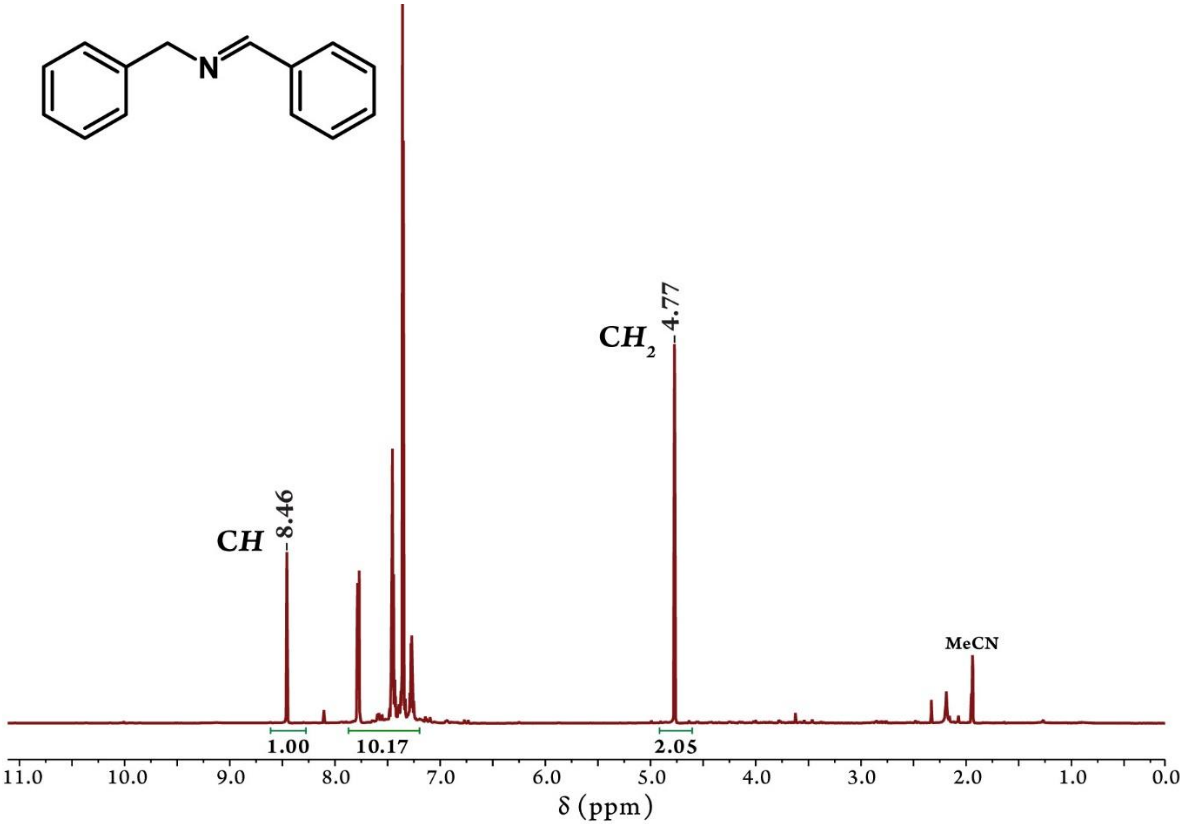

Figure 164. The ^{1}H-NMR spectra of the coupled product formed as a result of the controlled-potential electrolysis of benzylamine using ^{Br2}Fc as a redox mediator.

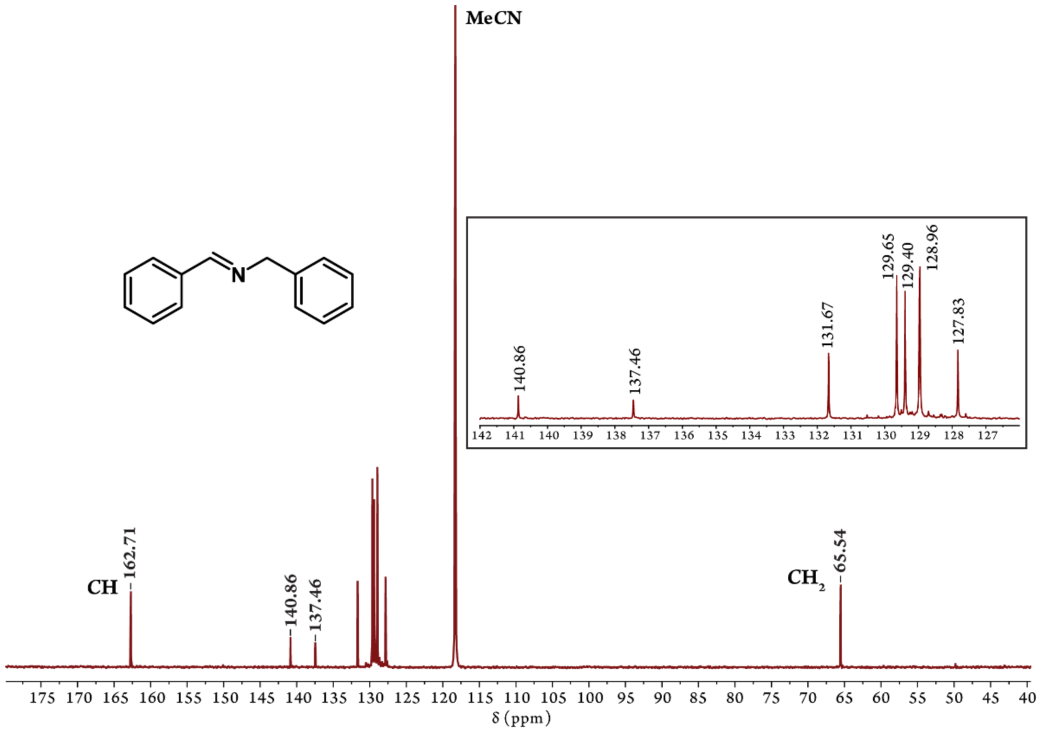

Figure 165. The ^{13}C-NMR spectra of the coupled product formed as a result of the controlled-potential electrolysis of benzylamine using ^{Br2}Fc as a redox mediator. Inset shows the aromatic region.

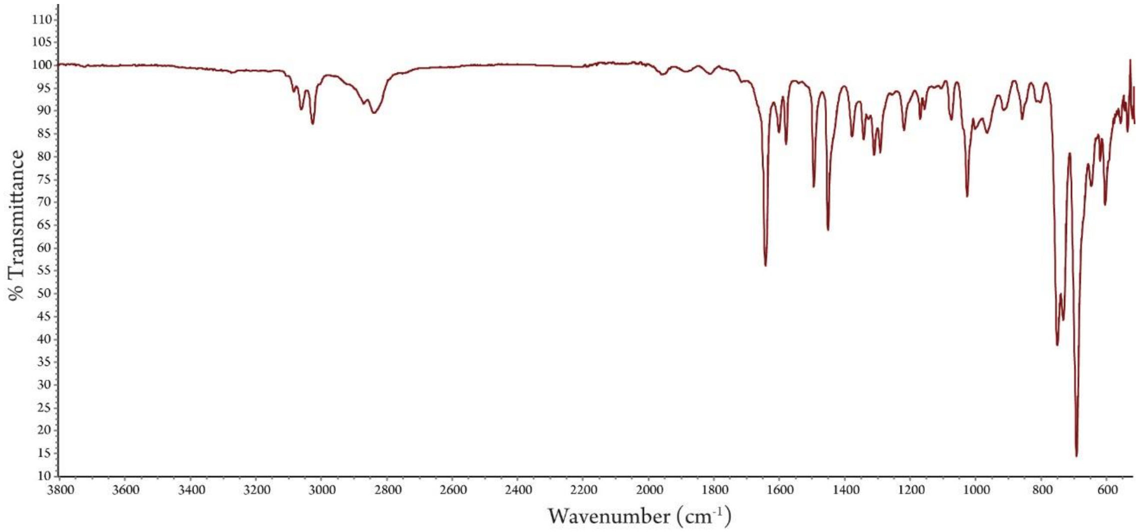

Figure 166. IR Spectrum of the major product of benzylamine oxidation.

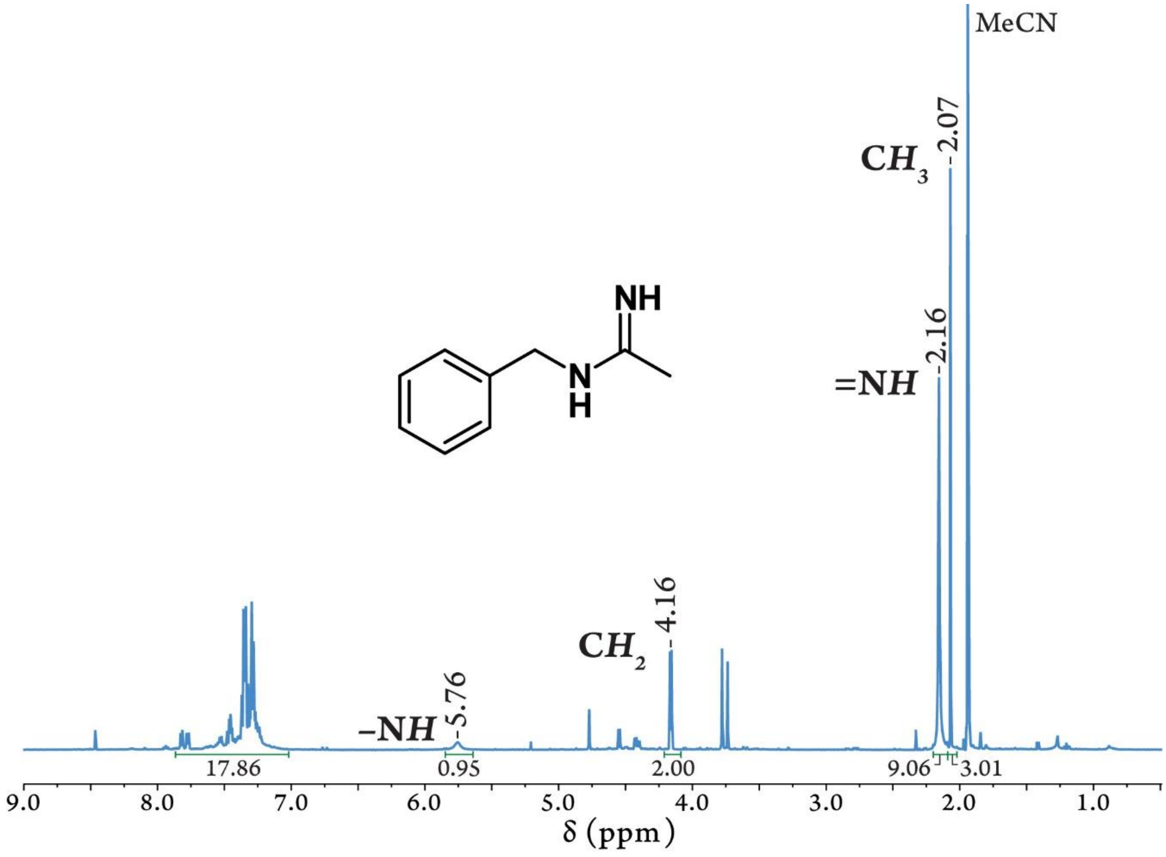

Figure 167. The ^{1}H-NMR spectra of the minor species mixture obtained from the controlled-potential electrolysis of benzylamine using ^{Br2}Fc as a redox mediator, with emphasis on peaks that correspond to a benzyl-amidine structure.

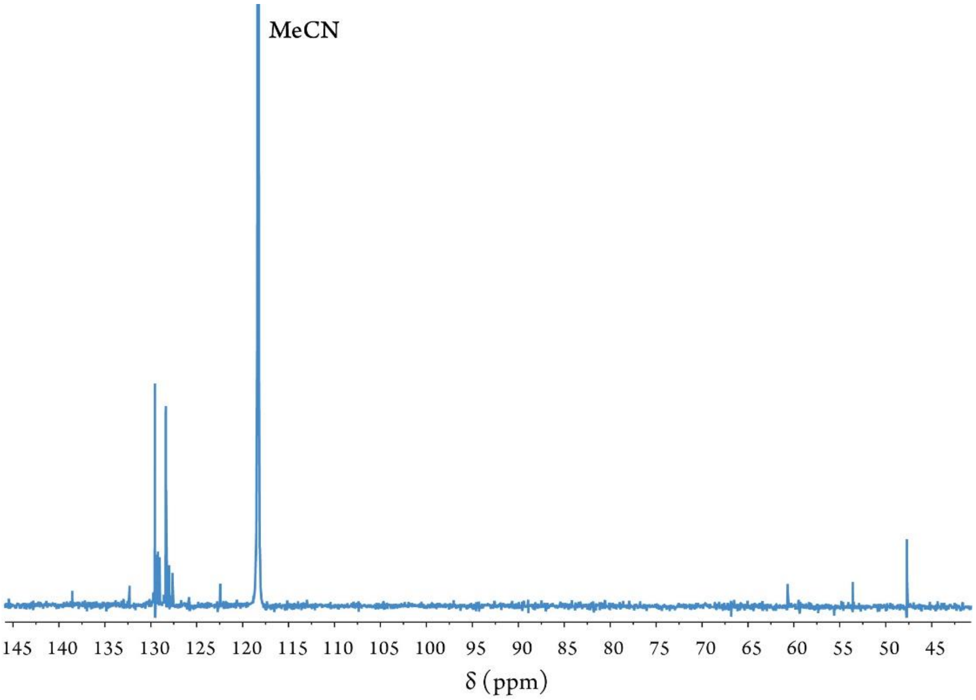

Figure 168. ^{13}C-NMR spectrum of the minor products of benzylamine oxidation.

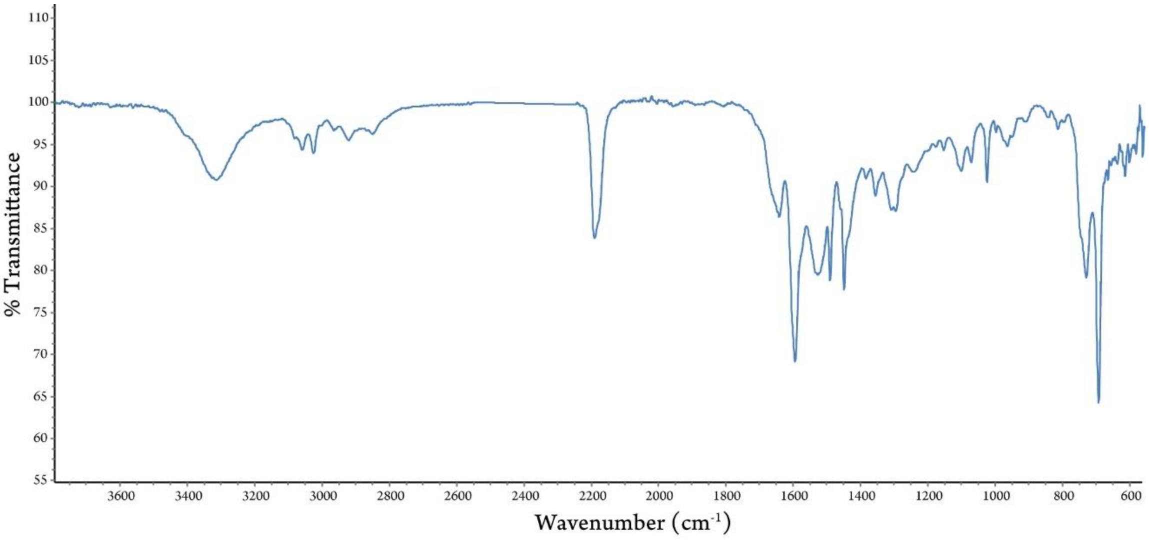

Figure 169. IR spectrum of the minor products of benzylamine oxidation.

REFERENCES

1. (a) Kealy, T. J.; Pauson, P. L., A New Type of Organo-Iron Compound. *Nature* **1951,** *168* (4285), 1039-1040; (b) Wilkinson, G.; Rosenblum, M.; Whiting, M. C.; Woodward, R. B., The Structure of Iron Bis-Cyclopentadienyl. *J. Am. Chem. Soc.* **1952,** *74* (8), 2125-2126.

2. (a) Haaland, A., Molecular Structure and Bonding in the 3d Metallocenes. *Acc. Chem. Res.* **1979,** *12* (11), 415-422; (b) Cantrill, S., An Iron-Clad Structure. *Nature* **2014,** *511* (7509), 11-11; (c) Seeman, J. I.; Cantrill, S., Wrong But Seminal. *Nat. Chem.* **2016,** *8* (3), 193-200.

3. (a) Fery-Forgues, S.; Delavaux-Nicot, B., Ferrocene and Ferrocenyl Derivatives in Luminescent Systems. *J. Photochem. Photobiol. A* **2000,** *132* (3), 137-159; (b) van Staveren, D. R.; Metzler-Nolte, N., Bioorganometallic Chemistry of Ferrocene. *Chem. Rev.* **2004,** *104* (12), 5931-5986; (c) Togni, A.; Hayashi, T., *Ferrocenes: Homogeneous Catalysis, Organic Synthesis, Materials Science*. Wiley: 2008; (d) Hagen, H.; Marzenell, P.; Jentzsch, E.; Wenz, F.; Veldwijk, M. R.; Mokhir, A., Aminoferrocene-Based Prodrugs Activated by Reactive Oxygen Species. *J. Med. Chem.* **2012,** *55* (2), 924-934; (e) Astruc, D., Why is Ferrocene so Exceptional? *Eur. J. Inorg. Chem.* **2017,** *2017* (1), 6-29; (f) Patra, M.; Gasser, G., The Medicinal Chemistry of Ferrocene and Its Derivatives. *Nat. Rev. Chem.* **2017,** *1* (9), 0066; (g) Fitzpatrick, K. P.; Schwamb, C. B.; Check, C. T.; Jang, K.-P.; Barsoum, D. N.; Scheidt, K. A., Development of Ferrocene-Based Planar Chiral Imidazopyridinium Salts for Catalysis. *Organometallics* **2020,** *39* (14), 2705-2712.

4. Soon after the discovery of the bis(*η*5-cyclopentadienyl) iron(II) complex in 1951, the term “ferrocene” was coined by Woodward and Whiting. They established the aromatic character of the cyclopentadienyl rings of ferrocene, coining its now ingrained name having the suffix “-ene” in analogy to organic aromatic compounds such as benzene, naphthalene, etc. Additionally, the prefix “ferro-” was used to specify the iron(II) oxidation state in ferrocene while the prefix “ferri-” was assigned to the one-electron oxidized counterpart with the iron(III) center and thus named the ferricenium ion. A common alternative spelling for the latter is ferricinium. Our review of the past seven decades of literature revealed that with a dramatic increase in applications of ferrocene and ferricenium ion in a variety of fields including materials, medicine and energy, the original name of the oxidized complex gradually fell out of common usage and was superseded by the name ferrocenium. The ratio of the usage of the names ferricenium/ferricinium and ferrocenium has reversed over the past several decades. Today, the oxidized ferrocene is commercially marketed as “ferrocenium” and either names are found in the current

literature. In 2005, IUPAC strongly recommended the name bis(*η*5-cyclopentadienyl) iron(+1) to avoid any ambiguity.

5. (a) Gagne, R. R.; Koval, C. A.; Lisensky, G. C., Ferrocene As an Internal Standard for Electrochemical Measurements. *Inorg. Chem.* **1980,** *19* (9), 2854-2855; (b) Gritzner, G.; Kuta, J., Recommendations on Reporting Electrode Potentials in Nonaqueous Solvents (Recommendations 1983). *Pure Appl. Chem.* **1984,** *56* (4), 461-466; (c) Kotz, J. C., The Electrochemistry of Transition Metal Organometallic Compounds. In *Topics in Organic Electrochemistry*, Fry, A. J.; Britton, W. E., Eds. Springer, Boston, MA: 1986; pp 81-176.

6. (a) Malischewski, M.; Adelhardt, M.; Sutter, J.; Meyer, K.; Seppelt, K., Isolation and Structural and Electronic Characterization of Salts of the Decamethylferrocene Dication. *Science* **2016,** *353* (6300), 678-682; (b) Goodwin, C. A. P.; Giansiracusa, M. J.; Greer, S. M.; Nicholas, H. M.; Evans, P.; Vonci, M.; Hill, S.; Chilton, N. F.; Mills, D. P., Isolation and Electronic Structures of Derivatized Manganocene, Ferrocene and Cobaltocene Anions. *Nat. Chem.* **2021,** *13* (3), 243-248.

7. Woodward, R. B.; Rosenblum, M.; Whiting, M. C., A New Aromatic System. *J. Am. Chem. Soc.* **1952,** *74* (13), 3458-3459.

8. (a) Prins, R.; Reinders, F. J., Electron Spin Resonance of the Cation of Ferrocene. *J. Am. Chem. Soc.* **1969,** *91* (17), 4929-4931; (b) Prins, R., Electronic Structure of the Ferricenium Cation. *Mol. Phys.* **1970,** *19* (5), 603-620; (c) Sohn, Y. S.; Hendrickson, D. N.; Gray, H. B., Electronic Structure of Ferricenium Ion. *J. Am. Chem. Soc.* **1970,** *92* (10), 3233-3234; (d) Rowe, M. D.; McCaffery, A. J., Electronic Structure of Ferricenium Ion from Absorption, MCD, and ESR Studies. *J. Chem. Phys.* **1973,** *59* (7), 3786-3794; (e) Bagus, P. S.; Walgren, U. I.; Almlof, J., A Theoretical Study of the Electronic Structure of Ferrocene and Ferricinium: Application to Mössbauer Isomer Shifts, Ionization Potentials, and Conformation. *J. Chem. Phys.* **1976,** *64* (6), 2324-2334.

9. Connelly, N. G.; Geiger, W. E., Chemical Redox Agents for Organometallic Chemistry. *Chem. Rev.* **1996,** *96* (2), 877-910.

10. (a) Sato, M.; Yamada, T.; Nishimura, A., Electrolytic Oxidation of Ferrocene In the Presence of Trace Amounts of Dissolved Oxygen. *Chem. Lett.* **1980,** *9* (8), 925-926; (b) Prins, R.; Korswagen, A. R.; Kortbeek, A. G. T. G., Decomposition of the Ferricenium Cation by Nucleophilic Reagents. *J. Organomet. Chem.* **1972,** *39* (2), 335-344; (c) Zotti, G.; Schiavon, G.; Zecchin, S.; Favretto, D., Dioxygen-Decomposition of Ferrocenium Molecules in Acetonitrile: The Nature of the Electrode-Fouling Films During Ferrocene Electrochemistry. *J. Electroanal. Chem.* **1998,** *456* (1), 217-221; (d) Singh, A.; Chowdhury, D. R.; Paul, A., A Kinetic Study of Ferrocenium Cation Decomposition Utilizing an Integrated Electrochemical

Methodology Composed of Cyclic Voltammetry and Amperometry. *Analyst* **2014,** *139* (22), 5747-5754.

11. Choi, H.; Hershberger, J. W.; Pinhas, A. R.; Ho, D. M., Isomerization of a Vinylcyclobutene to a Cyclohexadiene: A Nickel(I) Promoted Rearrangement. *Organometallics* **1991,** *10* (8), 2930-2936.

12. Today, ferrocene is readily available from more than 45 different commercial sources and it is as cheap as \$0.11 g^{-1}, so very few people choose to synthesize it in research laboratories. Ferricenium ion, however, is only available as the PF_6^- or BF_4^- salts through less than half the number of commercial suppliers and costs about 100 times more than the parent ferrocene complex.

13. Gray, H. B.; Hendrickson, D. N.; Sohn, Y. S., Magnetic Susceptibility Study of Various Ferricenium and Iron(III) Dicarbollide Compounds. *Inorg. Chem.* **1971,** *10* (8), 1559-1563.

14. Notably, a quick survey of the literature on the salts of ferricenium and its derivatives reveals that despite their wide application, especially those with weakly coordinating anions such as hexafluoroantimonate or fluoroarylborates analogs in recent reports, to date, information on the synthesis and characterization of these complexes is sparse and the reports lack the relevant experimental details.

15. (a) Krossing, I.; Raabe, I., Noncoordinating Anions—Fact or Fiction? A Survey of Likely Candidates. *Angew. Chem. Int. Ed.* **2004,** *43* (16), 2066-2090; (b) Aldrich, K. E.; Billow, B. S.; Holmes, D.; Bemowski, R. D.; Odom, A. L., Weakly Coordinating yet Ion Paired: Anion Effects on an Internal Rearrangement. *Organometallics* **2017,** *36* (7), 1227-1237.

16. (a) Mase, K.; Ohkubo, K.; Fukuzumi, S., Efficient Two-Electron Reduction of Dioxygen to Hydrogen Peroxide with One-Electron Reductants with a Small Overpotential Catalyzed by a Cobalt Chlorin Complex. *J. Am. Chem. Soc.* **2013,** *135* (7), 2800-2808; (b) Ehudin, M. A.; Gee, L. B.; Sabuncu, S.; Braun, A.; Moënne-Loccoz, P.; Hedman, B.; Hodgson, K. O.; Solomon, E. I.; Karlin, K. D., Tuning the Geometric and Electronic Structure of Synthetic High-Valent Heme Iron(IV)-Oxo Models in the Presence of a Lewis Acid and Various Axial Ligands. *J. Am. Chem. Soc.* **2019,** *141* (14), 5942-5960; (c) Zerk, T. J.; Saouma, C. T.; Mayer, J. M.; Tolman, W. B., Low Reorganization Energy for Electron Self-Exchange by a Formally Copper(III,II) Redox Couple. *Inorg. Chem.* **2019,** *58* (20), 14151-14158; (d) Krishnan, V. M.; Shopov, D. Y.; Bouchey, C. J.; Bailey, W. D.; Parveen, R.; Vlaisavljevich, B.; Tolman, W. B., Structural Characterization of the [CuOR]2+ Core. *J. Am. Chem. Soc.* **2021**, DOI: 10.1021/jacs.0c13470.

17. (a) O'Connor, A. R.; Nataro, C.; Golen, J. A.; Rheingold, A. L., Synthesis and Reactivity of $[N(C_6H_4Br)_3][B(C_6F_5)_4]$: the X-ray Crystal Structure of [Fe(C5H5)2]$[B(C_6F_5)_4]$. *J. Organomet. Chem.* **2004,** *689* (14), 2411-2414; (b) Rheingold, A. L.; Nataro, C., CSD Private Communication (CCDC# 1441545). **2015**.

18. Mews, N. M.; Berkefeld, A.; Hörner, G.; Schubert, H., Controlling Near-Infrared Chromophore Electronic Properties through Metal–Ligand Orbital Alignment. *J. Am. Chem. Soc.* **2017,** *139* (7), 2808-2815.

19. It is also worth mentioning that although ferricenium salts have been the subject of a variety of spectroscopic, electrochemical, and structural investigations over the past seven decades, these efforts have been mainly focused on the electron-rich ferricenium species and the very limited data available on the electron-deficient systems are sometimes ambiguous. This represents a surprising knowledge gap in the literature and the current study attempts to address some of that gap through a systematic and thorough evaluation of a series of highly organic soluble ferricenium derivatives.

20. Use of other very strong oxidizing agents such as nitrosonium, $[NO]^+$, salts or triarylaminium radical cations such as Magic Blue resulted in unwanted side reactions and will be discussed elsewhere.

21. Zhang, Y.; Santos, A. M.; Herdtweck, E.; Mink, J.; Kühn, F. E., Organonitrile Ligated Silver Complexes with Perfluorinated Weakly Coordinating Anions and Their Catalytic Application for Coupling Reactions. *New J. Chem.* **2005,** *29* (2), 366-370.

22. (a) Evans, J. C.; Lo, G. Y. S., Raman and Infrared Studies of Acetonitrile Complexed with Zinc Chloride. *Spectrochim. Acta* **1965,** *21* (6), 1033-1038; (b) Purcell, K. F.; Drago, R. S., Studies of the Bonding in Acetonitrile Adducts1. *J. Am. Chem. Soc.* **1966,** *88* (5), 919-924.

23. Song, L.; Trogler, W. C., $[(CO)_3(PPh_3)_2OsAg(O_2CCF_3)]$: A Model for an Intermediate on the Reaction Coordinate in Electron Transfer. *Angew. Chem. Int. Ed. Engl.* **1992,** *31* (6), 770-772.

24. (a) Carty, P.; Dove, M. F. A., The Reaction of Some Ferrocenyl Ketones with Anhydrous Silver Tetrafluoroborate, a New Route to Substituted Ferricenium salts. *J. Organomet. Chem.* **1971,** *28* (1), 125-132; (b) Bittner, C.; Bockfeld, D.; Tamm, M., Formation of Alkyne-Bridged Ferrocenophanes Using Ring-Closing Alkyne Metathesis on 1,1'-Diacetylenic Ferrocenes. *Beilstein J. Org. Chem.* **2019,** *15*, 2534-2543.

25. Yang, E. S.; Chan, M.-S.; Wahl, A. C., Rate of Electron Exchange Between Ferrocene and Ferricenium Ion from Nuclear Magnetic Resonance Studies. *J. Phys. Chem.* **1975,** *79* (19), 2049-2052.

26. (a) Gray, H. B.; Sohn, Y. S.; Hendrickson, N., Electronic Structure of Metallocenes. *J. Am. Chem. Soc.* **1971,** *93* (15), 3603-3612; (b) Anderson, S. E.; Rai, R., Mechanism of Spin Delocalization and Nature of the Ground state in Ferricenium Cations. *Chem. Phys.* **1973,** *2* (2), 216-225; (c) Duggan, D. M.; Hendrickson, D. N., Electronic Structure of Various Ferricenium Systems as Inferred from Raman, Infrared, Low-Temperature Electronic Absorption, and Electron Paramagnetic Resonance Measurements. *Inorg. Chem.* **1975,** *14* (5), 955-970.

27. (a) Reid, A. F.; Scaife, D. E.; Wailes, P. C., The Characterisation of Solid Cyclopentadienyl Metal Compounds by Their Near Infrared Reflection Spectra. *Spectrochim. Acta* **1964,** *20* (8), 1257-1268; (b) Cotton, F. A.; Marks, T. J., Infrared Study of the Structures of Cyclopentadienyl Compounds of Copper (I) and Mercury (II). *J. Am. Chem. Soc.* **1969,** *91* (26), 7281-7285.

28. Ding, W.; Sanderson, C. T.; Conover, R. C.; Johnson, M. K.; Amster, I. J.; Kutal, C., Characterization of the Low-Energy Electronic Excited States of Benzoyl-Substituted Ferrocenes. *Inorg. Chem.* **2003,** *42* (5), 1532-1537.

29. (a) Wexler, A. S., Integrated Intensities of Absorption Bands in Infrared Spectroscopy. *Applied Spectroscopy Reviews* **1967,** *1* (1), 29-98; (b) Socrates, G., *Infrared and Raman Characteristic Group Frequencies: Tables and Charts*. 3rd ed.; John Wiley & Sons, Ltd.: 2001.

30. Zeller, M.; Lufaso, M. W.; Curtin, L.; Hunter, A. D., CSD Private Communication (CCDC# 252665). **2004**, CSD Private Communication (CCDC# 252665).

31. Makal, A. M.; Plażuk, D.; Zakrzewski, J.; Misterkiewicz, B.; Woźniak, K., Experimental Charge Density Analysis of Symmetrically Substituted Ferrocene Derivatives. *Inorg. Chem.* **2010,** *49* (9), 4046-4059.

32. Butler, I. R.; Cullen, W. R.; Rettig, S. J.; Trotter, J., Structure of Benzoylferrocene. *Acta Cryst. C* **1988,** *44* (9), 1666-1667.

33. Gallagher, J. F.; Ferguson, G.; Ahmed, S. Z.; Glidewell, C.; Lewis, A., Accurate Redeterminations of 1,1'-Dibenzoylferrocene and (4-Nitrophenyl)ferrocene. *Acta Cryst. C* **1997,** *53* (12), 1772-1775.

34. (a) Bluemel, J.; Hebendanz, N.; Hudeczek, P.; Koehler, F. H.; Strauss, W., Synthesis and NMR Spectroscopy of Metallocenium Ions. Support for a New Ferromagnetic Coupling Mechanism in Decamethylmetallocenium Tetracyanoethenides. *J. Am. Chem. Soc.* **1992,** *114* (11), 4223-4230; (b) Helgaker, T.; Jaszuński, M.; Ruud, K., Ab Initio Methods for the Calculation of NMR Shielding and Indirect Spin−Spin Coupling Constants. *Chem. Rev.* **1999,** *99* (1), 293-352.

35. (a) Slocum, D. W.; Shenkin, P. S.; Engelmann, T. R.; Ernst, C. R., Fundamental Studies of Substituted Ferrocene Systems. I. Electronic Effects of Electron Donating Groups on the Ferrocene System. *Tetrahedron Lett.* **1971,** *12* (46), 4429-4432; (b) Slocum, D. W.; Ernst, C. R., Electronic Effects in Metallocenes and Certain Related Systems. In *Adv. Organomet. Chem.*, Stone, F. G. A.; West, R., Eds. Academic Press: 1972; Vol. 10, pp 79-114; (c) Pickett, T. E.; Richards, C. J., Assignment of ^{1}H-NMR Chemical Shifts in 1,2- and 1,1′-disubstituted ferrocenes. *Tetrahedron Lett.* **1999,** *40* (28), 5251-5254.

36. LeSuer, R. J.; Geiger, W. E., Improved Electrochemistry in Low-Polarity Media Using Tetrakis(pentafluorophenyl)borate Salts as Supporting Electrolytes. *Angew. Chem. Int. Ed.* **2000,** *39* (1), 248-250.

37. Lerner, H.-W.; Schödel, F.; Bru Roig, M.; Bolte, M., Tetra-n-butyl-ammonium Tetra-kis(penta-fluoro-phen-yl)borate. *Acta Cryst. E* **2006,** *62* (1), o372-o373.

38. Kim, E. H.; Lee, H. M.; Jeong, M. S.; Ryu, J. Y.; Lee, J.; Lee, B. Y., Methylaluminoxane-Free Chromium Catalytic System for Ethylene Tetramerization. *ACS Omega* **2017,** *2* (3), 765-773.

39. Kaspi-Kaneti, A. W.; Tuvi-Arad, I., Twisted and Bent Out of Shape: Symmetry and Chirality Analysis of Substituted Ferrocenes. *Organometallics* **2018,** *37* (19), 3314-3321.

40. (a) Wedeking, K.; Mu, Z.; Kehr, G.; Fröhlich, R.; Erker, G.; Chi, L.; Fuchs, H., Tetradecylferrocene: Ordered Molecular Array of an Organometallic Amphiphile in the Crystal and in a Two-dimensional Assembled Structure on a Surface. *Langmuir* **2006,** *22* (7), 3161-3165; (b) Wedeking, K.; Mu, Z.; Kehr, G.; Cano Sierra, J.; Mück Lichtenfeld, C.; Grimme, S.; Erker, G.; Fröhlich, R.; Chi, L.; Wang, W.; Zhong, D.; Fuchs, H., Oligoethylene Chains Terminated by Ferrocenyl End Groups: Synthesis, Structural Properties, and Two-Dimensional Self-Assembly on Surfaces. *Chem. Eur. J.* **2006,** *12* (6), 1618-1628.

41. Romanov, A. S.; Mulroy, J. M.; Khrustalev, V. N.; Antipin, M. Y.; Timofeeva, T. V., Monohalogenated Ferrocenes $C_5H_5FeC_5H_4X$ (X = Cl, Br and I) and a Second Polymorph of $C_5H_5FeC_5H_4I$. *Acta Cryst. C* **2009,** *65* (11), m426-m430.

42. Hnetinka, C. A.; Hunter, A. D.; Zeller, M.; Lesley, M. J. G., 1,1'-Di-bromo-ferrocene. *Acta Cryst. E* **2004,** *60* (12), m1806-m1807.

43. Morrison, C. A.; Bone, S. F.; Rankin, D. W. H.; Robertson, H. E.; Parsons, S.; Coxall, R. A.; Fraser, S.; Howell, J. A. S.; Yates, P. C.; Fey, N., Conformational Properties of Substituted Ferrocenes: Experimental and Theoretical Studies of the Molecular Structures of 1,1’-Di-tert-butylferrocene and Isopropylferrocene. *Organometallics* **2001,** *20* (11), 2309-2320.

44. LeSuer, R. J.; Buttolph, C.; Geiger, W. E., Comparison of the Conductivity Properties of the Tetrabutylammonium Salt of Tetrakis(pentafluorophenyl)borate Anion with Those of Traditional Supporting Electrolyte Anions in Nonaqueous Solvents. *Anal. Chem.* **2004,** *76* (21), 6395-6401.

45. Kadish, K. M.; Ding, J. Q.; Malinski, T., Resistance of Nonaqueous Solvent Systems Containing Tetraalkylammonium Salts. Evaluation of Heterogeneous Electron Transfer Rate Constants for The Ferrocene/Ferrocenium Couple. *Anal. Chem.* **1984,** *56* (9), 1741-1744.

46. (a) Jaffé, H. H., A Reëxamination of the Hammett Equation. *Chem. Rev.* **1953,** *53* (2), 191-261; (b) Hansch, C.; Leo, A.; Taft, R. W., A Survey of Hammett Substituent Constants and Resonance and Field Parameters. *Chem. Rev.* **1991,** *91* (2), 165-195.

47. Waniek, S. D.; Klett, J.; Förster, C.; Heinze, K., Polysubstituted Ferrocenes as Tunable Redox Mediators. *Beilstein J. Org. Chem.* **2018,** *14*, 1004-1015.

48. (a) Barrière, F.; Geiger, W. E., Use of Weakly Coordinating Anions to Develop an Integrated Approach to the Tuning of $\Delta E_{1/2}$ Values by Medium Effects. *J. Am. Chem. Soc.* **2006,** *128* (12), 3980-3989; (b) Geiger, W. E.; Barrière, F., Organometallic Electrochemistry Based on Electrolytes Containing Weakly-Coordinating Fluoroarylborate Anions. *Acc. Chem. Res.* **2010,** *43* (7), 1030-1039.

49. Aycock, D. F., Solvent Applications of 2-Methyltetrahydrofuran in Organometallic and Biphasic Reactions. *Org. Process Res. Dev.* **2007,** *11* (1), 156-159.

50. Gutmann, V., Solvent Effects on the Reactivities of Organometallic Compounds. *Coord. Chem. Rev.* **1976,** *18* (2), 225-255.

51. Ivanciuc, O.; Ivanciuc, T.; Filip, P. A.; Cabrol-Bass, D., Estimation of the Liquid Viscosity of Organic Compounds with a Quantitative Structure−Property Model. *J. Chem. Inf. Comput. Sci.* **1999,** *39* (3), 515-524.

52. Comelli, F.; Francesconi, R.; Bigi, A.; Rubini, K., Molar Heat Capacities, Densities, Viscosities, and Refractive Indices of Dimethyl Sulfoxide + Tetrahydropyran and + 2-Methyltetrahydrofuran at (293.15, 303.15, and 313.15) K. *J. Chem. Eng. Data* **2007,** *52* (2), 639-644.

53. Noviandri, I.; Brown, K. N.; Fleming, D. S.; Gulyas, P. T.; Lay, P. A.; Masters, A. F.; Phillips, L., The Decamethylferrocenium/Decamethylferrocene Redox Couple: A Superior Redox Standard to the Ferrocenium/Ferrocene Redox Couple for Studying Solvent Effects on the Thermodynamics of Electron Transfer. *J. Phys. Chem. B* **1999,** *103* (32), 6713-6722.

54. Wipf, D. O.; Kristensen, E. W.; Deakin, M. R.; Wightman, R. M., Fast-Scan Cyclic Voltammetry as a Method to Measure Rapid Heterogeneous Electron-Transfer Kinetics. *Anal. Chem.* **1988,** *60* (4), 306-310.

55. Elgrishi, N.; Rountree, K. J.; McCarthy, B. D.; Rountree, E. S.; Eisenhart, T. T.; Dempsey, J. L., A Practical Beginner's Guide to Cyclic Voltammetry. *J. Chem. Educ.* **2018,** *95* (2), 197-206.

56. Wang, Y.; Rogers, E. I.; Compton, R. G., The Measurement of the Diffusion Coefficients of Ferrocene and Ferrocenium and their Temperature Dependence in Acetonitrile Using Double Potential Step Microdisk Electrode Chronoamperometry. *J. Electroanal. Chem.* **2010,** *648* (1), 15-19.

57. (a) Valencia, D. P.; González, F. J., Estimation of Diffusion Coefficients by Using a Linear Correlation Between the Diffusion Coefficient and Molecular Weight. *J. Electroanal. Chem.* **2012,** *681*, 121-126; (b) Paul, A.; Borrelli, R.; Bouyanfif, H.; Gottis, S.; Sauvage, F., Tunable Redox Potential, Optical Properties, and Enhanced Stability of Modified Ferrocene-Based Complexes. *ACS Omega* **2019,** *4* (12), 14780-14789.

58. Hui, Y.; Webster, R. D., Absorption of Water into Organic Solvents Used for Electrochemistry under Conventional Operating Conditions. *Anal. Chem.* **2011,** *83* (3), 976-981.

59. (a) Friedman, H. L.; Mills, R., Hydrodynamic Approximation for Distinct Diffusion Coefficients. *J. Solution Chem.* **1986,** *15* (1), 69-80; (b) Costigliola, L.; Heyes, D. M.; Schrøder, T. B.; Dyre, J. C., Revisiting the Stokes-Einstein Relation without a Hydrodynamic Diameter. *J. Chem. Phys.* **2019,** *150* (2), 021101; (c) Evans, R.; Deng, Z.; Rogerson, A. K.; McLachlan, A. S.; Richards, J. J.; Nilsson, M.; Morris, G. A., Quantitative Interpretation of Diffusion-Ordered NMR Spectra: Can We Rationalize Small Molecule Diffusion Coefficients? *Angew. Chem. Int. Ed.* **2013,** *52* (11), 3199-3202.

60. Sheldrick, G. M. SHELXL-2018: Program for Crystal Structure Refinement; University of Göttingen: Göttingen, Germany, 2018.

61. Makal, A. M.; Plażuk, D.; Zakrzewski, J.; Misterkiewicz, B.; Woźniak, K. Experimental charge density analysis of symmetrically substituted ferrocene derivatives. *Inorg. Chem.* **2010**, *49*, 4046–4059.

62. (a) Wedeking, K.; Mu, Z.; Kehr, G.; Frohlich, R.; Erker, G.; Chi, L.; Fuchs, H. Tetradecylferrocene: Ordered molecular array of an organometallic amphiphile in the crystal and in a two-dimensional assembled structure on a surface. *Langmuir* **2006**, *22*, 3161–3165; (b) Wedeking, K.; Mu, Z.; Kehr, G.; Sierra, J. C.; Lichtenfeld, M. C.; Grimme, S.; Erker, G.; Fröhlich, R.; Chi, L.; Wang, W. Oligoethylene chains

terminated by ferrocenyl end groups: Synthesis, structural properties, and two-dimensional self-assembly on surfaces. *Chem. –Eur. J.* **2006**, *12*, 1618–1628.

63. Seiler, P.; Dunitz, J. D. The structure of triclinic ferrocene at 101, 123 and 148 K. *Acta Crystallogr., Sect. B Struct. Crystallogr. Cryst. Chem*. **1979**, *35*, 2020–2032.

64. O'Connor, A. R.; Nataro, C.; Golen, J. A.; Rheingold, A. L. Synthesis and reactivity of $[N(C_6H_4Br)_3][B(C_6F_5)_4]$: the X-ray crystal structure of $[Fe(C_5H_5)_2][B(C_6F_5)_4]$. *J. Organomet. Chem*. **2004**, *689*, 2411–2414.

65. Romanov, A. S.; Mulroy, J. M.; Khrustalev, V. N.; Antipin M. Y.; Timofeeva, T. V. Monohalogenated ferrocenes $C_5H_5FeC_5H_4X$ (X = Cl, Br and I) and a second polymorph of $C_5H_5FeC_5H_4I$. *Acta Crystallogr., Sect. C: Cryst. Struct. Commun*. **2009**, *65*, m426–m430.

66. Zeller, M.; Lufaso, M. W.; Curtin, L.; Hunter, A. D. *CSD Private Communication (CCDC# 252665)* **2004**.

67. Butler, I. R.; Cullen, W. R.; Rettig S. J.; Trotter, J. Structure of benzoylferrocene. *Acta Crystallogr. Sect. C Struct. Chem.* **1988**, *44*, 1666–1667.

68. Hnetinka, C. A.; Hunter, A. D.; Zeller, M.; Lesley, M. J. G. 1,1'-Dibromoferrocene. *Acta Crystallographica Section E: Structure Reports Online* **2004**, *60*, m1806–m1807.

69. Gallagher, J. F.; Ferguson, G.; Ahmed, S. Z.; Glidewell, C.; Lewis, A. Accurate redeterminations of 1,1'-Dibenzoylferrocene and (4-Nitrophenyl)ferrocene. *Acta Crystallogr., Sect. C (Cryst. Struct. Commun.)* **1997**, *53*, 1772–1775.

70. Smith, T. J.; Stevenson,K. J. ReferenceElectrodes. In Handbook of Electrochemistry, Zoski, C. G., Ed. Elsevier, **2007**, pp 73-110.

71. Kärkäs, M. D., Electrochemical strategies for C–H functionalization and C–N bond formation. *Chem. Soc. Rev.* **2018,** *47*, 5786-5865.

72. Pollok, D.; Waldvogel, S. R., Electro-organic synthesis – a 21st century technique. *Chem. Sci.* **2020,** *11*, 12386-12400.

73. Liu, J.; Lu, L.; Wood, D.; Lin, S., New Redox Strategies in Organic Synthesis by Means of Electrochemistry and Photochemistry. *ACS Cent. Sci.* **2020,** *6*, 1317-1340.

74. Wang, F.; Stahl, S. S., Electrochemical Oxidation of Organic Molecules at Lower Overpotential: Accessing Broader Functional Group Compatibility with Electron−Proton Transfer Mediators. *Acc. Chem. Res.* **2020,** *53*, 561-574.

75. Horn, E. J.; Rosen, B. R.; Chen, Y.; Tang, J.; Chen, K.; Eastgate, M. D.; Baran, P. S., Scalable and sustainable electrochemical allylic C-H oxidation. *Nature* **2016,** *533*, 77-81.

76. Basch, C. H.; Liao, J.; Xu, J.; Piane, J. J.; Watson, M. P., Harnessing Alkyl Amines as Electrophiles for Nickel-Catalyzed Cross Couplings via C–N Bond Activation. *J. Am. Chem. Soc.* **2017,** *139*, 5313-5316.

77. Hruszkewycz, D. P.; Miles, K. C.; Thiel, O. R.; Stahl, S. S., Co/NHPI-mediated aerobic oxygenation of benzylic C–H bonds in pharmaceutically relevant molecules. *Chem. Sci.* **2017,** *8*, 1282-1287.

78. Fu, N.; Sauer, G. S.; Saha, A.; Loo, A.; Lin, S., Metal-catalyzed electrochemical diazidation of alkenes. *Science* **2017,** *357*, 575.

79. Lennox, A. J. J.; Nutting, J. E.; Stahl, S. S., Selective electrochemical generation of benzylic radicals enabled by ferrocene-based electron-transfer mediators. *Chem. Sci.* **2018,** *9*, 356-361.

80. Deinhammer, R. S.; Ho, M.; Anderegg, J. W.; Porter, M. D., Electrochemical oxidation of amine-containing compounds: a route to the surface modification of glassy carbon electrodes. *Langmuir* **1994,** *10*, 1306-1313.

81. Torriero, A. A. J.; Shiddiky, M. J. A.; Burgar, I.; Bond, A. M., Homogeneous Electron-Transfer Reaction between Electrochemically Generated Ferrocenium Ions and Amine-Containing Compounds. *Organometallics* **2013,** *32*, 5731-5739.

82. Lin, M.-Y.; Xu, K.; Jiang, Y.-Y.; Liu, Y.-G.; Sun, B.-G.; Zeng, C.-C., Intermolecular Electrochemical C(sp3)-H/N-H Cross-coupling of Xanthenes with N-alkoxyamides: Radical Pathway Mediated by Ferrocene as a Redox Catalyst. *Adv. Synth. Catal.* **2018,** *360*, 1665-1672.

83. Hou, Z.-W.; Mao, Z.-Y.; Zhao, H.-B.; Melcamu, Y. Y.; Lu, X.; Song, J.; Xu, H.-C., Electrochemical C−H/N−H Functionalization for the Synthesis of Highly Functionalized (Aza)indoles. *Angew. Chem. Int. Ed.* **2016,** *55*, 9168-9172.

84. Torriero, A. A. J.; Morda, J.; Saw, J., Electrocatalytic Dealkylation of Amines Mediated by Ferrocene. *Organometallics* **2019,** *38*, 4280-4287.

85. Liu, L.; Wang, Z.; Fu, X.; Yan, C.-H., Azobisisobutyronitrile Initiated Aerobic Oxidative Transformation of Amines: Coupling of Primary Amines and Cyanation of Tertiary Amines. *Org. Lett.* **2012,** *14*, 5692-5695.

86. Dong, C.-p.; Higashiura, Y.; Marui, K.; Kumazawa, S.; Nomoto, A.; Ueshima, M.; Ogawa, A., Metal-Free Oxidative Coupling of Benzylamines to Imines under an

Oxygen Atmosphere Promoted Using Salicylic Acid Derivatives as Organocatalysts. *ACS Omega* **2016,** *1*, 799-807.

87. Fan, X.-N.; Ou, H.-D.; Deng, W.; Yao, Z.-J., Air-Stable Half-Sandwich Iridium Complexes as Aerobic Oxidation Catalysts for Imine Synthesis. *Inorg. Chem.* **2020,** *59*, 4800-4809.

88. Hu, J.; Wang, J.; Nguyen, T. H.; Zheng, N., The chemistry of amine radical cations produced by visible light photoredox catalysis. *Beilstein J. Org. Chem.* **2013,** *9*, 1977-2001.

89. Bhoi, Y. P.; Mishra, B. G., Synthesis, Characterization, and Photocatalytic Application of Type-II CdS/Bi2W2O9 Heterojunction Nanomaterials towards Aerobic Oxidation of Amines to Imines. *Eur. J. Inorg. Chem.* **2018,** *2018*, 2648-2658.

90. Deb, M.; Hazra, S.; Dolui, P.; Elias, A. J., Ferrocenium Promoted Oxidation of Benzyl Amines to Imines Using Water as the Solvent and Air as the Oxidant. *ACS Sustainable Chem. Eng.* **2019,** *7*, 479-486.

91. Barbier, B.; Pinson, J.; Desarmot, G.; Sanchez, M., Electrochemical Bonding of Amines to Carbon Fiber Surfaces Toward Improved Carbon-Epoxy Composites. *J. Electrochem. Soc.* **1990,** *137*, 1757-1764.

92. Savéant, J.-M., Molecular Catalysis of Electrochemical Reactions. Mechanistic Aspects. *Chem. Rev.* **2008,** *108*, 2348-2378.

93. Rountree, E. S.; McCarthy, B. D.; Eisenhart, T. T.; Dempsey, J. L., Evaluation of Homogeneous Electrocatalysts by Cyclic Voltammetry. *Inorg. Chem.* **2014,** *53*, 9983-10002.

94. Portis, L. C.; Bhat, V. V.; Mann, C. K., Electrochemical dealkylation of aliphatic tertiary and secondary amines. *J. Org. Chem.* **1970,** *35*, 2175-2178.

95. Ross, S. D., The mechanism of anodic dealkylation of aliphatic amines in acetonitrile. *Tetrahedron Lett.* **1973,** *14*, 1237-1240.

96. Adenier, A.; Chehimi, M. M.; Gallardo, I.; Pinson, J.; Vilà, N., Electrochemical Oxidation of Aliphatic Amines and Their Attachment to Carbon and Metal Surfaces. *Langmuir* **2004,** *20*, 8243-8253.

97. Wayner, D. D. M.; Dannenberg, J. J.; Griller, D., Oxidation potentials of α-aminoalkyl radicals: bond dissociation energies for related radical cations. *Chem. Phys. Lett.* **1986,** *131*, 189-191.

98. Smith, J. R. L.; Masheder, D., Amine oxidation. Part IX. The electrochemical oxidation of some tertiary amines: the effect of structure on reactivity. *Journal of the Chemical Society, Perkin Transactions 2* **1976**, 47-51.

99. Veer, S. D.; Katkar, K. V.; Akamanchi, K. G., Sulfated tungstate catalyzed activation of nitriles: addition of amines to nitriles for synthesis of amidines. *Tetrahedron Lett.* **2016,** *57*, 4039-4043.

100. Guilhem Rousselet, P. C., and Michel Maumy, Copper(I)-Induced Addition of Amines to Unactivated Nitriles: The First General One-Step Synthesis of Alkyl Amidines. . *Tetrahedron Lett.* **1993,** *34*, 6395-6398.

101. Rountree, E. S.; McCarthy, B. D.; Eisenhart, T. T.; Dempsey, J. L., Evaluation of Homogeneous Electrocatalysts by Cyclic Voltammetry. *Inorg. Chem.* **2014,** *53*, 9983-10002.